



An International ICT Journal
Featuring Industry–University–Institute Cooperation and
Indexed in Scopus

ISSN 1673-5188
CN 34-1294/TN

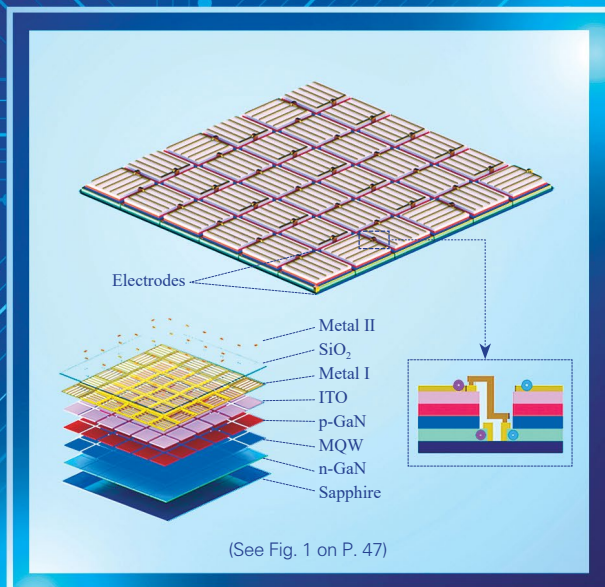
ZTE COMMUNICATIONS

中兴通讯技术(英文版)

<http://zte.magtechjournal.com>

December 2024, Vol. 22 No. 4

Special Topic: Optoelectronic Integrated Chips, Systems, and Key Technologies



ISSN 1673-5188



9 771673 518246

The 10th Editorial Board of ZTE Communications

Chairman

GAO Wen, Peking University (China)

Vice Chairmen

XU Ziyang, ZTE Corporation (China) | **XU Chengzhong**, University of Macau (China)

Members (Surname in Alphabetical Order)

AI Bo	Beijing Jiaotong University (China)
CAO Jiannong	The Hong Kong Polytechnic University (China)
CHEN Chang Wen	The Hong Kong Polytechnic University (China)
CHEN Yan	Northwestern University (USA)
CHI Nan	Fudan University (China)
CUI Shuguang	UC Davis (USA) and The Chinese University of Hong Kong, Shenzhen (China)
GAO Wen	Peking University (China)
GAO Yang	Nanjing University (China)
GAO Yue	Fudan University (China)
GE Xiaohu	Huazhong University of Science and Technology (China)
HE Yejun	Shenzhen University (China)
Victor C. M. LEUNG	The University of British Columbia (Canada)
LI Xiangyang	University of Science and Technology of China (China)
LI Zixue	ZTE Corporation (China)
LIAO Yong	Chongqing University (China)
LIN Xiaodong	ZTE Corporation (China)
LIU Chi	Beijing Institute of Technology (China)
LIU Jian	ZTE Corporation (China)
LIU Yue	Beijing Institute of Technology (China)
MA Jianhua	Hosei University (Japan)
MA Zheng	Southwest Jiaotong University (China)
PAN Yi	Shenzhen University of Advanced Technology, Chinese Academy of Sciences (China)
PENG Mugen	Beijing University of Posts and Telecommunications (China)
REN Fuji	Tokushima University (Japan)
REN Kui	Zhejiang University (China)
SHENG Min	Xidian University (China)
SU Zhou	Xi'an Jiaotong University (China)
SUN Huifang	Pengcheng Laboratory (China)
SUN Zhili	University of Surrey (UK)
TAO Meixia	Shanghai Jiao Tong University (China)
WANG Chengxiang	Southeast University (China)
WANG Haiming	Southeast University (China)
WANG Xiang	ZTE Corporation (China)
WANG Xiyu	ZTE Corporation (China)
WANG Yongjin	Nanjing University of Posts and Telecommunications (China)
XU Chengzhong	University of Macau (China)
XU Ziyang	ZTE Corporation (China)
YANG Kun	University of Essex (UK)
YU Hongfang	University of Electronic Science and Technology of China (China)
YUAN Jinhong	University of New South Wales (Australia)
ZENG Wenjun	Eastern Institute of Technology, Ningbo (China)
ZHANG Honggang	Zhejiang Lab (China)
ZHANG Jianhua	Beijing University of Posts and Telecommunications (China)
ZHANG Rui	The Chinese University of Hong Kong, Shenzhen (China)
ZHANG Wenqiang	Fudan University (China)
ZHANG Yueping	Nanyang Technological University (Singapore)
ZHOU Wanlei	City University of Macau (China)
ZHUANG Weihua	University of Waterloo (Canada)

Special Topic ► **Optoelectronic Integrated Chips, Systems, and Key Technologies**

- 01 Guest Editorial WANG Yongjin
- 03 Monolithically Integrated Photonic Structures for Stable On-Chip Solar Blind Communications
..... HE Rui, HU Qiang, RAN Junxue, WANG Junxi, WEI Tongbo
- 09 Research on High-Precision Stochastic Computing VLSI Structures for Deep Neural Network Accelerators ... WU Jingguo, ZHU Jingwei, XIONG Xiankui, YAO Haidong, WANG Chengchen, CHEN Yun
- 18 Design of LCoS-Based Twin 1×40 Wavelength Selective Switch
..... WANG Han, LIU Maoqi, FENG Zhenhua, LIU Minghuan, MAO Baiwei
- 29 Ultra-Low Linewidth Frequency Stabilized Integrated Lasers: A New Frontier in Integrated Photonics
..... GU Zhenqian, YANG Zhen, ZHA Lulu, HU Junhui, CHI Nan, SHEN Chao
- 40 Monolithically Integrating a 180° Bent Waveguide into a III-Nitride Optoelectronic On-Chip System
..... ZHANG Hao, YE Ziqi, YUAN Jialei, LIU Pengzhan, WANG Yongjin
- 46 Performance Characterization of Visible Light Communication Based on GaN High-Voltage LED/PD
..... LU Meixin, JIANG Zitong, FANG Li, YAN Yiqun, YAN Jiabin

Research Papers ►

- 53 Multi-View Structured Light 3D Measurement System
..... LU Ping, ZHANG Yingjie, DENG Fangwei, LIU Wei, HUANG Shijun
- 59 A Filtering Coaxial Probe for Passive Intermodulation Characterization
..... BAI Yongjiang, YANG Jiye, ZHU Shaohao, YANG Ye, YE Ming
- 67 Unsupervised Motion Removal for Dynamic SLAM
..... CHEN Hao, ZHANG Kaijiong, CHEN Jun, ZHANG Ziwen, JIA Xia
- 78 Video Enhancement Network Based on CNN and Transformer
..... YUAN Lang, HUI Chen, WU Yanfeng, LIAO Ronghua, JIANG Feng, GAO Ying
- 89 A Privacy-Preserving Scheme for Multi-Party Vertical Federated Learning
..... FAN Mochan, ZHANG Zhipeng, LI Difei, ZHANG Qiming, YAO Haidong

Roundup ►

- I Table of Contents for Volume 22, 2024

Serial parameters: CN 34-1294/TN*2003*q*16*98*en*P*¥30.00*2200*12*2024-12

Submission of a manuscript implies that the submitted work has not been published before (except as part of a thesis or lecture note or report or in the form of an abstract); that it is not under consideration for publication elsewhere; that its publication has been approved by all co-authors as well as by the authorities at the institute where the work has been carried out; that, if and when the manuscript is accepted for publication, the authors hand over the transferable copyrights of the accepted manuscript to *ZTE Communications*; and that the manuscript or parts thereof will not be published elsewhere in any language without the consent of the copyright holder. Copyrights include, without spatial or timely limitation, the mechanical, electronic and visual reproduction and distribution; electronic storage and retrieval; and all other forms of electronic publication or any other types of publication including all subsidiary rights.

Responsibility for content rests on authors of signed articles and not on the editorial board of *ZTE Communications* or its sponsors.

Statement

This magazine is a free publication for you. If you do not want to receive it in the future, you can send the "TD unsubscribe" mail to magazine@zte.com.cn. We will not send you this magazine again after receiving your email. Thank you for your support.

ZTE Communications Guidelines for Authors

Remit of Journal

ZTE Communications publishes original theoretical papers, research findings, and surveys on a broad range of communications topics, including communications and information system design, optical fiber and electro-optical engineering, microwave technology, radio wave propagation, antenna engineering, electromagnetics, signal and image processing, and power engineering. The journal is designed to be an integrated forum for university academics and industry researchers from around the world.

Manuscript Preparation

Manuscripts must be typed in English and submitted electronically in MS Word (or compatible) format. The word length is approximately 3 000 to 8 000, and no more than 8 figures or tables should be included. Authors are requested to submit mathematical material and graphics in an editable format.

Abstract and Keywords

Each manuscript must include an abstract of approximately 150 words written as a single paragraph. The abstract should not include mathematics or references and should not be repeated verbatim in the introduction. The abstract should be a self-contained overview of the aims, methods, experimental results, and significance of research outlined in the paper. Three to eight carefully chosen keywords must be provided with the abstract.

References

Manuscripts must be referenced at a level that conforms to international academic standards. All references must be numbered sequentially in-text and listed in corresponding order at the end of the paper. References that are not cited in-text should not be included in the reference list. References must be complete and formatted according to *ZTE Communications* Editorial Style. A minimum of 10 references should be provided. Footnotes should be avoided or kept to a minimum.

Copyright and Declaration

Authors are responsible for obtaining permission to reproduce any material for which they do not hold copyright. Permission to reproduce any part of this publication for commercial use must be obtained in advance from the editorial office of *ZTE Communications*. Authors agree that a) the manuscript is a product of research conducted by themselves and the stated co-authors; b) the manuscript has not been published elsewhere in its submitted form; c) the manuscript is not currently being considered for publication elsewhere. If the paper is an adaptation of a speech or presentation, acknowledgement of this is required within the paper. The number of co-authors should not exceed five.

Content and Structure

ZTE Communications seeks to publish original content that may build on existing literature in any field of communications. Authors should not dedicate a disproportionate amount of a paper to fundamental background, historical overviews, or chronologies that may be sufficiently dealt with by references. Authors are also requested to avoid the overuse of bullet points when structuring papers. The conclusion should include a commentary on the significance/future implications of the research as well as an overview of the material presented.

Peer Review and Editing

All manuscripts will be subject to a two-stage anonymous peer review as well as copyediting, and formatting. Authors may be asked to revise parts of a manuscript prior to publication.

Biographical Information

All authors are requested to provide a brief biography (approx. 100 words) that includes email address, educational background, career experience, research interests, awards, and publications.

Acknowledgements and Funding

A manuscript based on funded research must clearly state the program name, funding body, and grant number. Individuals who contributed to the manuscript should be acknowledged in a brief statement.

Address for Submission

<http://mc03.manuscriptcentral.com/ztecom>



Special Topic on Optoelectronic Integrated Chips, Systems, and Key Technologies

Guest Editor



WANG Yongjin is a professor with the GaN Optoelectronic Integration International Cooperation Joint Laboratory of Jiangsu Province at Nanjing University of Posts and Telecommunications, China. He received his PhD degree in microelectronics and solid-state electronics from Shanghai Institute of Microsystem and Information Technology, China in 2005. Prof. WANG held various research positions in Germany, Japan, and the UK with the support of Alexander von Humboldt Research Fellowship, Japan Society for the Promotion of Science Research Fellowship, and the Royal Academy of Engineering Research Fellowship, respectively. Since 2011, he has been working as a full professor at Nanjing University of Posts and Telecommunications. His current research interests focus on monolithic III-nitride photonic integration and all-light communication networks. He has authored over 150 technical publications including journal articles, conference proceedings, conference abstracts, and book chapters. Moreover, he holds five issued US patents and 30 issued Chinese patents.

Integrating electronics and photonics on a single chip is a key step towards low power consumption and efficient computing systems. In particular, multiple quantum well (MQW) diodes that inherently exhibit multifunctionalities of light emission, detection, modulation, and energy harvesting have great potential for the development of monolithic optoelectronic systems. Their emission spectra partially overlap with their responsivity spectra due to the same MQW active region, enabling monolithic photonic integration of optical transmitters, modulators, waveguides and receivers on a tiny chip. We can unite energy conservation, gravitational field and energy diagram theory to exploit the dual emission-detection characteristics of the MQW diode. We can also conclude that the gravitational effect creates irreversibility based on the following postulations: 1) individual objects cannot be completely isolated from their environment in reality, and the gravitational force must always act on them under any circumstances; 2) objects at different positions have different quantized states in a gravitation field and their masses, in turn, depends on their energy states; 3) the amount of work done against the gravitational force varies depending on the object's

movement from one location to another and back to its original position. Furthermore, the monolithic photonic circuit enables on-chip bidirectional real-time data transmission between arbitrary nodes within the optical network, and all communication nodes have equal and complete mapping characteristics, paving the way for sophisticated all-light interconnection networks to develop advanced information processing and computing systems.

This special issue aims to gather cutting-edge research and developments in the field of monolithic photonic integration. In this issue, a series of articles are presented to address the aforementioned challenges. These articles cover a wide range of topics, including wavelength selective switches, stabilized integrated lasers, monolithic III-nitride photonic integration and high-precision stochastic computing very large-scale integration (VLSI) structures. The call-for-papers of this special issue have brought excellent submissions in both quality and quantity. After two rounds of reviews, six papers have been selected for publication in this special issue which is organized as follows.

The first paper titled "Monolithically Integrated Photonic Structures for Stable On-Chip Solar Blind Communications" presents monolithically integrated AlGaIn photonic chips including light-emitting diodes, waveguides, and photodetectors. The stable on-chip solar-blind optical communication is experimentally demonstrated, confirming the great potential for future large-scale on-chip optical communication application.

The second paper titled "Research on High-Precision Sto-

DOI: 10.12142/ZTECOM.202404001

Citation (Format 1): WANG Y J. Editorial: optoelectronic integrated chips, systems, and key technologies [J]. *ZTE Communications*, 2024, 22(4): 1–2. DOI: 10.12142/ZTECOM.202404001

Citation (Format 2): Y. J. Wang, "Editorial: optoelectronic integrated chips, systems, and key technologies," *ZTE Communications*, vol. 22, no. 4, pp. 1–2, Dec. 2024. doi: 10.12142/ZTECOM.202404001.

chastic Computing VLSI Structures for Deep Neural Network Accelerators” proposes a probabilistic compensation algorithm to solve the accuracy problem of stochastic calculation, wherein a fully parallel neural network accelerator based on a deterministic method is designed. This work provides a promising way to implement deep neural networks and reduce hardware consumption.

The third paper titled “Design of LCoS-Based Twin 1×40 Wavelength Selective Switch” presents a compact architecture of twin 1×40 LCoS-based wavelength selective switches, which can be regarded as a $4f$ system in the wavelength direction and a $2f$ system in the switching direction. The wavelength selective switch is a crucial component of the reconfigurable optical add/drop multiplexer, which plays a pivotal role in the next-generation all-optical networks. This work establishes a solid foundation for the future development of high-performance wavelength selective switches with larger port counts.

The fourth paper titled “Ultra-Low Linewidth Frequency Stabilized Integrated Lasers: A New Frontier in Integrated Photonics” summarizes recent advancements in integrated photonics for achieving ultra-low linewidth lasers. It particularly focuses on the breakthroughs made through the integration of Brillouin lasers, which have shown significant potential in fields such as precision measurement, quantum communication, and atomic clocks.

The fifth paper titled “Monolithically Integrating a 180° Bent Waveguide into a III-Nitride Optoelectronic On-Chip System” presents an on-chip optoelectronic system on a III-nitride-on-silicon platform fabricated via a top-down ap-

proach. The system includes a near-ultraviolet light source, monitor, 180° bending waveguide, electro-absorption modulator, and receiver, and on-chip optical data communication is demonstrated through light propagation within the system, opening a feasible route towards monolithic integration of various III-nitride-based components onto a single chip to create future optoelectronic systems with low power consumption.

The sixth paper titled “Performance Characterization of Visible Light Communication Based on GaN High-Voltage LED/PD” reports a high-voltage series-connected light-emitting diode (LED) or photodetector based on the GaN integrated photoelectronic chip, wherein MQW diodes with identical structures are integrated on a single chip through wafer-scale micro-fabrication techniques, and connected in series to construct the high-voltage series-connected LED/photodetector. The light communication performance of the high-voltage series-connected LED/ photodetector is experimentally demonstrated.

To conclude, it is hoped that this special issue will serve as a valuable resource for researchers, practitioners, and students who are interested in monolithic optoelectronic system on a chip. We also hope that it will inspire further research in this field, leading to new and innovative solutions that will drive the evolution of monolithic photonic integration. Finally, we would like to express our sincere gratitude to all the authors, reviewers, and editorial staff who have contributed to the success of this special issue. Hopefully, the articles in this special issue are both insightful and informative for prospective readers in the field.



Monolithically Integrated Photonic Structures for Stable On-Chip Solar Blind Communications

HE Rui^{1,2}, HU Qiang^{1,2}, RAN Junxue^{1,2}, WANG Junxi^{1,2}, WEI Tongbo^{1,2}

(1. Research and Development Center for Wide Bandgap Semiconductors, Institute of Semiconductors, Chinese Academy of Sciences, Beijing 100083, China;

2. Center of Materials Science and Optoelectronics Engineering, University of Chinese Academy of Sciences, Beijing 100049, China)

DOI: 10.12142/ZTECOM.202404002

<https://kns.cnki.net/kcms/detail/34.1294.TN.20241028.1701.002.html>, published online October 29, 2024

Manuscript received: 2024-09-11

Abstract: A solar-blind multi-quantum well (MQW) structure wafer based on AlGaN materials is epitaxial growth by metal-organic chemical vapor deposition (MOCVD). The monolithically integrated photonic chips including light-emitting diodes (LEDs), waveguides, and photodetectors (PDs) are presented. The results of the finite-difference time-domain (FDTD) simulation confirm the strong light constraint of the waveguide designed with the triangular structure in the optical coupling region. Furthermore, in virtue of predominant ultraviolet transverse magnetic (TM) modes, the solar blind optical signal is more conducive to lateral transmission along the waveguide inside the integrated chip. The integrated PDs demonstrate sufficient photosensitivity to the optical signal from the integrated LEDs. When the LEDs are operated at 100 mA current, the photo-to-dark current ratio (PDCR) of the integrated PD is about seven orders of magnitude. The responsivity, specific detectivity, and external quantum efficiency of the integrated self-driven PD are 74.89 A/W, 4.22×10^{13} Jones, and $3.38 \times 10^4\%$, respectively. The stable on-chip optical information transmission capability of the monolithically integrated photonic chips confirms the great potential for application in large-scale on-chip optical communication in the future.

Keywords: monolithically integration; photonic chips; UVC; solar-blind communication

Citation (Format 1): HE R, HU Q, RAN J X, et al. Monolithically integrated photonic structures for stable on-chip solar blind communications [J]. *ZTE Communications*, 2024, 22(4): 3 – 8. DOI: 10.12142/ZTECOM.202404002

Citation (Format 2): R. He, Q. Hu, J. X. Ran, et al., “Monolithically integrated photonic structures for stable on-chip solar blind communications,” *ZTE Communications*, vol. 22, no. 4, pp. 3 – 8, Dec. 2024. doi: 10.12142/ZTECOM.202404002.

1 Introduction

The rapid development of III-V nitride epitaxial growth technology has driven the advancement and application of multifunctional photoelectronic integrated devices based on nitride materials^[1]. Due to the wide bandgap (6.2 eV~0.7 eV) of nitride materials, the corresponding nitride multiple quantum well (MQW) structure can cover wavelengths from deep ultraviolet to infrared^[2]. Currently, the application of MQW structure light-emitting diodes (LED) is no longer limited to solid-state lighting but is gradually expanding into fields

such as biochemical detection, sensing, optical communication, optical computing, and displays^[3-6]. As the core of future optical interconnects, on-chip optical communication technology consisting of light emission, transmission, and reception is becoming the key scientific technology driving the transition from on-chip electrical transmission to on-chip optical transmission^[7-8]. The bonding processes introduced by traditional silicon-based heterogeneous integration technology significantly increase production costs, and low yield and high instability are also inevitable^[9]. The epitaxial growth technology based on III-V nitride homogeneous integration can directly fabricate highly stable and multifunctional photonic integrated chips, providing a tremendous opportunity to advance on-chip optical communication technology.

In recent years, there have been numerous research reports on multifunctional on-chip integrated chips based on MQW structure light-emitting epitaxial wafers that can simultane-

This work was financially supported by the Key Field R&D Program of Guangdong Province under Grant No. 2021B0101300001, the National Key R&D Program of China under Grant No. 2022YFB3605003, the National Natural Science Foundation of China under Grant Nos. 52192614 and 62135013, Beijing Natural Science Foundation under Grant No. 4222077, Beijing Science and Technology Plan under Grant No. Z221100002722019, and Guangdong Basic and Applied Basic Research Foundation under Grant No. 2022B1515120081.

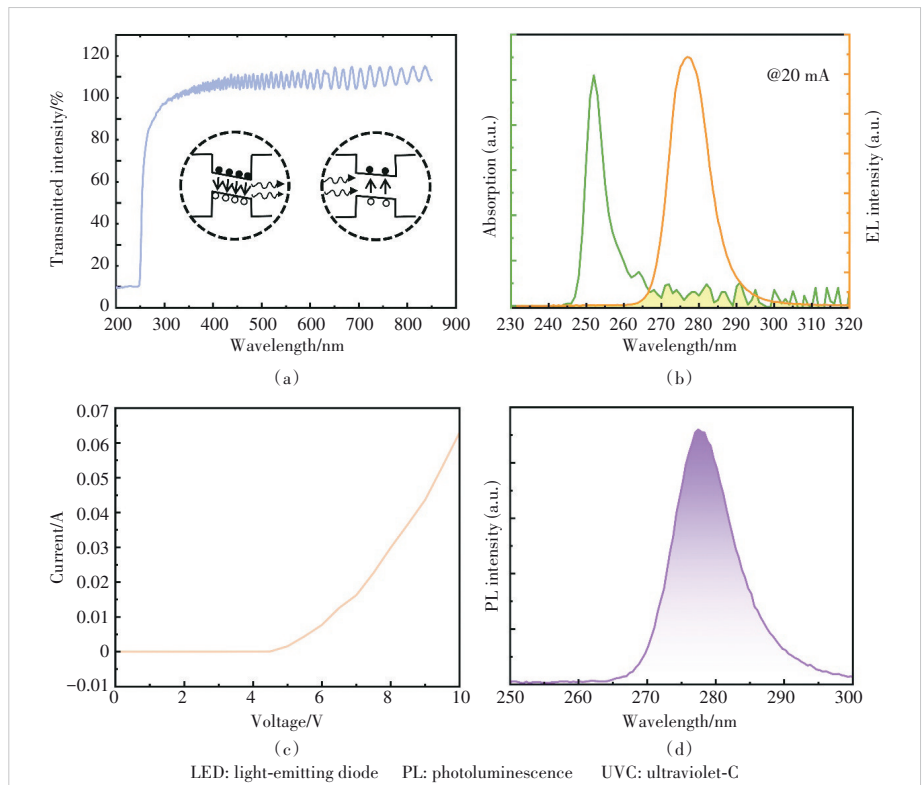
ously achieve both emission and detection^[10-13]. Unfortunately, the corresponding monolithic integrated photonic chips are mainly concentrated in the visible light band. The light emitted by visible light LEDs is divergent, which is not conducive to confining the optical signals within the integrated chip for on-chip optical communication. Moreover, the presence of unavoidable visible light in free environments necessitates consideration of how to avoid light noise interference when using visible light photonic integrated chips. In contrast, solar-blind photonic integrated chips have the following advantages: 1) The scattering of ultraviolet light by atmospheric particles creates a good application scenario free from ultraviolet light interference in ground-based free space. 2) Ultraviolet light is mainly composed of transverse magnetic (TM) modes, which is extremely beneficial for the lateral optical transmission of ultraviolet light signals within the integrated chips. 3) The carrier lifetime of deep ultraviolet light-emitting epitaxial wafers is lower, making it more advantageous to construct high-bandwidth photonic integrated chips for on-chip optical communication^[14-16].

In this work, we successfully realize monolithically integrated chip fabrication of solar blind LEDs, waveguides, and PDs on an AlGa_N MQW structure wafer. Combined with finite difference time domain (FDTD) simulation, the strong light constraint and advantages of horizontal transmission of solar blind TM modes are demonstrated. The photo-to-dark current ratio (PDCR) of the integrated self-driven PD is about seven orders of magnitude when the integrated LED is operated at 100 mA current. The responsivity, specific detectivity and external quantum efficiency (EQE) of the integrated self-driven PD are all excellent. This work will provide lots of experimental experience to promote the development of solar blind on-chip communication.

2 Experiment Details

The AlGa_N-based ultraviolet-C (UVC) MQW structure epilayers are grown on 2-inch c-plane sapphire substrates using metal organic chemical vapor deposition (MOCVD). The designed UVC LED structure consists of 2.5 μm thick AlN, 20-period AlN/Al_{0.6}Ga_{0.4}N SLs, a 2.0 μm n-Al_{0.67}Ga_{0.33}N layer, a 1.3 μm n-Al_{0.55}Ga_{0.45}N layer, 5-period Al_{0.50}Ga_{0.50}N/Al_{0.37}Ga_{0.63}N MQWs, an about 30 nm superlattices-electron barrier layer (SLs-EBL), an about 20 nm graded p-AlGa_N hole injection layer, and a 2 nm p-Al_{0.2}Ga_{0.8}N contact layer.

Here, a novel SLs-EBL structure is specially designed to expand the potential field region and enhance the performance of the integrated device. More detailed design information on the SLs-EBL structure is presented in our previous related work^[17]. Fig. 1a shows the optical transmission spectrum of the designed UVC LED structure. The well-defined oscillation curve demonstrates that the grown nitride epitaxial materials possess high quality. The growth of high-quality nitride epitaxy is fundamental to the fabrication of highly stable and uniform photonic integrated chips. The schematic diagram illustrates the physical mechanism of simultaneously achieving optical signal emission and reception using the same MQW structure LED epilayer in Fig. 1a. The one on the left is used as the integrated LED to emit light signals, and that on the right is used as the integrated PD to detect light signals. The part of photons from the integrated LED can be effectively absorbed by the integrated PD with the same MQWs structure. This phenomenon is caused by the partial overlap between the emission spectrum and the detection spectrum of the same MQW structure epilayer, as shown in Fig. 1b. The yellow shaded area represents the overlapping tail portion of the emission and detection spectra of the same MQW structure epilayer. This region provides the physical basis for constructing the on-chip optical information links. The excellent optoelectronic properties of the luminous epilayer are the necessary



▲ Figure 1. (a) Optical transmission spectrum of the UVC LED epilayer, (b) absorption and EL spectra of the UVC LED epilayer, where the yellow shadow is the overlap region of these spectra, (c) I-V characteristic of the integrated LED, and (d) PL spectrum of LED epilayer

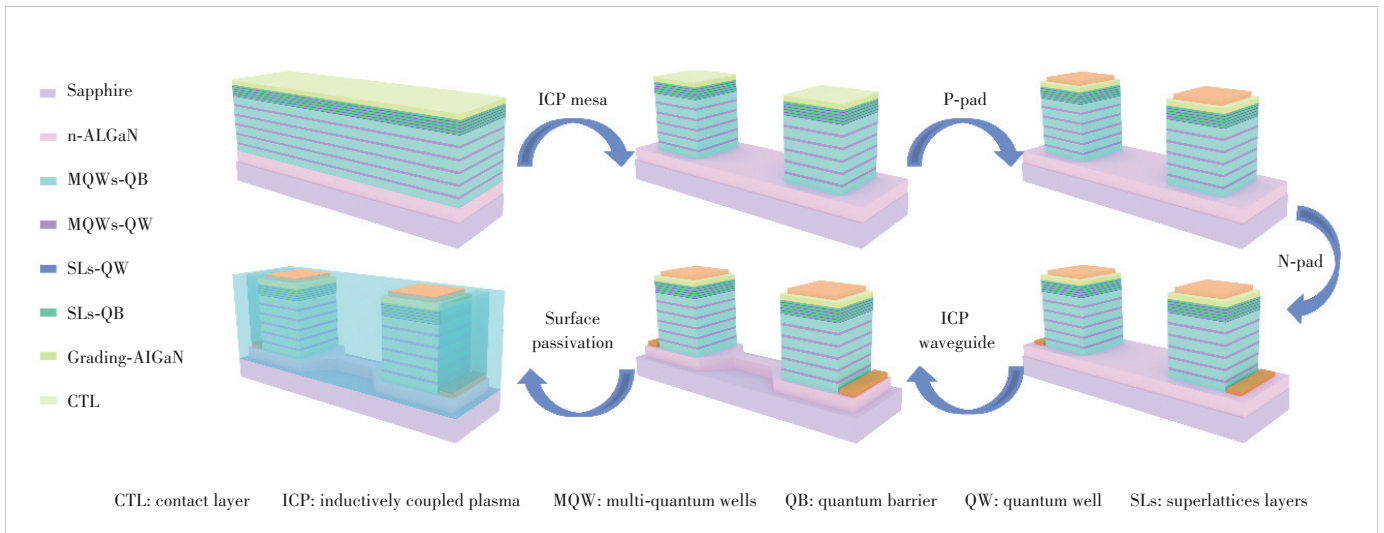
foundation for achieving efficient on-chip optical interconnects. Fig. 1c shows the I-V characteristic of the LED fabricated on the luminous epilayer with high quality. The low turn-on voltage implies reduced energy consumption. Furthermore, the photoluminescence (PL) spectrum in Fig. 1d shows an emission peak at approximately 277 nm, which falls within the solar-blind spectrum range. Ambient light causes minimal noise for solar-blind integrated chips, significantly broadening their application range, which is a major advantage of solar-blind integrated chips for future multifunctional large-scale integration applications.

The epilayer is fabricated as the monolithically integrated chips including integrated LEDs, waveguides, and PDs. Fig. 2 shows the fabrication processes of a monolithically integrated devices. Firstly, the mesa regions of the integrated LED and the integrated PD are defined by the inductively coupled plasma reactive ion etching (inductively coupled plasma-reactive ion etching, speed: 40 Å/s) with an etching depth of 500 nm. Secondly, Ti/Al/Ni/Au (20/60/30/100 nm) multi-layers are evaporated by an electron beam evaporator (EBE) and lifted off to form the p-contact metal electrodes of the integrated LED and integrated PD. Then the electrodes are treated by rapid thermal annealing (RTA) at 1 000 °C for 30 s in N₂ ambient to improve the ohmic contact performance. Similarly, Ni/Au (20/20 nm) multi-layers are deposited and lifted off to form the n-contact metal electrodes, followed by RTA at 700 °C for 1 min in N₂ atmosphere. Although two cathode electrodes are connected indirectly through the n-AlGaIn layer, the integrated LED and PD work independently. Subsequently, the structure of the waveguide is defined by photolithography and transferred into the n-AlGaIn layer through inductively coupled plasma (ICP) dry etching. It should be noted that for optimal optical confinement, the waveguides are vertically penetrated to the n-AlGaIn layer with a depth of 2.5 μm. Finally, a high-quality

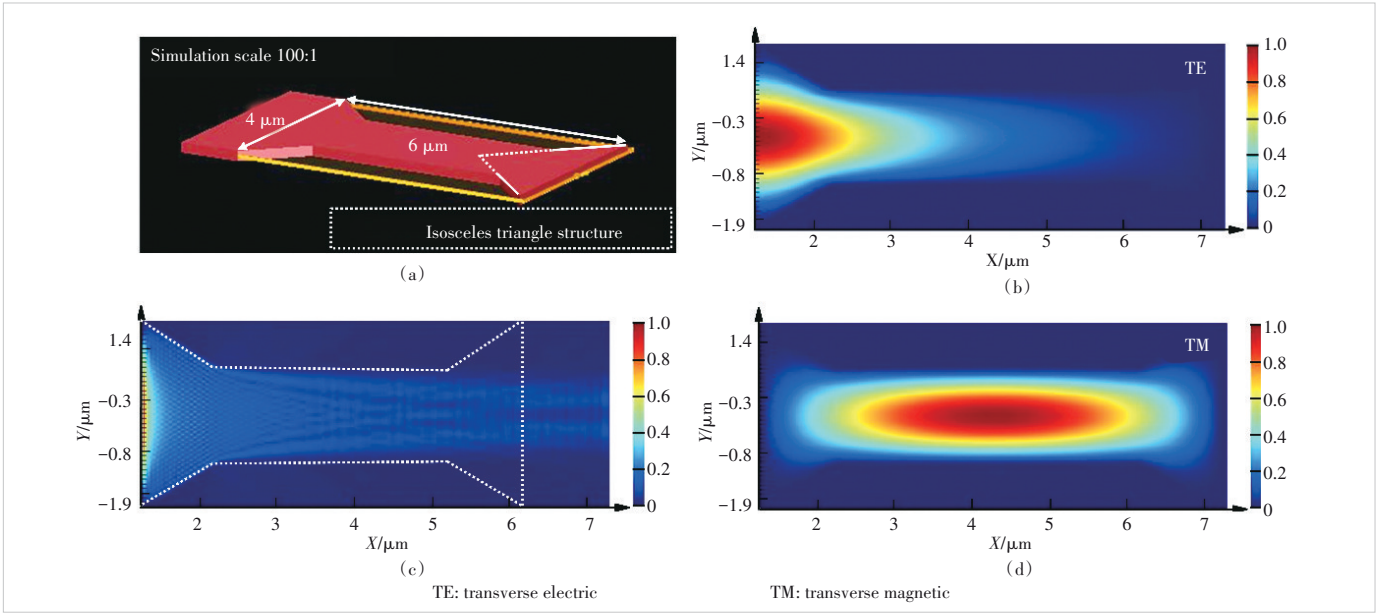
SiO₂ passivation protective layer with a thickness of 100 nm is deposited by plasma enhanced chemical vapor deposition (PECVD) and patterned by buffered oxide etch (BOE). It is important to emphasize that traditional ultraviolet LEDs use flip-chip packaging to allow more light to diverge, thereby improving light output efficiency. Here, we use gold wire bonding to package the monolithic integrated chips to better confine the ultraviolet light signal within the chip for lateral transmission, rather than allowing it to diverge.

3 Results and Discussions

FDTD simulation software is used to simulate the optical field distribution of the integrated waveguide. Fig. 3a presents the physical model of the integrated waveguide with an isosceles triangle structure. The simulation uses a scale of 100:1, so the actual waveguide length is 600 μm, and the base length of the triangle is 400 μm. Here, the refractive index for simulation is 2.42. Fig. 3b shows the optical field distribution when the optical signal propagates in the integrated waveguide. Due to the significant refractive index difference with the surrounding air environment, the integrated waveguide exhibits strong light confinement effects and demonstrates efficient optical information transmission capabilities. Furthermore, designing the waveguide structure as the isosceles triangle can further reduce optical crosstalk between adjacent devices during signal transmission, advancing the development of future large-scale photonic integration technology. We will further enhance the optical confinement of the integrated waveguide and strengthen the optical connection between the integrated LED and the integrated PD by optimizing the waveguide structure in subsequent work. Figs. 3c and 3d show the distribution of different mode light in the integrated waveguide. Notably, the TM mode light distributes better laterally in the integrated waveguide than the transverse electric (TE) mode light. It is well known that ultraviolet light is mainly composed of TM



▲ Figure 2. Fabrication processes of the monolithically integrated device using the designed UVC LED epilayer



▲ Figure 3. FDTD simulations of the waveguide structure: (a) schematic diagram of the simulated waveguide structure, (b) light field distribution in the n-AlGaIn waveguide, (c) TE, and (d) TM modes distribution in the channel waveguide

modes that are more conducive to the lateral transmission of optical signals on-chip^[18]. This is one of the main reasons why we choose solar-blind light for on-chip information transmission.

Fig. 4a shows the log-scaled current-voltage (I-V) plots for the integrated PD at the different injection current levels of the integrated LED from 0 mA to 100 mA. The dark currents under increased reverse bias voltages gradually increase from ~10 fA to ~1 nA due to high density dislocations in the AlGaIn epilayer. However, as the injection current of the integrated LED is increased from 0 to 100 mA, the photocurrents of the integrated PD rise by about 7 orders of magnitude at 0 V bias. To quantify the response ability of the MQW structure PD, the responsivity R , specific detectivity D^* , and EQE are key parameters determined by the following equations^[19-21].

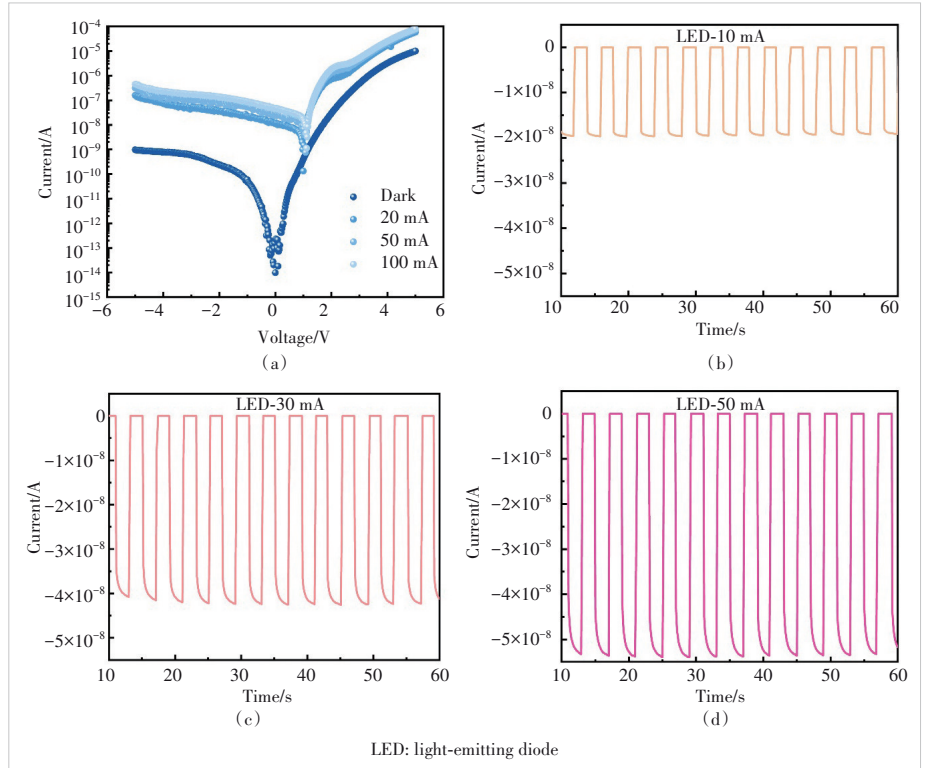
$$\Delta P = S \times I_p, \quad (1)$$

$$R = \frac{\Delta I}{\Delta P}, \quad (2)$$

$$D^* = \frac{\sqrt{A} R}{\sqrt{2eI_d}}, \quad (3)$$

$$EQE = \frac{hcR}{e\lambda}, \quad (4)$$

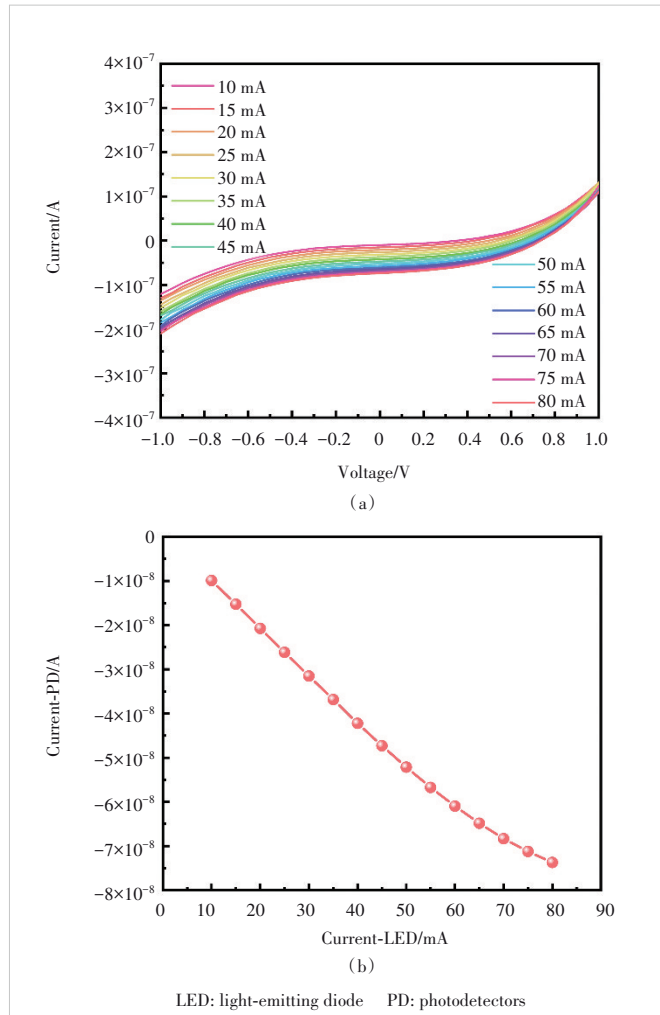
where S is the side wall area of the PD (about 1 000 μm^2), I_p



▲ Figure 4. (a) I-V plots of the integrated PD responding to illumination from the integrated LED operated at currents from 0 (dark) to 100 mA; induced photocurrent temporal trace of the integrated PD at 0 V bias with the cyclical light changes in the integrated LED under (b) 10 mA, (c) 30 mA, and (d) 50 mA, respectively

is the optical power density, ΔI is the photocurrent (subtracting the dark-current from the photo-excited current), ΔP is the incident light intensity, A is the effective illuminated area, e is the elementary electric charge, I_d is the dark-current, h is Planck's constant, c is the speed of light, and λ is the incident light wavelength. For the integrated PD, the calculated R is 74.89 A/W, D^* is 4.22×10^{13} Jones, and EQE is $3.38 \times 10^4\%$. The time-resolved photocurrents of the integrated PD in response to the turn-on and turn-off state of the illumination from the integrated LED are shown in Figs. 4b - 4d. The currents applied to the integrated LED under the turn-on state are 10 mA, 30 mA, and 50 mA, respectively. The smooth and consistent signal response benefits from high PDCR and negligible thermal effect, demonstrating excellent response properties of the MQW structure PD.

Fig. 5a shows the I-V plots for the integrated PD at the different injection current levels of the integrated LED from



▲ Figure 5. (a) Photocurrents of the integrated PD responding to illumination from the integrated LED operated at currents from 10 mA to 100 mA; (b) change trend of the integrated PD photocurrent under different integrated LED injection currents

10 mA to 80 mA. Obviously, the photocurrent of the integrated PD will change with the change of the currents applied to the integrated LED indicating the stable optical link established between the integrated LED and the integrated PD. As depicted in Fig. 5b, the measured photocurrent of the integrated PD without voltage bias is directly proportional to the intensity of the incident current of the integrated LED, which is the prerequisite for stable work of the on-chip communication integration system. The integrated LED is used as the emitter, the integrated PD as the receiver, and the waveguide is used to build the optical bridge between the integrated LED and the integrated PD. The solar-blind monolithically photonic integrated chip integrating optical signal transmitter-waveguide-receivers is expected to construct a stable optical communication system without ambient light interference for large-scale on-chip optical interconnection and optical computing in the future.

4 Conclusions

In summary, the monolithically integrated photonic chips including LEDs, waveguides, and PDs are fabricated on the solar blind epilayer with the MQW structure. Because of the significant refractive index different from surrounding air, the waveguide shows excellent strong light constraint improving the transmission efficiency. Furthermore, the dominant TM modes in solar blind light are conducive to transverse optical transmission of optical signals along the waveguide inside the integrated chips. The PDCR of the integrated self-driven PD is about seven orders of magnitude when the integrated LED is operated at 100 mA current. The responsivity, specific detectivity and EQE of the integrated self-driven PD are all at an advanced level. This work will promote the application of solar-blind photonic integration technology, laying an experimental foundation for the development of high-quality high-speed on-chip optical communication technology in the future.

Acknowledgement

We would like to thank Dr. WANG Lili of Institute of Semiconductors, Chinese Academy of Sciences, for the contribution to this paper.

References

- [1] REN A B, WANG H, ZHANG W, et al. Emerging light-emitting diodes for next-generation data communications [J]. Nature electronics, 2021, 4(8): 559 - 572. DOI: 10.1038/s41928-021-00624-7
- [2] LIANG D D, WEI T B, WANG J X, et al. Quasi van der Waals epitaxy nitride materials and devices on two dimension materials [J]. Nano energy, 2020, 69: 104463. DOI: 10.1016/j.nanoen.2020.104463
- [3] KNEISSL M, SEONG T Y, HAN J, et al. The emergence and prospects of deep-ultraviolet light-emitting diode technologies [J]. Nature photonics, 2019, 13(4): 233 - 244. DOI: 10.1038/s41566-019-0359-9
- [4] GUO L, GUO Y N, WANG J X, et al. Ultraviolet communication technique and its application [J]. Journal of semiconductors, 2021, 42(8): 081801.

- DOI: 10.1088/1674-4926/42/8/081801
- [5] YIN J H, YANG H Y, LUO Y M, et al. III-nitride microsensors for 360° angle detection [J]. IEEE electron device letters, 2022, 43(3): 458 - 461. DOI: 10.1109/LED.2022.3148232
- [6] ZHANG H, YAN J B, YE Z Q, et al. Monolithic GaN optoelectronic system on a Si substrate [J]. Applied physics letters, 2022, 121(18): 181103. DOI: 10.1063/5.0125324
- [7] LI K H, FU W Y, CHOI H W. Chip-scale GaN integration [J]. Progress in quantum electronics, 2020, 70: 100247. DOI: 10.1016/j.pquan-telec.2020.100247
- [8] SURYO W H, DANIEL P J, JAN G, et al. Beyond solid-state lighting: miniaturization, hybrid integration, and applications of GaN nano- and micro-LEDs [J]. Applied physics reviews, 2019, 6(4): 41315
- [9] LIU A Y, BOWERS J. Photonic integration with epitaxial III - V on silicon [J]. IEEE journal of selected topics in quantum electronics, 2018, 24(6): 6000412. DOI: 10.1109/JSTQE.2018.2854542
- [10] YAN L T, JIN Z X, LIN R Z, et al. InGaN micro-LED array with integrated emission and detection functions for color detection application [J]. Optics letters, 2023, 48(11): 2861 - 2864. DOI: 10.1364/OL.485939
- [11] HE R, WANG L L, CHEN R F, et al. Monolithically integrated photonic chips with asymmetric MQWs structure for suppressing Stokes shift [J]. Applied physics letters, 2023, 122(2): 021105. DOI: 10.1063/5.0131115
- [12] LI K H, FU W Y, CHEUNG Y F, et al. Monolithically integrated InGaN/GaN light-emitting diodes, photodetectors, and waveguides on Si substrate [J]. Optica, 2018, 5(5): 564. DOI: 10.1364/optica.5.000564
- [13] ZHANG F H, SHI Z, GAO X M, et al. On-chip multicomponent system made with an InGaN directional coupler [J]. Optics letters, 2018, 43(8): 1874 - 1877
- [14] GUO L, GUO Y N, YANG J K, et al. 275 nm deep ultraviolet AlGaIn-based micro-LED arrays for ultraviolet communication [J]. IEEE photonics journal, 2022, 14(1): 8202905. DOI: 10.1109/JPHOT.2021.3129648
- [15] SHAKYA J, KNABE K, KIM K H, et al. Polarization of III-nitride blue and ultraviolet light-emitting diodes [J]. Applied physics letters, 2005, 86(9): 091107. DOI: 10.1063/1.1875751
- [16] HE R, LIU N X, GAO Y Q, et al. Monolithically integrated UVC AlGaIn-based multiple quantum wells structure and photonic chips for solar-blind communications [J]. Nano energy, 2022, 104: 107928. DOI: 10.1016/j.nanoen.2022.107928
- [17] HE R, SONG Y J, LIU N X, et al. Solar-blind photonic integrated chips for real-time on-chip communication [J]. APL photonics, 2024, 9(7). DOI: 10.1063/5.0206657
- [18] KOLBE T, KNAUER A, CHUA C, et al. Optical polarization characteristics of ultraviolet (In) (Al)GaIn multiple quantum well light emitting diodes [J]. Applied physics letters, 2010, 97(17): 171105. DOI: 10.1063/1.3506585
- [19] JIN Z W, GAO L, ZHOU Q, et al. High-performance flexible ultraviolet photoconductors based on solution-processed ultrathin ZnO/Au nanoparticle composite films [J]. Scientific reports, 2014, 4: 4268. DOI: 10.1038/srep04268
- [20] RATHKANTHIWAR S, KALRA A, SOLANKE S V, et al. Gain mechanism and carrier transport in high responsivity AlGaIn-based solar blind metal semiconductor metal photodetectors [J]. Journal of applied physics, 2017, 121(16): 164502. DOI: 10.1063/1.4982354
- [21] HE R, WANG Y X, SONG Y J, et al. Selective area grown photonic integrated chips for completely suppressing the Stokes shift [J]. Applied physics letters, 2024, 124(25): 251103. DOI: 10.1063/5.0213979

Biographies

HE Rui is now pursuing her PhD degree in the Institute of Semiconductors, Chinese Academy of Sciences. She received her BS degree in applied physics from University of Science and Technology Beijing, China. Her research mainly focuses on the research of optoelectronic integrated devices based on wide bandgap semiconductor materials.

HU Qiang is currently an associate professor in Research and Development Center for Wide Bandgap Semiconductors, Institute of Semiconductors, Chinese Academy of Sciences. His research interests focus on wide gap semiconductor MOCVD epitaxy and power devices.

RAN Junxue received his PhD degree from Institute of Semiconductors, Chinese Academy of Sciences in 2006. He is currently an associate professor in Research and Development Center for Wide Bandgap Semiconductors, Institute of Semiconductors, Chinese Academy of Sciences. His research interests focus on wide gap semiconductor MOCVD epitaxy and power devices.

WANG Junxi is currently a professor in materials physics and chemistry, Institute of Semiconductors, Chinese Academy of Sciences. He received his bachelor's degree in physics from Northwestern University, China in 1998, and his doctoral degree in engineering from Institute of Semiconductors, Chinese Academy of Sciences in 2003. His research interests focus on wide gap semiconductor material epitaxy, deep ultraviolet light-emitting diode (DUV-LED) devices, advanced semiconductor materials, and their applications.

WEI Tongbo (tbwei@semi.ac.cn) is currently a professor in materials physics and chemistry, Institute of Semiconductors, Chinese Academy of Sciences. He received his doctoral degree in engineering from the Institute of Semiconductors, Chinese Academy of Sciences in July 2007. His research interests focus on wide bandgap semiconductor materials and devices, new micronano photoelectronic devices, deep ultraviolet light emitting devices, and nitride growth on two-dimensional materials.



Research on High-Precision Stochastic Computing VLSI Structures for Deep Neural Network Accelerators

WU Jingguo¹, ZHU Jingwei¹, XIONG Xiankui^{2,3},
YAO Haidong^{2,3}, WANG Chengchen^{2,3}, CHEN Yun¹

(1. Fudan University, Shanghai 200433, China;
2. State Key Laboratory of Mobile Network and Mobile Multimedia
Technology, Shenzhen 518055, China;
3. ZTE Corporation, Shenzhen 518057, China)

DOI: 10.12142/ZTECOM.202404003

<https://kns.cnki.net/kcms/detail/34.1294.TN.20241105.1346.002.html>,
published online November 5, 2024

Manuscript received: 2024-08-04

Abstract: Deep neural networks (DNN) are widely used in image recognition, image classification, and other fields. However, as the model size increases, the DNN hardware accelerators face the challenge of higher area overhead and energy consumption. In recent years, stochastic computing (SC) has been considered a way to realize deep neural networks and reduce hardware consumption. A probabilistic compensation algorithm is proposed to solve the accuracy problem of stochastic calculation, and a fully parallel neural network accelerator based on a deterministic method is designed. The software simulation results show that the accuracy of the probability compensation algorithm on the CIFAR-10 data set is 95.32%, which is 14.98% higher than that of the traditional SC algorithm. The accuracy of the deterministic algorithm on the CIFAR-10 dataset is 95.06%, which is 14.72% higher than that of the traditional SC algorithm. The results of Very Large Scale Integration Circuit (VLSI) hardware tests show that the normalized energy efficiency of the fully parallel neural network accelerator based on the deterministic method is improved by 31% compared with the circuit based on binary computing.

Keywords: stochastic computing; hardware accelerator; deep neural network

Citation (Format 1): WU J G, ZHU J W, XIONG X K, et al. Research on high-precision stochastic computing VLSI structures for deep neural network accelerators [J]. *ZTE Communications*, 2024, 22(4): 9 - 17. DOI: 10.12142/ZTECOM.202404003

Citation (Format 2): J. G. Wu, J. W. Zhu, X. K. Xiong, et al., "Research on high-precision stochastic computing VLSI structures for deep neural network accelerators," *ZTE Communications*, vol. 22, no. 4, pp. 9 - 17, Dec. 2024. doi: 10.12142/ZTECOM.202404003.

1 Introduction

Today, with the rapid development of high-speed data services such as the Internet and the Internet of Things, a large number of data interactions bring convenience to people's lives and at the same time, the constantly increasing data volume brings challenges to the efficiency of data processing algorithms and hardware performance. Although the integrated circuit industry follows Moore's Law, chip integration is getting higher and higher with the continuous reduction of process nodes, and chip performance also improves. However, as the traditional complementary metal oxide semiconductor (CMOS) process size is getting closer to the physical limit, new structures, new materials, and new lithography techniques cannot stop the argument that "Moore's Law is dead". The continuous reduction of chip feature size leads to many difficult problems in chip manufacturing, such as poor robustness and heat dissipation. These problems cannot be solved by integrating more transistors on the chip, at this time, it is necessary to find a new method to reduce the complexity of signal processing algorithms and circuit

power consumption under the existing process conditions. At this time, stochastic computing (SC) comes into view again.

Traditional stochastic computing refers to a computational paradigm that employs randomness as a fundamental resource for information processing. The data are represented and manipulated probabilistically, often using bitstreams or random sequences to encode values. The weighted representation of stochastic computing is different from that of binary. Stochastic computing converts binary input into a probabilistic bit stream, also known as a stochastic sequence, according to a certain data format, and re-designs the corresponding basic unit circuit according to the data format, so that the original complex operation logic can be used to achieve the same purpose with simple logic, that is, the algorithm realized by stochastic computing has lower computational complexity. It can reduce the hardware resource cost required to implement the operation logic. Stochastic computing focuses on the number of "1" in the stochastic sequence, and does not pay much attention to the specific position of "1" and "0" in the generated stochastic sequence. Although the chip manufacturing

process such as technology and soft error may bring about the phenomenon of a few bit errors, it will not have a great impact on the final result of stochastic computing. This is the high fault tolerance characteristic of stochastic computing. Since the performance of stochastic computing circuits is essentially anti-aging and is not affected by circuit topology and probabilistic coding, stochastic computing can provide a more relaxed circuit design space, which provides hope for the future application of emerging nanodevices. Stochastic computing not only reduces the complexity of circuit design but also reduces the requirement for device reliability. This suggests that stochastic computing is an alternative to the inherent reliability enhancement design of advanced technology nodes^[1].

In 2021, LI et al. optimized stochastic sequence generation, used separate weights and activation memory to load their respective stochastic sequence generator buffers, spread the generation cost of activation flow through cross-row broadcast of activation values, and corrected correlation through training, thus bridging the accuracy gap between stochastic computing and fixed-point neural networks^[2]. In 2022, HU et al.^[3] proposed a complete stochastic computing architecture and realized the flow sheet, which maximized fault tolerance and robustness, achieved an energy efficiency of 198.9 TOPS/W and an area efficiency of 2 630 GOPS/mm², and reduced the accuracy loss by 70%. Ref. [3] shows the great potential of low-cost IoT neural network processors. In 2022, CHEN et al.^[4] proposed a low-complexity bitstream expansion method to suppress the computation errors of stochastic computing and proposed a partition scheme with allocation decision to design hybrid stochastic binary computing multiplicative and additive units to improve the processing speed of bitstream with minimal overhead. In 2023, HU et al.^[5] proposed a hybrid stochastic multiplier combining unipolar coding and bipolar coding to achieve a balance between high precision and low hardware consumption and proposed a stochastic accumulator parallel counter to attain high precision stochastic bit stream to binary conversion with low hardware consumption. At the same time, the finite state machine was used to realize the high-precision Relu function circuit design. In 2023, FRASSER et al.^[6] used correlation and de-correlation to compute, and for the first time embedded a fully parallel convolutional neural network based on stochastic computing into a single FPGA chip, achieving better performance results than traditional binary logic and other stochastic computing implementations. In 2023, XIE et al.^[7] proposed a new stochastic computing accelerator for convolutional neural networks, which utilized the nuclear parallelism of convolutional layers to reduce hardware area and energy consumption effectively.

However, the accuracy of traditional stochastic computing is not enough, which makes the final result worse. To improve the calculation accuracy, this paper proposes a probability compensation algorithm based on the relative error distribution of the traditional stochastic computing multiplier, which

maps the data to the region with a small relative error through the function and then performs data inverse processing. The accuracy rate of the accelerator on the CIFAR-10 data set is 95.32%. In addition, a fully parallel neural network accelerator based on the deterministic method is designed, and the accuracy of the accelerator on the CIFAR-10 dataset is 95.06%. This design adopts TSMC 28 nm CMOS technology, and the energy efficiency is 1.371 TOPS/W.

The rest of the paper is organized as follows. Section 2 introduces the basic concepts and a brief review of SC. The third section gives the architecture design of the hardware accelerator. In Section 4, the experimental results of the probabilistic compensation algorithm and the accuracy, hardware evaluation, and comparison of all parallel neural network accelerators based on the deterministic method on multiple data sets are introduced. Finally, Section 5 draws the conclusion.

2 Background

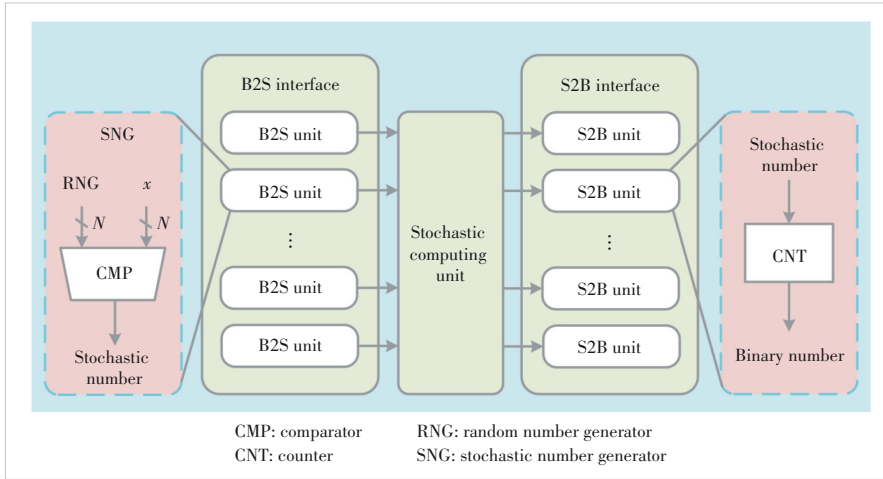
2.1 Stochastic Computing

Different from the binary weight representation method, stochastic computing is represented by converting the binary input into a finite-length stochastic bit stream, that is, the probability of the occurrence of “1” in the stochastic bit stream is represented by the corresponding binary value, which is the most common unipolar data format. For stochastic computing, each “1” in a stochastic bit stream has an equal weight. For a string of n -bit stochastic bit streams represented by the unipolar type, the corresponding binary value x is equal to the probability P_x of “1” appearing in the stochastic bit stream, so the representation range of unipolar type is $[0, 1]$, and the data represented by each “1” is $1/N$, that is, the accuracy of data represented by the unipolar type is $1/N$. The research process of stochastic computing is summarized. The structure of the stochastic computing paradigm in Fig. 1 is obtained.

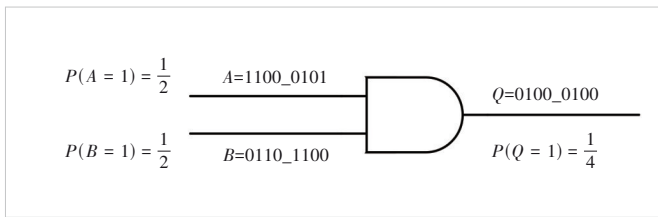
The structure of the stochastic computing paradigm is composed of three main parts. The first is the interface part of binary to a stochastic number, which is composed of a random number generator and a comparator. In the traditional structure, the random number generator uses the linear feedback shift register (LFSR) structure to generate random numbers. The second is the stochastic computing operation unit, which is represented by different basic gate units according to different data formats of stochastic computing. The last part is the stochastic number to the binary interface, which is generally composed of counters under the serial structure.

For stochastic sequences generated by unipolar data formats, multiplication is often performed with gates. An example of multiplication unit input and output for a unipolar data format is shown in Fig. 2.

The traditional stochastic computing multiplier is composed of a stochastic sequence generator, two inputs, a gate and a counter, and its structure is simple and clear. For the design



▲ Figure 1. Stochastic computing paradigm



▲ Figure 2. A stochastic computing multiplier unit in a unipolar data format

of this paper, int8 data are selected as the data input. Considering the data contain one symbol bit, int8 data can be split into symbol bits and numerical bits for multiplication. Therefore, the combination of seven-bit LFSR and seven-bit comparator is selected as the stochastic sequence generator. The stochastic sequence is generated by comparing the numerical bits of data input with the corresponding output values of LFSR. The counter is completed by the additional operation on the software side. When the stochastic sequence corresponding to the two inputs is 1, the resulting counter is increased by 1. For the seed selection of the random number generator, as long as the seeds are not the same, there is no fundamental impact on the stochastic computing multiplier. The current design does not consider the specific impact of other seed selections.

3 Accelerator Design

3.1 Probability Compensation Algorithm

The implementation of the stochastic multiplier is very simple, requiring only two inputs and a gate to implement binary multiplication logic, so it is often used to illustrate the simplicity of the logical unit of stochastic computing. However, simple logic often comes with certain disadvantages. Different from the binary accurate calculation, due to the randomness of stochastic computing, the calculation results also have stochastic properties, and the error of the calculation results is not uniform, resulting in poor perfor-

mance in the performance test of the convolutional neural network built by the traditional stochastic computing multiplier, which is an important problem to be solved in this paper.

3.1.1 Error Analysis of Stochastic Computational Multiplier

The software side uses the pyLFSR library of Python to make the software side model closer to the hardware model. A random int8 data input error test was carried out for the completed traditional stochastic computing multiplier model. The input data was in the form of fixed-point numbers. The errors between the calculated results and theoretical results were measured by mean relative error (MRE), mean error (ME), and maximum relative error (ERR_max), and the corresponding calculation formula was shown as follows.

$$\text{MRE} = \frac{1}{N} \cdot \sum_{i=1}^N \left| \frac{x_i - x_{\text{real}_i}}{x_{\text{real}_i}} \right|, \quad (1)$$

$$\text{ME} = \frac{1}{N} \cdot \sum_{i=1}^N \frac{x_i - x_{\text{real}_i}}{x_{\text{real}_i}}, \quad (2)$$

$$\text{ERR_max} = \max \left(\frac{x_i - x_{\text{real}_i}}{x_{\text{real}_i}} \right), \quad (3)$$

where N is the total number of test data, x_i is the calculation result of the stochastic computing multiplier, and x_{real_i} is the theoretical calculation result.

Random number generator seeds are selected as [1, 1, 0, 0, 1, 1, 1] and [1, 0, 1, 1, 1], and fixed-point random data input is generated by the randint function in the Python library. The results of the 10 000 random samples simulation show that MRE and ME of a traditional stochastic multiplier are 15.47% and 10.23%, and ERR_max is 127. To better understand the distribution of relative errors and make appropriate adjustments, the input data are divided into 10 intervals according to the seven-bit numerical bits on average. There are 100 two-dimensional intervals corresponding to the two inputs in pairs. Each interval generates 1 000 random fixed points within the interval range, and the simulation of relative error distribution is carried out. The resulting relative error distribution is shown in Fig. 3. To facilitate observation, the squares with small relative errors in the thermal map are filled with a light color system, and the squares with large relative errors in the thermal map are filled with a dark color system. The darker the color is, the larger the relative errors are. The color and



▲ Figure 3. Heatmap of the relative computational error distribution of the traditional stochastic computing multiplier

corresponding value are given in the legend on the right of the figure, and the relative error value of the square is marked in each square. By observing the thermal distribution diagram of relative error, it is found that the dark grid is concentrated in the upper left corner of the thermal map, that is, when the two input data are both small, the relative error of the calculated result is large, which is consistent with the previous ERRmax. In heat maps, the relative error is mostly less than 4%, and the further you go to the left, the greater the relative error is. Theoretically speaking, since x_{real} is in the denominator of the relative error formula, when the absolute error between x_{real}_i and x_i is at the same magnitude, the smaller x_{real}_i is, the greater the relative error will be. The relative error distribution of the thermal map is in agreement with the theoretical analysis results.

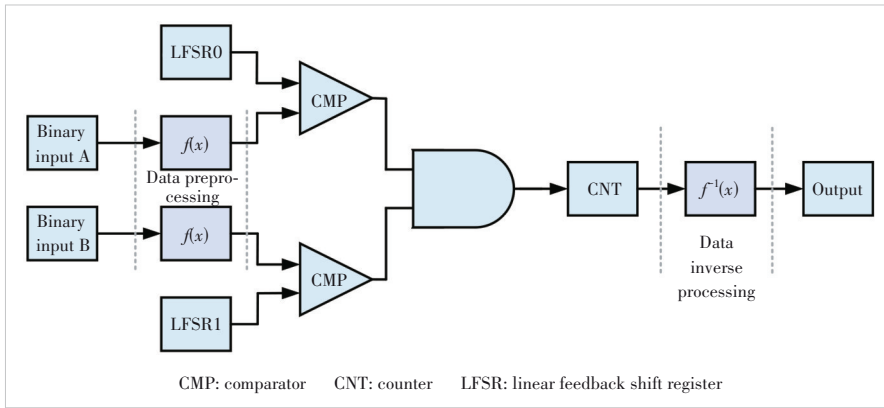
3.1.2 Research on Compensation Mechanism of Traditional Stochastic Computing Multiplier

To eliminate the serious influence of the local relative error on the whole relative error shown in the thermal map, the compensation mechanism of the stochastic computing multiplier is studied. Considering that the position with the greatest relative error appears on the far left and top, and the worst case is concentrated in the upper left corner, that is, the relative error of the calculation result is larger when one input datum is small, and the relative error of the calculation result is large when the two input data are small at the same time, which explores a situation where the data are mapped from the upper

left corner to the lower right corner by using accurate intermediate calculation. After the calculation, the accuracy compensation is carried out by reflecting in the upper left corner. The compensation method is called probability compensation, which means increasing the probability of the data interval with a small relative error in the calculation to improve the overall data accuracy. Fig. 4 is the flow chart of the probability compensation algorithm.

In Fig. 4, the probability compensation algorithm adds two steps of data preprocessing and data inverse processing based on traditional stochastic computing. After data preprocessing, binary input enters the comparator together with the random numbers generated by the random number generator LFSR for comparison. After stochastic computing and multiplication unit, the preprocessed stochastic sequence is converted into binary for data inverse processing. Utilizing data mapping, the probability compensation algorithm converts the data involved in the operation to the data region with high accuracy, to compensate for the accuracy of the traditional stochastic computing and multiplication algorithm.

For probability compensation, a function $f(x)$ should be found to satisfy certain conditions, and the data should be pre-processed by function mapping. To ensure fairness in mapping the two input data, the same function $f(x)$ is used for mapping. The data representation range of unipolar stochastic computing is $[0, 1]$, that is, the value range of the two input data is $[0, 1]$. Since the input data with large relative error is concentrated in the data interval close to 0, the function $f(x)$ should



▲ Figure 4. Flow chart of a probability compensation algorithm

map the data close to 0 to the data interval close to 1. The input data with small relative error should remain unchanged or change in a small amplitude as much as possible, so it is necessary to find a function, of which the domain and range are both $[0, 1]$. At the same time, since the inverse function of $f(x)$ needs to be used for data inverse processing, the function $f(x)$ must meet the requirement of the existence of an inverse function, and the influence of two input data mappings must be offset at the same time. To sum up, the function required for probability compensation should meet the following requirements.

- 1) The domain of $f(x)$ is $[0, 1]$, and the range is also $[0, 1]$;
- 2) $f(x)$ is monotone in the domain of definition, and most of the values are in the numerical interval with small relative error,

to meet the requirement of probability mapping and the existence of inverse function;

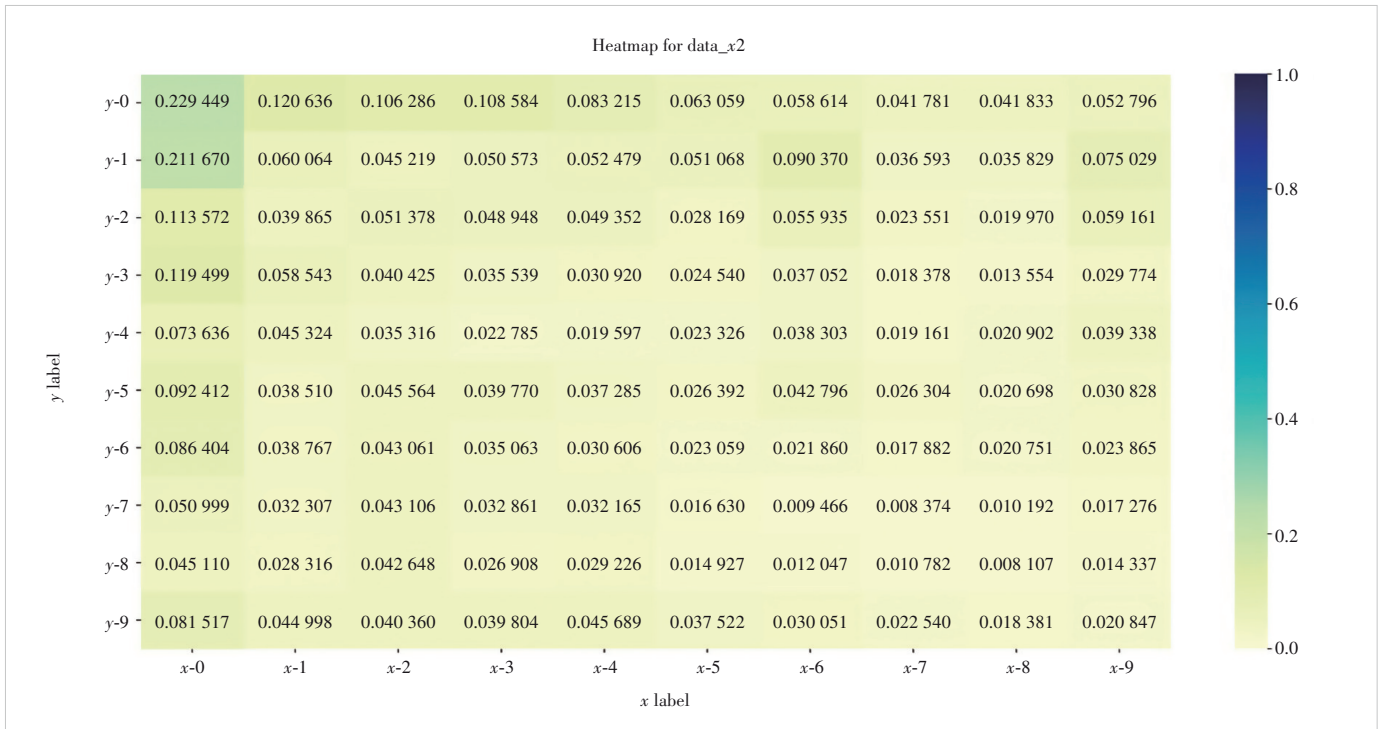
3) $f(x, y) = f(x) \times f(y)$, where x and y represent two input data. If this condition is met, the inverse function can simultaneously offset the influence of the mapping of two input data.

To find a function that meets the requirements, the entry point lies in the requirement that $f(x, y) = f(x) \times f(y)$. After deliberation, the power function of x can meet this requirement, so based on the power function, the function that meets the other two requirements is found. To

satisfy that most of the values of $f(x)$ are in the numerical interval with small relative error, the time function $f(x)$ should be above $f(x)=x$. Since the domain contains the point $x=0$, the satisfying function $f(x)$ is shown in Eq. (4).

$$f(x) = x^a, a \in (0, 1). \tag{4}$$

To facilitate subsequent data reverse processing and consider the complexity problem, the corresponding function $a=1/2$ is selected for simulation. The algorithm flow is consistent with that of Fig. 4. Random data with the same relative error distribution thermal map as that of the traditional stochastic computing multiplier in Fig. 3 are used, and the thermal map results obtained are shown in Fig. 5. The preprocessing func-



▲ Figure 5. Heatmap of the relative computational error distribution of the stochastic computing multiplier with probability compensation

tion is named according to the preprocessing function, where $a=1/2$ is denoted as probability compensation. After using the idea of probability compensation, the dark grid in the thermal map is completely eliminated, which means that the relatively large relative error value is perfectly compensated, and the feasibility of the idea of probability compensation is verified.

3.2 Fully Parallel Accelerator Hardware Design

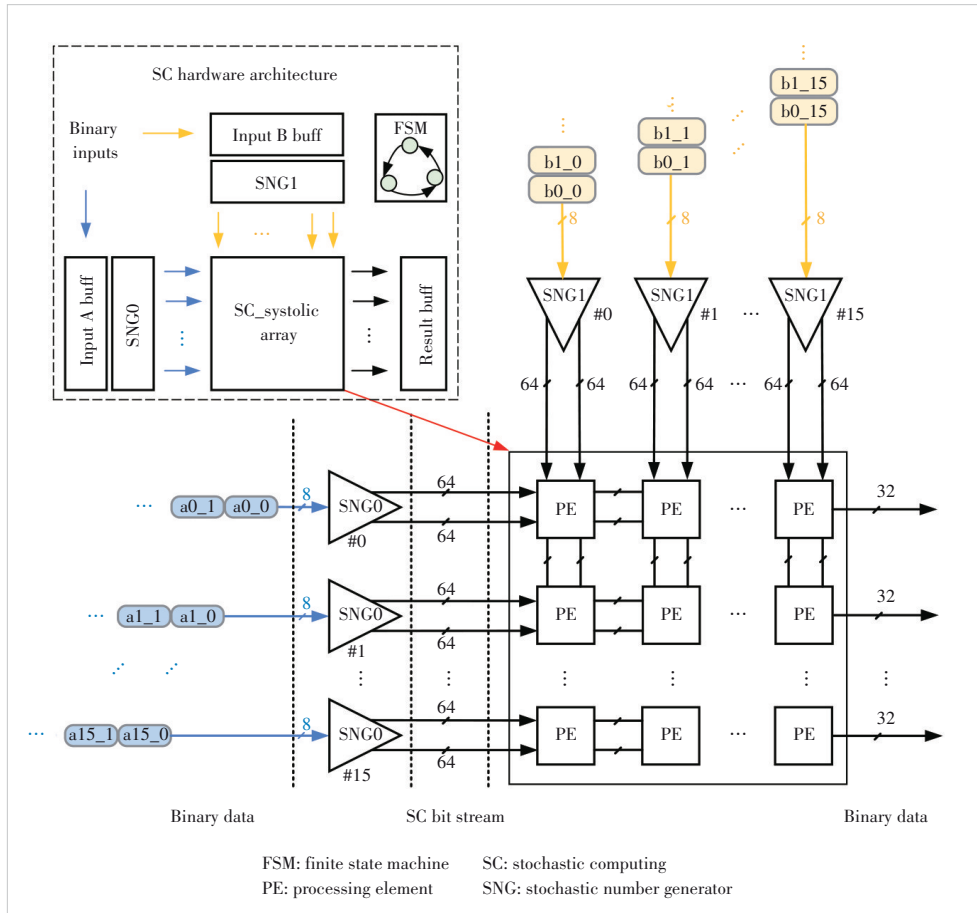
3.2.1 Accelerator Architecture

In the aspect of the fully parallel accelerator, the accuracy of matrix multiplication is improved based on the deterministic method. As shown in Fig. 6, the fully parallel stochastic computing systolic array accelerator consists of 7 modules: input A buff, input B buff, stochastic number generator 0 (SNG0), stochastic number generator 1 (SNG1), finite state machine (FSM), result buff, and SC_systolic array.

These modules are divided into three parts: the first part is composed of input A buff, input B buff, SNG0, and SNG1, which mainly completes the conversion of binary elements that need to be calculated in matrices A and B into the bit stream required for stochastic computing. The second part is composed of the SC_systolic array and result buff. This part is

the core computing unit in the entire hardware structure, which multiplies the stochastic computing bit stream that completes accumulation inside the unit, and finally puts the result into the result buff for caching. The third part is FSM, which completes the generation of data flow control signals, such as calculation start signals, result shift signals, and calculation end signals.

Similar to the serial accelerator architecture, the fully parallel accelerator proposed in this paper organizes all processing element (PE) units into a systolic array in the form of input and weight flow and partial product immobility. Input data enter the systolic array in a step form from left to right. PE units in the same row share the same stochastic computing parallel bit stream (from matrix A). This parallel bit stream will be passed one by one in the same row of PE cells on a clock cycle. The weight data also enter the systolic array in the form of a ladder from top to bottom, and the processing units in the same column share the same stochastic computing parallel bit stream (from matrix B), which will be passed one by one in the PE cells within the same column in the number of clock cycles. The final calculation result is controlled by a shift control signal and flows between PE units on a clock cycle, and is finally transmitted successively to the result buff.



▲ Figure 6. Hardware architecture of the fully parallel stochastic computing of the systolic array

3.2.2 PE Unit and Systolic Array Design

The PE unit in the fully parallel stochastic computing systolic array receives the parallel bit stream generated by the deterministic method and completes the dot product operation of the stochastic computing bit stream. In addition to the PE unit directly connected to the stochastic sequence generator, the remaining PE units receive the elements, the result, and the shift control signal from the previous PE unit. Ten internal registers are used to cache data and intermediate results and control signals.

In a fully parallel scheme, the multiplication of PE cells is performed using the partial product form, and four stochastic parallel bit streams, A_{high_sc} , A_{low_sc} , B_{high_sc} , and B_{low_sc} , are generated by a stochastic sequence generator. After each stochastic parallel bit stream is matched with a stochastic parallel bit stream generated by an-

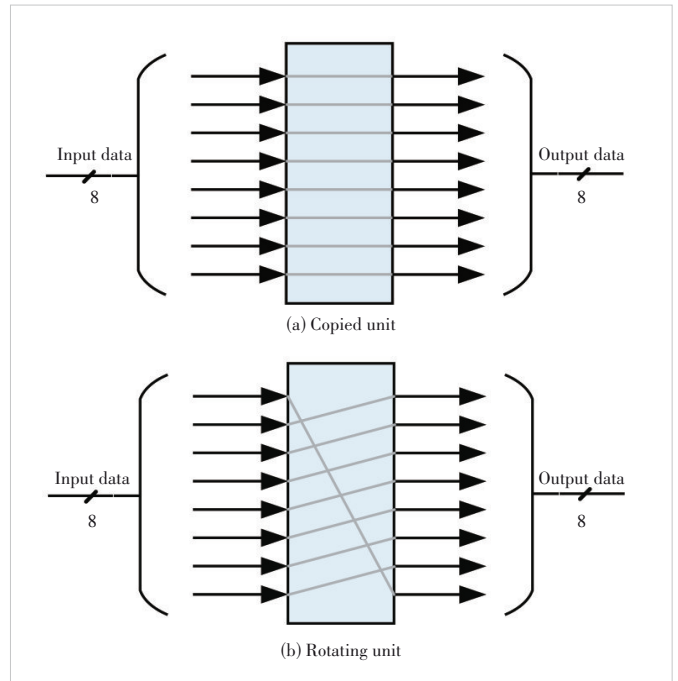
other matrix, the number of “1” in the phase and the result are calculated through an addition tree structure, where the addition tree used is equivalent to 64 inputs, and each input is a 1-bit full adder. After the results of the full adder are shifted, the final calculation result is obtained. The shift signal is shift controlled and sent by the FSM to determine when the final cumulative results inside the PE unit will be transmitted. When the processing unit PE has not completed the calculation, the shift signal is “0”, and the PE unit is responsible for receiving the result of the previous unit and passing it to the next unit. When the PE unit completes the final calculation, the shift signal is set to “1” and the final calculation results are transmitted in turn.

3.2.3 Stochastic Number Generator Design

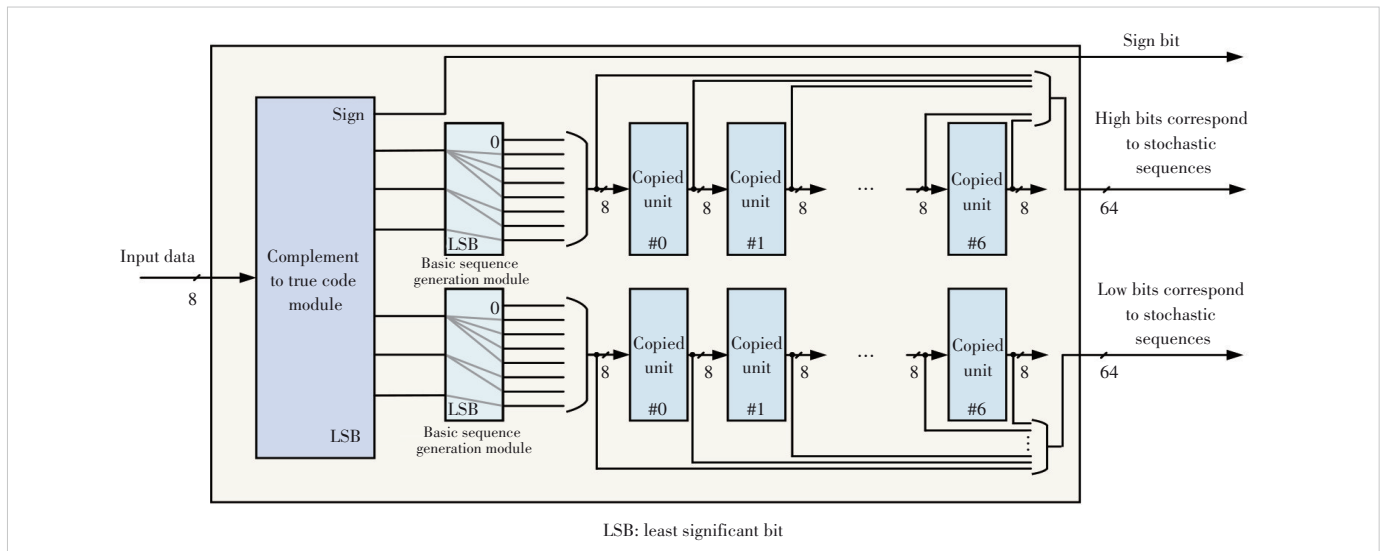
The stochastic sequence generator used in the fully parallel scheme uses a deterministic method to generate a stochastic computing parallel bit stream. The data in int8 format are divided into a 1-bit symbol bit and two 3-bit numerical bits by bit segmentation, and the lowest 1-bit numerical bit is discarded to match the partial product allocation, which is recorded as the round bit segmentation method. Fig. 7 shows the internal structure diagram of SNG in the hardware design of a fully parallel accelerator. When two 3-bit numerical bits enter the basic sequence generation module, each 3-bit numerical bit is copied by binary weight, and the highest bit is fixed as “0”, because the results generated by the copied and rotating methods are independent of the sorting method of the basic stochastic sequence. A base stochastic sequence of 8-bit without introducing additional hardware consumption is generated.

One datum in the int8 format corresponds to two basic stochastic sequences. In the matrix multiplication operation, the int8 input data in matrix A correspond to the internal opera-

tion of SNG0, and the two basic stochastic sequences generated in SNG0 are continuously copied 7 times using the copied unit. The high 64-bit width corresponds to the stochastic parallel bit stream A_high_sc, and the low bits correspond to the stochastic parallel bit stream A_low_sc. The internal line connection of the copied unit is shown in Fig. 8a. The input data of int8 in matrix B correspond to the internal operation of SNG1. SNG1 uses the rotating unit to replace the copied unit in SNG0, and the rest are completely consistent with SNG0. The SNG1 internal structure diagram is no longer listed here. The two basic stochastic sequences generated in



▲ Figure 8. Copied and rotating units



▲ Figure 7. Fully parallel random number generator

SNG1 are rotated 7 times by the rotating unit to obtain a 64-bit high corresponding to a stochastic parallel bit stream B_{high_sc} and a 64-bit low corresponding to a stochastic parallel bit stream B_{low_sc} . The internal line connections of the rotating unit are shown in Fig. 8b. Finally, four stochastic parallel bits are generated and transmitted into the systolic array. The generation process only changes the order of connections and the number of replicated connections without introducing additional hardware consumption.

4 Experiment and Analysis

4.1 Software Simulation Results and Analysis

The designed two accelerators are applied to the neural network through the `img2col` algorithm. The seeds used for each random number generator are the same as previously mentioned. The network used is Resnet 18^[8], and the quantization bit is 1-bit symbol bit plus 7-bit numerical bit. The MNIST^[9] and the CIFAR-10^[10] data sets are used for testing, and the test results obtained are shown in Table 1.

In the MNIST data set, there is no significant difference between schemes. The accuracy of all schemes except traditional schemes can reach more than 99% in the MNIST data set, and the accuracy of traditional SC schemes can also reach 98.56%. When tested on the more complex CIFAR-10 dataset, the accuracy of the traditional SC scheme is only 80.34%, 15% lower than that of binary. The precision is improved to 95.32% by the \sqrt{x} probability compensation SC scheme and 95.06% by the deterministic SC scheme.

4.2 Back-End Implementation Results and Analysis

The layout and cabling of the TSMC 28 nm process with process nodes are completed by using the layout tool IC compiler (ICC) and the core voltage is 0.9 V. The layout parameters achieved are shown in Table 2.

According to the process node scaling method^[11], the 65 nm process node used by the Eyeriss v2 accelerator^[12] is normalized to the 28 nm process node used in this work, and the clock frequency scaling parameters are shown in Eq. (5).

▼ **Table 1. Test results of neural network accelerator application based on stochastic computing**

DataSet	Method	Network Accuracy/%
MNIST	Binary	99.55
	Traditional SC	98.56
	\sqrt{x} Probability compensation SC	99.50
	Deterministic method SC	99.43
CIFAR-10	Binary	95.52
	Traditional SC	80.34
	\sqrt{x} Probability compensation SC	95.32
	Deterministic method SC	95.06

SC: stochastic computing

▼ **Table 2. Layout parameters of the neural network accelerator based on stochastic computing**

Method	Type	Clock Frequency/MHz	Area/mm ²	Power/mW
Traditional SC	Uncompensated	1 000	0.104	81.3
Fully parallel	Deterministic method	313	0.601	116.7

SC: stochastic computing

$$N_c = \frac{65}{28} . \quad (5)$$

Load capacitance scaling parameters are shown in Eq. (6).

$$N_{CL} = \frac{65}{28} . \quad (6)$$

Dynamic power consumption is the main power consumption in high-speed chips, and the dynamic power consumption formula of switches is shown in Eq. (7).

$$P = V^2 \cdot C_{Load} \cdot f . \quad (7)$$

Therefore, power scaling parameters are shown in Eq. (8).

$$N_p = \left(\frac{0.9}{1.2} \right)^2 \cdot \frac{28}{65} \cdot \frac{65}{28} = 0.5625 . \quad (8)$$

The energy efficiency ratio formula is shown as Eq. (9).

$$\text{GOPS/W} = \frac{\text{calculations per second}}{P} . \quad (9)$$

The energy efficiency ratio corresponding to the designed accelerator can be obtained according to Eq. (9). By combining Eqs. (5), (8), and (9), the normalized parameters of the energy efficiency ratio can be calculated as shown in Eq. (10).

$$N = \frac{1}{0.5625} \times \frac{65}{28} = 4.12698 . \quad (10)$$

Table 3 compares the results of the energy efficiency ratio between the neural network accelerator implemented in this work and the Eyeriss v2 accelerator^[12], in which the energy efficiency ratio in the Eyeriss v2 accelerator is normalized. It can be seen from the results of Table 3 that compared with the normalized energy efficiency ratio of the Eyeriss v2 accelera-

▼ **Table 3. Comparison of stochastic computing DNN implementations with other very large scale integration circuit (VLSI) deep neural networks (DNN)**

Accelerator	Type	Process Node/nm	EER (GOPS/W)	Normalized EER (GOPS/W)
Eyeriss v2 ^[12]	Binary computing	65	253.2	1 045.0
Classic serial	Uncompensated	28	6 297.7	6 297.7
Fully parallel	Deterministic method	28	1 371.0	1 371.0

EER: energy efficiency ratio

tor, the fully parallel stochastic computing neural network accelerator based on the deterministic method has improved by 31%. Although the normalized energy efficiency ratio of traditional stochastic computing neural network accelerators is the highest, the data set of this scheme is less accurate and should not be compared with.

5 Conclusions

In this paper, a probability compensation algorithm is proposed based on the relative error distribution of the traditional stochastic multiplier. The accuracy of the accelerator on the CIFAR-10 dataset is 95.32%. In addition, a fully parallel neural network accelerator based on the deterministic method is designed, and the accuracy of the accelerator on the CIFAR-10 dataset is 95.06%. This design adopts TSMC 28 nm CMOS technology, and the energy efficiency is 1.371 TOPS/W. Through hardware and software evaluation, the implementation results show that the proposed design is superior to the hardware implementation of DNN based on traditional binary computing logic in terms of energy efficiency ratio, and the network accuracy is superior to the traditional SC-DNN implementation.

References

- [1] ZHANG Z D, WANG R S, ZHANG Z, et al. Circuit reliability comparison between stochastic computing and binary computing [J]. *IEEE transactions on circuits and systems II: express briefs*, 2020, 67(12): 3342 – 3346. DOI: 10.1109/tcsii.2020.2993273
- [2] LI T M, ROMASZKAN W, PAMARTI S, et al. GEO: Generation and execution optimized stochastic computing accelerator for neural networks [C]//*Proceedings of 2021 Design, Automation & Test in Europe Conference & Exhibition (DATE)*. IEEE, 2021: 689 – 694. DOI: 10.23919/date51398.2021.9473911
- [3] HU Y X, ZHANG Y W, WANG R S, et al. A 28-nm 198.9-TOPS/W fault-tolerant stochastic computing neural network processor [J]. *IEEE solid-state circuits letters*, 2022, 5: 198 – 201. DOI: 10.1109/lssc.2022.3194954
- [4] CHEN Z Y, MA Y F, WANG Z F. Hybrid stochastic-binary computing for low-latency and high-precision inference of CNNs [J]. *IEEE transactions on circuits and systems I: regular papers*, 2022, 69(7): 2707 – 2720. DOI: 10.1109/tcsi.2022.3166524
- [5] HU S, HAN K N, HU J H. High performance and hardware efficient stochastic computing elements for deep neural network [C]//*Proceedings of 6th World Conference on Computing and Communication Technologies (WCCCT)*. IEEE, 2023: 181 – 186. DOI: 10.1109/wccct56755.2023.10052402
- [6] FRASSER C F, LINARES-SERRANO P, DE LOS RÍOS I D, et al. Fully parallel stochastic computing hardware implementation of convolutional neural networks for edge computing applications [J]. *IEEE transactions on neural networks and learning systems*, 2023, 34(12): 10408 – 10418. DOI: 10.1109/tnnls.2022.3166799
- [7] XIE Z P, YUAN C Y, LI L K, et al. Energy-efficient stochastic computing for convolutional neural networks by using kernel-wise parallelism [C]//*Proceedings of IEEE International Symposium on Circuits and Systems (ISCAS)*. IEEE, 2023: 1 – 5. DOI: 10.1109/iscas46773.2023.10181378
- [8] HE K M, ZHANG X Y, REN S Q, et al. Deep residual learning for image recognition [C]//*Conference on Computer Vision and Pattern Recognition (CVPR)*. IEEE, 2016: 770 – 778. DOI: 10.1109/cvpr.2016.90
- [9] LECUN Y, BOTTOU L, BENGIO Y, et al. Gradient-based learning applied to document recognition [J]. *Proceedings of the IEEE*, 1998, 86(11): 2278 – 2324. DOI: 10.1109/5.726791
- [10] KRIZHEVSKY A. Learning multiple layers of features from tiny images [EB/OL]. (2012-05-20) [2024-08-01]. https://www.researchgate.net/publication/265748773_Learning_Multiple_Layers_of_Features_from_Tiny_Images
- [11] NISHI Y, DOERONG R. *Handbook of semiconductor manufacturing technology* [M]. Boca Raton, USA: CRC Press, 2008
- [12] CHEN Y H, YANG T J, EMER J S, et al. Eyeriss v2: a flexible accelerator for emerging deep neural networks on mobile devices [J]. *IEEE journal on emerging and selected topics in circuits and systems*, 2019, 9(2): 292 – 308. DOI: 10.1109/JETCAS.2019.2910232

Biographies

WU Jingguo received his BS degree in microelectronics science and engineering from Xi'an Jiaotong University, China in 2021. He is currently pursuing for a master's degree at Fudan University, China. His main research interest is stochastic computing.

ZHU Jingwei is a PhD candidate in the School of Microelectronics, Fudan University, China. He received his MSc degree from Fudan University. His current research interests include neuromorphic computing, spiking neural networks and NoC.

XIONG Xiankui graduated from University of Electronic Science and Technology of China. He is the chief architect of the Wireless Department and the leader of the Prospect Team of the Smart Computing Technical Committee, ZTE Corporation. He has been engaged in long-term research on computing systems and architectures, advanced computing paradigms, and heterogeneous computing accelerators. He has led the system architecture design of the ZTE ATCA advanced telecom computing platform, server storage platform, smart NIC, and AI accelerator.

YAO Haidong graduated from the University of Science and Technology of China, and he is a senior expert in the field of wireless communications at ZTE Corporation. He is mainly engaged in the research and design of deep learning, large language model network architecture, and compilation and conversion technology.

WANG Chengchen graduated from the Department of Precision Instrument, Tsinghua University, China and is now working in ZTE Corporation. His research directions include computing in memory, optical calculation, and probability calculation.

CHEN Yun (chenyun@fudan.edu.cn) received her BSc degree from University of Science and Technology of China in 2000, and PhD degree from Fudan University, China in 2007. She joined Fudan University at the same year, where she has been a professor with the State Key Laboratory of ASIC and Systems. She has published more than 60 articles in renowned international journals and conferences and applied for more than 20 patents. Her research interests include baseband processing technologies for wireless communication and ultralow power FEC IC design. Pro. CHEN is a member of the Steering Committee of SIPS and the ASICON Technical Committee. She serves as a TPC Member for ASSCC. She also serves as the Chair Secretary for the Shanghai Chapter of IEEE SSCS, and the Co-Chair for the Circuit System Division, the Chinese Institute of Electronics. She is a senior member of IEEE.

Design of LCoS-Based Twin 1 × 40 Wavelength Selective Switch



WANG Han^{1,2}, LIU Maoqi^{1,2}, FENG Zhenhua^{3,4},
LIU Minghuan^{3,4}, MAO Baiwei^{3,4}

(1. School of Optical and Electronic Information, Huazhong University of Science and Technology, Wuhan 430074, China;

2. Wuhan National Laboratory for Optoelectronics, Huazhong University of Science and Technology, Wuhan 430074, China;

3. WDM System Department of Wireline Product R&D Institute, ZTE Corporation, Wuhan 430223, China;

4. State Key Laboratory of Mobile Network and Mobile Multimedia Technology, Shenzhen 518055, China)

DOI: 10.12142/ZTECOM.202404004

<https://kns.cnki.net/kcms/detail/34.1294.TN.20241120.1118.002.html>,
published online November 20, 2024

Manuscript received: 2024-06-24

Abstract: Wavelength selective switch (WSS) is the crucial component in the reconfigurable optical add/drop multiplexer (ROADM), which plays a pivotal role in the next-generation all-optical networks. We present a compact architecture of twin 1×40 liquid crystal on silicon (LCoS)-based WSS, which can be regarded as a 4f system in the wavelength direction and a 2f system in the switching direction. It is designed with theoretical analysis and simulation investigation. Polarization multiplexing is employed for two sources of twin WSS by polarization conversion before the common optical path. The WSS system attains a coupling efficacy exceeding 96% for 90% of the ports through simulation optimization. The 3 dB bandwidth can be achieved by more than 44 GHz at a 50 GHz grid for all 120 channels at all deflection ports. This work establishes a solid foundation for developing high-performance WSS with larger port counts.

Keywords: wavelength selective switch (WSS); liquid crystal on silicon (LCoS); optical structure design; insertion loss

Citation (Format 1): WANG H, LIU M Q, FENG Z H, et al. Design of LCoS-based twin 1×40 wavelength selective switch [J]. *ZTE Communications*, 2024, 22(4): 18 – 28. DOI: 10.12142/ZTECOM.202404004

Citation (Format 2): H. Wang, M. Q. Liu, Z. H. Feng, et al., “Design of LCoS-based twin 1×40 wavelength selective switch,” *ZTE Communications*, vol. 22, no. 4, pp. 18 – 28, Dec. 2024. doi: 10.12142/ZTECOM.202404004.

1 Introduction

Reconfigurable optical add/drop multiplexer (ROADM) is essential for enhancing wavelength routing flexibility to meet the growing requirements of data traffic capacity in future elastic optical networks^[1-3]. Wavelength selective switches (WSSes) serve as essential components for dynamically manipulating optical signals in both the spectrum and space domains, significantly enhancing the agility and reliability of the network. There are several technologies used in the WSS system for beam steering, including liquid crystals (LC), microelectromechanical systems (MEMS), and liquid crystals on silicon (LCoS). Owing to its high spatial resolution, phase-only modulation, high port isolation, and flexible deployment capability of channel bandwidth, LCoS-based WSS provides performance benefits and is the current promising and economical solution^[3-5]. Various efforts have been implemented to improve its port count, operation bandwidth,

spectral granularity, and responding time^[6-8]. Meanwhile, its insertion loss (IL), polarization dependent loss (PDL) and crosstalk (XT) should also be promoted to harness the power budget of the optical link and increase its cascability^[9].

As to LCoS-based WSS, PDL comes from the polarization-dependent characteristic of LCoS. By employing the polarization diversity optics with half-wave plate (HWP) or quarter-wave plate (QWP), the light orthogonal to the modulation direction of LCoS can also be used to achieve polarization independence^[10]. The XT is mainly caused by the high-order diffractions of the steered light beam with the finite pixelated array, the limited phase quantization and the physical effects, such as fringing field effect, phase flicker, and device non-uniformity. Besides, the unwanted coupling can also be produced due to the inappropriate arrangement of output fibers^[11]. Different phase pattern design methods have been developed to minimize the phase deviation from the ideal blazed grating, such as simulated annealing^[12], Gerchberg-Saxton (GS) algorithm^[13-14], the genetic algorithm^[15], and hybrid algorithms^[10]. The above methods can define the output fiber posi-

This work was supported by ZTE Industry-University-Institute Cooperation Funds under Grant No. IA20230614004.

tion to achieve less unintentional coupling according to the obtained accurate position of the signal and other orders of diffractions^[7]. Meanwhile, the wavefront encoding phase pattern of the off-axis lens is suggested instead of a blazed grating for defocusing the high-order diffractions^[16]. The IL arises from the absorption and scattering of the optical components, the diffraction loss of LCoS, and the coupling loss from the fiber array misalignment and optical aberration. For a given structured system, the absorption loss is the fixed system loss unless the components with better performance are employed^[11]. The diffraction efficiency of LCoS can be promoted by Computer Generated Holography (CGH)^[11-15], wavefront encoding^[16], and phase compensation^[17].

Finisar developed the first programmable LCoS-based WSS with 50 GHz channel spacing, achieving a neighboring port isolation greater than 25 dB for 90 separate 50 GHz channels at -8 dB loss for polarized light^[6]. A 1×9-port LCoS-based WSS with multicasting ability was designed with an insertion loss of -7.6 dB and a crosstalk of -19.4 dB^[10]. To expand the switching capability, efforts are devoted to increasing the port's number of WSS. A stacked switch architecture of WSSes was proposed to realize 40 independent 1×12 WSSes with a single 4k LCoS device. It can be configured to support a 1×144 port wavelength routing, or a 12×12 wavelength cross-connect, with an insertion loss of around -4.58 dB on average^[8]. Commercially, Finisar has developed a 1×20 port programmable LCoS-based WSS supporting a bandwidth of 6 THz and a bandwidth resolution of 6.25 GHz^[18]. From the perspective of practical applications, broadening the spectrum, minimizing the design footprint and increasing integration are crucial for advancing WSS technology. Recently, 20-dimensional WSS devices have been widely deployed in the current ROADM network^[19], and there is an increasing demand for WSS devices that offer higher dimensionality and integration. Higher-dimensional WSS requires larger deflection angles from the LCoS, demanding higher diffraction efficiency, especially in small-period grating set-up. Furthermore, the risk of crosstalk between channels increases with the number of ports, therefore novel isolation strategies and optimized optical paths are required to maintain the integrity of the optical signal. Precise alignment and advanced optical design are required to maintain high optical coupling efficiency with increased port numbers.

This work introduces an innovative theoretical method for designing optical paths in LCoS-based compact twin 1×40 WSS systems to meet commercial requirements. Our design stands out from existing commercial devices, which typically offer a maximum of 32 ports. The innovative twin structure significantly enhances integration, enabling the efficient accommodation of a larger number of ports. At the same time, it maintains performance metrics, such as insertion loss, crosstalk, and bandwidth, within commercial standards. A polarization diversity scheme and a polarization conversion system are

employed to facilitate efficient manipulation and control of polarization. Additionally, bending fiber arrays and a prism grating are designed to reduce conic diffraction and improve the coupling efficiency of the WSS. Computational simulations validate the design, achieving a coupling efficiency of 96% for 34 ports and over 80% for other ports. The 3 dB bandwidth meets commercial standards, reaching ≥ 44 GHz at a 50 GHz grid for all channels.

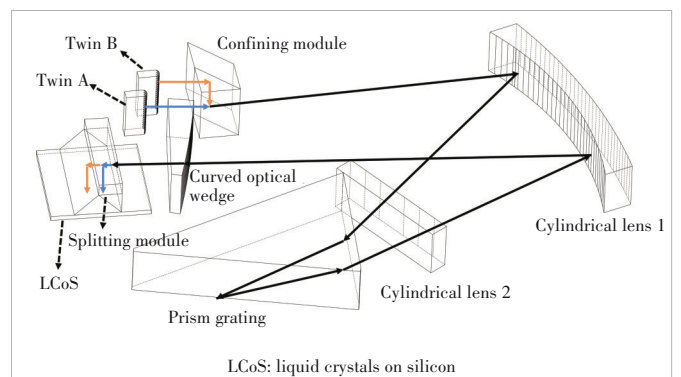
2 Optical Design of Twin WSS

2.1 Optical Architecture

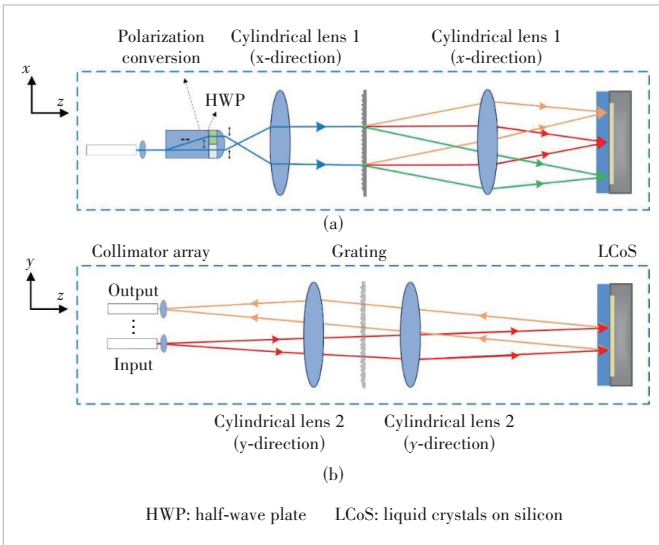
In developing commercial WSS, we aim to enhance port numbers, expand bandwidth, and integrate systems without compromising performance. To address the constraints of compactness and performance, we design a twin 1×40 WSS optical system as shown in Fig. 1. This system includes a fiber array and microlens array, a polarization conversion unit, cylindrical lens 1 and 2, a curved optical wedge, a confining module, and a splitting module before LCoS. The microlens array must be designed carefully to ensure that the returned light beam is coupled to the fiber array. In the polarization unit, the birefringent crystal and half-wave plate are used to manipulate the polarization states of light beams A and B for system multiplexing. The beam combiner before cylindrical lens 1 and the beam-splitting apparatus before LCoS aggregate and separate the light beams from twins A and B, respectively, leading to the zoning of the twin WSS on the LCoS. The prism grating is responsible for demultiplexing the wavelengths with high dispersion ability.

Fig. 2 shows the optical paths of WSS in the dispersion and switching directions. The WSS system employs a 4f configuration in the dispersion direction and a 2f configuration in the switching direction. In the dispersion direction, the signal light beam, after polarization modulation, is collimated by a cylindrical lens, then wavelength-demultiplexed by a prism grating, and reflected again by cylindrical lens 1, forming a 4f system. The dispersed light is imaged onto the LCoS device, creating a dispersed spectrum distribution along the y -axis.

The light beams from twins A and B are directed at the up-



▲ Figure 1. Twin WSS architecture

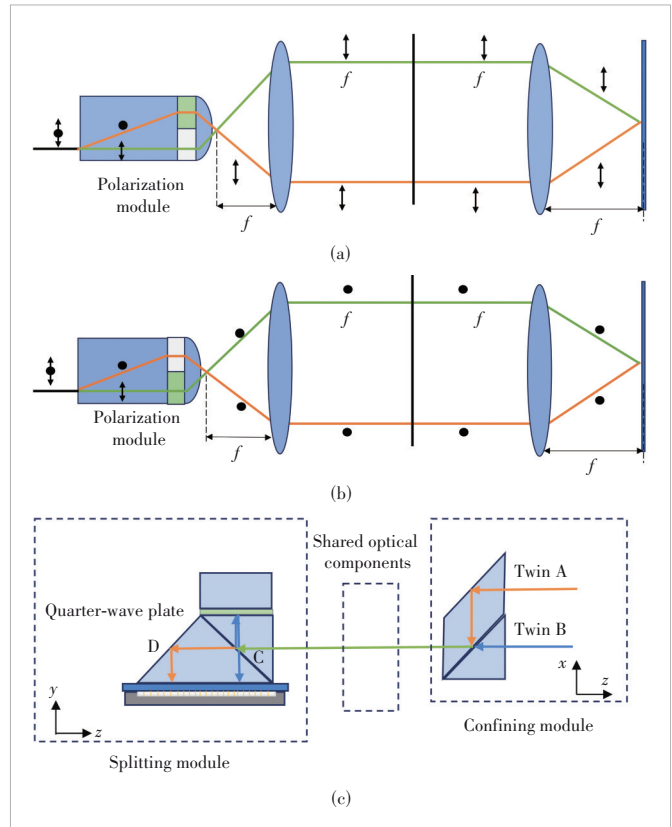


▲ Figure 2. Optical paths of WSS in (a) the dispersion direction and (b) the switching direction

per and lower halves of the LCoS, respectively. In the switching direction, cylindrical lens 2 and the LCoS constitute a 2f system. The dispersed light is imaged onto the LCoS, forming a rectangular dispersion spectrum within its active region. Phase grating holograms with various periods are imposed on the corresponding wavelength channels on the LCoS, facilitating the directional encoding of the light beams. The diffracted light from the LCoS emerges as the deflected collimation light corresponding to different output ports, which are focused by the micro-lens array onto the corresponding output ports, enabling low-loss optical switching between input and output ports for the given wavelength signal.

2.2 Twin WSS Structure Design

The LCoS utilized for our design has a resolution of 1 920 × 1 200 with a pixel pitch of 8 μm, resulting in a length of 15.36 mm and 9.60 mm in the dispersion and switching directions, respectively. To minimize cross-talk between channel A and channel B of the twin WSS, the beam spot size of 3ω in the y-direction on the LCoS is set to smaller than 4.8 mm, which is half the width of the LCoS. Additionally, a factor of 0.9 is applied, resulting in a requirement that 3ω diameter should be less than 4.32 mm. Considering device and assembly tolerances, over 99.99% of the optical energy remains within half the LCoS width, effectively isolating the control regions of the two twin devices. A polarization diversity scheme is proposed to improve beam utilization efficiency and provide the possibility of dual source WSS with twin A and twin B. The key component of the scheme is a set of polarization modules, including birefringent crystals, half-wave plates (represented by the green rectangular in Fig. 3), and silicon-based micro-cylindrical lenses. The beam emitting from the micro-lens array can be modulated by adjusting the position of birefringent



▲ Figure 3. Schematic illustration of symmetric polarization loops established in the WSS: (a) polarization diversity of source A; (b) polarization diversity of source B; (c) polarization multiplexing in the twin WSS

crystals and half-wave plates to P-polarized light (Fig. 3a) and S-polarized light (Fig. 3b). The cylindrical lens leads the two polarization components to spatially coincide in the receiving plane while compressing the waist of the Gaussian beam in the dispersion direction.

To multiplex the optical elements for the beam signals from different sources, a polarization conversion system is proposed with a confining module and a splitting module, as shown in Fig. 3c. In the figure, the blue line represents the S-polarization state of the light from twin A and the orange line represents the P-polarization state of the light from twin B. The confining module combines light with two polarization states and ensures that light from both sources follows the same transmission path in the WSS system. As the LCoS is polarization-dependent, the polarization components are preferably rotated into alignment with the polarization axis of the LCoS. The splitting module, strategically positioned adjacent to the LCoS in the receiving plane, separates different sources of beams and unifies their polarization states. This module can be exactly modulated by the LCoS. Light from twin A passes through the polarizing interface C and is reflected by surface D to the upper half of the LCoS. Conversely, light from twin B is reflected by interface C, and undergoes polarization

rotation via an overhead quarter-waveplate twice. Subsequently, the light is incident on the lower half of the LCoS, and the polarization component is converted to the same as the light from twin A, which can be accurately manipulated by the LCoS.

3 Design of Twin 1×40 WSS with Performance Restriction Analysis

3.1 Wavelength Range

The designed WSS covers the super C band from 1 524 nm to 1 572 nm, approximately corresponding to frequencies from 190.637 5 THz to 196.675 THz, with a total bandwidth of approximately 6 THz. To optimize LCoS utilization, it is assumed that this bandwidth completely occupies the LCoS. In addition, the prism grating is meticulously crafted to achieve a superior level of spectral resolution. The schematic diagram of the prism grating is shown in Fig. 4a with a top angle of δ , a grating constant of d , a blazing angle of δ , a prism medium refractive index of n_A , and a glue layer refractive index of n_B .

We preliminarily design a prism grating with 1 500 lines/mm and a wedge angle of 77.52° to satisfy the operation frequency band from 190.637 5 THz to 196.675 THz. As light passes through the prism grating, different wavelengths diverge at various angles due to the prism refraction and grating diffraction. Utilizing the grating equation and an incidence angle of 52° , the exit angles for the central, minimum, and maximum wavelength are calculated. After reflecting from the grating, the beam exhibits an angular dispersion of $4.299 6^\circ$. This dispersion angle is further magnified after passing through the prism, resulting in a final exit angular dispersion of $8.969 8^\circ$ from the prism grating.

The coverage area of the beam on the LCoS is determined by the focal length of cylindrical lens 1 and the angular dispersion of prism grating, which can be described as

$$2f_{\text{lens}\#1} \tan\left(\frac{\theta(\lambda_{\text{max}}) - \theta(\lambda_{\text{min}})}{2}\right) = L_{\text{LCoS}}. \quad (1)$$

Taking into account the size L_{LCoS} of the LCoS in the dispersion direction and the angular dispersion of prism grating $\Delta\theta = \theta(\lambda_{\text{max}}) - \theta(\lambda_{\text{min}})$, cylindrical lens 1 with a focal length of 90 mm is selected to ensure a sufficient wavelength range.

3.2 Bandwidth Tuning Accuracy

The light beam is dispersed by the prism grating with different diffraction angles for different wavelengths. Subsequently, the dispersed light is focused by the imaging lens before the LCoS. From the imaging relation of the focus lens, the position of wavelength λ along the dispersion direction $x(\lambda)$ on the LCoS can be expressed as

$$x(\lambda) = f_{\text{lens}\#1} \tan[\theta_{\text{out}}(\lambda) - \theta_{\text{out}}(\lambda_0)], \quad (2)$$

where the diffraction angles of the incident light at wavelength λ and 1 548 nm are denoted by $\theta_{\text{out}}(\lambda)$ and $\theta_{\text{out}}(\lambda_0)$, respectively.

From the diffraction equation, the diffraction angle $\theta_{\text{out}}(\lambda)$ can be obtained from

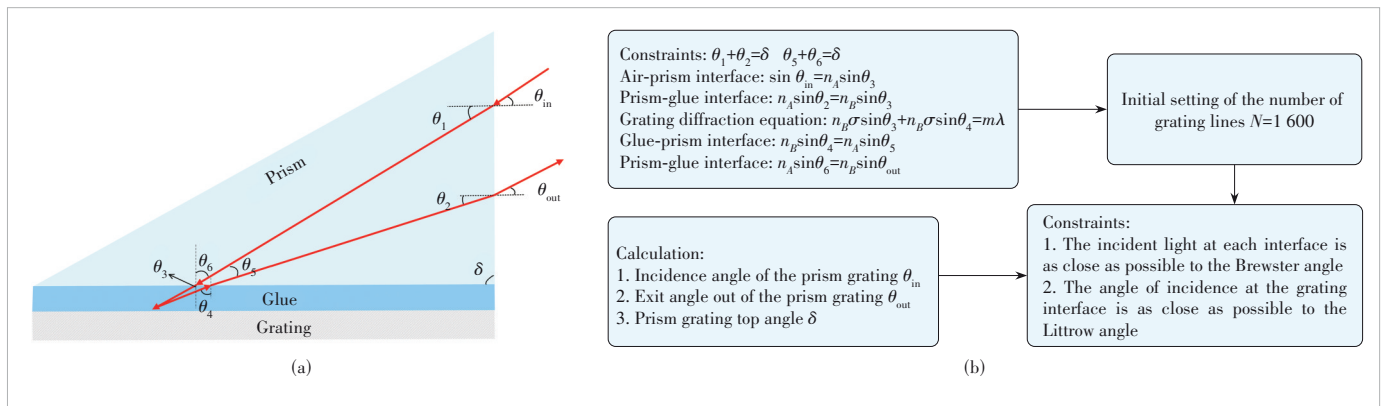
$$\sin\left[\sin^{-1}\left(\frac{\sin\theta_{\text{out}}(\lambda)}{n(\lambda)}\right) - \delta\right] - \sin\left[\sin^{-1}\left(\frac{\sin\theta_{\text{in}}}{n(\lambda)}\right) - \delta\right] = \frac{m\lambda}{n(\lambda)d}, \quad (3)$$

where $n(\lambda)$ can be calculated with the dispersion formula of prism material, m is the diffraction order, and d is the grating constant.

Assuming that the pixel pitch of the LCoS is d_{LCoS} , the spectral tuning accuracy R can be defined as the optical signal bandwidth corresponding to a change of one pixel on the LCoS, which can be expressed as

$$R = d_{\text{LCoS}} \frac{\partial\lambda}{\partial x}. \quad (4)$$

The smaller the spot size in the horizontal direction on the



▲ Figure 4. Schematic diagram of (a) prism grating and (b) its design process

LCoS, the sharper the spectral roll-off curve can be achieved. This enhances bandwidth characteristics.

Meanwhile, for the spectral resolution of a grating-based module, the finite width of the entrance slit should be taken into account rather than solely focusing on the diffraction limitation of the grating aperture. The minimum wavelength interval $(\Delta\lambda)_{\min}$ of two spectral components that are just resolvable according to the Rayleigh criterion can be described as

$$(\Delta\lambda)_{\min} \geq \left(\frac{\lambda}{a} + M \frac{b}{f_{\text{lens}\#1}} \right) \left(\frac{\partial\theta}{\partial\lambda} \right)^{-1}, \quad (5)$$

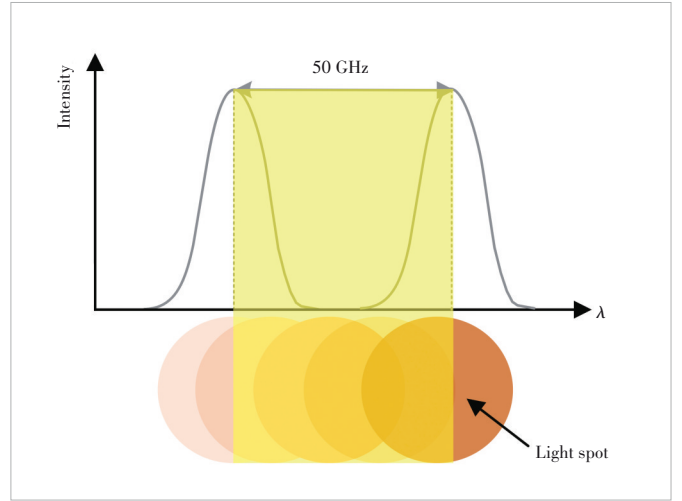
where λ is the operation wavelength, a is the system aperture determined by the aperture stop, b is the width of the entrance slit, $f_{\text{lens}\#1}$ is the focal length of the collimator lens between the entrance slit and the grating, and $\partial\theta/\partial\lambda$ represents the angular dispersion of the grating.

To meet the requirements for bandwidth tuning accuracy and minimum spectral resolution, we choose an LCoS pixel size of 8 μm and a focal length of 90 mm of lens#1. As a result, a bandwidth tuning accuracy of 6.25 GHz is achieved with a grating dispersion capability exceeding 0.002 $\text{rad}\cdot\text{nm}^{-1}$.

3.3.3 dB Bandwidth

Due to the wavelength continuity of the optical signal, the light spot will be overlapped in the margin of two neighbor channels, leading to the bandwidth for a grid channel smaller than the ideal bandwidth. The light spot size should be minimized to achieve better operational bandwidth performance. Given that the system is configured as a symmetric 4f, the Gaussian light spot on the LCoS surface aligns with that at the front focus of cylindrical lens 1. Thus, the waist of the light spot at the front focus of the cylindrical lens 1 must be carefully regulated using the micro-lens array and the lens positioned after the birefringent crystal. The system's bandwidth performance is evaluated by calculating the Gaussian beam waist required for the 3 dB and 0.5 dB bandwidths, as shown in Fig. 5.

Based on the equation of coupling efficiency between the optical fiber and the light spot, the fiber coupling efficiency is calculated for various ratios of the light spot being deflected to the desired direction. Fig. 6 illustrates the relations between the truncated position of the light spot and the coupling efficiency back into the fiber. To simulate an actual bandwidth testing scenario of an LCoS-WSS, we select a 50 GHz at a 6 dB window on the LCoS for the operation and calculate the 3 dB and 0.5 dB bandwidths. Assuming that the frequency range from 190.6375 THz to 196.675 THz corresponds to the 1920 pixels arranged horizontally on the LCoS, the 50 GHz grid channel occupies an average of 16 pixels. According to the results shown in Fig. 6, the following inequality must be satisfied to meet the WSS requirements^[20]:



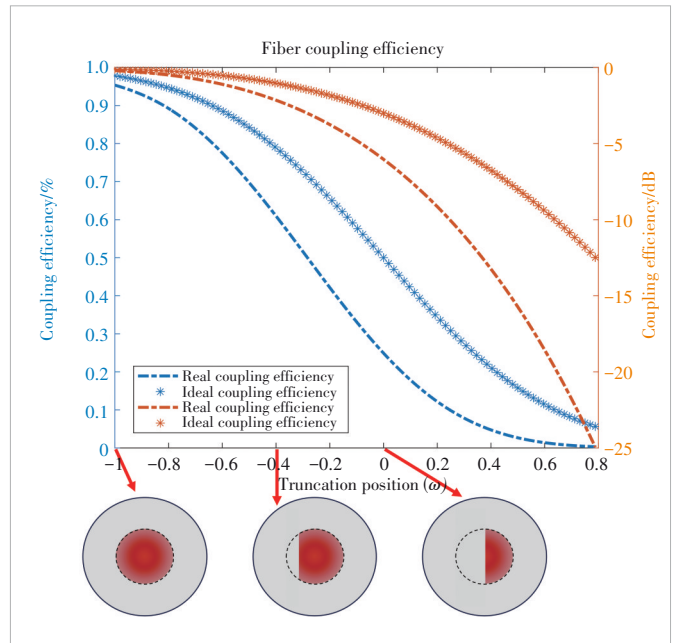
▲ Figure 5. Schematic diagram of the system's bandwidth

$$50 \text{ GHz} \times (1 - 2 \times 0.283 \omega_{\text{LCoS}}/d) > 46.0 \text{ GHz (3 dB)}$$

$$50 \text{ GHz} \times (1 - 2 \times 0.798 \omega_{\text{LCoS}}/d) > 37.5 \text{ GHz (0.5 dB)}, \quad (6)$$

where ω_{LCoS} is the beam waist on the LCoS, and d is the window width on the LCoS.

Our analysis indicates that the ratio ω_{LCoS}/d should be less than 0.14. Assuming an average value for the windowing operation, each 50 GHz channel on the LCoS is allocated with a window of 128 μm , which implies that ω_{LCoS} is less than 18 μm . It is also important to note that the light spot is distributed non-uniformly along the horizontal direction on the LCoS for different wavelengths. With Zemax simulation results, the window widths of the 50 GHz channels should be set at 117 μm , 124 μm , and



▲ Figure 6. Fiber coupling efficiency for different truncation ratios

134 μm of the LCoS for the wavelengths of 1 524 nm, 1 548 nm, and 1 572 nm, respectively. This leads to the maximum beam waists of 16.53 μm , 17.52 μm , and 18.93 μm . Considering these factors comprehensively, the beam waist on the LCoS surface should be designed as $\omega_{\text{LCoS}} \leq 16 \mu\text{m}$, resulting in a 3 dB bandwidth of 46 GHz and a 0.5 dB bandwidth of 37.5 GHz.

3.4 Port Isolation

The isolation (ISO) can be represented as

$$\text{ISO} = 10 \times \log_{10} \left(\exp \left(-\frac{2a^2}{\omega^2} \right) \right), \quad (7)$$

where a is the spacing of the fiber array, and ω is the beam size at the front focal plane of the micro-lens.

It assumes all light not directed at the target fiber contributes to crosstalk, whereas, in reality, only a small fan-shaped region leaks into adjacent ports. This suggests that the calculation results of Eq. (7) are much more stringent for design.

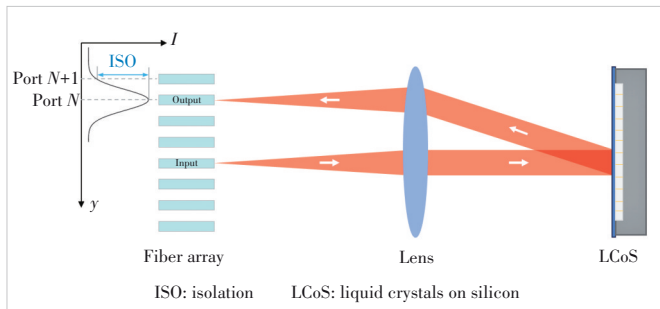
The port isolation of a WSS is primarily determined by the beam waist radius and the spacing of the fiber array (Fig. 7). Due to the limitation of steering efficiency, the period of the blazed grating displayed on the LCoS must exceed seven pixels. Consequently, the maximum steering angle is less than 1.38 degrees for a pixel size of 8 μm and less than 3.39 degrees for a pixel size of 3.74 μm . Increasing the spacing between fibers will inevitably reduce the number of available ports unless port isolation is compromised. For the given ISO of 25 dB, a fiber array of 40 ports with a spacing of 250 μm and a micro-lens array with a focal length of 0.73 μm are used.

3.5 Insertion Loss

Regarding the entire system structure, the insertion loss can be characterized as encompassing the prism grating loss, optical component absorption loss, LCoS diffraction loss, and fiber coupling, among other factors.

$$\text{IL} = \text{IL}_{\text{GRISM}} + \text{IL}_{\text{LCoS}} + \text{IL}_{\text{absorb}} + \text{IL}_{\text{coupling}} + \text{IL}_{\text{other}}. \quad (8)$$

Table 1 presents a theoretical analysis of the intrinsic insertion loss of the WSS. Generally, the difference between the experimental and theoretical values is small and could be attrib-



▲ Figure 7. Port isolation of a WSS system

▼ Table 1. Intrinsic loss of WSS

Component	Transmission	Pass	Loss/dB
Grism	0.87	2	-1.21
Intrinsic LCoS reflectivity	0.87	1	-0.60
System absorption	0.85	2	-1.42
Fiber coupling	0.85	1	-0.71
Total			-3.94

LCoS: liquid crystals on silicon WSS: wavelength selective switch

uted to the misalignment of the system and the diffraction efficiency of the LCoS. Particularly, the system adopts a polarization-insensitive prism grating, which has approximately the same diffraction efficiency for beams with different polarization states. The PDL can be controlled within 0.2 dB.

4 Simulation Performance Analysis

4.1 System Modeling Construction and Parameter Optimization

In our design, we have developed a microlens fiber array, polarization multiplexing module, beam combining module, cylindrical lens prism grating, and optical wedge with the entire system dimensioning approximately 110 mm × 90 mm × 15 mm. The simulation involves modeling a micro-lens array with a spacing of 250 μm and setting the input spectral range to 6 THz (between 1 524 nm and 1 572 nm). The central wavelength is set at 1 548 nm, with equal weighting given to the marginal wavelengths of 1 524 nm and 1 572 nm. The aperture value of the Gaussian beams is set to 5.2 μm . Additionally, the simulation included the emulation of a fiber optic array on the diaphragm surface, with the micro-lens array positioned after the diaphragm. In the system simulation, the micro-lens acts as a single lens with a radius of curvature of 1.849 mm and a thickness of 2.57 mm. It enlarges the size of the incoming Gaussian beam waist to 69 μm . Behind the micro-lens, a collection of Fourier lenses is positioned, with a combined focal length of 150 mm prior to optimization. Simultaneously, the micro-lens array is put in the front focal plane of lens#1, which causes the beam to become collimated and form parallel light. Once the lens group focuses the beam into parallel light by the lens group, it reaches the prism grating positioned on its back focal plane. The distance between the grating and lens#1 is typically no more than 90 mm, which ensures that the collimated light emitted from the Fourier lens group experiences minimal loss and reduces the overall size of the system. Then the prism grating disperses the incident light into three different wavelengths: 1 524 nm, 1 548 nm, and 1 572 nm. Lens #1 is constructed as a cylindrical mirror with curvature on both sides to eliminate any distortions in the system. The initial focal length of lens#1 is 90 mm before optimization. Upon passing through lens#1, the Gaussian beam undergoes compression, formatting a slender elongated spot. This

spot takes the form of a lengthy circle before optimization. After two passes through lens#1, a curved optical wedge is introduced behind it to counteract optical path length and eradicate chromatic aberration. The beam then strikes the LCoS in parallel, which is replaced by a planar reflector in simulation. Fig. 8a illustrates the layout of the optical components in simulation and the transmission paths of three beams of light of different wavelengths. The LCoS is modeled to include the mechanical structure surface, and the front and rear surfaces. The LCoS is simulated as a reflective grating, with diffractive surfaces added in different directions to represent diffraction in the x - and y -directions, as shown in Fig. 8b. To minimize the number of system optimization procedures, we initially alter the LCoS surface by rotating it at a specific angle to align with the relevant port. This allows us to adjust the rotation angle of the mirror instead of modifying the diffraction angle of the LCoS.

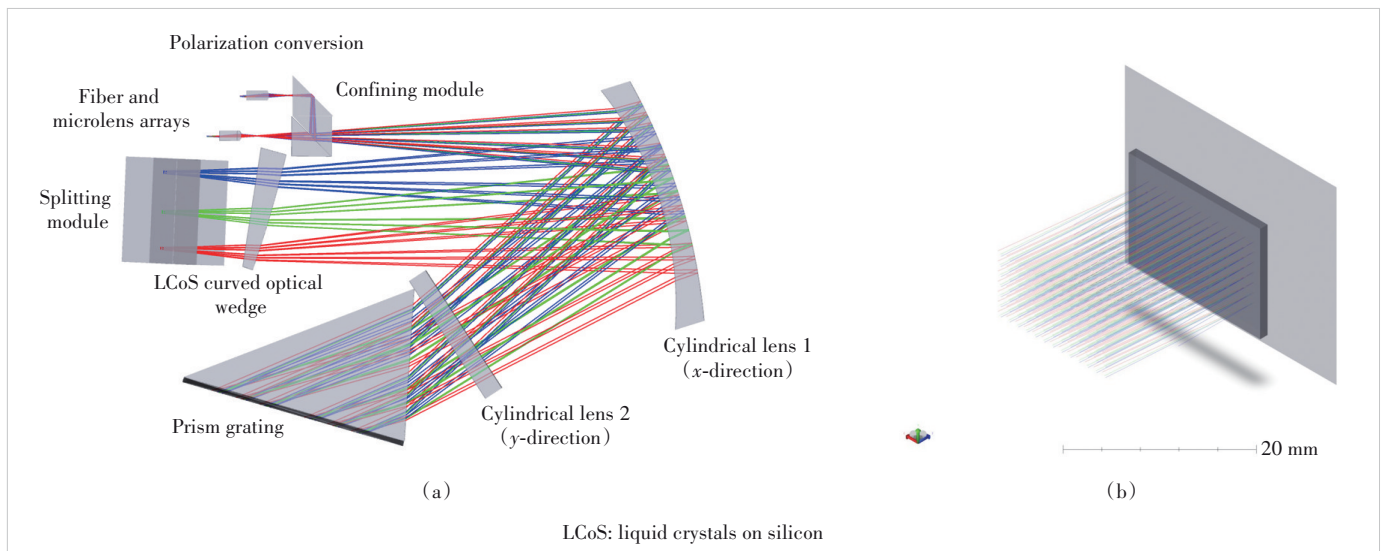
The simulation aims to achieve precise wavelength resolution while maximizing the number of ports. This is achieved by adjusting the deflection angle of the reflector, which is used to simulate the diffraction of the LCoS. Previous analysis has shown that, for the spot on the LCoS, increasing the size of its y -axis direction within the active area will result in a larger coverage of the LCoS. This would lead to more effective pixel coverage, higher diffraction efficiency, and less system transmission insertion loss. Meanwhile, the wavelength resolution can be enhanced by reducing the beam size in the x -direction of the LCoS. Eventually, to achieve the two primary goals of increasing the number of ports and improving the spectral resolution, the approach automatically optimizes the system by defining the merit function for the relevant parameters, performing iterative optimization, and utilizing the Zemax-Damped Least Squares local optimization algorithm.

The optimization of the beam incident on the LCoS is achieved by manipulating operands through the repeated modification of normalized coordinates for each wavelength within the merit function. Simultaneously, we impose restrictions on the dimensions of WSS, the width of the glass rim of the cylindrical lens, the distance between the glass layers, and the thickness of the glass. These constraints aim to prevent our gadget from undergoing significant deformation during optimization and to minimize the challenges associated with processing the component to achieve optimal results. We also adjust the optical wedge slope, the curvature of the cylindrical mirror, thickness, and air spacing to optimize the properties of the beam on the LCoS. The approach for optimizing the beam size at the exit port of the micro-lens is identical to the one used for optimizing the beam size on the LCoS. The objective is to regulate the size of the beam as it reaches the front of the micro-lens array, ensuring the beam waist size of the Gaussian beam received at the front of the micro-lens is essentially identical to that at the emitting port. This alignment guarantees improved efficiency in coupling throughout the deflection process. The merit function used in the simulation can be expressed as

$$(\text{MF})^2 = \sum_i W_i (V_i - T_i)^2 / \sum_i W_i, \quad (9)$$

where MF is the merit function, V_i is the actual value of the variable, T_i is the target value of the variable, and W_i is the weight of the variable. As mentioned before, T_i can be set as variables that affect the quality of the beams at the exit port of the micro-lens and on the LCoS. Specific variable type settings are given in Table 2.

Taking into account the symmetry of the whole optical system and optimizing for speed, our simulation establishes a to-



▲ Figure 8. Schematic diagram of the optical structure of WSS in Zemax: (a) overall component layout and (b) model of LCoS

▼Table 2. Target variable settings in Zemax

T_i	Variables	Operand
T_1	Coupling efficiency	POPD(0)
T_2	Beam width on LCoS	POPD(23)
T_3	Beam size of the waist near LCoS plane	POPD(7)
T_4	Overlap of beams of different polarization on LCoS	DIFF
T_5	Width of beam coverage in x -direction of LCoS	REAX
T_6	Coordinate values of different ports returning to FA	REAX
T_7	Beam size of different ports returning to FA	POPD(23)

DIFF: difference of two operands

POPD: physical optics propagation data

FA: fiber array

 REAX: real ray x -coordinate

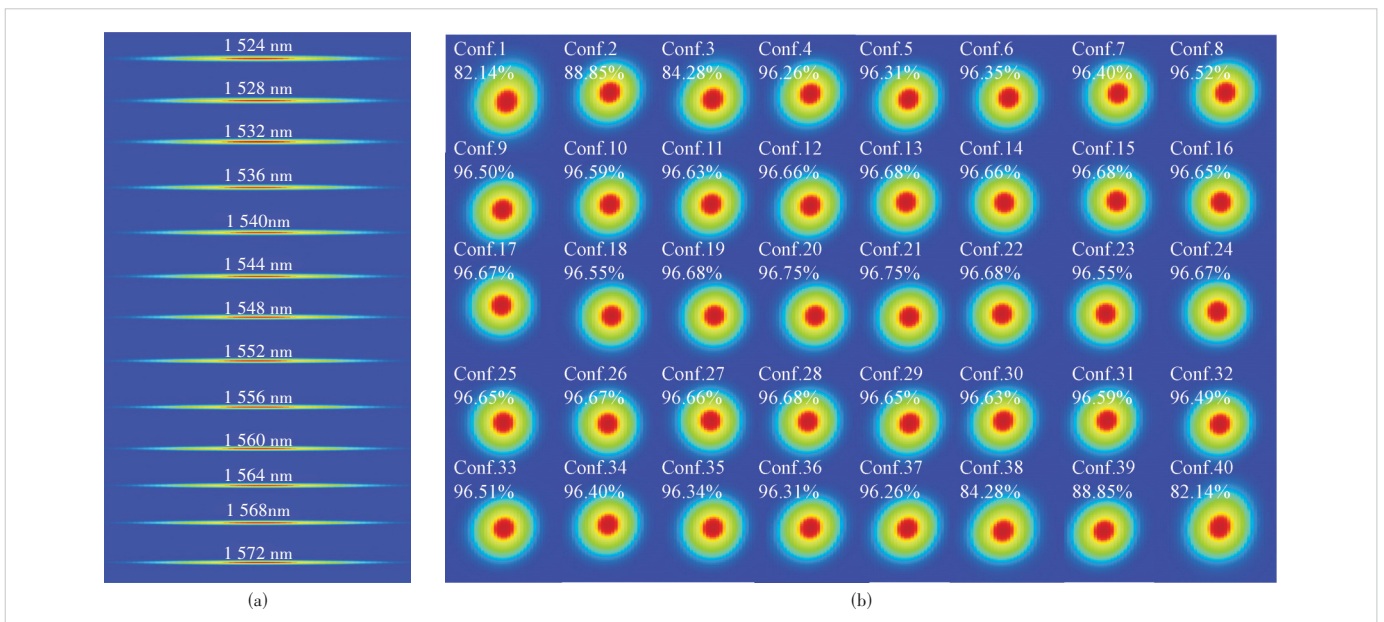
LCoS: liquid crystals on silicon

tal of 40 multi-configurations, corresponding to ports 20 to 40 of the optical system. Each port is associated with two polarization states. During the optimization process, we thoroughly assess the performance of all ports to get the most optimum system evaluation. The merit function of the system primarily assesses the coupling efficiency between each port, the extent of overlap between beams with different polarization states, the size of the beam waist on the LCoS, and the 3 dB bandwidth of the 50 GHz grid. Initially, the curvature and rotation angle of the components, as well as the distances between them, are simulated and tuned individually, which is aimed to achieve a coupling efficiency of 95% for the central wavelength returning to the central port, while also ensuring that the P-polarization and S-polarization of the beams overlap at the LCoS. Once the location and parameters of the components are confirmed, the angle and curvature of the curved optical wedge are adjusted to optimize the

coupling efficiency for the wavelengths returning to the center port, which ensures that the LCoS can cover a wavelength range from 1 524 nm to 1 572 nm as required. Subsequently, curved fiber arrays are adopted to compensate for the coupling mismatch caused by conic diffraction and thereby enhance the coupling effectiveness of various port switching. To improve the overall system performance, it is necessary to modify the objective and weight values based on the optimization findings, which will result in reduced merit function values. Once this optimization process is finished, the bandwidth of the proposed WSS is simulated and evaluated to determine if it satisfies the relevant requirements. This process continues until the system index is optimized to match the criteria.

4.2 Performance of Designed WSS

In this system, we primarily focus on several key aspects: system size, spot size on the LCoS, coupling efficiency of the output ports, and bandwidth performance. The overall system size is 110 mm×90 mm. The Gaussian beam on the LCoS, featuring 12 sampling wavelengths, is depicted in Fig. 9a. It is observed that the Gaussian beams of different wavelengths are arranged in a columnar distribution as shown in the figure, with a uniform width and centered alignment in the x -direction on the LCoS, where the spot radius is 1.015 mm and the dispersion direction spot radius is 16 μm . Through physical optics propagation calculations in Zemax, we derived the ideal coupling efficiency for different ports, with the coupling efficiency of twins A and B ranging from 96.75% to 82.14% for almost all ports. As shown in Fig. 9b, the coupling effi-



▲ Figure 9. Deflection performance of the WSS system in Zemax: (a) layout of Gaussian beams on the LCoS and (b) shape of the beam to be coupled into the fiber

▼ Table 3. Coupling efficiency of beam deflection for three wavelength channels and 40 ports

Port	1 524 nm	1 550 nm	1 572 nm	Port	1 524 nm	1 550 nm	1 572 nm
1	87.00%	81.61%	60.24%	21	93.03%	96.72%	94.15%
2	91.16%	89.09%	77.83%	22	93.12%	96.65%	93.91%
3	89.42%	84.24%	87.70%	23	93.01%	96.52%	94.09%
4	91.57%	96.24%	86.84%	24	92.98%	96.65%	93.75%
5	91.80%	96.28%	90.88%	25	92.85%	96.63%	93.80%
6	92.02%	96.32%	90.82%	26	93.03%	96.65%	93.78%
7	92.07%	96.39%	91.14%	27	93.04%	96.64%	93.48%
8	92.53%	96.49%	91.60%	28	92.83%	96.65%	93.50%
9	92.36%	96.47%	92.57%	29	92.94%	96.63%	93.38%
10	92.81%	96.56%	92.54%	30	92.81%	96.60%	93.00%
11	92.81%	96.60%	93.00%	31	92.81%	96.56%	92.54%
12	92.94%	96.63%	93.38%	32	92.36%	96.47%	92.57%
13	92.83%	96.65%	93.50%	33	92.53%	96.49%	91.60%
14	93.04%	96.64%	93.48%	34	92.07%	96.39%	91.14%
15	93.03%	96.65%	93.78%	35	92.02%	96.32%	90.82%
16	92.85%	96.63%	93.80%	36	91.80%	96.28%	90.88%
17	92.98%	96.65%	93.75%	37	91.57%	96.24%	86.84%
18	93.01%	96.52%	94.09%	38	89.42%	84.24%	87.70%
19	93.12%	96.65%	93.91%	39	91.16%	89.09%	77.83%
20	93.03%	96.72%	94.15%	40	87.01%	81.61%	60.24%

ciency of twins A and B fulfills the design criteria. Table 3 illustrates the coupling efficiency of beam deflection for three wavelength channels (1 524 nm, 1 550 nm, and 1 572 nm). The coupling efficiency for beam deflection for the 1 572 nm channel experiences a notable decrease, which can be improved by further modifying the characteristics of the optical wedge and lens#1.

The bandwidths of the simulated system are also tested. By opening windows on the LCoS for long, medium, and short wavelengths, beams with a 50 GHz bandwidth are scanned at a frequency precision of 1 GHz to determine the coupling efficiency at single-frequency points. This procedure verified the 3 dB bandwidth and 0.5 dB bandwidth for the central port output. In the case of deflection of all ports, more than 44 GHz of 3 dB bandwidth can be achieved at a 50 GHz grid for all channels (120×50 GHz), as shown in Fig. 10. The theoretical calculations anticipate a 3 dB bandwidth exceeding 46 GHz. Discrepancies between this prediction and the Zemax simulations may stem from aberrations influencing the beam spot shape and the departure from an ideal 4f optical system configuration in practical implementations.

5 Conclusions

A twin 1×40 WSS is designed with theoretical analysis and simulation investigation. Polarization multiplexing is employed for the two sources of the twin WSS by polarization conversion before the common optical path. The polarization separation module realizes polarization demultiplexing before the light beam launches onto the LCoS. The parameters of prism grating are carefully designed to cover the super C band on the active area of the LCoS and obtain enough dispersion ability for fine bandwidth manipulation. The beam waist on the LCoS is carefully regulated with the micro-lens array and the lens after the birefringent crystal to guarantee optimal 3 dB bandwidth performance. The space of the fiber array is optimized to harness the isolation between the neighbor ports. Simulation results demonstrate that the coupling efficiency of our LCoS-based WSS can exceed 80%, reaching over 96% for 90% of the ports. Additionally, a 3 dB bandwidth of more than 44 GHz is obtained at a 50 GHz grid across all channels. In future studies, we will explore more ports and develop a new structure suitable for higher performance.

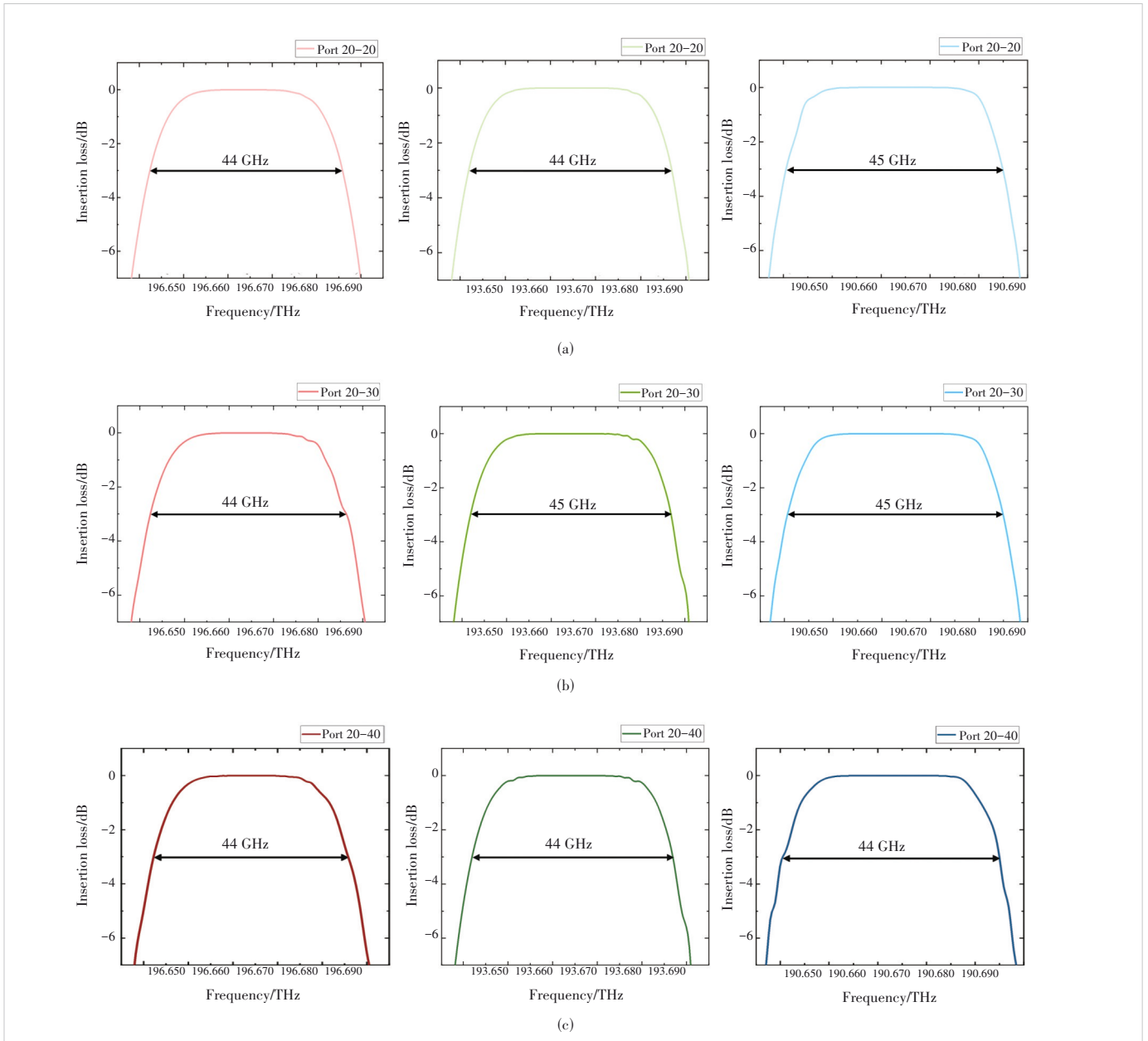
ration module realizes polarization demultiplexing before the light beam launches onto the LCoS. The parameters of prism grating are carefully designed to cover the super C band on the active area of the LCoS and obtain enough dispersion ability for fine bandwidth manipulation. The beam waist on the LCoS is carefully regulated with the micro-lens array and the lens after the birefringent crystal to guarantee optimal 3 dB bandwidth performance. The space of the fiber array is optimized to harness the isolation between the neighbor ports. Simulation results demonstrate that the coupling efficiency of our LCoS-based WSS can exceed 80%, reaching over 96% for 90% of the ports. Additionally, a 3 dB bandwidth of more than 44 GHz is obtained at a 50 GHz grid across all channels. In future studies, we will explore more ports and develop a new structure suitable for higher performance.

Acknowledgment

The authors gratefully acknowledge the support provided by ZTE Corporation for the research project on wavelength-selective switches. We are deeply indebted to Dr. YOU Quan, Ms. CHEN Wen, Mr. LI Yuzhe and Dr. LIU Chen for their unwavering support, expert guidance, and insightful discussions throughout this study. Their expertise and dedication significantly enriched the research process. We express our sincere appreciation to everyone who contributed to the success of this endeavor.

References

- [1] KOZDROWSKI S, ŻOTKIEWICZ M, SUJECKI S. Optimization of optical networks based on CDC-ROADM technology [J]. Applied sciences, 2019, 9 (3): 399. DOI: 10.3390/app9030399
- [2] FORD J E, AKSYUK V A, BISHOP D J, et al. Wavelength add-drop switching using tilting micromirrors [J]. Journal of lightwave technology, 1999, 17(5): 904 - 911. DOI: 10.1109/50.762910
- [3] DOERR C R, STULZ L W, LEVY D S, et al. Silica-waveguide 1×9 wavelength-selective cross connect [C]//Optical Fiber Communication Conference. OSA, 2002. DOI:10.1109/OFC.2002.1036752
- [4] BAXTER G, FRISKEN S, ABAKOUMOV D, et al. Highly programmable wavelength selective switch based on liquid crystal on silicon switching elements [C]//Proc. Optical Fiber Communication Conference and the National Fiber Optic Engineers Conference. IEEE, 2006. DOI: 10.1109/OFC.2006.215365
- [5] MA Y R, STEWART L, ARMSTRONG J, et al. Recent progress of wavelength selective switch [J]. Journal of lightwave technology, 2021, 39(4): 896 - 903. DOI: 10.1109/JLT.2020.3022375
- [6] HAN T, PLUMRIDGE J, FRISKEN S, et al. LCoS-based matrix switching for 2 × 4 WSS for fully flexible channel selection [C]//Proc. International Conference on Photonics in Switching (PS). IEEE, 2012: 1 - 3
- [7] YANG H N, ROBERTSON B, CHU D P. Crosstalk reduction in holographic wavelength selective switches based on phase-only LCoS devices [C]//Proc. Optical Fiber Communication Conference. OSA, 2014. DOI: 10.1364/ofc.2014.th2a.23
- [8] YANG H N, ROBERTSON B, WILKINSON P, et al. Small phase pattern 2D beam steering and a single LCOS design of 40 1 × 12 stacked wavelength selective switches [J]. Optics express, 2016, 24(11): 12240 - 12253. DOI: 10.1364/OE.24.012240
- [9] HE J, NORWOOD R A, BRANDT-PEARCE M, et al. A survey on recent



▲ Figure 10. Bandwidth performance at 50 GHz grid with the center wavelengths of 1524 nm, 1548 nm, and 1572 nm from left to right for the deflections from port 20 to 20, 30, and 40, respectively

- advances in optical communications [J]. *Computers & electrical engineering*, 2014, 40(1): 216 - 240. DOI: 10.1016/j.compeleceng.2013.11.017
- [10] ROBERTSON B, YANG H N, REDMOND M M, et al. Demonstration of multi-casting in a 1×9 LCoS wavelength selective switch [J]. *Journal of lightwave technology*, 2014, 32(3): 402 - 410. DOI: 10.1109/JLT.2013.2293919
- [11] WANG M, ZONG L J, MAO L, et al. LCoS SLM study and its application in wavelength selective switch [J]. *Photonics*, 2017, 4(2): 22. DOI: 10.3390/photonics4020022
- [12] MILEWSKI G, ENGSTRÖM D, BENGTTSSON J. Diffractive optical elements designed for highly precise far-field generation in the presence of artifacts typical for pixelated spatial light modulators [J]. *Applied optics*, 2007, 46(1): 95 - 105. DOI: 10.1364/AO.46.000095
- [13] PERSSON M, ENGSTRÖM D, BENGTTSSON J, et al. Realistic treatment of spatial light modulator pixelation in real-time design algorithms for holographic spot generation [C]//Proc. Digital Holography and Three-Dimensional Imaging. OSA, 2011. DOI: 10.1364/dh.2011.dwc32
- [14] PERSSON M, ENGSTRÖM D, GOKSÖR M. Reducing the effect of pixel crosstalk in phase only spatial light modulators [J]. *Optics express*, 2012, 20(20): 22334 - 22343. DOI: 10.1364/OE.20.022334
- [15] NIE J W, DONG L Y, TONG X W, et al. Phase flicker minimisation for crosstalk suppression in optical switches based on digital liquid crystal on silicon devices [J]. *Optics express*, 2021, 29(7): 10556 - 10567. DOI: 10.1364/OE.415800
- [16] ROBERTSON B, ZHANG Z C, YANG H N, et al. Reduction of crosstalk in a colourless multicasting LCOS-based wavelength selective switch by

the application of wavefront encoding [C]//Proc. Next-Generation Optical Communication: Components, Sub-Systems, and Systems. SPIE, 2012. DOI: 10.1117/12.907281

- [17] HUANG L H., RAO C H. Wavefront sensorless adaptive optics: a general model-based approach [J]. Optics express, 2011, 19(1): 371 - 379. DOI: 10.1364/OE.19.000371
- [18] FRISKEN S J. Polarization diverse wavelength selective switch: US20170214482 [P]. 2017
- [19] ZHOU Y R, KEENS J, WAKIM W. High capacity innovations enabling scalable optical transmission networks [J]. Journal of lightwave technology, 2023, 41(3): 957 - 967. DOI: 10.1109/JLT.2022.3206277
- [20] MAROM D M, NEILSON D T, GREYWALL D S, et al. Wavelength-selective $1 \times K$ switches using free-space optics and MEMS micromirrors: theory, design, and implementation [J]. Journal of lightwave technology, 2005, 23(4): 1620 - 1630. DOI: 10.1109/JLT.2005.844213

Biographies

WANG Han received her BS degree from Beijing Jiaotong University, China and is pursuing a master's degree at Huazhong University of Science and Technology, China. Her research interests include the optical design of wavelength selective switches and LCoS algorithms, with a current focus on designing multi-band integrated WSS and $M \times N$ WSS.

LIU Maoqi received his bachelor's degree from the School of Optical and Electronic Information, Huazhong University of Science and Technology, China. Currently, he is a joint PhD student at the National Engineering Laboratory for Next Generation Internet Access System, Huazhong University of Science and Technology, and the Photonics Research Institute, Hong Kong Polytechnic University, China. His research primarily focuses on multi-band WSS, aiming to improve their efficiency and scalability in modern optical networks. Additionally, he explores the integration of optical fiber communication and sensing, seeking innovative solutions to combining these technologies for multifunctional applications in 6G telecommunications.

FENG Zhenhua received his PhD from Huazhong University of Science and Technology, China in 2017. He has been engaged in the research and development of optical fiber communication systems and algorithms for about five years with more than 70 journal and conference publications and about 10 granted patents. His research interests mainly lie in the design and verification of optical transmission systems and DSP algorithms.

LIU Minghuan received his PhD from Changchun Institute of Optics, Fine Mechanics and Physics, Chinese Academy of Sciences. He has worked in the Wavelength Division System Department of the Cable Research Institute, ZTE Corporation since June 2023, engaged in the work related to WSS design.

MAO Baiwei (mao.baiwei@zte.com.cn) received his PhD from Nankai University, China in 2022. He has worked in the Wavelength Division System Department of the Cable Research Institute, ZTE Corporation since July 2022, engaged in optical transmission system planning and optimization.



Ultra-Low Linewidth Frequency Stabilized Integrated Lasers: A New Frontier in Integrated Photonics

GU Zhenqian, YANG Zhen, ZHA Lulu, HU Junhui,
CHI Nan, SHEN Chao
(School of Information Science and Technology, Fudan University,
Shanghai 200438, China)

DOI: 10.12142/ZTECOM.202404005

<https://kns.cnki.net/kcms/detail/34.1294.TN.20241111.1530.002.html>,
published online November 12, 2024

Manuscript received: 2024-10-22

Abstract: With the advancement of photonic integration technology, ultra-low linewidth frequency-stabilized lasers have demonstrated significant potential in precision measurement, quantum communication, atomic clocks, etc. This review summarizes the latest developments in integrated photonics for achieving ultra-low linewidth lasers, particularly breakthroughs made by integrating Brillouin lasers. We discuss the design principles, manufacturing processes, performance characteristics, and potential value of these lasers in various applications.

Keywords: photonic integrated circuit (PIC); ultra-low linewidth; Brillouin lasers; high Q-factor

Citation (Format 1): GU Z Q, YANG Z, ZHA L L, et al. Ultra-low linewidth frequency stabilized integrated lasers: a new frontier in integrated photonics [J]. *ZTE Communications*, 2024, 22(4): 29 – 39. DOI: 10.12142/ZTECOM.202404005

Citation (Format 2): Z. Q. Gu, Z. Yang, L. L. Zha, et al., “Ultra-low linewidth frequency stabilized integrated lasers: a new frontier in integrated photonics,” *ZTE Communications*, vol. 22, no. 4, pp. 29 – 39, Dec. 2024. doi: 10.12142/ZTECOM.202404005.

1 Introduction

Photonic integrated circuits (PICs) offer a pathway to reduce costs, complexity, power consumption, and sizes by integrating various optical functions at the chip scale^[1-4]. However, many high-end applications, such as quantum communication^[5], atomic clocks^[6], and precision measurement^[7-9], require wavelengths and performance levels that current silicon-based photonic platforms struggle to achieve. To meet these demands, next-generation photonic integration requires ultra-broadband photonic circuit platforms spanning from ultraviolet to infrared^[10-11]. These platforms should possess low loss, high power handling capabilities, and a rich array of linear and nonlinear circuit functionalities.

With the advent of the information age, the demand for precision measurement and high-speed communication continues to grow^[12-14]. Ultra-low linewidth lasers have become increasingly important due to their advantages in frequency stability and coherence^[12-19]. Traditional ultra-low linewidth laser systems, due to their size and cost, have been constrained in application across various fields. The development of integrated

photonics offers the potential to create miniaturized, low-cost and, ultra-low linewidth lasers^[20-21]. This article reviews the latest advancement in integrated photonics for achieving ultra-low linewidth lasers, with a particular focus on integrated Brillouin lasers that utilize phonons generated through light-matter interactions to achieve linewidth narrowing^[22-24].

2 Development of Integrated Photonics

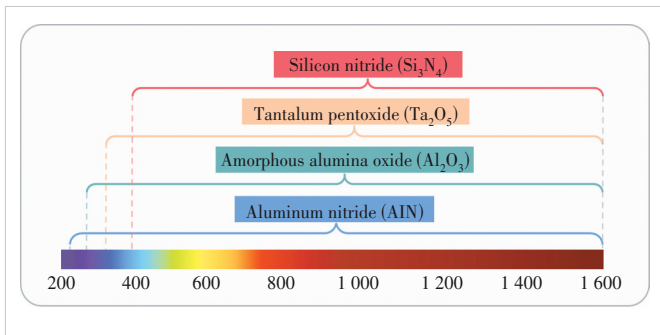
Integrated photonics has become a hotspot in engineering technology in recent years. By integrating active devices such as lasers, optical amplifiers, modulators, and photodetectors, along with various passive components on a single chip, integrated photonics enables complete optical systems. PICs have a wide range of applications, including high-speed optical communication^[25], quantum communication^[1, 26-27], biosensing^[28-29], and precision measurement^[6-9]. This technology provides effective means to reduce costs, simplify system complexity, and decrease power consumption and sizes.

Silicon-based photonic integration technology has garnered significant attention due to its compatibility with mature complementary metal-oxide-semiconductor (CMOS) processes^[30-33]. This compatibility not only lowers manufacturing costs but also allows for the use of existing CMOS foundries and related manufacturing ecosystems^[34]. The advantages of silicon-based photonic integration lie in the high refractive in-

This research is partially funded by the Natural Science Foundation of China Project under Grant Nos. 61925104 and 62031011, and the Key Research and Development Program of Jiangsu Province under Grant No. BE2021008-5.

dex contrast with oxide materials, enabling strong confinement of optical modes within waveguides^[35]. Additionally, the silicon-on-insulator (SOI) waveguide structure exhibits extremely low propagation loss. Moreover, III-V active materials can be easily integrated with SOI technology to achieve heterogeneous integration, providing optical gain for photonic integrated circuits and further enhancing their complexity and performance^[36-37].

However, silicon materials have certain limitations. The indirect bandgap of silicon (1.1 eV) results in higher waveguide loss and lower transparency at shorter wavelengths, such as visible and ultraviolet light^[38]. Furthermore, silicon's power handling capacity is limited due to nonlinear losses, which restricts its performance in some high-end applications^[39]. To overcome these limitations, researchers are exploring novel integrated photonic platforms based on wide bandgap semiconductor materials^[40-42]. Materials such as silicon nitride (Si_3N_4)^[43-44], aluminum oxide (Al_2O_3)^[10, 45], aluminum nitride (AlN)^[46-47], and tantalum pentoxide (Ta_2O_5)^[48] have become focal points in integrated photonics research due to their excellent optical transparency, low-loss characteristics, and outstanding mechanical and chemical stability. Fig. 1 illustrates the application space of different wavelength windows ranging from ultraviolet (200 nm) to infrared (2 350 nm).



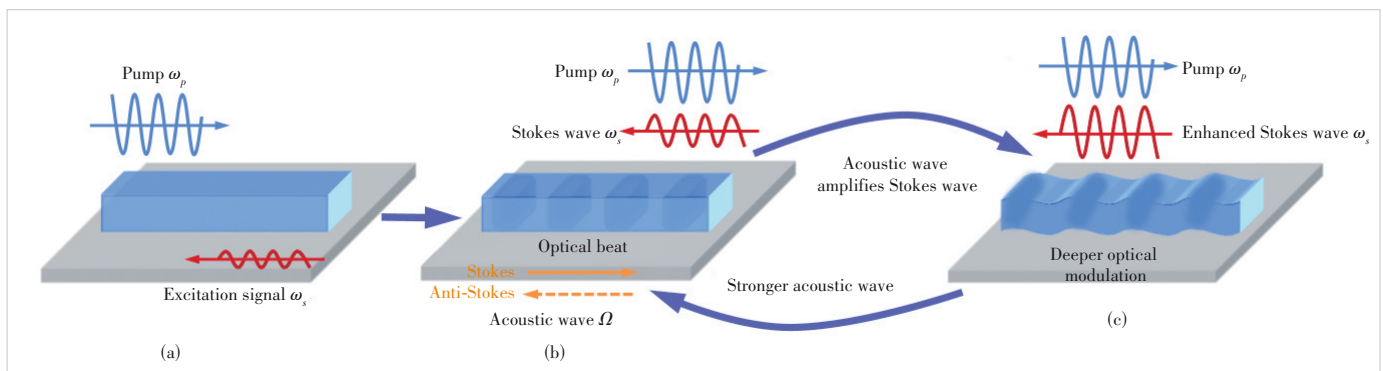
▲ Figure 1. Next generation optical waveguide platforms and wavelength transparency based on the bandgap (Si_3N_4 , Ta_2O_5 , Al_2O_3 , and AlN)^[49]

Si_3N_4 is particularly noteworthy due to its extremely low transmission loss in the visible to infrared wavelength range. Coupled with its high refractive index contrast, Si_3N_4 provides an ideal platform for realizing compact photonic devices with high-performance^[50-51]. Al_2O_3 stands out for its low-loss characteristics and high refractive index in the ultraviolet to visible wavelength range, making it a key candidate material for high-precision optical sensors and spectrometers^[10]. Meanwhile, AlN offers transparency in the ultraviolet range and a high electro-optic coefficient, indicating its potential applications in high-speed electro-optic modulators and ultraviolet photonics^[52].

Future research will focus on further reducing waveguide losses, improving Q-factors, achieving a broader wavelength tuning range, and enhancing the environmental stability of lasers. Additionally, the development of new materials, innovations in manufacturing processes, and the exploration of nonlinear optical effects will further propel the advancement of integrated photonics technology. With continuous technological breakthroughs and expanding applications, integrated photonics is set to play an increasingly crucial role in future scientific exploration and commercial applications.

3 Principles and Applications of Brillouin Lasers

Brillouin lasers represent a class of advanced lasers that achieve linewidth narrowing through the interaction of light with phonons generated via light-matter interactions. These lasers produce highly coherent and spectrally pure laser output by leveraging the nonlinear interactions between photons and phonons, demonstrating significant potential and value in applications ranging from the visible to the infrared wavelength range^[24, 53-55]. Fig. 2 illustrates the principle diagram of Brillouin lasers, showcasing the interaction between optical and acoustic modes, which forms the basis of stimulated Brillouin scattering (SBS). In the case of backward stimulated Brillouin scattering (BSBS), a pump signal with a frequency of ω_p interacts with a counter-propagating signal of frequency ω_s , which can either be an excited signal or a pump scattering signal



▲ Figure 2. Stimulated Brillouin scattering: (a) an optical pump interacts in the medium with a counterpropagating seed at the Brillouin frequency shift; (b) when the optical beat generated by said tones matches the Brillouin frequency shift, electrostriction induces an acoustic wave; (c) a stronger Stokes wave is created. The proposed deeper optical modulation generates a stronger grating^[58]

generated by thermal phonons. This interaction creates an optical beat pattern. When $\omega_p - \omega_s = \Omega$, the beat pattern enhances the acoustic wave through electrostriction. This enhanced acoustic signal, in turn, amplifies the Stokes wave via the photoelastic effect, creating a traveling refractive index grating. The pump light is strongly reflected by this refractive index grating, and due to the Doppler shift, the reflected wave precisely matches the Stokes frequency. The amplified Stokes signal further strengthens the acoustic mode, leading to a stimulated cycle where Stokes/anti-Stokes signals are further amplified^[56].

3.1 Brillouin Laser Principles

The phenomenon of Brillouin scattering is central to the working mechanism of Brillouin lasers. It describes the interaction between photons and phonons as light propagates through a medium, resulting in a slight change in light frequency^[57-59]. The specific principles are illustrated in Fig. 3, where SBS is identified as an inelastic scattering process. During this process, energy and momentum must be conserved. It can be categorized into Stokes (redshift) or anti-Stokes (blue-shift) processes. The Stokes process generates phonons, lowering the energy of the photons, while the anti-Stokes process absorbs phonons, increasing the energy of the photons. SBS primarily involves two possible interaction processes based on the propagation directions of the pump and Stokes light: BSBS and forward stimulated Brillouin scattering (FSBS).

In Brillouin lasers, this interaction is utilized to narrow the laser linewidth. Depending on the implementation, Brillouin lasers are mainly divided into two categories: fiber-based^[60-63] and waveguide-based^[64-66]. Waveguide-based Brillouin lasers leverage the confined optical modes within waveguides to interact with phonons, producing laser output with high coherence. These lasers can achieve sub-hertz linewidths, providing new technological pathways for applications in precision mea-

surement, quantum communication, and atomic clocks^[56].

3.2 Technical Advantages and Applications

The unique advantage of Brillouin lasers lies in their ability to significantly narrow the linewidth of the pump laser through nonlinear phonon interactions, resulting in laser output characterized by low white noise, low close-to-carrier frequency noise, and low relative intensity noise (RIN)^[67-69]. These features make Brillouin lasers indispensable in fields that require extremely narrow linewidth and high stability, such as precision measurement and quantum communication. Additionally, the ultra-narrow linewidth of Brillouin lasers shows great potential for applications in optical frequency standards, microwave photonics, and optical atomic clocks^[67-72].

With the advancement in materials science and micro-nano fabrication technologies, the integration and performance of Brillouin lasers are expected to improve further. Future research will focus on enhancing the frequency stability of these lasers, reducing system costs, and exploring new integration platforms and materials to enable broader applications^[56]. In particular, using wide bandgap semiconductor materials, such as Si_3N_4 , Al_2O_3 , and AlN , will offer new possibilities for extending Brillouin lasers' operation from the ultraviolet to the infrared wavelength range.

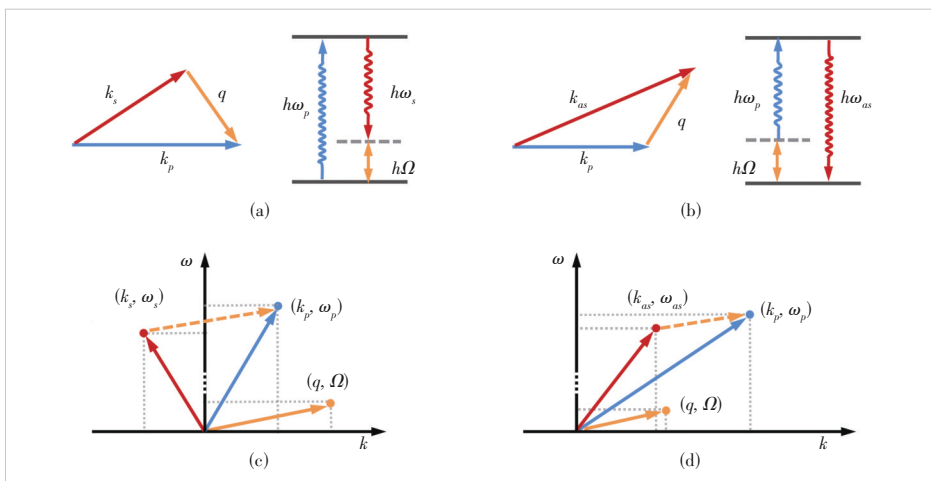
4 Design and Fabrication of Integrated Brillouin Lasers

The design and fabrication of integrated Brillouin lasers is a complex process requiring a balance among several critical parameters. The primary objective is to achieve a high Q-factor for narrow linewidth laser output while maintaining low waveguide loss to ensure high efficiency of the laser^[71-76]. During the design process, the interaction between the pump light and Stokes light must be carefully considered. This interaction is achieved through precise waveguide structure design to enable efficient energy conversion and phase matching.

Waveguide loss is a crucial factor in the design as it directly impacts the performance and threshold of the laser. Losses arise not only from the inherent absorption of the material but also from the geometric structure of the waveguide, sidewall roughness, and surface scattering^[72, 77].

To minimize these losses, designers employ various techniques including optimizing the cross-sectional shape of the waveguide, using low-roughness sidewalls and applying special coatings to reduce scattering.

The mode volume and Q-factor are two other key parameters influencing



▲ Figure 3. (a) Stokes process generates phonons, (b) anti-Stokes process absorbs phonons, (c) schematic of phase matching conditions for BSBS, and (d) schematic of phase matching conditions for FSBS

the performance of the laser. A high Q-factor resonator can enhance the intracavity optical field, thereby reducing the laser linewidth. Optimizing the mode volume helps achieve efficient pump and signal collection, which is critical for high-power laser output^[78]. Fig. 4 shows a resonator with an intrinsic Q-factor as high as 720 million at a wavelength of 1 615 nm. The intrinsic linewidth of the resonator is 258 kHz, with a waveguide loss of 0.034 dB/m, and it is used to achieve a Brillouin laser with a threshold power of 380 μ W. This study achieves high performance by combining a single-mode TM waveguide design with blanket etching and low-pressure chemical vapor deposition (LPCVD) of an 80 nm Si_3N_4 waveguide core. This core is integrated with a thermally grown under oxide cladding and a tetraethyl orthosilicate plasma-enhanced chemical vapor deposition (TEOS-PECVD) upper oxide cladding to reduce scattering losses^[74].

The loaded and intrinsic Q-values are measured using a laser that tunes from 1 550 nm to 1 630 nm (Velocity TLB-6700), with a measured maximum of 720 million at 1 615 nm, corresponding to a propagation loss of 0.034 dB/m. An intrinsic linewidth of 258 kHz and a loaded linewidth of 386 kHz are measured using Mach-Zehnder interferometer (MZI) and

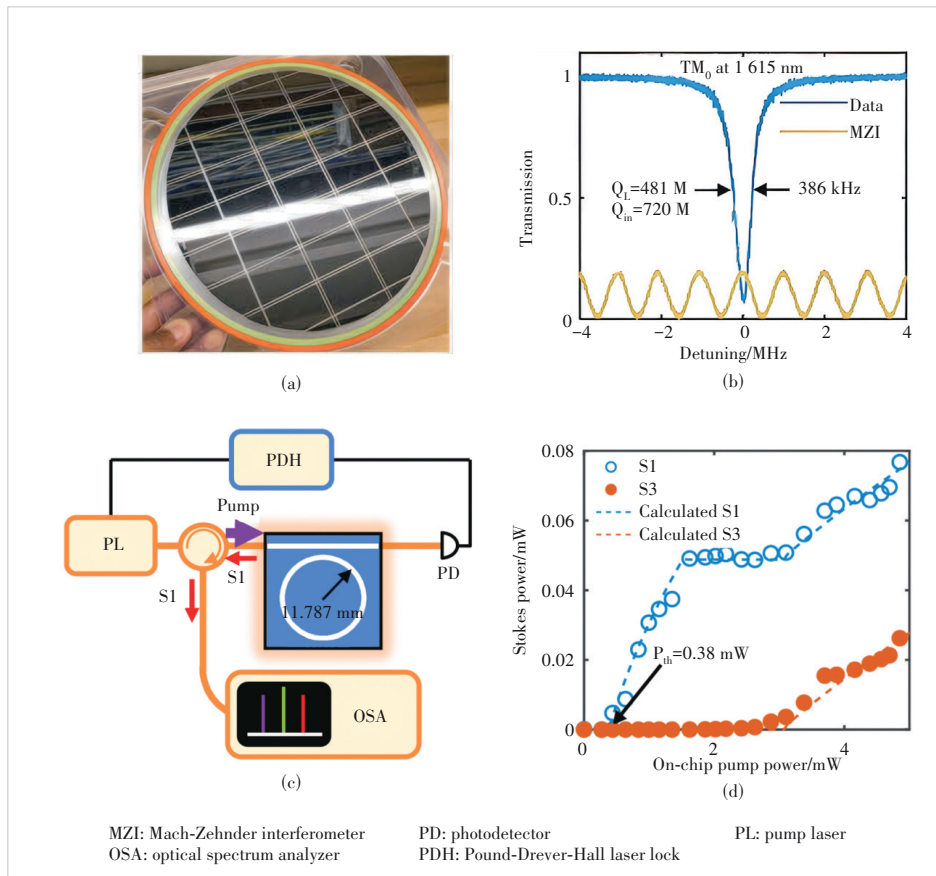
ringdown techniques. They demonstrate a 380 μ W threshold for the first order Stokes (S1) Brillouin lasing operating at 1 570 nm. A tunable laser is locked to the resonator using the Pound-Drever-Hall technique. Measurement of S1 on an optical spectrum analyzer (OSA) as a function of input pump power at 1 570 nm, shown in Fig. 4d, indicates a clear S1 threshold and a threshold power of 380 μ W. Using the cascaded Brillouin laser model, we can simulate the S1 and S3 Stokes power shown as dashed curves in Fig. 4c, with the measured loaded and intrinsic Q at 1 570 nm and an estimated Brillouin gain of 0.043 mW^{-1} .

Material selection is crucial for the performance of integrated Brillouin lasers. Si_3N_4 is preferred due to its excellent optical and mechanical properties and low loss across a wide wavelength range^[54, 74]. However, to cover a broader wavelength range or achieve specific functionalities, researchers are also exploring other materials such as lithium niobate on insulator (LNOI)^[79], arsenic trisulfide (As_2S_3)^[80-82], arsenic selenide (As_2Se_3)^[83], and tantalum pentoxide (Ta_2O_5). These materials possess varying optical characteristics and mechanical properties, making them suitable for different application scenarios.

The fabrication of waveguides typically begins with the deposition of a Si_3N_4 thin film on a silicon substrate, a process that can be accomplished using LPCVD or PECVD techniques^[51, 84]. After deposition, waveguide structures are formed through photolithography and etching processes. Precise control of the etching process is required to ensure the accuracy of the waveguide dimensions and the smoothness of the sidewalls, thereby reducing scattering loss.

After the waveguide structure is formed, a cladding layer is usually deposited to further reduce waveguide loss and protect the waveguide from environmental effects. The annealing step is crucial for eliminating internal stresses in the material and improving its optical quality, especially for Si_3N_4 , where appropriate thermal treatment can significantly enhance its optical properties.

Heterogeneous integration techniques allow different material components to be integrated onto a single chip, facilitating the creation of more complex photonic circuits. For instance, integrating Si_3N_4 waveguides



▲ Figure 4. (a) A 200 mm wafer after the manufacturing and dicing process; (b) resonance spectrum scan at 1 615 nm using a 1.078 MHz FSR Mach-Zehnder interferometer; (c) setup for the SBS laser; (d) measured on-chip power for S1 and S3 with the calculated curves, indicating a threshold of 0.38 mW ^[74]

with III-V semiconductor lasers or detectors can construct complete photonic systems with signal amplification and detection functionalities^[43].

Lastly, packaging technology is vital for protecting the laser from external environmental influences, ensuring long-term stability and reliability. The packaging process must consider optical coupling efficiency, thermal management, and compatibility with external fiber or electronic systems.

In summary, the design and fabrication of integrated Brillouin lasers require careful consideration of the waveguide loss, mode volume, Q-factor, material selection, and packaging. Advanced fabrication techniques and material choices are essential for optimizing laser performance and expanding its application potential.

5 Performance Optimization and Testing Methods

Optimizing the performance of integrated Brillouin lasers involves reducing the waveguide loss, increasing the Q-factor, and optimizing the linewidth. These parameters directly impact the laser's coherence, stability, and overall performance. Researchers employ various strategies and testing methods to achieve these optimization goals.

5.1 Reducing Waveguide Loss

The waveguide loss is a critical factor limiting laser efficiency. By optimizing the geometric structure of the waveguide, reducing sidewall roughness, and using low-loss materials, significant reductions in loss can be achieved. For in-

stance, using Si_3N_4 materials and precise chemical vapor deposition (CVD) techniques can achieve loss levels as low as sub-decibel per meter.

5.2 Increasing Q-Factor

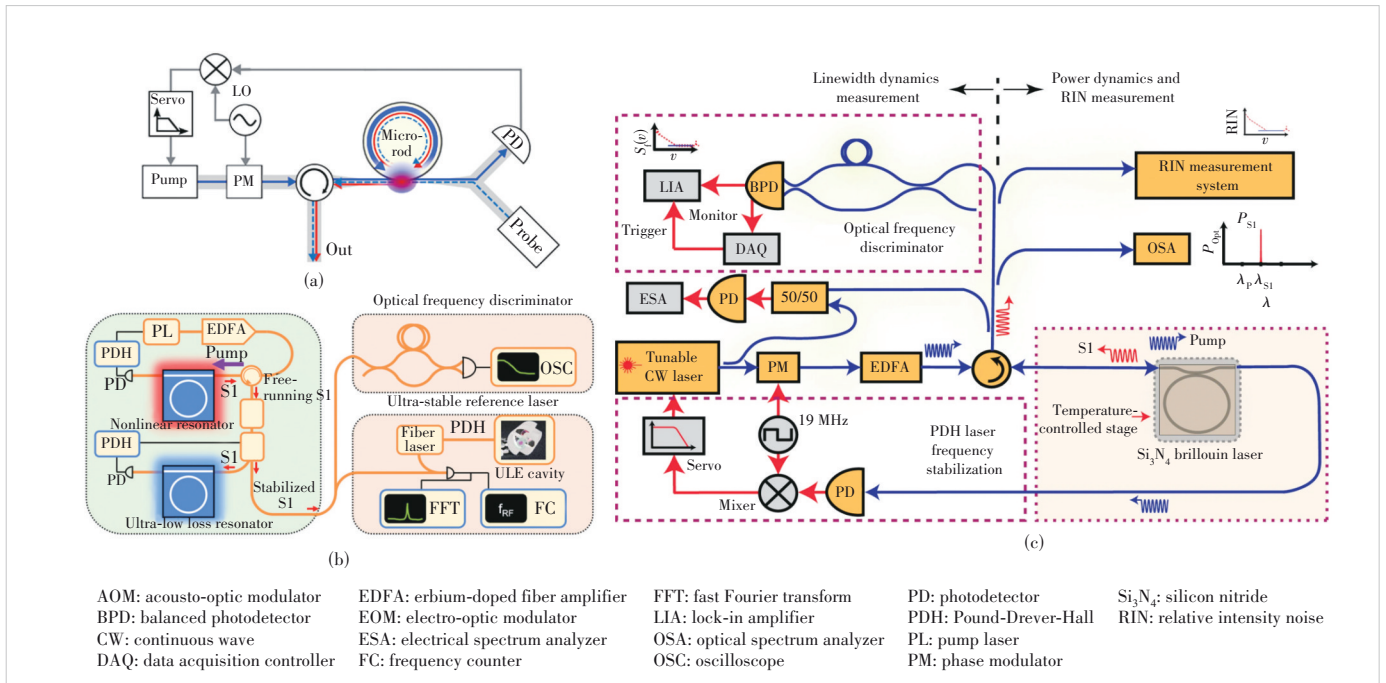
The Q-factor is an indicator of the resonator's quality and directly affects the laser's linewidth. Designing high-Q resonator structures and using high-quality materials can improve the laser's Q-factor^[56]. For example, by precisely controlling the size and shape of the waveguide, Q-factors up to tens of millions can be achieved^[72, 85].

5.3 Optimizing Linewidth

The linewidth of the laser is a critical indicator of its coherence. By precisely controlling the interaction between the pump light and Stokes light, sub-hertz linewidths can be achieved. Additionally, high-precision measurement equipment like radio-frequency-calibrated MZI can be used to accurately measure and optimize the laser's linewidth^[86 - 88].

5.4 Testing Methods

Various testing methods are employed to evaluate laser performance^[87 - 89]. High-precision optical spectrum analyzers are used to measure the laser's linewidth, while radio-frequency-calibrated MZIs are used to measure frequency noise^[80, 86]. These testing methods not only evaluate the laser's performance but also guide further optimization efforts. Fig. 5 shows the measurement system for various parameters of the Brillouin laser.



▲ Figure 5. (a) Measurement setup of Brillouin laser loaded $Q^{[68]}$; (b) Brillouin laser stabilization and frequency noise measurement^[90]; (c) measurement setup of Brillouin laser linewidth, phase noise, relative intensity noise (RIN) and power dynamics^[71]

6 Application Examples of Integrated Brillouin Lasers

Integrated Brillouin lasers, with their superior performance, demonstrate tremendous potential in various fields including atomic clocks, coherent communication, quantum communication, precision measurement, and spectroscopy.

6.1 Atomic Clocks

In atomic clocks, ultra-narrow linewidth lasers are crucial for achieving high precision in time measurement^[6]. By locking the laser frequency to atomic transitions, extremely high-frequency stability can be attained. For instance, using an integrated Brillouin laser as the frequency source in atomic clocks can provide unprecedented time measurement accuracy.

6.2 Coherent Communication

In coherent communication systems, SBS lasers offer significant advantages. Firstly, due to their ultra-narrow linewidth and high coherence, SBS lasers can substantially reduce phase noise, thereby enhancing the quality and reach of signal transmission. This characteristic is particularly crucial in coherent optical communication systems, as phase noise directly impacts the accuracy of demodulating the modulated signal. Additionally, the low RIN of SBS lasers further improves the system's signal-to-noise ratio, ensuring data integrity and reliability in long-distance fiber optic communications^[71].

Moreover, the high-frequency stability and low noise char-

acteristics of SBS lasers make local oscillators and signal sources in coherent communication systems ideal. Precise control of the output frequency and phase of SBS lasers enables efficient wavelength division multiplexing (WDM) and dense wavelength division multiplexing (DWDM), significantly increasing the bandwidth and capacity of communication systems.

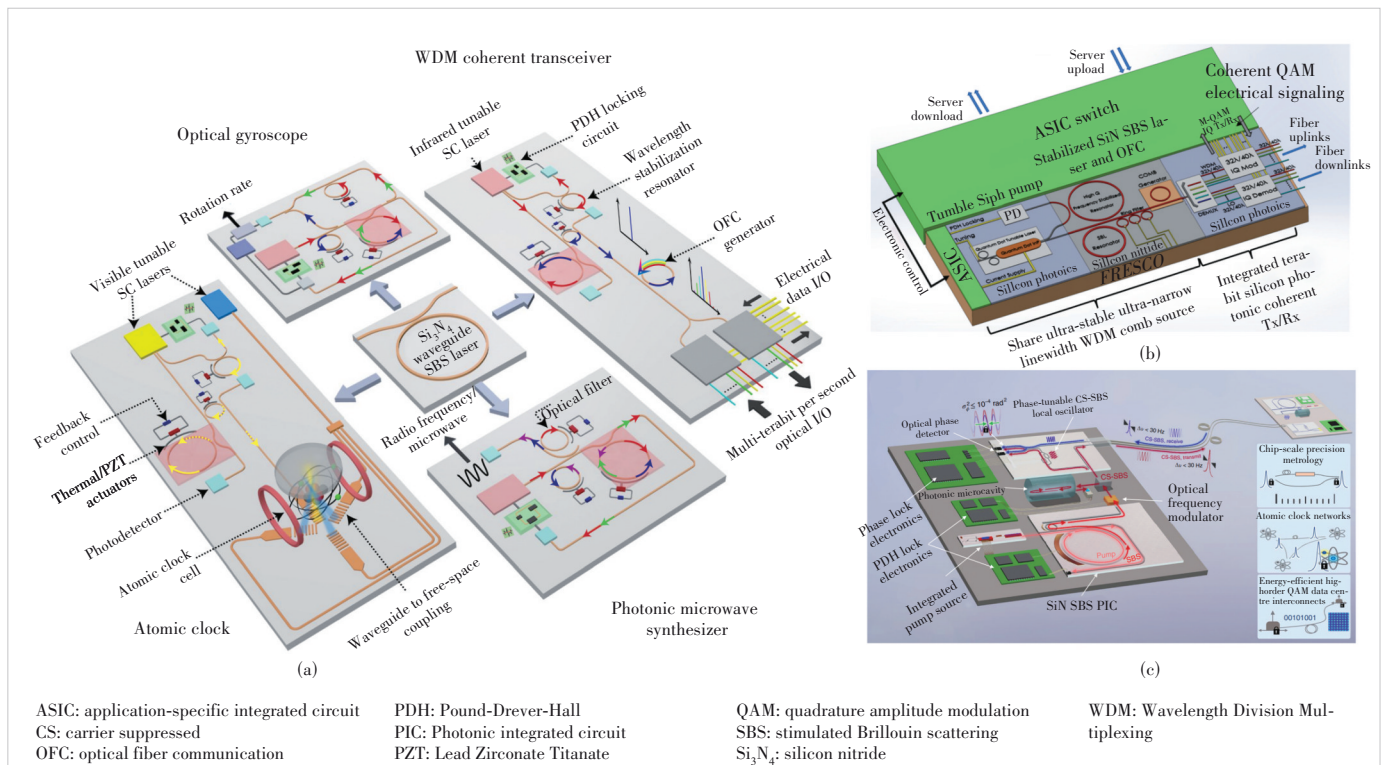
SBS lasers also possess flexible tuning capabilities, providing unique advantages in dynamic spectrum allocation and agile optical networks. Studies have shown that the SBS effect can achieve rapid and precise laser wavelength tuning, meeting diverse communication needs.

6.3 Quantum Communication

In quantum communication, integrated Brillouin lasers can generate entangled photon pairs, supporting quantum key distribution (QKD) and quantum computing. Their high coherence and stability make them ideal for implementing quantum communication networks^[91 - 92].

6.4 Precision Measurement and Spectroscopy

The high coherence and low linewidth characteristics of integrated Brillouin lasers are invaluable in precision measurement and spectroscopy. They enable high-resolution spectroscopy, allowing for precise detection of molecular structures and chemical reactions. Fig. 6 illustrates some application examples of SBS lasers.



▲ Figure 6. Applications of SBS laser: (a) chip-scale atomic clock, integrated laser optical gyroscope, WDM coherent transceiver, and low-noise, photonic microwave synthesizer^[71], (b) example applications in coherent optical communication^[93] and (c) optically synchronized precision fibre link^[94]

6.5 Experimental Validation

Researchers have experimentally validated the performance of integrated Brillouin lasers. For instance, an integrated Brillouin laser utilizing silicon nitride waveguides achieved a remarkable linewidth of 269 Hz at a wavelength of 674 nm, showcasing excellent coherence, as illustrated in Fig. 7^[95]. Just above threshold (III), we see a dramatic 100× narrowing of the linewidth to 120 kHz as SBS dominates the emission. At all points above the threshold, we measure the frequency noise of S1 using an optical frequency discriminator (OFD). The fundamental linewidth (4ν) is defined as the far-from-carrier white frequency noise floor in Hz^2/Hz , multiplied by π . In Fig. 7c, the noise floor for each pump power input is indicated by horizontal dashed lines (III-VI). As the pump power increases beyond the S1 threshold, the fundamental linewidth drops dramatically from 1.1 kHz (IV) to 269.7 Hz (VI). These linewidth results are summarized in Fig. 4d, indicating the integral linewidths for points (I-II) below the threshold and the fundamental linewidths for the frequency noise curves in (III-VI) in Fig. 4c. We cannot provide the required on-chip pump power, 59.4 mW, to achieve the lasing of the second order Stokes (S2). Future work will look further into noise properties measured using stabilized pump sources and exploring linewidth behavior as S1 approaches the S2 lasing threshold. Additionally, SBS laser demonstrations at a wavelength of 698 nm showcase the versatility of

this laser design, suitable for probing neutral strontium atomic clock transitions.

7 Technical Challenges and Future Directions

Achieving ultra-narrow linewidth laser output with integrated Brillouin lasers has seen significant progress, yet several technical challenges remain. Key issues include reducing waveguide loss, increasing the Q-factor, achieving a broader wavelength tuning range, and enhancing stability against environmental changes. Reducing waveguide loss is critical for improving laser efficiency and linewidth. Future research will focus on new material combinations and waveguide designs to minimize scattering and absorption losses, such as through improved CVD techniques that control material composition and structure at the atomic level. Enhancing the Q-factor is essential for achieving narrow linewidth and high-frequency stability. Researchers will optimize the geometric parameters of resonators and use materials with high refractive index contrast. The development of advanced photonic crystals and metamaterials may also provide new opportunities for achieving higher Q-factor resonators.

7.1 Expanding the Wavelength Tuning Range

To enable integrated Brillouin lasers to cover a broader wavelength range from ultraviolet to infrared, researchers need to develop new material systems and design strategies.

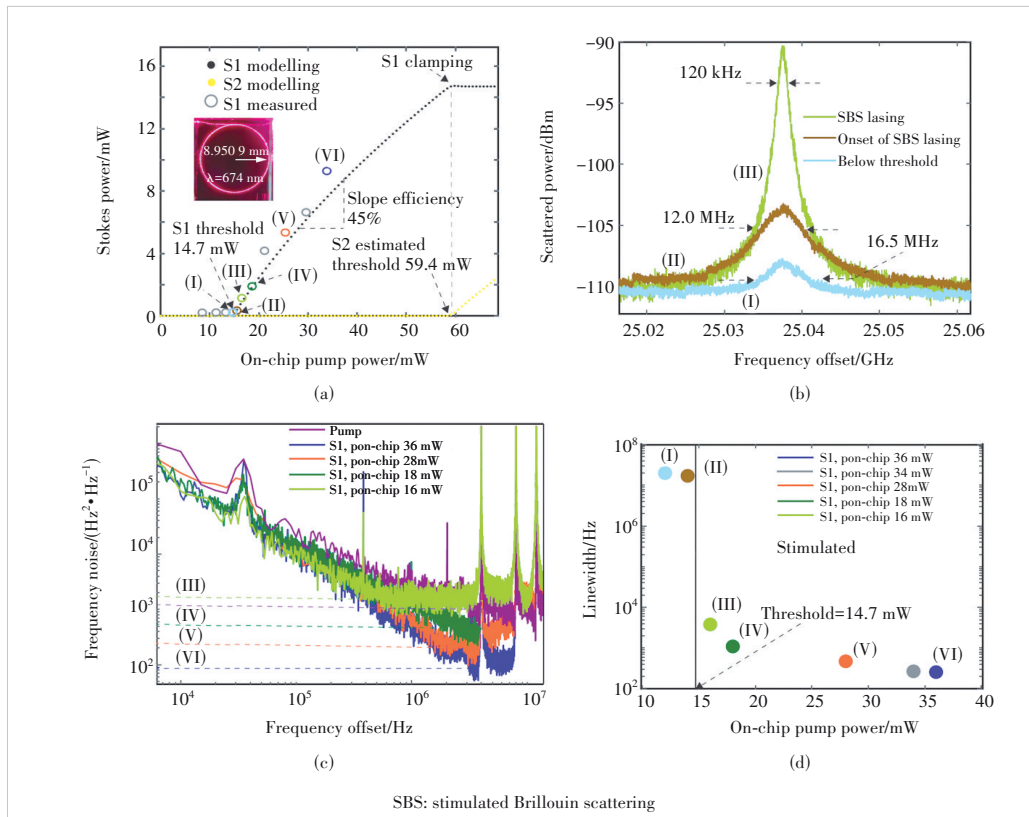
This may include employing multi-material heterogeneous integration techniques and developing novel wavelength-selective elements, such as gratings and filters.

7.2 Enhancing Environmental Stability

The environmental stability of integrated Brillouin lasers is crucial for their reliability in practical applications^[95-97]. Future research will focus on developing effective thermal management and mechanical support structures, as well as exploring materials that are insensitive to changes in temperature, pressure, and chemical environments.

7.3 Exploring New Effects and Amplification Techniques

To further enhance laser



▲ Figure 7. Measurements of the Stokes threshold, power, and linewidth of the 674 nm SBS laser^[95]

performance, future research will explore new nonlinear optical effects, such as four-wave mixing (FWM) and second-harmonic generation (SHG). These effects can be used to achieve broader wavelength tuning and more complex signal processing functions^[21]. Additionally, developing more efficient pumping and signal amplification techniques will be key to improving laser performance.

7.4 Expanding Integrated Photonics Platforms

The expansion of integrated photonics platforms will support a wider range of applications, including quantum information processing, precision measurement, and atomic clocks. This will require further development of materials and devices to enable full-spectrum operation from ultraviolet to infrared, ensuring compatibility with existing technologies^[70].

8 Summary

Integrated Brillouin lasers, as a significant branch of integrated photonics, have made remarkable progress in achieving ultra-narrow linewidth lasers. With their compact size, low cost, and high stability, these lasers are poised to play a crucial role in future scientific and commercial applications. As technology continues to advance, we anticipate that integrated Brillouin lasers will find applications and innovations in an expanding array of fields.

The development of ultra-narrow linewidth and frequency-stabilized integrated lasers offers new opportunities for precision science and commercial applications. The application of integrated photonics technology makes it possible to create compact, low-cost, and highly reliable laser systems. These systems have significant potential in high-end applications such as atomic clocks, quantum communication, and precision measurement. The high coherence and low noise characteristics of integrated Brillouin lasers provide new tools for precision measurement and are crucial for building quantum communication networks.

Despite the significant progress made in integrated Brillouin laser technology, a lot of challenges persist, and there is ample room for further enhancement. Future research will focus on further reducing waveguide loss, increasing the Q-factor, achieving a broader wavelength tuning range, and enhancing the environmental stability of the lasers. Additionally, the development of new materials, innovations in manufacturing processes, and exploration of nonlinear optical effects will further enhance the performance of integrated Brillouin lasers.

The development of integrated Brillouin lasers requires support from traditional disciplines such as physics, materials science, and optical engineering, and will benefit from interdisciplinary integration and innovation. For instance, advancements in quantum information science will provide new application scenarios for integrated Brillouin lasers, while developments in micro-nano fabrication technology will enhance the integration and performance of these lasers.

As technology matures and costs decrease, integrated Brillouin lasers are expected to gain wider adoption in the commercial market. From precision instrument manufacturing to communication network construction, and from fundamental scientific research to industrial process control, these lasers will play an important role. Over the coming years, integrated Brillouin lasers are expected to drive technological advancement and industrial upgrades in multiple fields.

The future of integrated Brillouin lasers is promising, and their importance in integrated photonics continues to rise. With ongoing technological breakthroughs and expanding applications, integrated Brillouin lasers are set to play an increasingly critical role, opening new avenues for scientific exploration and commercial applications.

References

- [1] SHEN C, LEE C M, STEGENBURGS E, et al. Semipolar III-nitride quantum well waveguide photodetector integrated with laser diode for on-chip photonic system [J]. *Applied physics express*, 2017, 10(4): 042201. DOI: 10.7567/apex.10.042201
- [2] SHEN C, NG T K, LEONARD J T, et al. High-modulation-efficiency, integrated waveguide modulator - laser diode at 448 nm [J]. *ACS photonics*, 2016, 3(2): 262 - 268. DOI: 10.1021/acsp Photonics.5b00599
- [3] SHEN C, NG T K, JANJUA B, et al. Optical gain and absorption of 420 nm InGaN-based laser diodes grown on m-plane GaN substrate [C]//*Proceedings of Asia Communications and Photonics Conference 2014*. OSA, 2014: 1. DOI: 10.1364/acpc.2014.aw4a.1
- [4] SHEN C, LEE C M, NG T K, et al. High gain semiconductor optical amplifier—laser diode at visible wavelength [C]//*International Electron Devices Meeting (IEDM)*. IEEE, 2016: 2241 - 2244. DOI: 10.1109/iedm.2016.7838473
- [5] ORIEUX A, DIAMANTI E. Recent advances on integrated quantum communications [J]. *Journal of optics*, 2016, 18(8): 083002. DOI: 10.1088/2040-8978/18/8/083002
- [6] LUDLOW A D, BOYD M M, YE J, et al. Optical atomic clocks [J]. *Reviews of modern physics*, 2015, 87(2): 637 - 701. DOI: 10.1103/revmodphys.87.637
- [7] LEVINE J. Introduction to time and frequency metrology [J]. *Review of scientific instruments*, 1999, 70(6): 2567 - 2596. DOI: 10.1063/1.1149844
- [8] YE J, KIMBLE H J, KATORI H. Quantum state engineering and precision metrology using state-insensitive light traps [J]. *Science*, 2008, 320(5884): 1734 - 1738. DOI: 10.1126/science.1148259
- [9] SINCLAIR L C, DESCHÊNES J D, SWANN W C, et al. Compact fiber frequency combs for precision measurement outside the metrology lab [C]//*Latin America Optics and Photonics Conference*. OSA, 2018. DOI: 10.1364/laop.2018.w2d.1
- [10] SORACE-AGASKAR C, KHARAS D, YEGNANARAYANAN S, et al. Versatile silicon nitride and alumina integrated photonic platforms for the ultraviolet to short-wave infrared [J]. *IEEE journal of selected topics in quantum electronics*, 2019, 25(5): 1 - 15. DOI: 10.1109/jstqe.2019.2904443
- [11] PARK H, ZHANG C, TRAN M A, et al. Heterogeneous silicon nitride photonics [J]. *Optica*, 2020, 7(4): 336. DOI: 10.1364/optica.391809
- [12] HU J H, HU F C, JIA J L, et al. 46.4 Gbps visible light communication system utilizing a compact tricolor laser transmitter [J]. *Optics express*, 2022, 30(3): 4365 - 4373. DOI: 10.1364/OE.447546
- [13] HU J H, GUO Z Y, SHI J Y, et al. A metasurface-based full-color circular auto-focusing Airy beam transmitter for stable high-speed underwater

- wireless optical communications [J]. *Nature communications*, 2024, 15 (1): 2944. DOI: 10.1038/s41467-024-47105-x
- [14] WANG J F, HU J H, LABORATORY P C, et al. High-speed GaN-based laser diode with modulation bandwidth exceeding 5 GHz for 20 Gbps visible light communication [J]. *Photonics research*, 2024, 12(6): 1186 – 1193. DOI: 10.1364/prj.516829
- [15] KESSLER T, HAGEMANN C, GREBING C, et al. A sub-40-mHz-linewidth laser based on a silicon single-crystal optical cavity [J]. *Nature photonics*, 2012, 6(10): 687 – 692. DOI: 10.1038/nphoton.2012.217
- [16] KIKUCHI K. Fundamentals of coherent optical fiber communications [J]. *Journal of lightwave technology*, 2016, 34(1): 157 – 179. DOI: 10.1109/jlt.2015.2463719
- [17] FOX R W, OATES C W, HOLLBERG L W. 1. Stabilizing diode lasers to high-finesse cavities [J]. *Experimental methods in the physical sciences cavity-enhanced spectroscopies*, 2003, (40):1 – 41. DOI: 10.1016/S1079-4042(03)80017-6
- [18] BRODNIK G M, HARRINGTON M W, BOSE D, et al. Chip-scale, optical-frequency-stabilized PLL for DSP-free, low-power coherent QAM in the DCI [C]/Optical Fiber Communication Conference and Exhibition (OFC). IEEE, 2020. DOI: 10.1364/ofc.2020.m3a.6
- [19] BAI Z X, ZHAO Z A, TIAN M H, et al. A comprehensive review on the development and applications of narrow-linewidth lasers [J]. *Microwave and optical technology letters*, 2022, 64(12): 2244 – 2255. DOI: 10.1002/mop.33046
- [20] GERTLER S, OTTERSTROM N T, GEHL M, et al. Narrowband microwave-photonic Notch filters using Brillouin-based signal transduction in silicon [J]. *Nature communications*, 2022, 13: 1947. DOI: 10.1038/s41467-022-29590-0
- [21] LIU K K, WANG J W, CHAUHAN N, et al. Integrated photonic molecule Brillouin laser with a high-power sub-100-mHz fundamental linewidth [J]. *Optics letters*, 2023, 49(1): 45. DOI: 10.1364/ol.503126
- [22] HILL K O, KAWASAKI B S, JOHNSON D C. Cw Brillouin laser [J]. *Applied physics letters*, 1976, 28(10): 608 – 609. DOI: 10.1063/1.88583
- [23] YUAN Z Q, WANG H M, WU L E, et al. Linewidth enhancement factor in a microcavity Brillouin laser [J]. *Optica*, 2020, 7(9): 1150 – 1153. DOI: 10.1364/optica.394311
- [24] EGGLETON B J, POULTON C G, PANT R. Inducing and harnessing stimulated Brillouin scattering in photonic integrated circuits [J]. *Advances in optics and photonics*, 2013, 5(4): 536 – 587. DOI: 10.1364/aop.5.000536
- [25] MARPAUNG D, YAO J P, CAPMANY J. Integrated microwave photonics [J]. *Nature photonics*, 2019, 13(2): 80 – 90. DOI: 10.1038/s41566-018-0310-5
- [26] POLITI A, CRYAN M J, RARITY J G, et al. Silica-on-silicon waveguide quantum circuits [J]. *Science*, 2008, 320(5876): 646 – 649. DOI: 10.1126/science.1155441
- [27] LABONTÉ L, ALIBART O, D'AURIA V, et al. Integrated photonics for quantum communications and metrology [J]. *PRX quantum*, 2024, 5(1): 010101. DOI: 10.1103/prxquantum.5.010101
- [28] DE VOS K, BARTOLOZZI I, SCHACHT E, et al. Silicon-on-insulator microring resonator for sensitive and label-free biosensing [J]. *Optics express*, 2007, 15(12): 7610. DOI: 10.1364/oe.15.007610
- [29] KOHLER D, SCHINDLER G, HAHN L, et al. Biophotonic sensors with integrated Si₃N₄-organic hybrid (SiNOH) lasers for point-of-care diagnostics [J]. *Light: science & applications*, 2021, 10: 64. DOI: 10.1038/s41377-021-00486-w
- [30] MILLER D A B. Optical interconnects to silicon [J]. *IEEE journal of selected topics in quantum electronics*, 2000, 6(6): 1312 – 1317. DOI: 10.1109/2944.902184
- [31] SOREF R. The past, present, and future of silicon photonics [J]. *IEEE journal of selected topics in quantum electronics*, 2006, 12(6): 1678 – 1687. DOI: 10.1109/jstqe.2006.883151
- [32] REED G. *Silicon Photonics* [M/OL]. New York: John Wiley & Sons. (2008-04-18) [2024-06-22]. <https://onlinelibrary.wiley.com/doi/book/10.1002/9780470994535?msocid=271754324752654020fd45de467c6460>. DOI: 10.1002/9780470994535
- [33] DOERR C R. Silicon photonic integration in telecommunications [J]. *Frontiers in physics*, 2015, 3: 37. DOI: 10.3389/fphy.2015.00037
- [34] PINGUET T, DENTON S, GLOECKNER S, et al. High-volume manufacturing platform for silicon photonics [J]. *Proceedings of the IEEE*, 2018, 106(12): 2281 – 2290. DOI: 10.1109/jproc.2018.2859198
- [35] XIAO X, XU H, LI X Y, et al. 25 Gbit/s silicon microring modulator based on misalignment-tolerant interleaved PN junctions [J]. *Optics express*, 2012, 20(3): 2507. DOI: 10.1364/oe.20.002507
- [36] O MARSHALL, M HSU, Z C WANG, et al. Heterogeneous integration on silicon photonics [J]. *Proceedings of the IEEE*, 2018, 106(12): 2258 – 2269. DOI: 10.1021/nl404513
- [37] LIU S T, WU X R, JUNG D, et al. High-channel-count 20 GHz passively mode-locked quantum dot laser directly grown on Si with 41 Tbit/s transmission capacity [J]. *Optica*, 2019, 6(2): 128 – 134. DOI: 10.1364/optica.6.000128
- [38] TRAN M A, ZHANG C, MORIN T J, et al. Extending the spectrum of fully integrated photonics to submicrometre wavelengths [J]. *Nature*, 2022, 610(7930): 54 – 60. DOI: 10.1038/s41586-022-05119-9
- [39] SINGH N, XIN M, VERMEULEN D, et al. Octave-spanning coherent supercontinuum generation in silicon on insulator from 1.06 μm to beyond 2.4 μm [J]. *Light: science & applications*, 2017, 7(1): 17131. DOI: 10.1038/lsa.2017.131
- [40] SUN W, TAN C K, WIERER J J Jr, et al. Ultra-broadband optical gain in III-nitride digital alloys [J]. *Scientific reports*, 2018, 8: 3109. DOI: 10.1038/s41598-018-21434-6
- [41] BOUCAUD P, BHAT N, AL KHALFIOUI M, et al. Perspectives for III-nitride photonic platforms [J]. *Nano futures*, 2024, 8(2): 022001. DOI: 10.1088/2399-1984/ad41aa
- [42] YAN W, WEI Z X, YANG Y C, et al. Ultra-broadband magneto-optical isolators and circulators on a silicon nitride photonics platform [J]. *Optica*, 2024, 11(3): 376 – 384. DOI: 10.1364/optica.506366
- [43] D J BLUMENTHAL, R HEIDEMAN, D GEUZEBROEK, et al. Silicon Nitride in Silicon Photonics [J]. *Proceedings of the IEEE*, 2018, 106(12): 2209 – 2231. DOI: 10.1109/JPROC.2018.2861576
- [44] S BRAMHAVAR, C SORACE-AGASKAR, D KHARAS, et al., A visible-light integrated photonic platform for atomic systems [EB/OL]. [2024-06-22]. <https://doi.org/10.1117/12.2509822>. doi: 10.1117/12.2509822
- [45] ASLAN M M, WEBSTER N A, BYARD C L, et al. Low-loss optical waveguides for the near ultra-violet and visible spectral regions with Al₂O₃ thin films from atomic layer deposition [J]. *Thin solid films*, 2010, 518 (17): 4935 – 4940. DOI: 10.1016/j.tsf.2010.03.011
- [46] SOLTANI M, SOREF R, PALACIOS T, et al. AlGaIn/AlIn integrated photonics platform for the ultraviolet and visible spectral range [J]. *Optics express*, 2016, 24(22): 25415 – 25423. DOI: 10.1364/oe.24.025415
- [47] LIU X W, BRUCH A W, TANG H X, et al. Aluminum nitride photonic integrated circuits: from piezo-optomechanics to nonlinear optics [J]. *Advances in optics and photonics*, 2023, 15(1): 236 – 317. DOI: 10.1364/aop.479017
- [48] BELT M, DAVENPORT M L, BOWERS J E, et al. Ultra-low-loss Ta₂O₅-core/SiO₂-clad planar waveguides on Si substrates [J]. *Optica*, 2017, 4(5): 532 – 536. DOI: 10.1364/optica.4.000532
- [49] BLUMENTHAL D J. Photonic integration for UV to IR applications [J]. *APL photonics*, 2020, 5(2): 020903. DOI: 10.1063/1.5131683
- [50] BAUTERS J F, HECK M J R, JOHN D, et al. Ultra-low-loss high-aspect-ratio Si₃N₄ waveguides [J]. *Optics express*, 2011, 19(4): 3163. DOI: 10.1364/oe.19.003163
- [51] HUFFMAN T A, BRODNIK G M, PINHO C, et al. Integrated resonators in an ultralow loss Si₃N₄/SiO₂ platform for multifunction applications [J]. *IEEE journal of selected topics in quantum electronics*, 2018, 24(4): 1 – 9. DOI: 10.1109/jstqe.2018.2818459
- [52] LU T J, FANTO M, CHOI H, et al. Aluminum nitride integrated photonics platform for the ultraviolet to visible spectrum [J]. *Optics express*,

- 2018, 26(9): 11147 – 11160. DOI: 10.1364/oe.26.011147
- [53] WOLFF C, SOREF R, POULTON C G, et al. Germanium as a material for stimulated Brillouin scattering in the mid-infrared [J]. *Optics express*, 2014, 22(25): 30735 – 30747. DOI: 10.1364/oe.22.030735
- [54] GYGER F, LIU J Q, YANG F, et al. Observation of stimulated Brillouin scattering in silicon nitride integrated waveguides [J]. *Physical review letters*, 2020, 124: 013902. DOI: 10.1103/physrevlett.124.013902
- [55] JIN D, BAI Z X, LU Z W, et al. 22.5-W narrow-linewidth diamond Brillouin laser at 1064 nm [J]. *Optics letters*, 2022, 47(20): 5360 – 5363. DOI: 10.1364/ol.471447
- [56] MERKLEIN M, KABAKOVA I V, ZARIFI A, et al. 100 years of Brillouin scattering: historical and future perspectives [J]. *Applied physics reviews*, 2022, 9(4). DOI: 10.1063/5.0095488
- [57] BRILLOUIN L. Diffusion de la lumière et des rayons X par un corps transparent homogène [J]. *Annales de physique*, 1922, 9(17): 88 – 122. DOI: 10.1051/anphys/192209170088
- [58] GARMIRE E. Perspectives on stimulated Brillouin scattering [J]. *New journal of physics*, 2017, 19(1): 011003. DOI: 10.1088/1367-2630/aa5447
- [59] SAFAVI-NAEINI A H, VAN THOURHOUT D, BAETS R, et al. Controlling phonons and photons at the wavelength scale: integrated photonics meets integrated photonics: publisher's note [J]. *Optica*, 2019, 6(4): 410. DOI: 10.1364/optica.6.000213
- [60] NIKLES M, THEVENAZ L, ROBERT P A. Brillouin gain spectrum characterization in single-mode optical fibers [J]. *Journal of lightwave technology*, 1997, 15(10): 1842 – 1851. DOI: 10.1109/50.633570
- [61] GENG J H, STAINES S, WANG Z L, et al. Highly stable low-noise Brillouin fiber laser with ultranarrow spectral linewidth [J]. *IEEE photonics technology letters*, 2006, 18(17): 1813 – 1815. DOI: 10.1109/LPT.2006.881145
- [62] KOPYAKOV A, SAUER M, CHOWDHURY D. Stimulated Brillouin scattering in optical fibers [J]. *Advances in optics and photonics*, 2009, 2(1): 1 – 59. DOI: 10.1364/aop.2.000001
- [63] CHEN M, MENG Z, ZHANG Y C, et al. Ultranarrow-linewidth Brillouin/erbium fiber laser based on 45-cm erbium-doped fiber [J]. *IEEE photonics journal*, 2015, 7(1): 1500606. DOI: 10.1109/JPHOT.2015.2399354
- [64] PANT R, POULTON C G, CHOI D Y, et al. On-chip stimulated Brillouin scattering [J]. *Optics express*, 2011, 19(9): 8285 – 8290. DOI: 10.1364/oe.19.008285
- [65] POULTON C G, PANT R, EGGLETON B J. Acoustic confinement and stimulated Brillouin scattering in integrated optical waveguides [J]. *Journal of the optical society of America B*, 2013, 30(10): 2657 – 2664. DOI: 10.1364/josab.30.002657
- [66] SHIN H, QIU W J, JARECKI R, et al. Tailorable stimulated Brillouin scattering in nanoscale silicon waveguides [J]. *Nature communications*, 2013, 4: 1944. DOI: 10.1038/ncomms2943
- [67] GENG J H, JIANG S B. Pump-to-stokes transfer of relative intensity noise in Brillouin fiber ring lasers [J]. *Optics letters*, 2006, 32(1): 11 – 13. DOI: 10.1364/ol.32.000011
- [68] LOH W, BECKER J, COLE D C, et al. A microrod-resonator Brillouin laser with 240 Hz absolute linewidth [J]. *New journal of physics*, 2016, 18(4): 045001. DOI: 10.1088/1367-2630/18/4/045001
- [69] BEHUNIN R O, OTTERSTROM N T, RAKICH P T, et al. Fundamental noise dynamics in cascaded-order Brillouin lasers [J]. *Physical review A*, 2018, 98(2): 023832. DOI: 10.1103/physreva.98.023832
- [70] D J BLUMENTHAL, I KABAKOVA, P T RAKICH, et al. Integrated Brillouin lasers and their applications [J]. *Semiconductors and semimetals*, 2022, (110): 107 – 180. DOI: 10.1016/bs.semsem.2022.05.004
- [71] GUNDAVARAPU S, BRODNIK G M, PUCKETT M, et al. Sub-hertz fundamental linewidth photonic integrated Brillouin laser [J]. *Nature photonics*, 2019, 13(1): 60 – 67. DOI: 10.1038/s41566-018-0313-2
- [72] EGGLETON B J, POULTON C G, RAKICH P T, et al. Brillouin integrated photonics [J]. *Nature photonics*, 2019, 13(10): 664 – 677. DOI: 10.1038/s41566-019-0498-z
- [73] PUCKETT M W, LIU K K, CHAUHAN N, et al. 422 Million intrinsic quality factor planar integrated all-waveguide resonator with sub-MHz linewidth [J]. *Nature communications*, 2021, 12: 934. DOI: 10.1038/s41467-021-21205-4
- [74] LIU K K, JIN N J, CHENG H T, et al. Ultralow 0.034 dB/m loss wafer-scale integrated photonics realizing 720 million Q and 380 μ W threshold Brillouin lasing [J]. *Optics letters*, 2022, 47(7): 1855 – 1858. DOI: 10.1364/ol.454392
- [75] JIN D, BAI Z X, CHEN Y F, et al. A narrow-linewidth high-power fused silica Brillouin laser [J]. *Applied physics letters*, 2023, 123(5). DOI: 10.1063/5.0159079
- [76] CHAUHAN N, ISICHENKO A, LIU K K, et al. Visible 780 nm SBS laser with mW level threshold in an ultra-high 145 million Q integrated waveguide resonator [C]//*Proceedings of CLEO. IEEE*, 2023, 604(7906). DOI: 10.1364/cleo_si.2023.sf1k.6
- [77] CHAUHAN N, WANG J W, BOSE D, et al. Ultra-low loss visible light waveguides for integrated atomic, molecular, and quantum photonics [J]. *Optics express*, 2022, 30(5): 6960. DOI: 10.1364/oe.448938
- [78] JIN D, BAI Z X, CHEN Y F, et al. Intrinsic cascade-free intramode scattering Brillouin laser [J]. *APL photonics*, 2023, 8(8). DOI: 10.1063/5.0155283
- [79] WANG W Y, YU Y, LI Y F, et al. Tailorable Brillouin light scattering in a lithium niobate waveguide [J]. *Applied sciences*, 2021, 11(18): 8390. DOI: 10.3390/app11188390
- [80] KABAKOVA I V, PANT R, CHOI D Y, et al. Narrow linewidth Brillouin laser based on chalcogenide photonic chip [J]. *Optics letters*, 2013, 38(17): 3208. DOI: 10.1364/ol.38.003208
- [81] KIM D G, HAN S, HWANG J, et al. Universal light-guiding geometry for on-chip resonators having extremely high Q-factor [J]. *Nature communications*, 2020, 11: 5933. DOI: 10.1038/s41467-020-19799-2
- [82] LAI C K, CHOI D Y, ATHANASIOS N J, et al. Hybrid chalcogenide-germanosilicate waveguides for high performance stimulated Brillouin scattering applications [J]. *Advanced functional materials*, 2022, 32(3): 2105230. DOI: 10.1002/adfm.202105230
- [83] LAI C K, MERKLEIN M, CHOI D Y, et al. Photosensitivity and optical nonlinearity in arsenic selenide planar waveguides [J]. *Optical materials express*, 2023, 13(10): 2808. DOI: 10.1364/ome.499219
- [84] BAUTERS J F, HECK M J R, JOHN D D, et al. Planar waveguides with less than 0.1 dB/m propagation loss fabricated with wafer bonding [J]. *Optics express*, 2011, 19(24): 24090. DOI: 10.1364/oe.19.024090
- [85] YANG K Y, OH D Y, LEE S H, et al. Bridging ultrahigh-Q devices and photonic circuits [J]. *Nature photonics*, 2018, 12(5): 297 – 302. DOI: 10.1038/s41566-018-0132-5
- [86] LI J, LEE H, YANG K Y, et al. Sideband spectroscopy and dispersion measurement in microcavities [J]. *Optics express*, 2012, 20(24): 26337. DOI: 10.1364/oe.20.026337
- [87] BAI Z X, ZHAO Z A, QI Y Y, et al. Narrow-linewidth laser linewidth measurement technology [J]. *Frontiers in physics*, 2021, 9: 768165. DOI: 10.3389/fphy.2021.768165
- [88] CHEN J Q, CHEN C, SUN J J, et al. Linewidth measurement of a narrow-linewidth laser: principles, methods, and systems [J]. *Sensors*, 2024, 24(11): 3656. DOI: 10.3390/s24113656
- [89] WANG K, CHENG M, SHI H T, et al. Demonstration of forward Brillouin gain in a hybrid photonic—phononic silicon waveguide [J]. *ACS photonics*, 2021, 8(9): 2755 – 2763. DOI: 10.1021/acsp Photonics.1c00880
- [90] LIU K K, DALLYN J H, BRODNIK G M, et al. Photonic circuits for laser stabilization with integrated ultra-high Q and Brillouin laser resonators [J]. *APL photonics*, 2022, 7(9). DOI: 10.1063/5.0091686
- [91] ELSHAARI A W, PERNICE W, SRINIVASAN K, et al. Hybrid integrated quantum photonic circuits [J]. *Nature photonics*, 2020, 14(5): 285 – 298. DOI: 10.1038/s41566-020-0609-x
- [92] WANG J W, SCIARRINO F, LAING A, et al. Integrated photonic quantum technologies [J]. *Nature photonics*, 2020, 14(5): 273 – 284. DOI: 10.1038/s41566-019-0532-1

- [93] BLUMENTHAL D J, BALLANI H, BEHUNIN R O, et al. Frequency-stabilized links for coherent WDM fiber interconnects in the datacenter [J]. *Journal of lightwave technology*, 2020, 38(13): 3376 – 3386. DOI: 10.1109/JLT.2020.2985275
- [94] BRODNIK G M, HARRINGTON M W, DALLYN J H, et al. Optically synchronized fibre links using spectrally pure chip-scale lasers [J]. *Nature photonics*, 2021, 15: 588 – 593. DOI: 10.1038/s41566-021-00831-w
- [95] LOH W, GREEN A A S, BAYNES F N, et al. Dual-microcavity narrow-linewidth Brillouin laser [J]. *Optica*, 2015, 2(3): 225. DOI: 10.1364/optica.2.000225
- [96] LOH W, YEGNANARAYANAN S, O’DONNELL F, et al. Ultra-narrow linewidth Brillouin laser with nanokelvin temperature self-referencing [J]. *Optica*, 2019, 6(2): 152. DOI: 10.1364/optica.6.000152
- [97] LOH W, KHARAS D, MAXSON R, et al. Cooling of an integrated Brillouin laser below the thermal limit [J]. *Optics express*, 2022, 30(13): 22562. DOI: 10.1364/oe.451622

Biographies

GU Zhenqian received his BS degree in electronic information engineering from Wuhan University, China in 2023. He is currently pursuing a PhD degree at the School of Information Science and Engineering, Fudan University, China. His research interests include visible light communication, GaN-based lasers, narrow linewidth lasers and integrated lasers.

YANG Zhen received her BS degree in material physics from Anhui University, China in 2020, and MS degree in physics from Shanghai Jiao Tong University, China in 2023. She is currently pursuing a PhD degree at Fudan University, China. Her research interests include visible light communication, photonic integrated technologies such as narrow linewidth lasers, integrated lasers, and photodetectors.

ZHA Lulu received her BS degree in communication engineering from Nanjing University of Posts and Telecommunications, China in 2021. She is currently pursuing her MS degree at the School of Information Science and Engineering, Fudan University, China. Her research interests include wireless optical com-

munication, Micro-LED arrays, and high-speed laser communication.

HU Junhui received his bachelor’s degree in electrical engineering from Wuhan University, China in 2021. Now he is a PhD candidate at the School of Information Science and Technology, Fudan University, China. His current research focuses on the design and analysis of high modulation bandwidth GaN-based short-wavelength lasers, as well as their application in high-speed visible light communication (VLC) systems. He has published more than 20 peer-reviewed publications in the fields of semiconductor lasers, VLC, and underwater wireless optical communication (UWOC) in internationally renowned journals such as *Nature Communications* and *Optics Express*.

CHI Nan received her BS and PhD degrees in electrical engineering from the Beijing University of Posts and Telecommunications, China in 1996 and 2001, respectively. From July 2001 to December 2004, she was an assistant professor with the Research Center COM, Technical University of Denmark. From January 2005 to April 2006, she was a research associate with the University of Bristol, UK. In June 2006, she joined Wuhan National Laboratory for Optoelectronics, Huazhong University of Science and Technology, China, where she was a full professor. In June 2008, she was with the School of Information Science and Engineering, Fudan University, China. She is the author or co-author of more than 200 papers. She was the Chair of the APOC 2007 OsRT workshop and ACP 2010. She was the Technical Program Committee Member of many conferences such as APOC 08, ICAIT09, ACP 2011, WOCC 2012, ACP 2013, and IWO 2014. Her research interests include coherent optical transmission, visible light communication, and optical packet/burst switching. She was the recipient of the New Century Excellent Talents Awards from the Education Ministry of China, Shanghai Shu Guang scholarship, Japanese OKAWA intelligence Fund Award, Pujiang talent of Shanghai City, and Ten Outstanding IT Young Persons Awards of Shanghai City.

SHEN Chao (chaoshen@fudan.edu.cn) received his BSc degree in materials physics from Fudan University, China and PhD degree in electrical engineering from KAUST, Saudi Arabia. He is currently a professor at the School of Information Science and Technology, Fudan University. He has published over 100 peer-reviewed publications in the fields of III-nitride optoelectronics devices, semiconductor lasers, superluminescent diodes, photonics integrated circuit, visible light communications (VLC), and underwater wireless optical communications (UWOC). Prof. SHEN has served as a TPC member and invited speaker in many IEEE, Optica, and SPIE conferences, and is the associated editor of IEEE Photonics Journal. He is the recipient of the 2022 Okawa Foundation Research Grant.

Monolithically Integrating a 180° Bent Waveguide into a III-Nitride Optoelectronic On-Chip System



ZHANG Hao, YE Ziqi, YUAN Jialei, LIU Pengzhan,
WANG Yongjin

(GaN Optoelectronic Integration International Cooperation Joint Laboratory of Jiangsu Province, Nanjing University of Posts and Telecommunications, Nanjing 210003, China)

DOI: 10.12142/ZTECOM.202404006

<https://kns.cnki.net/kcms/detail/34.1294.TN.20241111.1721.004.html>,
published online November 13, 2024

Manuscript received: 2024-08-04

Abstract: GaN-based devices have developed significantly in recent years due to their promising applications and research potential. A major goal is to monolithically integrate various GaN-based components onto a single chip to create future optoelectronic systems with low power consumption. This miniaturized integration not only enhances multifunctional performance but also reduces material, processing, and packaging costs. In this study, we present an optoelectronic on-chip system fabricated using a top-down approach on a III-nitride-on-silicon wafer. The system includes a near-ultraviolet light source, a monitor, a 180° bent waveguide, an electro-absorption modulator, and a receiver, all integrated without the need for regrowth or post-growth doping. 35 Mbit/s optical data communication is demonstrated through light propagation within the system, confirming its potential for compact GaN-based optoelectronic solutions.

Keywords: optoelectronic integration; bent waveguide; on-chip system; III-nitride-on-Si

Citation (Format 1): ZHANG H, YE Z Q, YUAN J L, et al. Monolithically integrating a 180° bent waveguide into a III-nitride optoelectronic on-chip system [J]. *ZTE Communications*, 2024, 22(4): 40 - 45. DOI: 10.12142/ZTECOM.202404006

Citation (Format 2): H. Zhang, Z. Q. Ye, J. L. Yuan, et al., "Monolithically integrating a 180° bent waveguide into a III-nitride optoelectronic on-chip system," *ZTE Communications*, vol. 22, no. 4, pp. 40 - 45, Dec. 2024. doi: 10.12142/ZTECOM.202404006.

1 Introduction

The integration of photonic devices on a single chip is a critical advancement in the field of semiconductor optoelectronics, particularly for the development of monolithic systems that combine various functionalities^[1-5]. One of the primary challenges in advancing silicon photonics lies in the absence of monolithically integrated light sources. This limitation becomes especially pronounced in the ultraviolet and visible spectra, where III-nitride semiconductors offer significant advantages due to their superior optoelectronic properties. Compared with other materials, III-nitride semiconductors are more suitable for integration in these wavelength ranges. Importantly, the process of integrating on-chip light sources using III-nitrides is relatively simple, making them an ideal candidate for optoelectronic applications. The multi-quantum well (MQW) light-emitting diode (LED) serves as a particularly promising device for such integration

efforts. Its emission and absorption spectra demonstrate a considerable degree of overlap, which allows for the simultaneous integration of both optical transmitters and detectors at the wafer level^[6-8]. This overlap has been exploited in various applications, like visible light communication (VLC)^[9-12], where the rapid modulation of LED intensity facilitates high-speed data transmission.

Recent advancement has demonstrated the potential for a top-down approach to integrating various optoelectronic devices on a single III-nitride chip without requiring complex post-doping or post-growth processes. This method has been used to create microsystems that include both active and passive components^[13-15]. For instance, experiments have shown that MQW diodes can serve as both the transmitter and receiver in a primitive optical communication system, where one device operates in emission modes and the other in detection modes. The integration of these devices on a single chip has been made possible through the use of integrated waveguides (WG), which facilitates optical interconnection^[6,8]. Furthermore, the monolithic integration of transmitters, modulators, waveguides, and receivers has been successfully achieved, with all components sharing an identical MQW structure^[16].

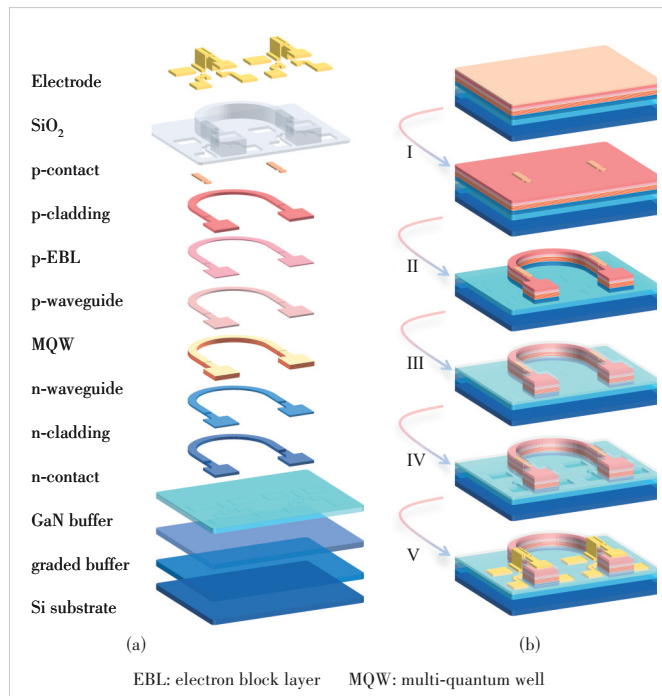
This work was supported in part by the National Natural Science Foundation of China under Grant No. U21A20495, National Key Research and Development Program of China under Grant No. 2022YFE0112000, and Higher Education Discipline Innovation Project under Grant No. D17018.

To date, the scalable development of optical interconnection has been faced with the problem of effectively guiding light in extremely narrow bends. However, most existing research focuses on on-chip systems with straight waveguides^[13–16], and how to integrate large-angle bent waveguides in these systems remains a key challenge that needs to be explored in depth, especially on III-V and silicon nitride platforms. Solving this problem will be a key factor in promoting the continued progress of optoelectronic integrated systems.

In this paper, we study a monolithic III-nitride optoelectronic microsystem that integrates a near-ultraviolet light source, a monitor, a 180° bent waveguide, an electro-absorption modulator (EAM), and a receiver. The aforementioned components are integrated with an as-grown III-nitride-on-Si wafer uniformly, employing a top-down approach. Detailed characterizations are presented and on-chip optical data communication is demonstrated.

2 Fabrication

The layered structure of the chip and diagram of the fabrication process are shown in Fig. 1. As shown in Fig. 1a, the Si substrate is at the bottom layer. The epitaxial structure is composed of a buffer layer with graded aluminum components, a 2.1 μm-thick unintentionally doped GaN buffer layer, a 2.45 μm-thick Si-doped Al_{0.03}Ga_{0.97}N n-contact layer, a 750 nm-thick Al_{0.1}Ga_{0.9}N n-cladding layer, an 80 nm-thick GaN n-waveguide, the 4-cycle 3 nm/10 nm thick In_{0.02}Ga_{0.98}N / Al_{0.08}Ga_{0.92}N MQWs, a 7 nm-thick Al_{0.08}Ga_{0.92}N last quantum



▲ Figure 1. (a) Layered structure of the III-nitride-on-Si optoelectronic system integrated with a 180° bent waveguide; (b) diagram of the top-down manufacturing process

barrier, a 60 nm-thick GaN p-waveguide, a 20 nm-thick Al_{0.25}Ga_{0.75}N electron block layer (EBL), a 500 nm-thick Al_{0.1}Ga_{0.9}N p-cladding layer, and a 30 nm-thick Mg-doped GaN p-contact layer from bottom to top. As shown in Fig. 1b, the active pattern was transferred to a photoresist using a standard photolithography process. The wafer was then etched for 200 nm precisely using an inductive coupling plasma to remove the excess p-contact. The p-mesa of 2.2 μm height was etched out and the n-contact layer was exposed. Two trenches were formed at the same time. A 200 nm-thick SiO₂ passivation layer was deposited on the chip by plasma-enhanced chemical vapor deposition and patterned to realize electrical isolation. 20 nm/200 nm-thick Ni/Au electrode films were deposited by electron beam evaporation and the metal electrode was patterned by lift-off technology. A rapid thermal annealing process was then used to improve the ohmic contact performance in a pure nitrogen environment at 550 °C for 60 s.

3 Results and Discussions

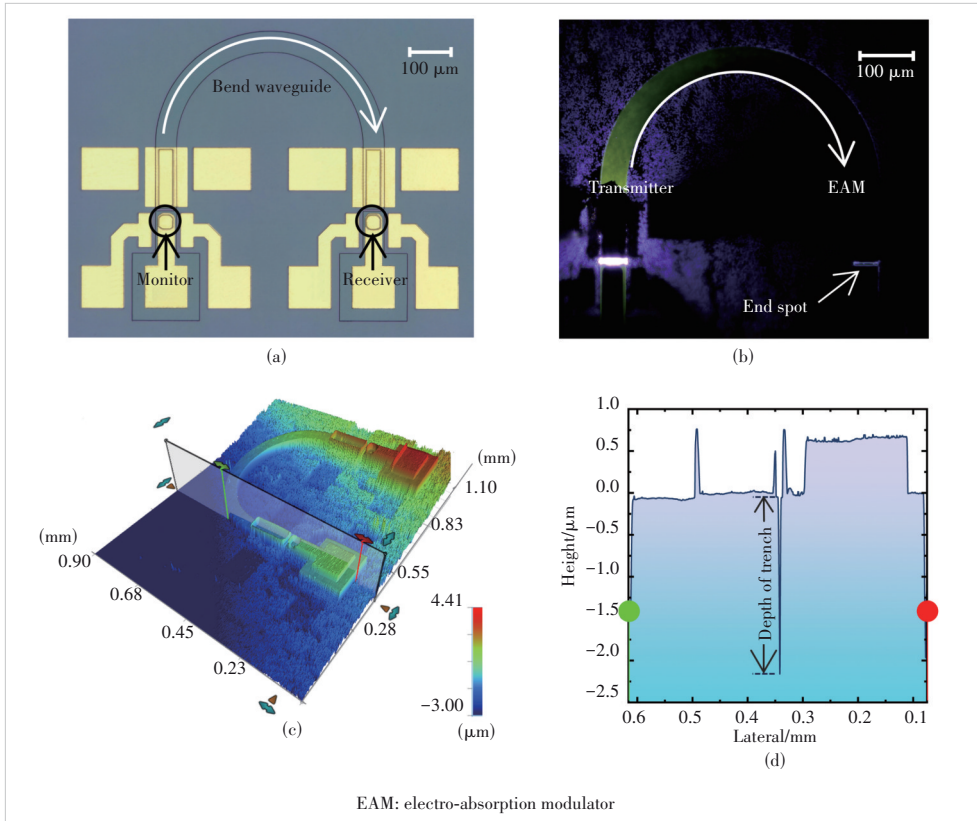
Fig. 2 illustrates the morphological characteristics of the optoelectronic chip. The fabricated chip consists of a monitor, an EAM, a waveguide, a modulator, and a receiver, as shown in the top-view optical microscope image in Fig. 2a. Fig. 2b displays the light spot at the end of the 180° bent waveguide when the transmitter is activated in a dark environment, with the light propagating along the waveguide. The bent waveguide has a width of 50 μm, and the arc length at the center of the waveguide is approximately 740 μm. Fig. 2c presents a 3D surface scan of the chip height, obtained using a high-precision profilometer (DektakXT, Bruker Corporation). The cross-sectional data are shown in Fig. 2d. Electrical isolation between the two devices on the same side is achieved through isolation trenches with a width of 5 μm and an etching depth of 2.2 μm.

Fig. 3 presents the electro-optical characteristics of the active region of the photonic device. The current-voltage (I-V) curve of the transmitter is shown in Fig. 3a, with an inset displaying the voltage-capacitance (V-C) curve of the EAM. The results indicate that the transmitter exhibits typical diode behavior, with a turn-on voltage of around 4 V. When a forward voltage is applied, the capacitance of the EAM initially increases and then decreases to a negative value. This decrease is caused by the radiative recombination of injected carriers within the quantum wells. The electroluminescence (EL) spectrum and spectral responsivity (SR) curve of the photonic chip are shown in Fig. 3b. The spectral analysis is conducted using a high-resolution spectrometer (HR4000, Ocean Insight Corporation) and a quantum efficiency measurement system (Oriel IQE200B, Newport Corporation). The interaction between the Stokes shift and the quantum-confined Stark effect (QCSE) in the photonic chip is reflected in the EL and SR curves. It is well-known that MQW diodes exhibit a distinct Stokes shift between emission (low energy) and absorption (high energy). It

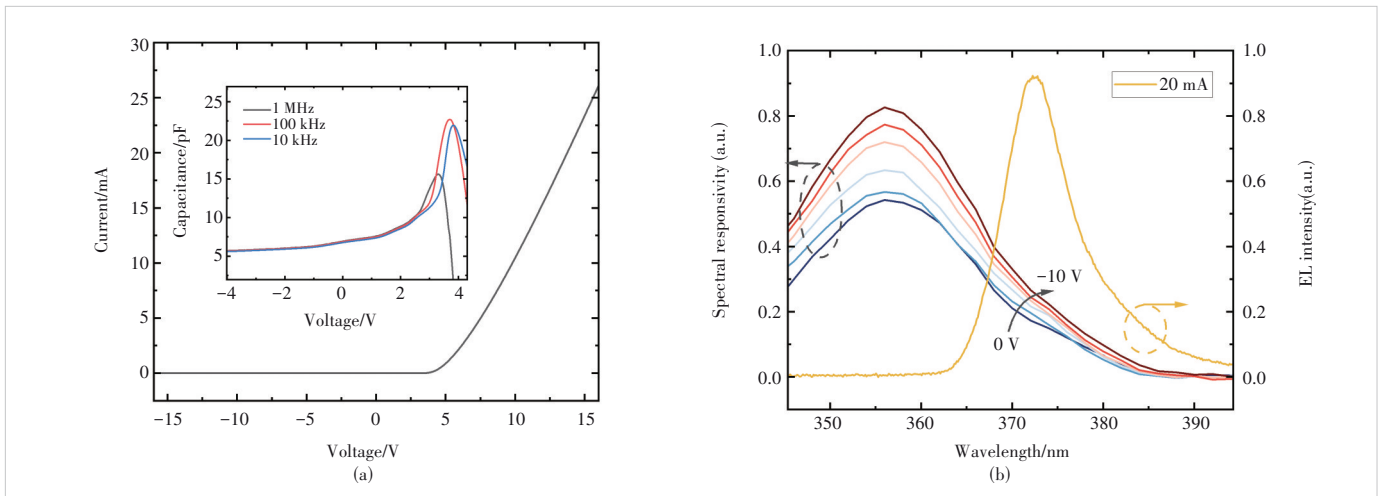
is generally accepted that the EL emission originates from the recombination of localized excitons, while the absorption edge of the spectrum corresponds to the absorption of free excitons^[17]. When the transmitter's injection current is fixed at 20 mA and the EAM's bias voltage is increased from 0 V to -10 V in steps of -2 V, the overall spectral responsivity

shows an increasing trend. The overlap between the EL spectrum and the SR curve enables the MQW diode not only to detect light emitted by another diode with the same structure but also to modulate the light intensity under different reverse bias voltages. As a result, two on-chip MQW diodes with identical structures can serve as the light source and EAM, respectively.

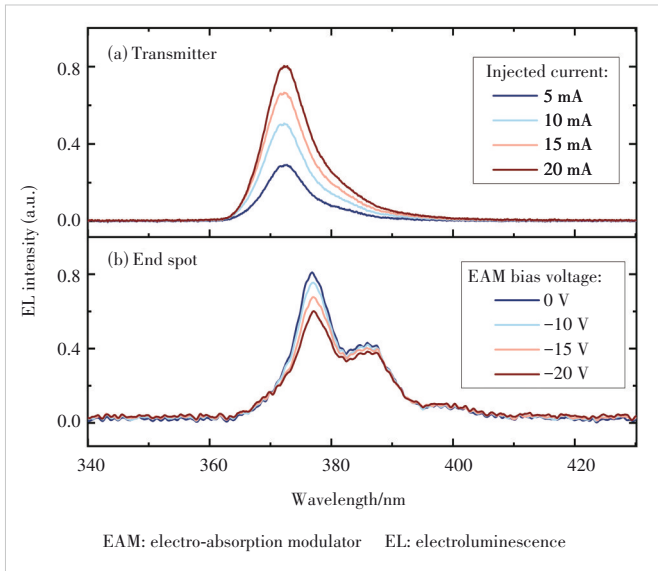
To optically prove that the light from the transmitter can still effectively reach the receiver after propagating through the 180° bent waveguide and generate a light spot on its end face, the spectra of the light spots at both ends of the waveguide are measured, as shown in Fig. 4. The spectra measured at the transmitter/monitor trench are shown in Fig. 4a when the transmitter is stably injected with currents of 5 mA, 10 mA, 15 mA, and 20 mA. The spectra measured at the EAM/receiver trench are shown in Fig.4b while the transmitter is injected with a fixed current of 10 mA, and the EAM is biased with different voltages. The applied bias voltage causes the quantum well band to tilt, and in conjunction with the quantum-limited Stark effect, the EAM can modulate light. A comparison of Figs. 4a and 4b reveals when light propagates through a transmission me-



▲ Figure 2. (a) Birdview of the on-chip system under an optical microscope; (b) luminescence image of the optoelectronic chip; (c) characterization of the mesa height using a stylus profilometer; (d) height characterization along the cross-section in (c)



▲ Figure 3. (a) I-V curve of the transmitter, where the inset is the capacitance-voltage curve of the EAM; (b) electroluminescence spectrum and spectral responsivity curves of optoelectronic chip

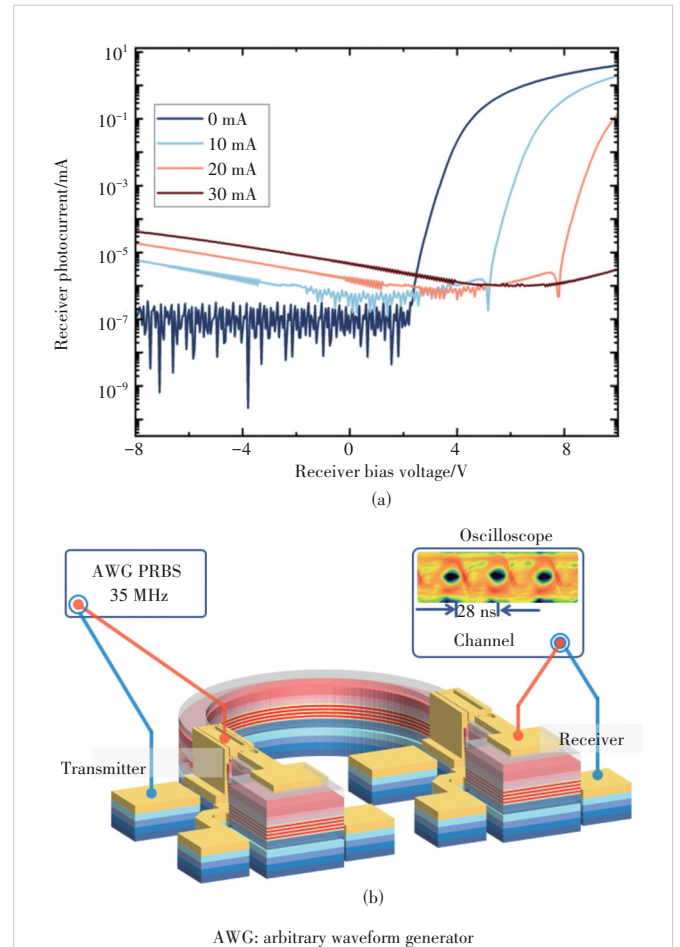


▲ **Figure 4.** (a) Electroluminescence spectra of the LED with several different injection currents; (b) spectra of the end spot when the EAM is under different modulation voltages

dium with a quantum well structure sandwiched in the waveguide, the spectrum will be redshifted due to asymmetric absorption^[15]. It should be noted that no isolated system is unaffected by the gravitational field, which creates irreversibility. Theoretically, even if a perfect light-emitting device exists, it will absorb higher photon energy than it emits because gravitational fields would cause the irreversibility between the photon emission and absorption process^[18 - 19]. The object at different positions has different quantized states in a gravitation field and thus, its mass related to its total internal energy is different at different energy states, because the total internal energy equals its mass times the speed of light squared, $E = mc^2$. According to the law of conservation of energy, the total energy of the system is conserved. Therefore, the work done during the process from one position to another position is not symmetric to that done during the return trip, which creates irreversibility. The frequency difference can be expressed as $\omega_{\text{det}} - \omega_{\text{emi}} = (E_{\text{gap}}gH) / hc^2$, where ω_{det} is the frequency of the detected light, ω_{emi} is the frequency of the emitted light, E_{gap} is the energy gap between the conduction and valence bands in a gravitational field, h is the Planck constant, c is the velocity of light, g is the normalized acceleration, and H is related to the geometrical height between the conduction and valence bands in a gravitational field. The frequency difference is tiny because the physical height H of the energy gap is small. However, both EL spectra and responsivity spectra are broad. Moreover, the shift in the EL versus responsivity spectra in reality is also caused by either the loss of energy in the excited state to lattice modes or changes in molecular configuration and vibrational modes. Therefore, there is an asymmetric overlap between the emission and the detection spectra.

The experimental results indicate that the asymmetric absorption would cause spectral redshift in a quantum well diode, and self-absorption is a fundamental phenomenon in quantum wells. This suggests that the next monolithic GaN optoelectronic integration could be improved through some spectral fine-tuning techniques, such as selective area growth^[20] and transfer processes^[21].

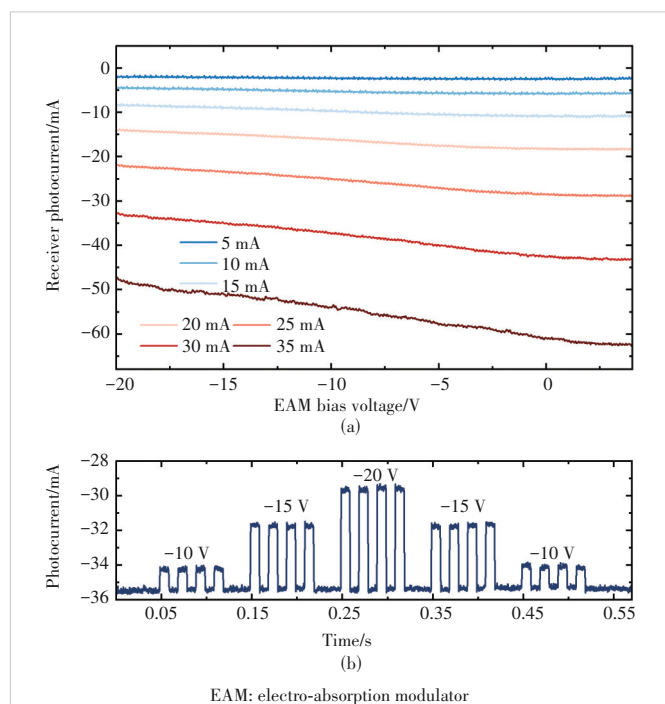
The characterization and testing of optical transmission and reception between two on-chip diodes with identical structures are shown in Fig. 5. As mentioned earlier, quantum well diodes can absorb photons emitted by another diode of the same structure and generate a corresponding photocurrent. To evaluate the optical response between the quantum well diodes at both ends of the curved waveguide, the two diodes are used as a light-emitting transmitter and receiver, respectively, as illustrated in Fig. 5b. When the injection current of the transmitter increases from 0 to 30 mA, the photocurrent of the receiver varies with the applied voltage, as shown in Fig. 5a. A higher injection current in the transmitter results in stronger emitted light, producing more photons. Consequently, under the same



▲ **Figure 5.** (a) Receiver photocurrent versus applied voltage at different transmitter injection currents; (b) 35 Mbit/s on-chip data transmission test with emission modulation mode

applied voltage, a larger injection current in the transmitter leads to a greater photocurrent in the receiver. It is evident that the larger the reverse bias voltage applied, the greater the photocurrent generated by the diode. This trend is consistent with the SR curve plotted in Fig. 3b. Fig. 5b demonstrates the 35 Mbit/s on-chip small-signal data transmission between the transmitter using emission modulation and the receiver. The transmitter is driven by a pseudo-random binary sequences-11 (PRBS11) signal from an arbitrary waveform generator (AWG) with a 2-peak-to-peak voltage (V_{pp}) amplitude, 7 V bias voltage, Hi-Z output impedance, default phase, and a frequency of 35 MHz. These parameters are synchronized with another channel to trigger the oscilloscope. After a few seconds, a clear eye diagram appears on the oscilloscope, as shown in Fig. 5(b). This confirms that the photonic chip with a 180° bent waveguide is capable of on-chip optical signal transmission using emission modulation.

After the characterization of the emission modulation mode of the transmitter, the absorption modulation mode of the quantum well diode as an EAM was characterized, as shown in Fig. 6. Four channels of the Keysight B1500A semiconductor parameter analyzer were connected to the transmitter, EAM, and receiver. The transmitter was provided with a constant DC drive, the EAM was supplied with a reverse bias voltage in a sweep mode, and the I-V characteristics of the receiver were measured. The drive current was sequentially set to 5 mA, 10 mA, 15 mA, 20 mA, 25 mA, 30 mA, and 35 mA.



▲ Figure 6. (a) Photocurrent change of the receiver as the voltage biased on the modulator varies with the transmitter under different operating currents; (b) waveforms of the receiver's photocurrent when EAM is modulated

For each transmitter current condition, the I-V characteristics of the receiver were measured as the EAM bias voltage was swept from 4 V to -20 V. Fig. 6a shows the relationship between the photocurrent of the receiver and the reverse bias voltage applied to the modulator. The change in absorption is attributed to the QCSE induced by the external field^[22-23]. At the same modulation voltage, as the injection current increases, the transmitter's light intensity also increases, leading to more pronounced changes in the amplitude of the photocurrent. Fig. 6b displays the photocurrent waveform during on-chip optical data transmission using the absorption modulation mode. The transmitter was driven by a constant 20 mA current, and the EAM switched between zero and different reverse bias voltages to modulate the absorption of the light transmitted through the waveguide. This reduced the light reaching the receiver, causing corresponding changes in the photocurrent output from the receiver thereby achieving on-chip electro-absorption modulation in the photonic chip. When the reverse bias voltage of the EAM is 20 V, the total power consumption of the system on chip is about 250 mW.

4 Conclusions

In summary, a monolithic optoelectronic on-chip system integrated with 180° bent waveguide was fabricated from a III-nitride-on-Si wafer. The experimental results demonstrate that the light transmitted through the curved waveguide can be extracted by the receiver at the end of the waveguide, and that the absorption modulation signal on the propagation path can be detected. The monolithic integration method adopted in this paper simplifies the fabrication process, avoiding complex post-doping and growth steps, while achieving a highly integrated design of the transmitter, modulator, waveguide, and receiver. Through the shared MQW structure, the system demonstrates excellent scalability, particularly with the successful integration of large-angle bent waveguides. This provides strong support for realizing bidirectional optical signal modulation in III-nitride optoelectronic systems, laying the foundation for further development of monolithic optoelectronic systems in the future.

References

- [1] SUN C, WADE M T, LEE Y, et al. Single-chip microprocessor that communicates directly using light [J]. *Nature*, 2015, 528(7583): 534 - 538. DOI: 10.1038/nature16454
- [2] ATABAKI A H, MOAZENI S, PAVANELLO F, et al. Integrating photonics with silicon nanoelectronics for the next generation of systems on a chip [J]. *Nature*, 2018, 556(7701): 349 - 354. DOI: 10.1038/s41586-018-0028-z
- [3] AMANO H. Development of GaN-based blue LEDs and metalorganic vapor phase epitaxy of GaN and related materials [J]. *Progress in crystal growth and characterization of materials*, 2016, 62(2): 126 - 135. DOI: 10.1016/j.pcrysgrow.2016.04.006
- [4] MIKULICS M, MAYER J, HARDTDEGEN H H. Cutting-edge nano-LED

- technology [J]. *Journal of applied physics*, 2022, 131(11): 110903. DOI: 10.1063/5.0087279
- [5] TABALLIONE C, VAN DER MEER R, SNIJDERS H J, et al. A universal fully reconfigurable 12-mode quantum photonic processor [J]. *Materials for quantum technology*, 2021, 1(3): 035002. DOI: 10.1088/2633-4356/ac168c
- [6] WANG Y J, WANG X, ZHU B C, et al. Full-duplex light communication with a monolithic multicomponent system [J]. *Light, science & applications*, 2018, 7: 83. DOI: 10.1038/s41377-018-0083-0
- [7] FENG M X, WANG J, ZHOU R, et al. On-chip integration of GaN-based laser, modulator, and photodetector grown on Si [J]. *IEEE journal of selected topics in quantum electronics*, 2018, 24(6): 8200305. DOI: 10.1109/JSTQE.2018.2815906
- [8] LI K H, FU W Y, CHEUNG Y F, et al. Monolithically integrated InGaN/GaN light-emitting diodes, photodetectors, and waveguides on Si substrate [J]. *Optica*, 2018, 5(5): 564. DOI: 10.1364/optica.5.000564
- [9] CHI N, HAAS H, KAVEHRAD M, et al. Visible light communications: demand factors, benefits and opportunities [J]. *IEEE wireless communications*, 2015, 22(2): 5 – 7. DOI: 10.1109/MWC.2015.7096278
- [10] ISLIM M S, FERREIRA R X, HE X Y, et al. Towards 10 Gb/s orthogonal frequency division multiplexing-based visible light communication using a GaN violet micro-LED [J]. *Photonics research*, 2017, 5(2): A35. DOI: 10.1364/prj.5.000a35
- [11] CHI N, ZHOU Y J, LIANG S Y, et al. Enabling technologies for high-speed visible light communication employing CAP modulation [J]. *Journal of lightwave technology*, 2018, 36(2): 510 – 518. DOI: 10.1109/JLT.2017.2783906
- [12] ZHOU Y J, ZHU X, HU F C, et al. Common-anode LED on a Si substrate for beyond 15 Gbit/s underwater visible light communication [J]. *Photonics research*, 2019, 7(9): 1019. DOI: 10.1364/prj.7.001019
- [13] ZHANG H, YAN J B, YE Z Q, et al. Monolithic GaN optoelectronic system on a Si substrate [J]. *Applied physics letters*, 2022, 121(18): 181103. DOI: 10.1063/5.0125324
- [14] ZHANG H, YE Z Q, YAN J B, et al. Multiplexing of bias-controlled modulation modes on a monolithic III-nitride optoelectronic chip [J]. *Optics letters*, 2023, 48(19): 5069 – 5072. DOI: 10.1364/OL.503429
- [15] ZHANG H, YE Z Q, FU J W, et al. Asymmetric-absorption-induced spectral redshift in a monolithic III-nitride on-chip system [J]. *Optics express*, 2024, 32(10): 18193 – 18200. DOI: 10.1364/OE.525174
- [16] XIE M Y, JIANG Y, GAO X M, et al. Uniting a III-nitride transmitter, waveguide, modulator, and receiver on a single chip [J]. *Advanced engineering materials*, 2021, 23(12): 2100582. DOI: 10.1002/adem.202100582
- [17] CHICHIBU S, AZUHATA T, SOTA T, et al. Spontaneous emission of localized excitons in InGaN single and multi-quantum well structures [J]. *Applied physics letters*, 1996, 69(27): 4188 – 4190. DOI: 10.1063/1.116981
- [18] WANG Y. Gravitational effect creates the irreversibility [EB/OL]. [2023-11-14]. <https://physicscommunity.nature.com/posts/gravitational-effect-creates-the-irreversibility>
- [19] LIU P, QI Z, FU J, et al. Unification of irreversibility and energy diagram theory [J]. *ACS omega*, 2023, 8(22): 20004 – 20008. DOI: 10.1021/acsoomega.3c02189
- [20] SUGIYAMA M. Selective area growth of III-V semiconductors: from fundamental aspects to device structures [C]//The 22nd International Conference on Indium Phosphide and Related Materials (IPRM). IEEE, 2010: 1 – 6. DOI: 10.1109/ICIPRM.2010.5515910
- [21] SHI Z, GAO X M, YUAN J L, et al. Transferrable monolithic III-nitride photonic circuit for multifunctional optoelectronics [J]. *Applied physics letters*, 2017, 111(24): 241104. DOI: 10.1063/1.5010892
- [22] MILLER D A, CHEMLA D S, DAMEN T C, et al. Electric field dependence of optical absorption near the band gap of quantum-well structures [J]. *Physical review B. B. condensed matter*, 1985, 32(2): 1043 – 1060. DOI: 10.1103/physrevb.32.1043
- [23] WEINER J S, MILLER D A B, CHEMLA D S. Quadratic electro-optic effect due to the quantum-confined Stark effect in quantum wells [J]. *Applied physics letters*, 1987, 50(13): 842 – 844. DOI: 10.1063/1.98008

Biographies

ZHANG Hao received his BS degree in automation from Nanjing Institute of Technology, China and MS degree in electronics and communication engineering from Nanjing University of Posts and Telecommunications, China in 2016 and 2019, respectively. In 2019, he won the Grand Prize of the “Challenge Cup” National College Students’ Extracurricular Academic Works Competition. He is pursuing his PhD degree in signal and information processing at Nanjing University of Posts and Telecommunications. His research interests focus on GaN optoelectronics integration and applications. In the last three years, he has published three research papers as the first author, and his research work has been featured on *Semiconductor Today* and selected as an OSA Editor’s Pick.

YE Ziqi received her BS and MS degrees in communication engineering from Nanjing University of Posts and Telecommunications, China in 2019 and 2022, where she is currently pursuing her PhD degree in communication and information system. Her current research interests include monolithic integration GaN LED and visible light communications.

YUAN Jialei received his MS degree in communication engineering from Nanjing University of Posts and Telecommunications, China in 2018, where he is currently pursuing his PhD degree in communication and information system. His current research interests include monolithic integration GaN LED and visible light communications.

LIU Pengzhan received his MS degree from Nanjing university of posts and telecommunications, China. Now he is a PhD student there under the supervision of Prof. CAO Ziping and WANG Yongjin. He is mainly engaged in the research of all light wireless optical communication networks and integrated GaN optoelectronic devices.

WANG Yongjin (wangyj@njupt.edu.cn) received his PhD degree in microelectronics and solid state electronics from Shanghai Institute of Microsystem and Information Technology, Chinese Academy of Sciences in 2005. He received plenty of scholarships including the Humboldt Foundation Scholarship, the JSPS Special Researcher Scholarship, and the Royal Society for Engineering Scholarship. In addition, he was engaged in the research work at the University of Freiburg, Germany, Tohoku University, Japan, Germany Forschungszentrum Jülich, and University of Bristol, UK. Since 2011, he has been a professor at Nanjing University of Posts and Telecommunications, China. Now, he is the chief investigator of National Micro-Nano Devices and the Information System Innovation Introduction Base. His current research is to conduct III-nitride monolithic photonic circuits and all light wireless optical communication Networks. He has published more than 100 research papers in this field.

Performance Characterization of Visible Light Communication Based on GaN High-Voltage LED/PD



LU Meixin, JIANG Zitong, FANG Li, YAN Yiqun,
YAN Jiabin

(Nanjing University of Posts and Telecommunications,
Nanjing 210003, China)

DOI: 10.12142/ZTECOM.202404007

<https://kns.cnki.net/kcms/detail/34.1294.TN.20241126.1516.002.html>,
published online November 26, 2024

Manuscript received: 2024-11-07

Abstract: While considerable research has been conducted on the structural principles, fabrication techniques, and photoelectric properties of high-voltage light-emitting diodes (LEDs), their performance in light communication remains underexplored. A high-voltage series-connected LED or photodetector (HVS-LED/PD) based on the gallium nitride (GaN) integrated photoelectronic chip is presented in this paper. Multi-quantum wells (MQW) diodes with identical structures are integrated onto a single chip through wafer-scale micro-fabrication techniques and connected in series to construct the HVS-LED/PD. The advantages of the HVS-LED/PD in communication are explored by testing its performance as both a light transmitter and a PD. The series connection enhances the device's 3 dB bandwidth, allowing it to increase from 1.56 MHz to a minimum of 2.16 MHz when functioning as an LED, and from 47.42 kHz to at least 85.83 kHz when operating as a PD. The results demonstrate that the light communication performance of HVS-LED/PD is better than that of a single GaN MQW diode with bandwidth and transmission quantity, which enriches the research of GaN-based high-voltage devices.

Keywords: high-voltage LEDs; high-voltage PDs; GaN MQW diode array; communication characterization; visible light communication

Citation (Format 1): LU M X, JIANG Z T, FANG L, et al. Performance characterization of visible light communication based on GaN high-voltage LED/PD [J]. *ZTE Communications*, 2024, 22(4): 46 – 52. DOI: 10.12142/ZTECOM.202404007

Citation (Format 2): M. X. Lu, Z. T. Jiang, L. Fang, et al., "Performance characterization of visible light communication based on GaN high-voltage LED/PD," *ZTE Communications*, vol. 22, no. 4, pp. 46 – 52, Dec. 2024. doi: 10.12142/ZTECOM.202404007.

1 Introduction

Light-emitting diodes (LEDs) are solid-state semiconductor devices that can convert electrical signals into visible light signals, featuring high energy efficiency, low power, and fast response speed^[1-3]. With the development of semiconductor technology, LED has been widely used in electronic screen displays, home/street lighting, and other fields, in which high-power LEDs have garnered significant attention^[4-6]. High-power LED devices have important application potential in visible light communication (VLC)^[7-9], especially long-distance communications. Enlarging the device size is a common method for realizing a high-power LED^[10-11]. However, large LEDs easily suffer from uneven current distribution

and efficiency drop^[12-13]. Another type of high-power LED is obtained by connecting several small-sized LEDs in series^[14-15], called high-voltage series-connected (HVS) LED. The HVS-LED exhibits a low operating current and effectively addresses the issue of overcrowded current, leading to reduced alternating current/direct current (AC/DC) conversion power loss, enhanced reliability, and lower packaging cost^[16-18].

Previously published works on HVS-LED mainly focus on optical characterization^[19-20] and fabrication technologies^[21-22]. However, only a few reports studied the influence of series structure on the light communication performance of the HVS-LED. Moreover, the performance of gallium nitride (GaN) multi-quantum wells (MQW) photodiodes (PDs) in series also has not been explored. Recently, advancements in the communication performance of LEDs and PDs have promoted their applications in high-speed data transmission and optical measurements, encompassing high-speed imaging and videography^[23], time-resolved fluorescence sensing^[24], motion detection^[25], and numerous other fields^[26-27]. Therefore, this paper proposes a visible light communication system based on GaN HVS-LED/PD and comprehensively characterizes the

This work is jointly supported by the National Natural Science Foundation of China under Grant Nos. 62004103, 62105162, 62005130, 61827804, 62274096, and 61904086, the Natural Science Foundation of Jiangsu Province under Grant No. BK20200743, the Natural Science Foundation of the Higher Education Institutions of Jiangsu Province under Grant No. 22KJA510003, the Natural Science Foundation of Nanjing University of Posts and Telecommunications under Grant No. NY223084, the "111" project under Grant No. D17018, and the Postgraduate Research & Practice Innovation Program of Jiangsu Province under Grant No. SJCX230257.

system's performance with varying numbers of components connected in series.

2 Device Structure and Fabrication

The HVS-LED chip integrates 36 GaN-based MQW diodes of an identical structure. The device size is $7.6 \text{ mm} \times 7.6 \text{ mm}$ and the size of each diode is $1.25 \text{ mm} \times 1.25 \text{ mm}$. A serpentine circuit configuration is employed, resulting in a more uniform current distribution across the chip. Figs. 1a and 1b reveal the chip images when one LED and five LEDs are working, respectively. Fig. 1c displays the three-dimensional structure of the chip. The comb metal is the p-electrode of the LED, which is designed to make the current distribution more uniform while shielding the light emission minimally. The ring metal is the n-electrode of the LED. Multiple LEDs are connected in series on the chip by connecting the p-electrode of the former LED and the n-electrode of the latter LED.

The epilayer structure diagram of the chip is illustrated in Fig. 1d. The GaN-based epitaxial layers on the sapphire substrate consist of an n-GaN layer, an MQW layer, and a p-GaN layer from bottom to top. The GaN chip is fabricated using a wafer-level manufacturing process. The details are described as follows. First, a transparent indium tin oxide (ITO) thin film layer is grown on the p-GaN layer by magnetron sputtering. Second, a photoresist is coated and exposed, revealing the areas to be etched, and wet etching is processed to pattern the ITO layer. Then, inductively coupled plasma (ICP) dry etching is used for the n-GaN layer. Third, the coated and exposed photoresist reveals the areas of isolation trenches, and the ICP dry etching is applied to the underlying sapphire substrate. Fourth, a photoresist layer is spin-coated on a wafer and patterned to the geometry of Metal I by lithography. Metal I is then depos-

ited by the electron beam evaporation and patterned by the lift-off process. Fifth, a layer of silicon dioxide (SiO_2) is grown on the GaN layer using plasma-enhanced chemical vapor deposition (PECVD). Subsequently, the SiO_2 layer is patterned to form the through-holes between metal layers. Sixth, a photoresist layer is coated and patterned to the geometry of Metal II by lithography. Metal II is then deposited by the electron beam evaporation and patterned by the lift-off process. Finally, the wafer is thinned and cut into separate chips of HVS-LED.

3 Photoelectric Characteristics

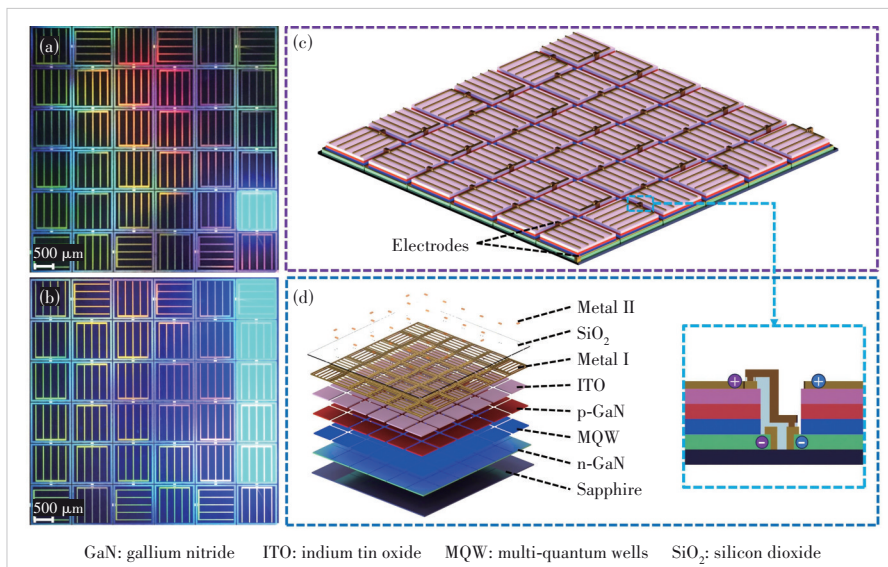
The current-voltage (IV) characteristics of the HVS-LED are measured using a semiconductor device analyzer (Agilent Technologies B1500A), and the results are displayed in Fig. 2a. An individual LED operates at a turn-on voltage of about 2.4 V and the turn-on voltage of the device is proportional to the number of LEDs in series, as shown in Fig. 2b. For the array with 36 LEDs in series, the turn-on voltage is about 84.6 V.

The external quantum efficiency (EQE) of the LED device is measured using an integrating sphere (Labsphere) equipped with a calibrated detector. The EQE curves for a single LED and five LEDs in series versus injection current are shown in Fig. 2c. The EQE of the five LEDs connected in series is marginally greater than that of an individual LED. The peak EQE of a single LED is 44.46% achieved at the injection current of 13 mA. As a comparison, the peak EQE of the five LEDs in series is 45.15% achieved at the injection current of 17 mA. The results indicate that the series array of LEDs can increase the output light power without introducing obvious current spreading issues that would deteriorate the efficiency of the device.

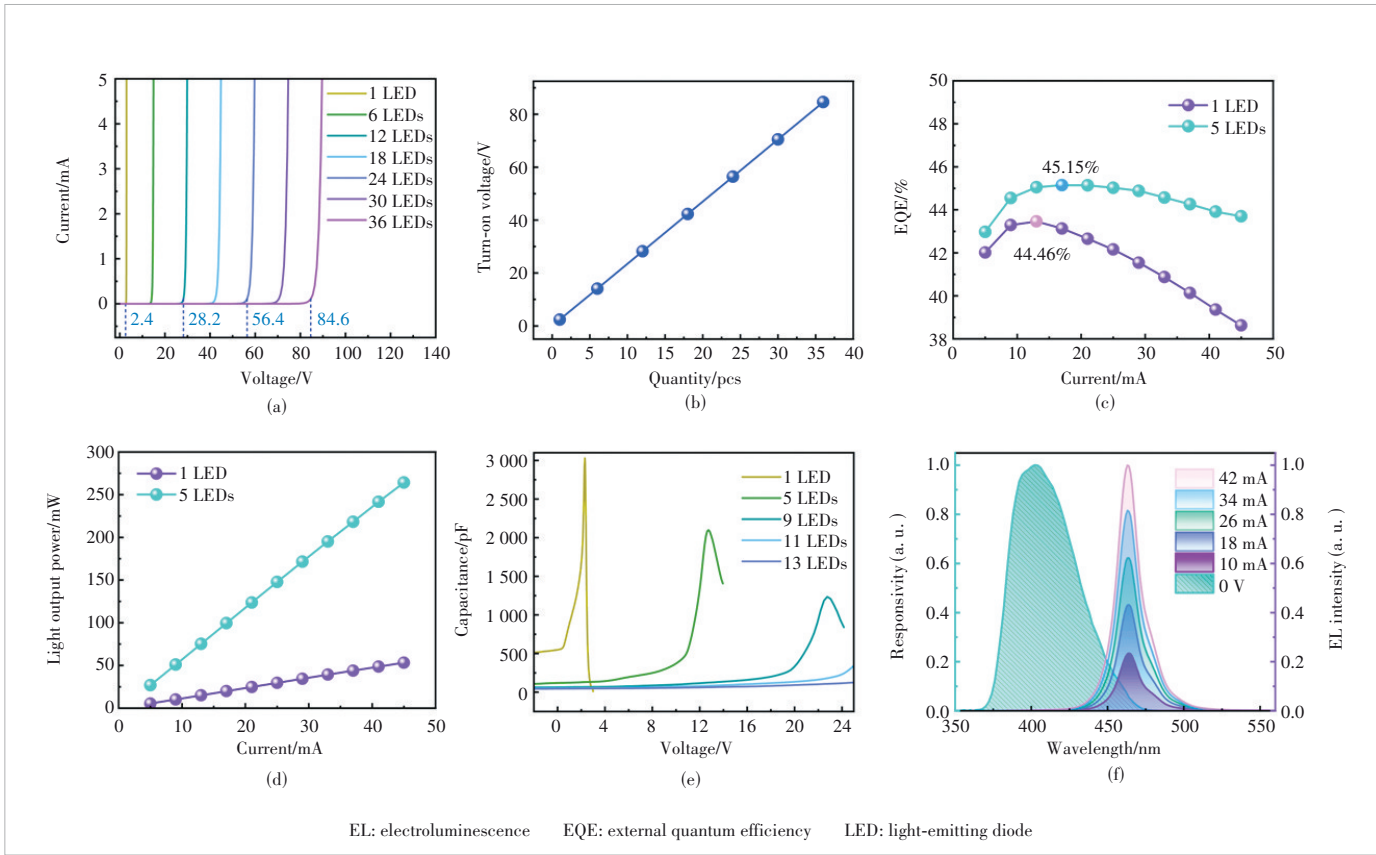
Fig. 2d demonstrates a linear rise in light output power with the injection current. Under identical current conditions, the optical power output of LEDs connected in series surpasses that achieved by a single LED configuration.

The capacitance-voltage (CV) curves for different numbers of LEDs in series are measured by the semiconductor device analyzer (Agilent Technologies B1500A) at a measurement frequency of 100 kHz, as shown in Fig. 2e. The device capacitance decreases with the increase of LED quantity in series. The reciprocal of the total capacitance of the series capacitor is equal to the sum of the reciprocal capacitance of each capacitor.

The curve on the left side of Fig. 2f presents the response spectrum (RS) of a single GaN MQW LED under zero bias voltage. The curves on the right side of Fig. 2f depict the electroluminescence



▲ Figure 1. Morphology of HVS-LED: (a) optical image of the fabricated chip with one LED illuminated; (b) optical image of the fabricated chip with five LEDs illuminated; (c) three-dimensional structure of the chip; (d) chip epilayer structure, where the inset shows the details of electrode connection



▲ Figure 2. Electric and photoelectric characteristics of HVS-LED: (a) IV characteristics of LEDs with different quantities in series; (b) turn-on voltage for different numbers of LEDs in series; (c) EQE for a single LED and five LEDs in series; (d) light output power for a single LED and five LEDs in series; (e) CV curves for different numbers of LEDs in series; (f) the EL spectra and RS of a single LED

(EL) spectra under different injection currents from 10 mA to 42 mA, with peak emission wavelengths of 464 nm. The partial overlap of RS and EL spectra indicates that the light emitted by the HVS-LED can be detected by the identical structure diode employed as a PD.

4 Communication Performance

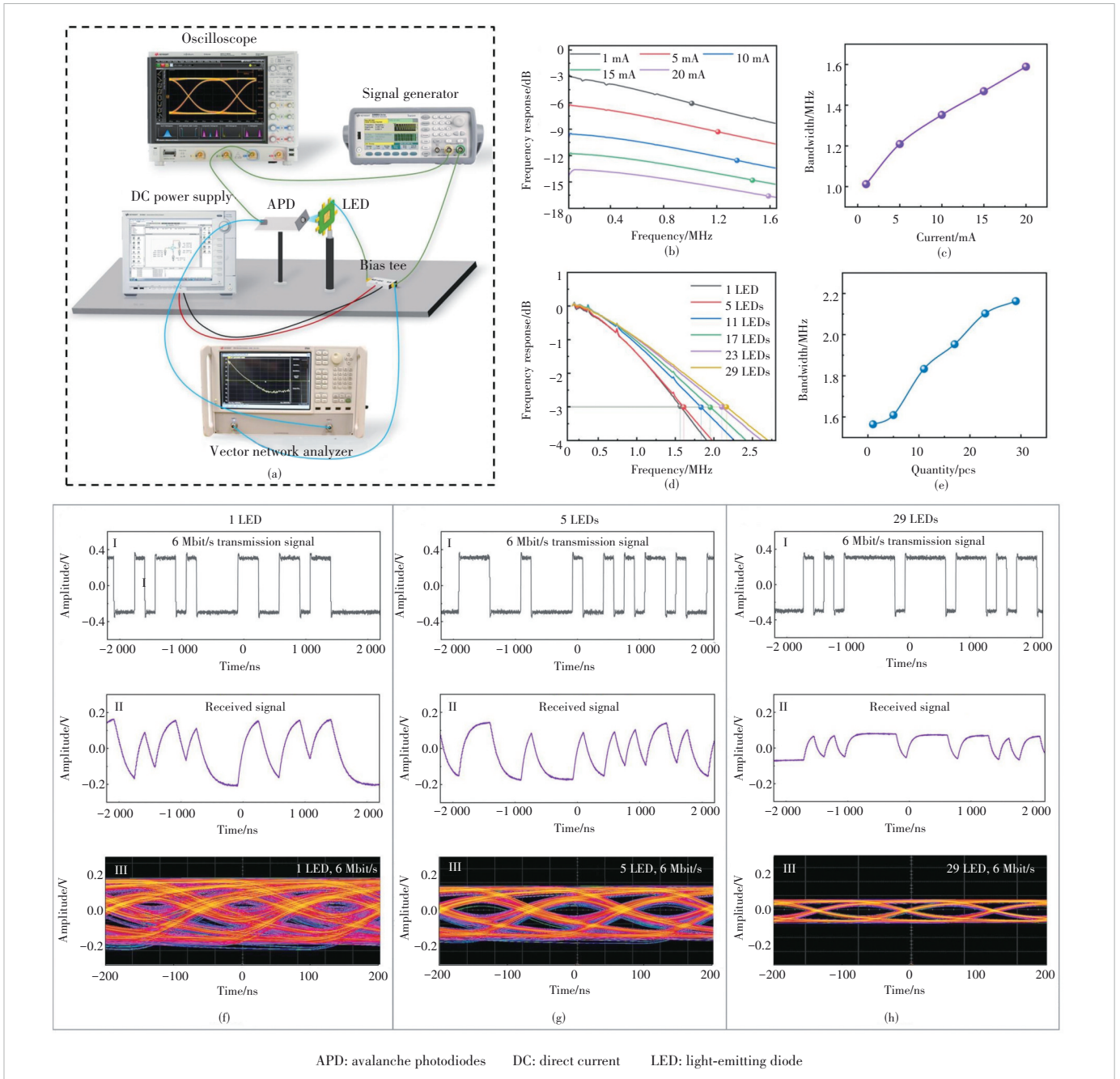
4.1 GaN MQW Diode Array as a Light Transmitter

Fig. 3a shows a test platform to verify the HVS-LED’s ability for communication. A GaN-based HVS-LED is employed as the light transmitter and an avalanche photodiodes (APD) module from Hamamatsu, Japan, with a 4 kHz to 100 MHz bandwidth, is used as the PD. The frequency responses of the HVS-LED are measured by a vector network analyzer (Keysight ENA Network Analyzer E5080A that operates from 9 kHz to 4.5 GHz) configured in a dual-channel setup. One channel is connected to the HVS-LED via a voltage bias module, while the other is directly connected to APD. By utilizing a semiconductor device analyzer (Agilent Technologies B1500A), a DC bias is applied to the HVS-LED, which is then superimposed with a low-power test signal from the vector network analyzer, resulting in their conversion into an optical signal. The optical

signal is subsequently captured by the APD, converted into an electrical signal, and then routed to another channel of the vector network analyzer for visualization.

Fig. 3b depicts the variation in frequency responses of five series-connected LEDs when the injection current increases from 1 mA to 20 mA. The dynamic resistance of the HVS-LED decreases as the bias current increases. This results in more AC signal power being loaded onto the source impedance compared with the load impedance, manifesting as a relative power reduction at higher currents. Furthermore, the 3 dB bandwidth of the device exhibits an increase with the rising injection current, as illustrated in Fig. 3c. This phenomenon can be attributed to the fact that the dynamic resistance of the device decreases due to alterations in the static operating point as the injection current increases, which leads to the expansion of the 3 dB bandwidth.

To determine the relationship between 3 dB bandwidth and LED quantity in series, the injection current on the device is fixed at 5 mA, and the frequency response curves for different numbers of LEDs in series are measured. To directly investigate the impact of LED quantity in series on the device bandwidth, the frequency response of LEDs with different numbers is normalized as shown in Fig. 3d. The 3 dB bandwidth versus



▲ Figure 3. Communication performance of HVS-LED: (a) the test platform for verifying HVS-LED's ability for communication; (b) 3 dB bandwidth of the device under different currents when five LEDs are connected in series; (c) 3 dB bandwidth versus injection current; (d) frequency response curves for different numbers of LEDs in series at 5 mA after normalization; (e) 3 dB bandwidth versus LED quantity in series; (f - h) waveform I shows transmission signal curves, waveform II received signal curves, and picture III eye diagram with a PRBS wave at 6 Mbit/s applied to the device when (f) one LED, (g) five LEDs, and (h) 29 LEDs are connected in series

LED quantity in series is derived from Fig. 3e. The 3 dB bandwidth of the device exhibits an increase with a rising number of LEDs. Theoretically, the bandwidth is inversely proportional to the product of resistance and capacitance. The resistance consists of the source resistance and the LED series resistance. When the LED quantity in series is small, the fixed source resistance plays a dominant role in the total resistance, and the

bandwidth increases with the LED quantity due to the decline of capacitance. However, as the LED quantity in series increases to a certain point, the LED series resistance becomes dominant, which is proportional to the quantity and counteracts the capacitance decline. Therefore, the curve trend in Fig. 3e becomes saturated under a large series quantity.

An oscilloscope (Keysight DSOS604A) is utilized to mea-

sure and analyze the received signal. GaN-based HVS-LED is employed as the light transmitter. A functional signal generator (Keysight 33600A Series, Trueform) is configured in a dual-channel setup with one channel connected to the HVS-LED via a voltage bias module, and the other channel connected to the oscilloscope, transmitting a pseudo-random binary sequence (PRBS) signal at 6 Mbit/s. A constant DC bias of 5 mA is applied to the HVS-LED using a semiconductor device analyzer (Agilent Technologies B1500A) to provide high voltage and ensure stable operation. Subsequently, the optical signal of the HVS-LED is captured by an APD, converted into an electrical signal, and then routed to another channel of the oscilloscope for visualization.

Figs. 3f, 3g, and 3h illustrate the corresponding transceiver signals and eye diagrams of a single LED, five LEDs, and 29 LEDs, respectively. Waveform I is the transmitted signal obtained by the oscilloscope directly connected to the signal generator, waveform II is the received signal detected through the optical communication link, and picture III is the corresponding eye diagram of the received signal. It can be observed that the amplitude of the received signal decreases as the number of LEDs increases. The reasons are as follows. The light field emitted by the device expands as the number of LEDs connected in series increases. Since the area of light detected by the APD remains constant, the ratio of detected light intensity to the total light field decreases. Concurrently, while the total AC signal supplied to the device remains unchanged, connecting additional LEDs in series will reduce the AC voltage applied across each LED. These factors collectively contribute to a decrease in the amplitude of the received signal. Furthermore, as the number of series-connected elements increases, the eye diagram of the 6 Mbit/s signal waveform changes from a blurred ribbon line to a distinct and slender trace. This transition is accompanied by a reduction in jitter and noise, as well as an enhancement in the mitigation of inter-symbol interference. This observation indicates the superior communication capabilities of HVS-LED compared to a single GaN MQW diode.

4.2 GaN MQW Diode Array as a PD

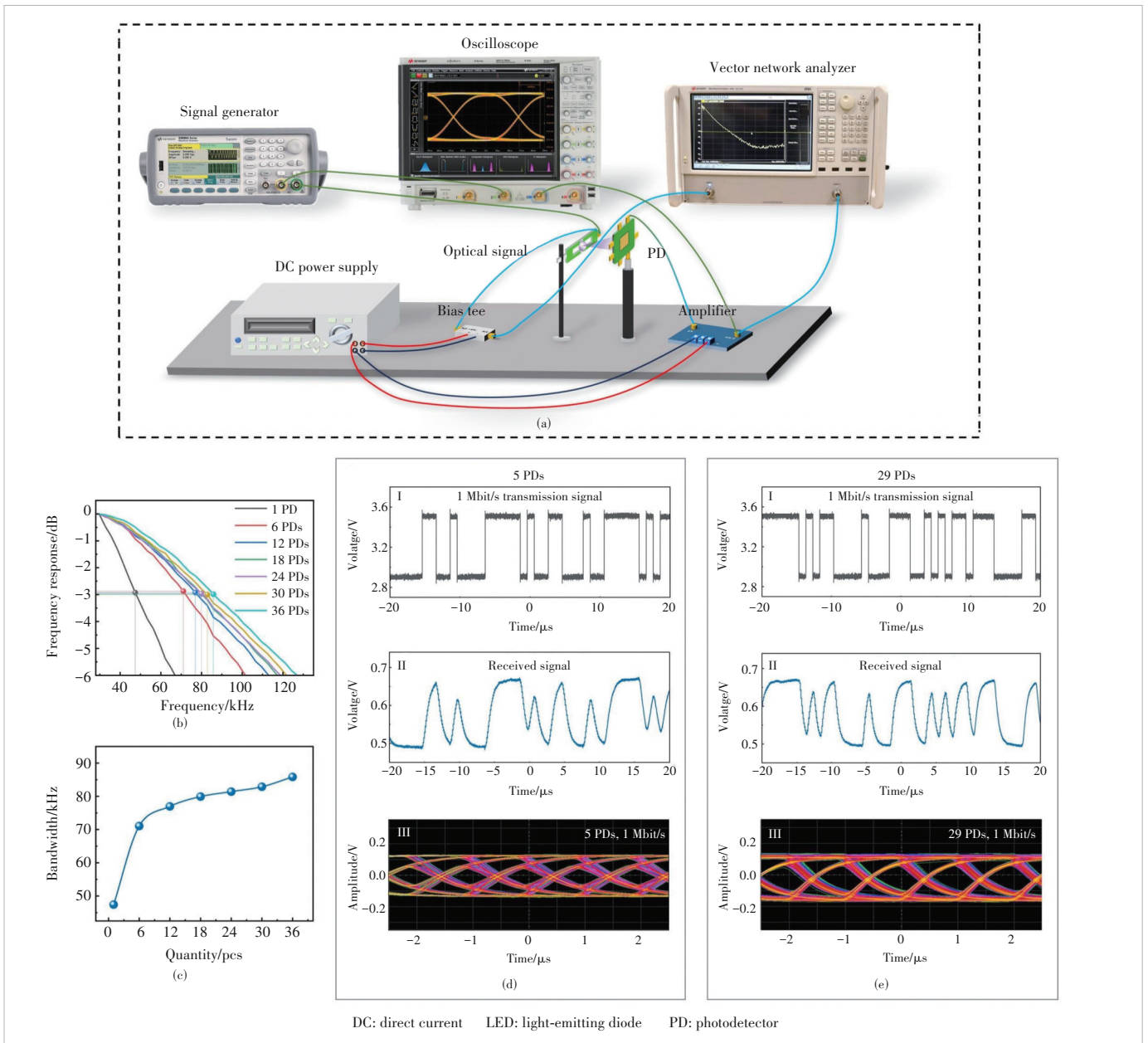
The test system to verify the HVS-PD's communication performance is displayed in Fig. 4a. An ultraviolet LED with a 3 dB bandwidth at about 2.55 MHz is employed as a light transmitter and the HVS-PD is utilized as a PD. The peak emission wavelength of the ultraviolet LED is 386 nm, and the electroluminescence spectrum of the ultraviolet LED is completely covered by the response spectrum of the HVS-PD, which means that the ultraviolet LED can be efficiently detected by the HVS-PD. The frequency responses of the HVS-PD are measured by a vector network analyzer (Keysight ENA Network Analyzer E5080A that operates from 9 kHz to 4.5 GHz) configured in a dual-channel setup. One channel is connected to the ultraviolet LED via a voltage bias module,

while the other is directly connected with the HVS-PD. A constant DC bias of 5 mA is applied to the ultraviolet LED. The DC bias signal and the low-power test signal from the vector network analyzer are superimposed on the ultraviolet LED and converted into an optical signal. The optical signal is subsequently captured by the HVS-PD, converted into an electrical signal, and then routed to the channel of the vector network analyzer.

To directly investigate the impact of PD quantity in series on device bandwidth, the frequency responses varying with different numbers of PDs are normalized as shown in Fig. 4b. The 3 dB bandwidth value of each group is marked. The relationship curve between the 3 dB bandwidth and the quantity of PDs in series is obtained in Fig. 4c. It can be found that the 3 dB bandwidth of the device increases with an increasing number of low-power PDs in series. This phenomenon can be attributed to the decrease in capacitance due to the increasing number of PDs connected in series. Furthermore, since the HVS-PD is connected to a high-impedance measurement device, the impact of reduced capacitance outweighs the influence of increased resistance.

An oscilloscope (Keysight DSOS604A) is used to further validate the received signal quality. An ultraviolet LED serves as the light source while the GaN MQW diode array functions as the HVS-PD. The functional signal generator (Keysight 33600A Series, Trueform) is in a dual-channel mode. One channel of the functional signal generator is dedicated to driving the ultraviolet LED, ensuring stable optical signal generation. The other channel transmits a PRBS signal at a bit rate of 1 Mbit/s directly to the oscilloscope for reference and synchronization. The HVS-PD receives and converts the optical signal from the ultraviolet LED into an electrical signal. The electrical signal is amplified to enhance its clarity and signal-to-noise ratio, and then routed to the second channel of the oscilloscope for detailed visualization and analysis of the received signal quality.

The eye diagrams of the communication signals obtained by five PDs and 29 PDs in series are illustrated in Figs. 4d and 4e, respectively. Waveform I is the transmitted signal obtained by the oscilloscope directly connected to the signal generator, waveform II is the received signal detected through the optical communication link, and picture III is the corresponding eye diagram of the received signal. It can be observed that the amplitude of the received signal exhibits an upward trend as the number of PDs increases. Moreover, when operating with five PDs to capture a communication bit rate of 1 Mbit/s, the eye diagram exhibits noticeable noise and jitter. By connecting 29 PDs in series, the reliability of the transmission is enhanced, as evidenced by an increase in the relative amplitude of the eye-opening within the eye diagram. Furthermore, the enlargement of the eye width is indicative of a decrease in jitter, which enhances signal stability and transmission quality. The experimental findings validate improved communication performance of HVS-PD.



▲ Figure 4. Communication performance of HVS-PD: (a) the communication test system; (b) frequency response curves for different numbers of PDs in series with the ultraviolet LED under an injection current of 5 mA; (c) 3 dB bandwidth versus PD quantity in series after normalization; (d - e) waveform I shows transmission signal curves, waveform II received signal curves, and picture III eye diagrams with a PRBS wave at 1 Mbit/s applied to the device when (d) five PDs or (e) 29 PDs are connected in series

5 Conclusions

In this paper, an HVS-LED/PD based on a GaN-integrated photoelectronic chip is designed, and the communication performance of the device is characterized. Experimental results show that the series configuration of GaN MQW diodes significantly enhances output optical power while effectively addressing current spreading issues that may compromise device efficiency. Moreover, as more GaN MQW diodes are connected in series, the 3 dB bandwidth broadens, resulting in a clearer eye diagram. This diagram demonstrates significant

stability and reduced jitter, thereby reflecting an enhancement in communication quality. Moreover, it is expected that the HVS-LED/PD will facilitate potential applications in advanced VLC systems.

References

- [1] TAKI T, STRASSBURG M. Review—visible LEDs: more than efficient light [J]. *ECS journal of solid state science and technology*, 2019, 9(1): 015017. DOI: 10.1149/2.0402001jss
- [2] SHEN H B, CAO W R, SHEWMON N T, et al. High-efficiency, low turn-

- on voltage blue-violet quantum-dot-based light-emitting diodes [J]. *Nano letters*, 2015, 15(2): 1211 – 1216. DOI: 10.1021/nl504328f
- [3] CHANG Y H, HSU T C, LIOU F J, et al. High-bandwidth InGaN/GaN semipolar micro-LED acting as a fast photodetector for visible light communications [J]. *Optics express*, 2021, 29(23): 37245 – 37252. DOI: 10.1364/OE.439990
- [4] TSAO J Y, CRAWFORD M H, COLTRIN M E, et al. Toward smart and ultra-efficient solid-state lighting [J]. *Advanced optical materials*, 2014, 2(9): 809 – 836. DOI: 10.1002/adom.201400131
- [5] KRAMES M R, SHCHEKIN O B, MUELLER-MACH R, et al. Status and future of high-power light-emitting diodes for solid-state lighting [J]. *Journal of display technology*, 2007, 3(2): 160 – 175. DOI: 10.1109/JDT.2007.895339
- [6] MERAJ M, RAHMAN S, IQBAL A, et al. High brightness and high voltage dimmable LED driver for advanced lighting system [J]. *IEEE access*, 2019, 7: 95643 – 95652. DOI: 10.1109/ACCESS.2019.2928859
- [7] HUANG Y, GUO Z Y, WANG X J, et al. GaN-based high-response frequency and high-optical power matrix micro-LED for visible light communication [J]. *IEEE electron device letters*, 2020, 41(10): 1536 – 1539. DOI: 10.1109/LED.2020.3021282
- [8] KOMINE T, NAKAGAWA M. Integrated system of white LED visible-light communication and power-line communication [C]//Proc. 13th IEEE International Symposium on Personal, Indoor and Mobile Radio Communications. IEEE, 2002: 1762 – 1766. DOI: 10.1109/PIMRC.2002.1045482
- [9] ARVANITAKIS G N, BIAN R, MCKENDRY J J D, et al. Gb/s underwater wireless optical communications using series-connected GaN micro-LED arrays [J]. *IEEE photonics journal*, 2020, 12(2): 7901210. DOI: 10.1109/JPHOT.2019.2959656
- [10] CHU J T, HUANG H W, KAO C C, et al. Fabrication of large-area GaN-based light-emitting diodes on Cu substrate [J]. *Japanese journal of applied physics*, 2005, 44(4S): 2509. DOI: 10.1143/jjap.44.2509
- [11] ZHENG R S, TAGUCHI T. Optical design of large-area GaN-based LEDs [C]//Proc. Light-Emitting Diodes: Research, Manufacturing, and Applications VII. SPIE, 2003: 105 – 112. DOI: 10.1117/12.476554
- [12] AVRUTIN V, HAFIZ S A, ZHANG F, et al. Saga of efficiency degradation at high injection in InGaN light emitting diodes [J]. *Turkish journal of physics*, 2014, 38: 269 – 313. DOI: 10.3906/fiz-1407-23
- [13] ZHAN T, ZHANG Y, MA J, et al. Characteristics of GaN-based high-voltage LEDs compared to traditional high power LEDs [J]. *IEEE photonics technology letters*, 2013, 25(9): 844 – 847. DOI: 10.1109/LPT.2013.2251878
- [14] FAN Z Y, LIN J Y, JIANG H X. III-nitride micro-emitter arrays: development and applications [J]. *Journal of physics D: applied physics*, 2008, 41(9): 094001. DOI: 10.1088/0022-3727/41/9/094001
- [15] ZHAN T, ZHANG Y, LI J, et al. The design and fabrication of a GaN-based monolithic light-emitting diode array [J]. *Journal of semiconductors*, 2013, 34(9): 094010. DOI: 10.1088/1674-4926/34/9/094010
- [16] FAN X, GUO W L, SUN J. Reliability of high-voltage GaN-based light-emitting diodes [J]. *IEEE transactions on device and materials reliability*, 2019, 19(2): 402 – 408. DOI: 10.1109/TDMR.2019.2917005
- [17] ZHANG Y B, XU J W, DING M D, et al. Wafer-level light emitting diode (WL-LED) chip simplified package for very-high power solid-state lighting (SSL) source [J]. *IEEE electron device letters*, 2016, 37(2): 197 – 200. DOI: 10.1109/LED.2015.2509462
- [18] CHEN Z H, ZHANG Q, WANG K, et al. Reliability test and failure analysis of high power LED packages [J]. *Journal of semiconductors*, 2011, 32(1): 014007. DOI: 10.1088/1674-4926/32/1/014007
- [19] WANG C H, LIN D W, LEE C Y, et al. Efficiency and droop improvement in GaN-based high-voltage light-emitting diodes [J]. *IEEE electron device letters*, 2011, 32(8): 1098 – 1100. DOI: 10.1109/LED.2011.2153176
- [20] TIEN C H, CHEN K Y, HSU C P, et al. Enhanced light output power of thin film GaN-based high voltage light-emitting diodes [J]. *Optics express*, 2014, 22(S6): A1462. DOI: 10.1364/oe.22.0a1462
- [21] ZHOU S J, ZHENG C J, LV J J, et al. Effect of profile and size of isolation trench on the optical and electrical performance of GaN-based high-voltage LEDs [J]. *Applied surface science*, 2016, 366: 299 – 303. DOI: 10.1016/j.apsusc.2016.01.068
- [22] ZHOU S J, YUAN S, LIU Y C, et al. Highly efficient and reliable high power LEDs with patterned sapphire substrate and strip-shaped distributed current blocking layer [J]. *Applied surface science*, 2015, 355: 1013 – 1019. DOI: 10.1016/j.apsusc.2015.07.194
- [23] KORNIENKO V, KRISTENSSON E, EHN A, et al. Beyond MHz image recordings using LEDs and the FRAME concept [J]. *Scientific reports*, 2020, 10(1): 16650. DOI: 10.1038/s41598-020-73738-1
- [24] O'HAGAN W J, MCKENNA M, SHERRINGTON D C, et al. MHz LED source for nanosecond fluorescence sensing [J]. *Measurement science and technology*, 2002, 13(1): 84 – 91. DOI: 10.1088/0957-0233/13/1/311
- [25] LI X, HAN M Y, CHEN M P, et al. Integrated sensing and communication chip based on III-nitride for motion detection [J]. *ACS omega*, 2023, 8(16): 14656 – 14661. DOI: 10.1021/acsomega.3c00521
- [26] WANG Y J, GAO Y, WANG L L, et al. Underwater blue light communication using vertical-structure GaN light emitting diode [J]. *Journal of electronics and information technology*, 2022, 44(8): 2703 – 2709. DOI: 10.11999/JEIT220328
- [27] JAMES SINGH K, HUANG Y M, AHMED T, et al. Micro-LED as a promising candidate for high-speed visible light communication [J]. *Applied sciences*, 2020, 10(20): 7384. DOI: 10.3390/app10207384

Biographies

LU Meixin is an undergraduate at the School of Communication and Information Engineering, Nanjing University of Posts and Telecommunications, China. Her research focuses on sensors, GaN-based optoelectronic devices, and visible light communications systems.

JIANG Zitong is an undergraduate at the School of Communication and Information Engineering, Nanjing University of Posts and Telecommunications, China. Her research focuses on quantum sensing technology, strong magnetic field measurement, and visible light communications systems.

FANG Li received his BS degree in electronic information engineering from Qingdao University of Technology, China in 2022. He is currently pursuing an MS degree in electronic information with the Nanjing University of Posts and Telecommunications, China. His current research interests include GaN-based optoelectronic devices, optoelectronic integrated circuit (OEIC), thermoelectric/photoelectric energy harvesters, and RF MEMS devices.

YAN Yiqun received her BS degree in communication engineering from Qingdao University of Technology, China in 2023. She is currently pursuing an MS degree in electronic information with the Nanjing University of Posts and Telecommunications, China. Her current research interests include GaN-based optoelectronic devices, acoustic sensors, and photoelectric energy harvesters.

YAN Jiabin (jbyan@njupt.edu.cn) received his BS degree in microelectronics from Shanghai University, China and PhD degree in microelectronics and solid state electronics from Southeast University, China in 2013 and 2018, respectively. He is currently an associate professor with the Peter Grünberg Research Center, Nanjing University of Posts and Telecommunications, China. The discipline of his research focuses on GaN-based optoelectronic devices, optoelectronic integrated circuit (OEIC), thermoelectric/photoelectric energy harvesters, and RF MEMS devices.



Multi-View Structured Light 3D Measurement System

LU Ping¹, ZHANG Yingjie², DENG Fangwei¹, LIU Wei², HUANG Shijun¹

(1. ZTE Corporation, Shenzhen 518057, China;
2. Southern University of Science and Technology, Shenzhen 513000, China)

DOI: 10.12142/ZTECOM.202404008

<https://kns.cnki.net/kcms/detail/34.1294.tn.20241105.1427.004.html>,
published online November 6, 2024

Manuscript received: 2023–10–22

Abstract: Vision-based measurement technology benefits high-quality manufacturers through improved dimensional precision, enhanced geometric tolerance, and increased product yield. The monocular 3D structured light visual sensing method is popular for detecting online parts since it can reach micron-meter depth accuracy. However, the line-of-sight requirement of a single viewpoint vision system often fails when hiding occurs due to the object's surface structure, such as edges, slopes, and holes. To address this issue, a multi-view 3D structured light vision system is proposed in this paper to achieve high accuracy, i.e., Z-direction repeatability, and reduce hiding probability during mechanical dimension measurement. The main contribution of this paper includes the use of industrial cameras with high resolution and high frame rates to achieve high-precision 3D reconstruction. Moreover, a multi-wavelength (heterodyne) phase expansion method is employed for high-precision phase calculation. By leveraging multiple industrial cameras, the system overcomes field of view occlusions, thereby broadening the 3D reconstruction field of view. Finally, the system achieves a Z-axis repetition accuracy of 0.48 μm .

Keywords: 3D measurement; structured light; multi-view

Citation (Format 1): LU P, ZHANG Y J, DENG F W, et al. Multi-view structured light 3D measurement system [J]. *ZTE Communications*, 2024, 22(4): 53 – 58. DOI: 10.12142/ZTECOM.202404008

Citation (Format 2): P. Lu, Y. J. Zhang, F. W. Deng, et al., "Multi-view structured light 3D measurement system," *ZTE Communications*, vol. 22, no. 4, pp. 53 – 58, Dec. 2024. doi: 10.12142/ZTECOM.202404008.

1 Introduction

Efficient quality inspection of workpieces plays an important role in manufacturing. Thus, there is a growing demand for full-featured quality inspection methods. Traditionally, the primary quality inspection method used in manufacturing is 2D machine vision, which relies on industrial cameras and computer vision algorithms. This method has been beneficial in past years due to its elemental precision and effectiveness for various production tasks. However, 2D machine vision is increasingly inadequate for achieving higher production efficiency in the context of rapid advancements in intelligent manufacturing. 2D machine vision can only inspect the two-dimensional aspects of workpieces, such as length, width, and radius. These measurements alone are insufficient for evaluating more complex workpieces. In today's global economy, quality inspection increasingly requires

capabilities such as hole detection and elevation measurement. As the focus shifts from 2D to 3D, the assessment scale expands significantly. Therefore, machine vision now plays a crucial role in quality inspection.

Traditional machine vision technology based on 2D image processing has revolutionized industrial production, manufacturing processes, product testing, and other fields. However, intelligent manufacturing imposes higher requirements for machine vision technology. Traditional 2D machine vision is susceptible to light conditions, cannot measure the three-dimensional dimensions of space, and relies on manually adding input parameters, which are inadequate for the further development of intelligent manufacturing. In contrast, 3D vision^[1] can measure flatness, angles, position, and other three-dimensional dimensions, making it the trend for automatic detection in intelligent manufacturing.

2 Recent Research on Structured Light Measurement

There has been extensive research on 3D shape measurement based on structured light. In the industrial field, products like the KEYENCE LJ8000 series and LMI 2600 series

This work was supported by the 2023 Guangdong Basic and Applied Basic Research Fund Regional Joint Fund Key Project under Grant No. 2023B1515120017, 2023 Key Project of Guangdong Provincial Department of Education for General Universities under Grant No. 2023ZDZX3024, and ZTE Industry-University-Institute Cooperation Funds under Grant No. K2133Z167.

utilize line laser profile meters. These systems require highly precise moving equipment to achieve accurate regional dimensional measurements. However, the limitation of the angles of incident and reflected light can lead to occlusions and the missing point cloud, particularly with workpieces that have stairs and height differences. To address these issues, different movements and angles are necessary, but this often results in decreased precision with longer working distances and wider line widths. These products generally have an accuracy of a few microns.

Recent research has been conducted to improve the efficiency of 3D machine vision measurement. A temporally encoded structured light system was used to obtain accurate 3D measurements^[2]. This system took into account lens distortion in both the camera and projector, which are key components of the structured system. The proposed method could achieve an average measurement error of approximately 1 mm. Additionally, a multi-view structured light system has gained attention. A stereo vision method for 3D measurement method was proposed to develop an automatic measurement system, which enhanced measurement accuracy to about 0.1 mm^[3]. One study suggested grouping two arbitrary cameras into a single system, allowing each group to generate data into a universal coordinate^[4]. This approach further improved the measurement accuracy to around 0.02 mm. Moreover, binary defocusing technology has been used in 3D structured light measurement to accelerate the process. An improved method that combines 1D and 2D fringe modulations was introduced, helping to improve both efficiency and accuracy^[5]. This method can reduce measurement errors by 16.9%.

From the research results above, we can find that there is no proven technique for 3D machine vision shape measurement at the microns level^[6]. The best-achieved precision in 3D machine vision technology remains about 1 micron, with no further breakthroughs reported^[7-8]. The current mainstream solution to machine vision uses mono or stereo cameras to reconstruct the surface. However, there is still an empty area in the multi-camera for structured light to solve the larger measurement view. Besides, it is necessary to speed up the reconstruction to adapt to the production task.

This work focuses on high-precision 3D machine vision measurement using a multi-lens structured light system, alongside optimizing the point cloud reconstruction algorithm for experimental demonstration.

For the multi-lens structured light system, calibration accuracy greatly determines and affects the system's accuracy during 3D measurement. Therefore, achieving high-precision system calibration is a key challenge for the system designed in this project. In addition, processing the large amounts of data obtained from high-resolution cameras poses difficulties. The data must be filtered to remove environmental noise and redundant information, which is essential for improving processing speed while maintaining measurement accuracy. Further-

more, enhancing detection speed and efficiency is necessary to meet the demands of industrial production.

The monocular structured light and passive optical measurement schemes mentioned above are greatly affected by the interference of ambient light. The visual field of the monocular vision measurement system can be easily blocked by irregular objects. In scenarios involving high drops, there can be issues such as violent data jumps. Improvements are necessary to meet the measurement requirements for real time, high efficiency, and high precision in the 3C electronics manufacturing industry, particularly for electronic chips and precision electronic components, as well as for packaging chips and printed circuit boards (PCBs) made of materials like plastics, ceramics, and glass with low reflectivity. The proposed method has the following improvements:

1) We use a four-mesh high-resolution camera to generate multi-view images, which ensures data processing speed and partially addresses the occlusion problem. Our algorithm can also be used to optimize data redundancy and information overlap.

2) We adopt a high-resolution blue-ray projection module with a 459 nm wavelength to minimize ambient light interference and provide a high-brightness measurement light source for the structured light measurement system.

3) We utilize a sinusoidal grating coding scheme with multi-frequency heterodyne and a four-step phase shift method to unwrap the sinusoidal phase, avoiding phase calculation errors caused by binarization and increasing the system's robustness against surface texture interference.

3 Methods

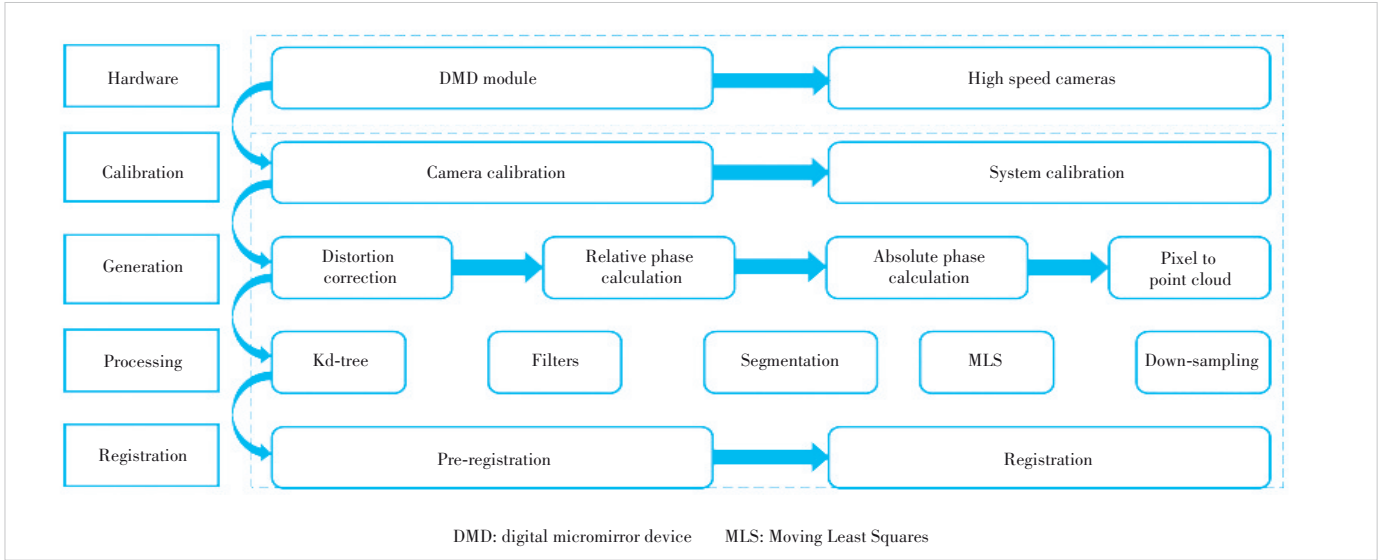
To realize the high speed and high accuracy of 3D measurement, a system that combines high-resolution cameras with projector modules is proposed in this paper. Multi-cameras in this system use the redundancy of point cloud data from individual structured light systems to enhance accuracy. The multi-camera setup can also fill the missing area obscured by workpieces in a single structured light system.

In this section, we introduce sequential projection and other post-processing methods. Fig. 1 describes the flowchart of the system setup from hardware to algorithms.

3.1 Sequential Projection

The measurement techniques include sequential projections, continuously varying patterns, and others. Compared to other techniques^[9], sequential projections have higher accuracy than some alternative methods. However, they need to project a sequence of patterns, which requires the objects under test to be stabilized for better measurement results. Sequential projections can be categorized into different types, including binary codes, gray codes, and phase shifts. The primary focus of this work is the phase shift method^[10].

The phase shift method uses a set of sinusoidal patterns to



▲ Figure 1. Proposed system setup formed by hardware and software

facilitate 3D reconstruction. The intensities for each pixel (x, y) of the three projected fringe patterns are described as follows:

$$I_1(x, y) = I_0(x, y) + I_{\text{mod}}(x, y) \cos(\varphi(x, y) - \vartheta), \quad (1)$$

$$I_2(x, y) = I_0(x, y) + I_{\text{mod}}(x, y) \cos(\varphi(x, y)), \quad (2)$$

$$I_3(x, y) = I_0(x, y) + I_{\text{mod}}(x, y) \cos(\varphi(x, y) + \vartheta), \quad (3)$$

where $I_1(x, y)$, $I_2(x, y)$ and $I_3(x, y)$ are the intensities of three fringe patterns. $I_0(x, y)$ is the direct current (DC) component (background), $I_{\text{mod}}(x, y)$ is the modulation signal amplitude, $\varphi(x, y)$ is the phase, and ϑ is the constant phase-shift angle.

Phase expansion converts the wrapped phase to the absolute phase. The phase information $\varphi(x, y)$ can be retrieved from the intensity in the three patterns^[11]:

$$\varphi' = \arctan \left[\sqrt{3} \frac{I_1(x, y) - I_3(x, y)}{2I_2(x, y) - I_1(x, y) - I_3(x, y)} \right]. \quad (4)$$

3.2 Improved Calibration Methods

In terms of calibration methods, the mainstream is to use ZHANG's method^[12] because of its simplicity and robustness. However, this method also has its disadvantages. In a structured light system calibration process, the projected patterns are used to boost calibration. The chessboard calibration board is always used to extract the corners. However, if the boards are covered with sinusoidal patterns, accurately extracting these corners becomes challenging due to interference from the patterns. To address this issue, an improved calibra-

tion method uses a circle calibration board instead of a chessboard. This approach allows for clearer separation of the circle points from the background, facilitating easier extraction of the corner points regardless of the existence of projected patterns. Fig. 2 shows that the circle calibration board outperforms the chessboard calibration board in terms of reprojected errors of the extracted corners. We can see that the black-and-white chessboard calibration board in Fig. 2 has the highest phase change, while the circle calibration board shows the lowest phase change (the ideal phase is constant in a single line).

3.3 Point Cloud Processing Algorithm

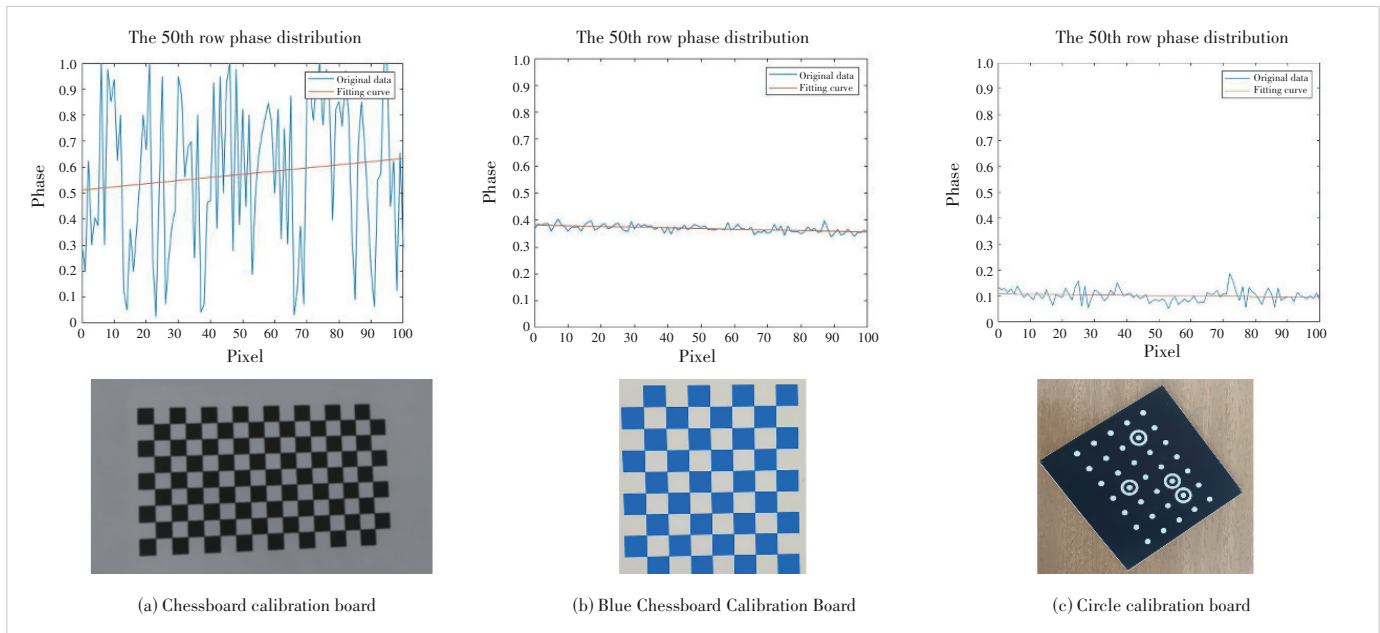
After generating the point clouds, processing methods and algorithms are more important in the industrial field. In the context of this work, the coplanarity calculation method is proposed.

During the PCB production process, sometimes the pins on PCBs may be skewed due to human disturbance or assembly errors. Therefore, it is important to find out whether the pins are vertical or not. To find the coplanarity of the pins on the PCBs, the analysis software should locate the top surfaces of the pins. The plane formulations are obtained by fitting the points of the top surfaces with the random sampling and consensus (RANSAC) algorithm or the least mean square method. All pins' surface plane formulations can calculate the distances between each other. The difference between the maximum and minimum distances represents coplanarity, which indicates the fluctuation of pins.

4 Experiments

4.1 Hardware System Setup

To realize the high resolution and high measurement frequency in 3D reconstruction, the camera performance must be



▲ Figure 2. Different calibration board’s phase distribution

reliable. Therefore, we chose four Basler CoaXPress 2.0 boA5320-150cm cameras (each with a resolution of 16 MP) and the DLP4710 module with a resolution of 1080P for projection. In this way, the DLP module can achieve a frequency of up to 120 Hz for projected patterns, enabling the camera to capture frames immediately as they are projected. This hardware selection helps to enhance the system’s performance.

In the real measurement situation, the objects under test are about 6 cm×9 cm. To make the cameras’ view cover the object, the overlapped field of view must be larger than the object itself. This allows the four cameras to capture the images of the object. We designed a multi-camera system and used SolidWorks to simulate the overlapped field of view to find the optimal measurement. The 3D module and simulated results are shown in Fig. 3.

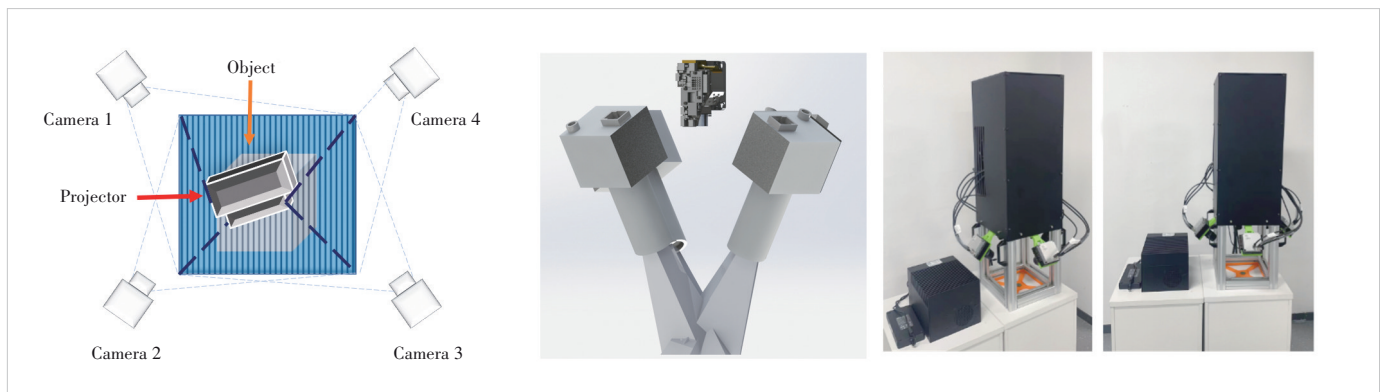
4.2 System Workflow

The main workflow of this work is shown in Fig. 4. Once the

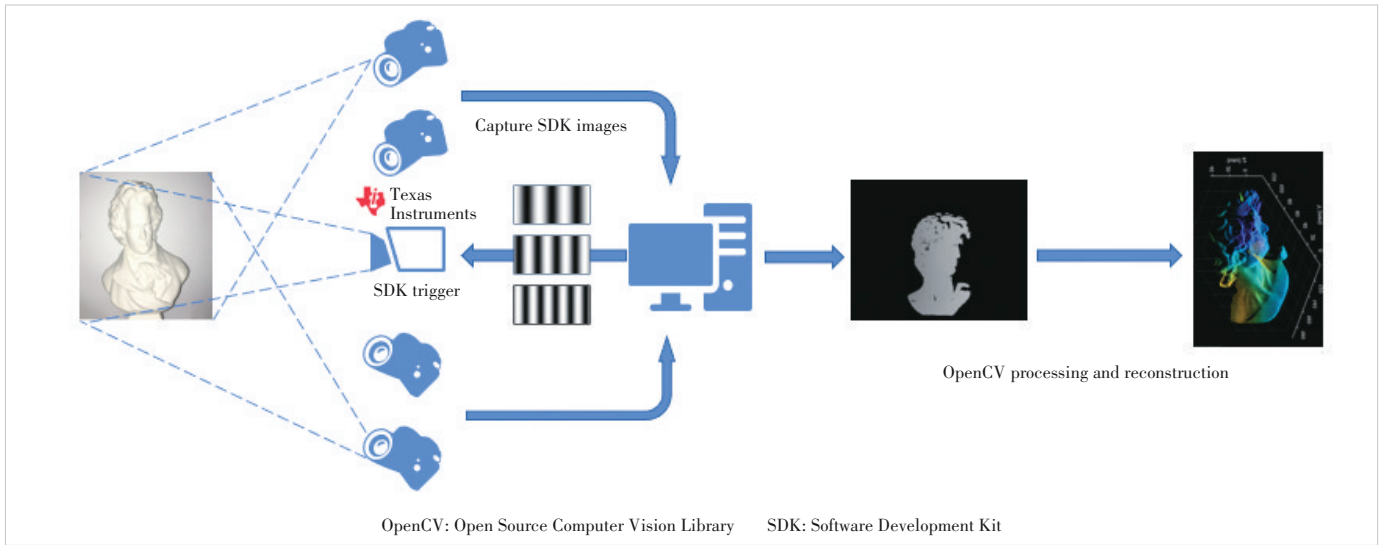
tested object is placed within the view field of the system, the PC is triggered to execute the measurement program. The projector projects a set of sequential sinusoidal patterns and triggers the cameras simultaneously. The triggered cameras capture the images and transmit them to PC for further processing. Using calibration parameters and processed images, the PC reconstructs the test object in the form of point clouds.

4.3 Experiment Results

Table 1 shows the experiment results with different workpieces, which contains the DIY PCB (PCB 1), the actual power supply module (PCB 2), and other test samples. The results were compared to the coordinate measuring machine (CMM) and the Mega Phase 3D structured light camera M051090, and the measurements from CMM were compared to the real values. The experiment demonstrated that with our equipment, the repeatability error calculated using Root Mean Square (RMS) reached 0.001 mm in actual measurements, and



▲ Figure 3. Hardware setup for the experiments



▲ Figure 4. Workflow of the proposed multi-view 3D structured light vision system

▼ Table 1. Different tested objects and their measurement results

Tested Objects	Our Method/mm	Our Method RMS/mm	CMM/mm	CMM RMS/mm	M051090/mm	M051090 RMS/mm
Cellphone middle frame	0.446 5	0.001 53	0.454 0	0.000 82	0.447 1	0.001 85
	0.444 7		0.455 2		0.448 4	
	0.445 0		0.453 4		0.447 8	
	0.444 3		0.453 4		0.446 3	
	0.448 0		0.453 2		0.447 9	
Ceramic ball	19.993 4	0.000 15	20.004 5	0.000 04	20.014 5	0.000 31
	19.993 7		20.004 5		20.015 6	
	19.993 6		20.004 6		20.015 3	
	19.993 8		20.004 5		20.016 1	
	19.993 6		20.004 5		20.016 4	
PCB 1	7.226 2	0.015 15	7.258 8	0.007 81	7.296 6	0.017 21
	7.259 2		7.263 0		7.272 4	
	7.238 2		7.257 2		7.282 8	
	7.228 0		7.274 5		7.299 8	
PCB 2	7.304 9	0.040 76	7.302 8	0.030 59	7.328 9	0.044 17
	7.259 2		7.326 0		7.381 2	
	7.311 9		7.372 9		7.398 9	
	7.358 8		7.352 4		7.415 9	

CMM: Coordinate Measuring Machine PCB: Printed Circuit Board RMS: Root Mean Square

the absolute error reached 0.01 mm, which is more accurate than the measurements from M051090.

As shown in Table 1, the proposed system performs well in real industrial situations, and the RMS error is reliable and stable compared to the results from CMM.

5 Conclusions

The proposed system uses high-speed cameras and high-frequency projectors to achieve high accuracy in 3D recon-

struction and measurement. The experiment results show that the system's repeatability and accuracy meet the requirements of real manufacturing situations when compared to the CMM and M051090. The proposed system works out the accuracy problem in the 3C industrial field and provides insights when measuring irregularly shaped objects using multiple camera systems.

In future, the proposed system can be further improved into a more integrated form and the cameras' view can be enlarged

by switching to wider-view lens. Moreover, the system aims to become more autonomous for industrial applications.

Reference

- [1] HOCKEN R J, PEREIRA P H. Coordinate measuring machines and systems, second edition [M]. Boca Raton: CRC Press, 2011
- [2] KUNZMANN H, TRAPET E, WÄLDELE F. A uniform concept for calibration, acceptance test, and periodic inspection of coordinate measuring machines using reference objects [J]. CIRP annals, 1990, 39(1): 561 - 564. DOI: 10.1016/s0007-8506(07)61119-6
- [3] EI-HAKIM S F, BERALDIN J A, BLAIS F. Comparative evaluation of the performance of passive and active 3D vision systems [C]//Digital Photogrammetry and Remote Sensing'95. SPIE, 1995: 14 - 25. DOI: 10.1117/12.227862
- [4] VILAÇA J L, FONSECA J C, PINHO A M. Calibration procedure for 3D measurement systems using two cameras and a laser line [J]. Optics & laser technology, 2009, 41(2): 112 - 119. DOI: 10.1016/j.optlastec.2008.05.012
- [5] GENG J. Structured-light 3D surface imaging: a tutorial [J]. Advances in optics and photonics, 2011, 3(2): 128. DOI: 10.1364/aop.3.000128
- [6] MOTTA J M S T, DE CARVALHO G C, MCMASTER R S. Robot calibration using a 3D vision-based measurement system with a single camera [J]. Robotics and computer-integrated manufacturing, 2001, 17(6): 487 - 497. DOI: 10.1016/s0736-5845(01)00024-2
- [7] GALLUCCI A, ZNAMENSKIY D, PETKOVIC M. Prediction of 3D body parts from face shape and anthropometric measurements [J]. Journal of image and graphics, 2020, 8(3): 67 - 77. DOI: 10.18178/joig.8.3.67-74
- [8] FURUNO T, FUJITA S, WANG D H, et al. 3D bow and posture measurements for virtual reality customer service training system [J]. Journal of image and graphics, 2021, 9(4): 152 - 156. DOI: 10.18178/joig.9.4.152-156
- [9] AILANI V, PRAKASH D, VENKATESH K S. Self localization with edge detection in 3D space [J]. Journal of image and graphics, 2013, 1(2): 99 - 103. DOI: 10.12720/joig.1.2.99-103
- [10] LEE H M, CHOI W C. Algorithm of 3D spatial coordinates measurement using a camera image [J]. Journal of image and graphics, 2015, 3(1): 30 - 33. DOI: 10.18178/joig.3.1.30-33
- [11] HU H H, GAO J, ZHOU H Y, et al. A combined binary defocusing technique with multi-frequency phase error compensation in 3D shape measurement [J]. Optics and lasers in engineering, 2020, 124: 105806. DOI: 10.1016/j.optlaseng.2019.105806
- [12] ZHANG Z. A flexible new technique for camera calibration [J]. IEEE transactions on pattern analysis and machine intelligence, 2000, 22(11): 1330 - 1334. DOI: 10.1109/34.888718

Biographies

LU Ping is the deputy president of ZTE Corporation, where he is also the general manager of the Industrial Digitalization Solution Dept., and the executive deputy director of State Key Laboratory of Mobile Network and Mobile Multimedia Technology. His research interests include cloud computing, big data, augmented reality, and multimedia service-based technologies. He has supported and participated in multiple major national science and technology projects and national science and technology support projects. He has published multiple papers and authored two books.

ZHANG Yingjie is a second year graduate student at Southern University of Science and Technology, China, with research interests in machine vision and 3D structured light technology.

DENG Fangwei is the product director of the Industry Digital Solution Department of ZTE Corporation. His research direction is to provide industry digital bases and mobile robots for industrial digital transformation, as well as supporting products.

LIU Wei (liuw2@sustech.edu.cn) is a research professor with Southern University of Science and Technology, China. His research focuses on robotic perception, such as sensing, tracking, localization and navigation.

HUANG Shijun is a senior strategic planner at ZTE Corporation. His research interests include machine vision, artificial intelligence, computer vision and deep learning.



A Filtering Coaxial Probe for Passive Intermodulation Characterization

BAI Yongjiang¹, YANG Jiye¹, ZHU Shaohao²,
YANG Ye², YE Ming¹

(1. Xi'an University of Architecture and Technology, Xi'an 710055, China;
2. ZTE Corporation, Shenzhen 518057, China)

DOI: 10.12142/ZTECOM.202404009

<https://kns.cnki.net/kcms/detail/34.1294.TN.20241029.1436.002.html>,
published online October 29, 2024

Manuscript received: 2024-06-05

Abstract: Passive intermodulation (PIM) in communication systems is an unwanted interference caused by weak nonlinear current-voltage characteristics of radio frequency (RF) passive components. Characterization of PIM is important for both the study of PIM mechanisms and the location/suppression of PIM sources. PIM probes, made of open-ended coaxial transmission lines, have almost the same coupling strength to carriers and PIM products, and are usually used for near-field PIM characterization. Namely, it doesn't have any filtering capability. Therefore, it cannot stop the carrier power from entering into PIM tester's receiver, which may trigger active intermodulation of the receiver and degrade the PIM tester's performance. To overcome this drawback, a passive filtering coaxial probe is proposed here. Compared with existing passive coaxial PIM probes, it has stronger coupling strength for PIM products than for carriers. Thus, the probe itself can block part of the carrier power entering into the PIM tester's receiver. This advantage helps improve PIM tester's overall performance. Both theoretical analysis and experiments are conducted for demonstration. The proposed probe brings more possibility to PIM characterization.

Keywords: coupling gap; passive intermodulation; filtering coaxial probe

Citation (Format 1): BAI Y J, YANG J Y, ZHU S H, et al. A filtering coaxial probe for passive intermodulation characterization [J]. *ZTE Communications*, 2024, 22(4): 59 – 66. DOI: 10.12142/ZTECOM.202404009

Citation (Format 2): Y. J. Bai, J. Y. Yang, S. H. Zhu, et al., "A filtering coaxial probe for passive intermodulation characterization," *ZTE Communications*, vol. 22, no. 4, pp. 59 – 66, Dec. 2024. doi: 10.12142/ZTECOM.202404009.

1 Introduction

Passive intermodulation (PIM) refers to the new output signals generated when two or more high-power carrier signals pass through radio frequency (RF) passive components with weak nonlinear current-voltage characteristics. When PIM products fall into the frequency band of a receiver, the sensitivity of communication systems may be reduced^[1]. In recent years, due to its negative effect on mobile communications^[2], aerospace^[3], military and other fields^[4], research on PIM has attracted much attention from both industry and academia.

At present, the research on PIM mainly focuses on the physical mechanisms^[5], detection^[6-8], suppression^[9] and modeling^[10]. The physical mechanisms of PIM include material nonlinearity and contact nonlinearity. Due to its complexity, the physics behind PIM behavior of RF components/systems is not yet well understood, and thus, it is not easy to model PIM quantitatively. So, the PIM tester is an indispensable diagnostic tool for PIM researchers/engineers.

Regarding PIM measurement, PIM includes conducted PIM (e.g., RF connectors and cables) and radiated PIM (e.g., antennas). With the development of RF systems, some non-

conventional test methods of PIM have been proposed, such as the near-field detection method^[11], the RF cancellation method^[12] and the acoustic vibration method^[13]. Suppression of PIM is the ultimate goal of PIM research and characterization.

Near-field detection of PIM, the purpose of this work, has the potential to find out locations/sources of PIM in a real RF system which is beneficial for suppression of PIM by either hardware-based or software-based methods. For example, there may be multiple PIM sources in a complicated RF system, like a rusted/loose RF connector, or a cracked microstrip line. If one can locate the PIM source, efforts can be made to suppress it/them. To develop such a tool, many kinds of PIM probes for near-field PIM detection have been studied, including the electromagnetic probe^[11], the antenna probe^[14], the print circuit board (PCB) probe^[15], the waveguide probe^[16], etc. Each kind of PIM probes has its own pros and cons. For example, the electromagnetic probe usually has a higher spatial resolution. The antenna probe usually has relatively larger detection distance. Here, the detection distance refers to the distance between the PIM probe and the device under test (DUT). The waveguide probe in

Ref. [16] is efficient for the measurement duration since it only needs two one-dimensional scans for a two-dimensional PIM mapping result.

All of the passive and active probes mentioned above have no filtering capability. In other words, to some degree, they are wideband probes. When these probes are used for PIM location, they couple both high-level carriers and low-level PIM products. Thus, to avoid exciting the nonlinearity of PIM testers' receivers, a high-performance duplexer with stringent specifications on both the PIM level and frequency selectivity is required. For example, the out-of-band rejection of the duplexer used in a PIM test system is usually at least 100 dB.

In this paper, a passive filtering PIM probe based on a half-wavelength coaxial transmission line resonator is proposed. Theoretical analysis, electromagnetic simulation and experimental measurement are conducted to demonstrate the probes' working principle and its potential advantages over conventional passive non-filtering PIM probes. The most important difference of the proposed probe is that its coupling strength of PIM products can be higher than that of carriers. As described below, this unique characteristic is expected to be beneficial for improving PIM testers' performances such as larger dynamic range, lower requirement on components, more flexibility, and lower cost.

2 Principle and Theory

2.1 Principle of the Proposed Probe

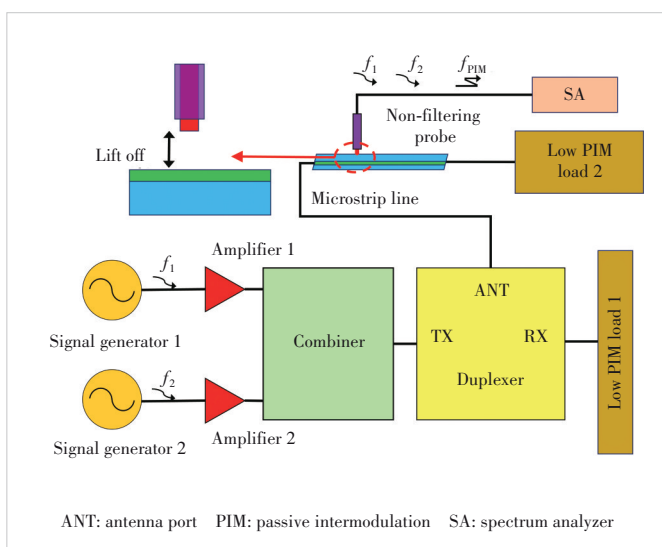
In a typical near-field PIM test system, two signal generators output two sinusoidal signals (denoted as carriers in a PIM community) with the same power but different frequencies, as shown in Fig. 1. After being amplified by power am-

plifiers (PA), the two carriers are combined to form a dual-tone and high-power excitation signal finally input into the transmit port of a low-PIM duplexer with high-performance. Then, high-power carriers output from the antenna port of the duplexer and enter into the DUT (here, a microstrip line is used for demonstration). Both the high-power carriers and the generated forward PIM of the DUT will be absorbed by the low PIM load connected with the DUT. The generated reverse PIM goes back to the antenna port of the duplexer and it can be detected at the receive port of the duplexer.

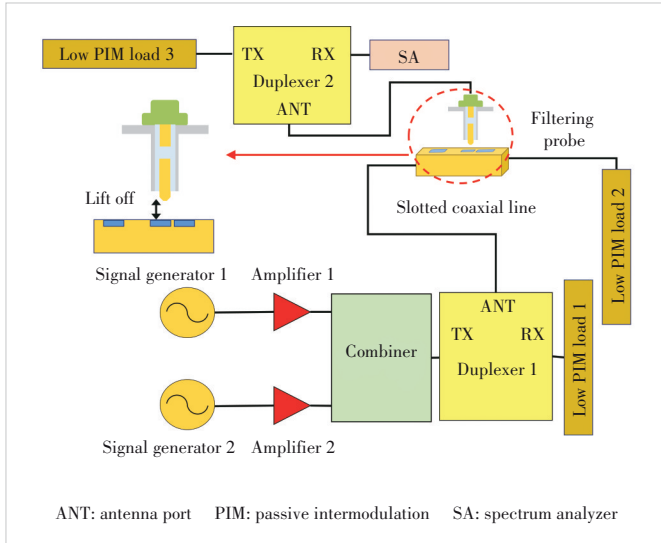
At the same time, both the carriers and the PIM products enter into the near-field PIM probe after experiencing a specific but almost the same attenuation (equal to the insertion loss between the input port of DUT and the output port of the PIM probe), which is quantitatively specified by coupling strength. Usually, coupling strength is mainly determined by the lift-off distance L_l of the PIM probe as shown in Fig. 1. Finally, all of these signals go into the receiver, represented by a spectrum analyzer (SA) here. In this conventional PIM test system, it is obvious that stronger coupling strength means lower insertion loss for both the carriers and PIM products. On one side, the former suggests lower minimum detectable PIM level; on the other side, the latter indicates higher carrier power entering into SA, which may ignite SA's nonlinearity and thus degrade the system's noise floor, increasing the minimum detectable PIM level. This trade-off limits the performance or design flexibility of the conventional PIM test system.

To overcome this trade-off, a low PIM filter/duplexer is usually added between the PIM probe and the SA to filter out the carriers. Since the carriers entering into the probe are attenuated by the added filter/duplexer, it is less likely to excite an observable intermodulation of the SA. However, due to the strong nonlinearity of SA, requirements on the filter/duplexer may be stringent. Thus, when designing a PIM tester with a conventional PIM probe, one may need to pay much attention to the specifications of the filter/duplexer as well as SA.

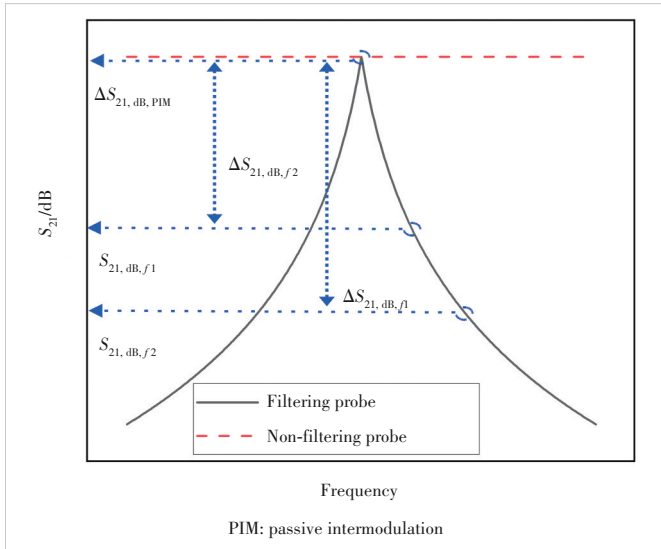
To lighten the burden of the filter/duplexer/SA in a PIM tester, a half wavelength coaxial transmission line-based PIM probe is introduced due to its filtering capability, as shown in Fig. 2. Compared with the conventional PIM probe in Fig. 1, which is made of coaxial transmission line without any frequency selectivity, the proposed probe is essentially a resonator and thus it has frequency selectivity. In detail, with proper design parameters, the proposed filtering PIM probe has a resonant peak close to the frequency of the desired PIM, as shown in Fig. 3. It should be noted that the y-axis in Fig. 3, S_{21} , represents transmission S-parameters between the input port of DUT and the port of PIM probes. The filtering PIM probe has a stronger coupling strength of PIM than that of carriers. In other words, the filtering PIM probe can block the carriers, avoiding/suppressing the excitation



▲ Figure 1. Schematic diagram of near-field PIM test systems based on a non-filtering PIM probe (usually, there is a duplexer between the probe and SA)



▲ Figure 2. Schematic diagram of the near-field PIM test system based on a filtering PIM probe



▲ Figure 3. Schematic diagram of transmission S -parameters between the input port of the device under test (DUT) and the output port of the PIM probe

of active nonlinearity of SA.

Compared with conventional probes, the advantage of the filtering PIM probe may bring the following improvements. First, carriers with higher power can be used because this increase in carrier power will be attenuated by the filtering probe. For example, suppose the acceptable output carrier power at the probe's port (this specification ensures avoiding nonlinearity of SA) is 0 dBm and the filtering probe has 10 dB larger attenuation to carriers than non-filtering probes. Then, if the PIM test system works well for non-filtering probes when carriers' power at the input port of DUT is 43 dBm, the system is expected to work well too for filtering probes when input carrier power to DUT is 53 dBm.

Second, the PIM test system equipped with filtering probes has a higher sensitivity than its non-filtering counterpart. Here, sensitivity means the measurable lowest PIM level. Suppose the noise floor of SA is -125 dBm. To ensure the stability of measurement results, the measurable lowest power of the SA is set to -115 dBm (10 dB higher than the noise floor, known as the 10 dB rule). We suppose the acceptable coupling strength of the non-filtering probe is 30 dB (stronger coupling will excite nonlinearity of SA), which indicates the sensitivity is -85 dBm. For filtering probes, as mentioned above, assuming that the filtering probe has a 10 dB larger attenuation to carriers than non-filtering probes (their attenuation at the PIM frequency is the same), the acceptable coupling strength of the filtering probe is 20 dB which indicates the sensitivity is -95 dBm, 10 dB higher than its non-filtering counterpart.

A similar analysis also shows that the PIM test system using filtering probes has lower requirements on out-of-band rejection specification of filter/duplexer and on intermodulation specifications of SA. Even more, if the filtering probe has enough frequency selectivity, it may be possible to block the carriers going into the SA absolutely and thus one can remove the filter/duplexer, which will be helpful for system integration. A thorough analysis will be detailed in the subsequent subsection.

2.2 Theoretical Analysis

Assuming that the transmission S -parameter S_{21} from the input port of DUT to the output port of PIM probes for carrier 1, carrier 2 and PIM is $S_{21,\text{dB},f1}$, $S_{21,\text{dB},f2}$ and $S_{21,\text{dB},\text{PIM}}$, respectively. The carrier power fed into the DUT is denoted as $P_{\text{dBm},c}$ (usually, carrier 1 has the same power with carrier 2). Suppose that the PIM power of the DUT $P_{\text{dBm},\text{DUT},\text{PIM}}$ can be described as:

$$P_{\text{dBm},\text{DUT},\text{PIM}} = P_{\text{dBm},0} + kP_{\text{dBm},c}, \quad (1)$$

where $P_{\text{dBm},0}$ and k are constants for a given DUT. Usually, for common passive devices, k ranges from 2 to 3. $P_{\text{dBm},0}$ is the DUT's PIM level when the applied carrier power is 0 dBm. By ignoring the insertion loss from the output port of PIM probes to the input port of SA, the carrier power for carrier 1 $P_{\text{dBm},f1}$ and carrier 2 $P_{\text{dBm},f2}$ entering into the SA should be:

$$P_{\text{dBm},f1} = P_{\text{dBm},c} + S_{21,\text{dB},f1}, \quad (2)$$

$$P_{\text{dBm},f2} = P_{\text{dBm},c} + S_{21,\text{dB},f2}. \quad (3)$$

Since $S_{21,\text{dB},f1}$ is usually different from $S_{21,\text{dB},f2}$, the carrier power going into the SA will be different. The PIM power generated by the DUT and entering into the SA $P_{\text{dBm},\text{PIM}}$ is:

$$P_{\text{dBm},\text{PIM}} = P_{\text{dBm},\text{DUT},\text{PIM}} + S_{21,\text{dB},\text{PIM}}. \quad (4)$$

As mentioned above, when dual tone carriers go into the SA, the intermodulation of the SA, $P_{\text{dBm,SA,PIM}}$, may be excited and it can be described as:

$$P_{\text{dBm,SA,PIM}} = P_{\text{dBm,1}} + k_1 P_{\text{dBm,f1}} + k_2 P_{\text{dBm,f2}}. \quad (5)$$

Similar to Eq. (1), $P_{\text{dBm,1}}$, k_1 , and k_2 are constants for a given SA. In case of the third order PIM with a lower band, $f_{\text{pim}} = 2f_1 - f_2$, $k_1 \approx 2$ and $k_2 \approx 1$.

As described above, there are two PIM products presented in SA. One is the PIM generated by DUT and coupled into SA $P_{\text{dBm,PIM}}$. The other is the PIM generated by SA, $P_{\text{dBm,SA,PIM}}$. Another factor influencing PIM tests is the noise floor of SA, $P_{\text{dBm,SA,Noise}}$. Depending on the specifications and measurement setup of SA and the input carrier power $P_{\text{dBm,f1}}$ and $P_{\text{dBm,f2}}$, $P_{\text{dBm,SA,PIM}}$ can be either higher than or lower than $P_{\text{dBm,SA,Noise}}$. Their maximum value determines the sensitivity of PIM tests. Considering that the nonlinearity of SA is more likely to be a problem in PIM tests, we assume $P_{\text{dBm,SA,PIM}} > P_{\text{dBm,SA,Noise}}$ in the following analysis. Considering the 10 dB rule, the following condition should be satisfied if one wants to obtain the accurate results of DUT's PIM:

$$P_{\text{dBm,SA,PIM}} + 10 < P_{\text{dBm,PIM}}. \quad (6)$$

Namely, the PIM level generated by DUT and coupled into SA should be at least 10 dB higher than the PIM level of SA excited by coupled carriers. By introducing Eqs. (1) – (5) into Eq. (6), we can obtain:

$$P_{\text{dBm,0}} + kP_{\text{dBm,c}} + S_{21,\text{dB,PIM}} > P_{\text{dBm,1}} + (k_1 + k_2)P_{\text{dBm,c}} + k_1 S_{21,\text{dB,f1}} + k_2 S_{21,\text{dB,f2}} + 10. \quad (7)$$

In a standard PIM test, $P_{\text{dBm,c}}$ is usually set as 43 dBm. For a given PIM test system, $P_{\text{dBm,1}}$, k_1 and k_2 are constants. For a given DUT, $P_{\text{dBm,0}}$ and k are constants. $S_{21,\text{dB,PIM}}$, $S_{21,\text{dB,f1}}$ and $S_{21,\text{dB,f2}}$ are constants related with PIM probes. They depend on both the design and the setup (e. g., lift-off distance) of the probe. We introduce $\Delta S_{21,\text{dB,f1}}$ and $\Delta S_{21,\text{dB,f2}}$ as measure of the frequency selectivity of the proposed filtering probe:

$$\begin{cases} \Delta S_{21,\text{dB,f1}} = S_{21,\text{dB,PIM}} - S_{21,\text{dB,f1}} \\ \Delta S_{21,\text{dB,f2}} = S_{21,\text{dB,PIM}} - S_{21,\text{dB,f2}} \end{cases}. \quad (8)$$

So, $\Delta S_{21,\text{dB,f1}}$ and $\Delta S_{21,\text{dB,f2}}$ represent differences of coupling strength between carriers and PIM. By introducing Eq. (8) into Eq. (7), one can obtain:

$$S_{21,\text{dB,PIM}}(1 - k_1 - k_2) > -P_{\text{dBm,0}} + P_{\text{dBm,1}} + (k_1 + k_2 - k)P_{\text{dBm,c}} + 10 - k_1 \Delta S_{21,\text{dB,f1}} - k_2 \Delta S_{21,\text{dB,f2}}. \quad (9)$$

Define $C_0 = P_{\text{dBm,1}} - P_{\text{dBm,0}} + (k_1 + k_2 - k)P_{\text{dBm,c}} + 10$, and Eq.(9) can be written as:

$$S_{21,\text{dB,PIM}} < \frac{k_1 \Delta S_{21,\text{dB,f1}} + k_2 \Delta S_{21,\text{dB,f2}} - C_0}{k_1 + k_2 - 1}. \quad (10)$$

To interpret Eq.(10), we take the third order PIM $2f_1 - f_2$ as an example to give a case study, and it can be supposed that: $P_{\text{dBm,1}} = 45$, $P_{\text{dBm,0}} = -20$, $k_1 = 2$, $k_2 = 1$, $k = 3$, and $P_{\text{dBm,c}} = 43$. Thus, Eq. (10) can be written as:

$$S_{21,\text{dB,PIM}} < \frac{2\Delta S_{21,\text{dB,f1}} + \Delta S_{21,\text{dB,f2}} - 75}{2}. \quad (11)$$

For the non-filtering probe ($\Delta S_{21,\text{dB,f1}} = \Delta S_{21,\text{dB,f2}} = 0$), Eq.(11) becomes:

$$S_{21,\text{dB,PIM}} < -37.5. \quad (12)$$

For the filtering probe, suppose $\Delta S_{21,\text{dB,f1}} = 10$, $\Delta S_{21,\text{dB,f2}} = 15$, and Eq. (11) becomes:

$$S_{21,\text{dB,PIM}} < -20. \quad (13)$$

Eqs. (12) and (13) indicate that the coupling strength of non-filtering/filtering probes should be weaker than $-37.5/-20$ dB, respectively. In other words, a filtering probe can be designed with stronger coupling strength than a non-filtering probe. So, we can conclude that a filtering probe has higher sensitivity than a non-filtering probe.

Eq. (9) can be used as a guide for designing PIM test systems. It relates the system's performance with DUT, SA/receiver, and applied carrier power. The most important point is that it shows how filtering probes' frequency selectivity interacts with systems' sensitivity. More quantitative versions of Eq. (9) can be determined after obtaining the related constants from experimental measurements.

3 Verifications and Discussions

3.1 Design and Simulation

Electromagnetic simulations are conducted to obtain an optimized design of the filtering PIM probe. The resonant frequency is mainly determined by the length of the half-wavelength coaxial transmission line resonator. The small air gap between the inner conductor of the half-wavelength resonator and the inner conductor of the feed connector determines the depth of resonant peaks. Finally, the design of a filtering probe that works around 1 800 MHz is obtained. The total length of the resonator is 68 mm. It should be noted that part of the resonator is filled with Teflon which has a relative dielectric constant ≈ 2 . This dielectric filling will make the resonator a bit shorter than an all air-filled resonator.

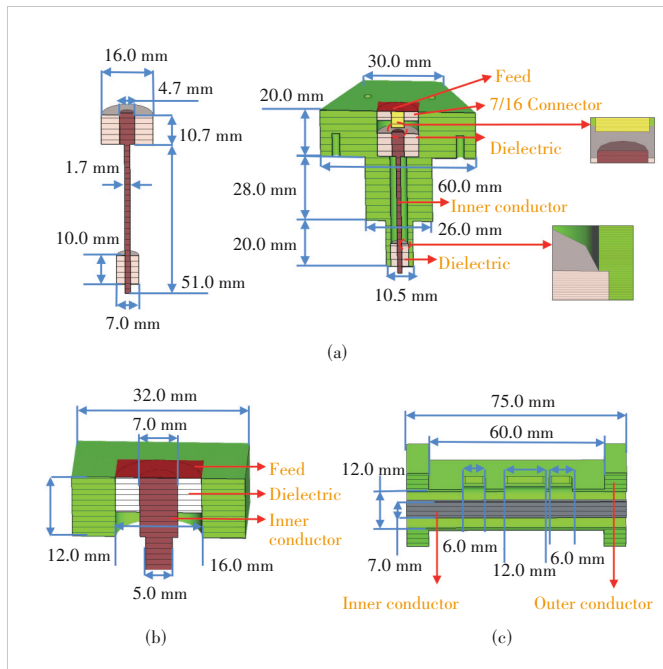
For comparison, we also simulate a commercially available RF connector (model: L29-kfd-9) as a non-filtering PIM probe. A coaxial transmission line with a perforated outer conductor is simulated as DUT. In simulation, the coupling strength of the probe can be adjusted by tuning the lift-off distance. The lift-off distance is swept from 0 to 4 mm with a step of 1 mm. The schematic view and size of the DUT and probes are shown in Fig. 4. The inner conductor of the resonator is fixed by two dielectric rings, which are fixed by the interference fit.

Compared with the non-filtering probe, as shown in Fig. 5, the filtering probe has frequency selectivity as expected. In addition, for both probes, the coupling strength increases as lift-off distance decreases. As analyzed above, this frequency selectivity is helpful to low PIM tests as well as PIM tests at high carrier power. In addition, it can be referred that the lift-off distance is an important factor in the PIM test.

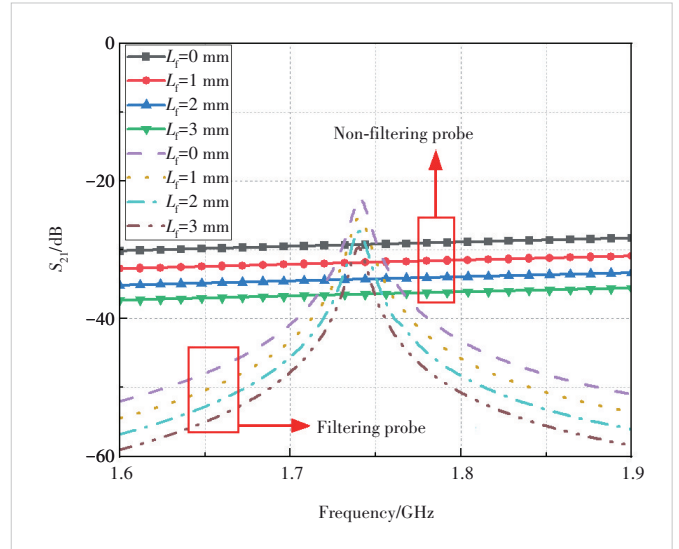
A more detailed comparison is given in Fig. 6. The difference of S_{21} in the filtering probe and non-filtering probe at the PIM frequency of 1.74 GHz is 0.2 dB. Thus, it is considered that the coupling strength of the two probes at the PIM frequency is the same. From Fig. 6, we can find that at carrier 1 (1.81 GHz), $\Delta S_{21, dB, f1} = 22.3$ dB, while at carrier 2 (1.88 GHz), $\Delta S_{21, dB, f2} = 28.9$ dB. Therefore, as for suppressing excitation of the intermodulation of SA, the filtering probe has an advantage over the non-filtering probe.

3.2 Experiments

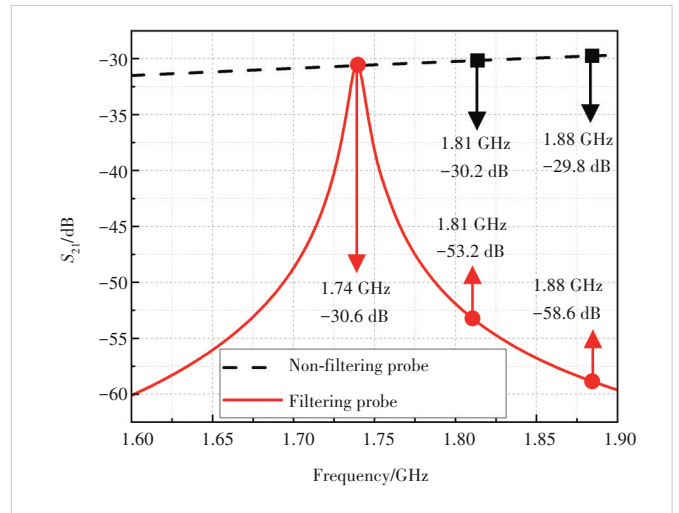
To verify the analysis/simulation mentioned above, a fil-



▲ Figure 4. Simulation model and size of (a) filtering probe, (b) non-filtering probe and (c) DUT (the DIN connector is neglected)

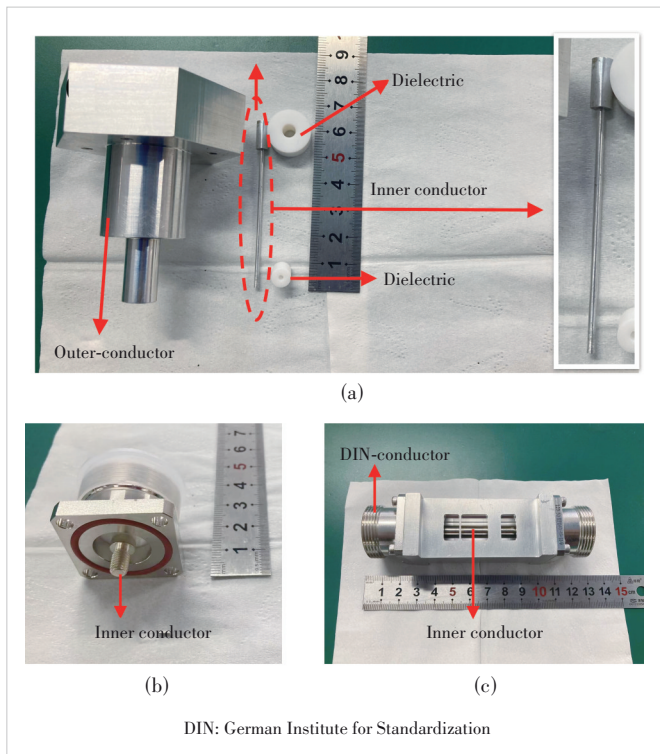


▲ Figure 5. Simulation results on transmission S_{21} between the input port of DUT and the output port of PIM probe (L_r represents lift-off distance)



▲ Figure 6. A detailed comparison of S_{21} in the filtering probe and the non-filtering probe

tering probe and a slotted coaxial line are fabricated by the standard computer numerical control (CNC) process, as shown in Fig. 7. To reduce the PIM level of the probe, it is recommended that non-magnetic metal or metallic coating (such as silver) should be used and metallic contact should be avoided. A commercially available L29-kfd-9 connector is used as a non-filtering PIM probe. A specially designed coaxial transmission line is used as DUT. The outer conductor is perforated to facilitate near-field PIM detection. The inner conductor is electroplated with a nickel of $15 \mu\text{m}$ to introduce strong nonlinearity. To accurately control the probe position, especially the lift-off distance, some mechanic setups are used. As mentioned above, the inner conductor of the filtering probe is fixed inside the probe using two Teflon dielectric rings. We have measured S_{11} of the filtering probe



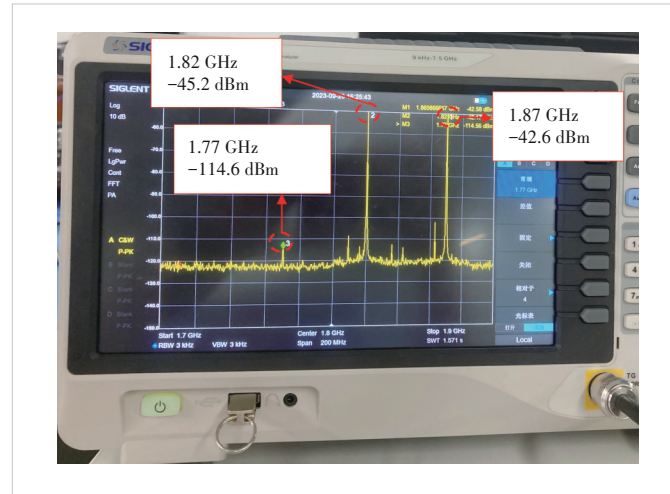
▲ Figure 7. Fabricated (a) filtering probe, (b) non-filtering probe and (c) DUT

without DUT as well as S_{21} when the probe is loaded with DUT. These measurement results show similar behavior with simulations.

Using the slotted coaxial line as DUT, a preliminary near-field PIM test was carried out using a home made PIM setup working at the DCS1800 (a digital cellular system working at 1 800 MHz) band. First of all, we measured the nonlinearity of the SA and obtained results show when the carrier power fed into SA was lower than -43 dBm, the intermodulation generated by the SA itself would not affect the PIM test, as shown in Fig. 8. It can be seen that when carrier power is about -42 dBm, the intermodulation of SA can be below -110 dBm.

Next, two groups of measurements were conducted to demonstrate the advantages of the proposed filtering probe. In both groups, the frequency of carriers 1 and 2 is 1 815 MHz and 1 870 MHz, respectively. The third-order PIM at $f_{PIM} = 1.76$ GHz is measured which equals the center frequency of the filtering probe. The lift-off distance is almost the same, namely, around 0.5 mm, for both kinds of probes. The inner conductor of DUT is brass.

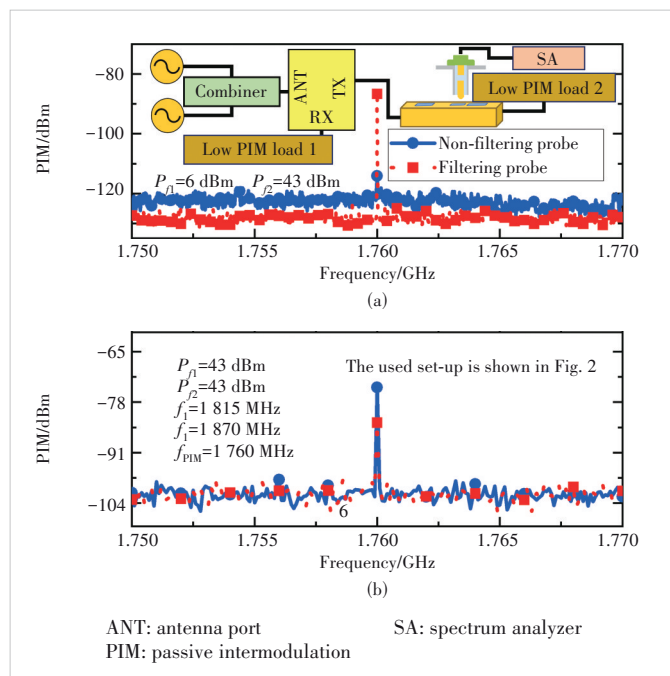
In the first group, we use a test set-up shown in Fig. 9a without the two power amplifiers, duplexer 2 or PIM load 3. Power of carriers input into the DUT is around 6 dBm (enough for exciting the intermodulation of the SA). As shown in Fig. 9a, the observed intermodulation (IM) power is around -115 dBm and -85 dBm for filtering probes and non-filtering probes, respec-



▲ Figure 8. Measurement results of the nonlinearity of the SA

tively. This means that, compared with the non-filtering probe, the power of carriers going into the SA is less for the filtering probe. In other words, compared with the non-filtering probe, the filtering probe brings about more attenuation to carriers, as described in Section 3.1.

In the second group of measurements, the used set-up is the same with the set-up shown in Fig. 2. The conductive foam with strong RF nonlinearity is placed onto the inner conductor of the perforated coaxial transmission line. At the PIM frequency, the observed coupling loss of non-filtering



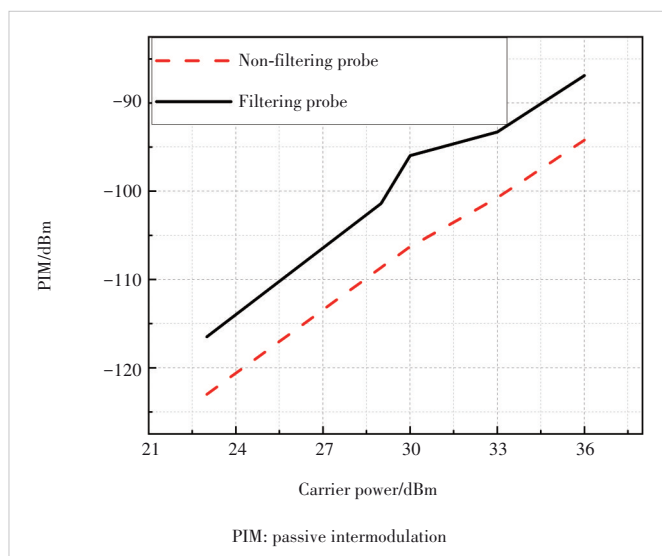
▲ Figure 9. Two groups of measurements: (a) the first group and (b) the second group

probes is higher than that of filtering probes. Thus, the directly measured PIM of the filtering probe is higher than that of the non-filtering probe, as shown in Fig. 9b. Carrier power input into DUT is set to 43 dBm. The PIM level is about -74.4 dBm for the filtering probe and about -84.5 dBm for the non-filtering probe. So, it is demonstrated that the proposed filtering probe has a stronger coupling capability to the DUT's PIM than non-filtering probes. Thus, it can be inferred that the filtering probe shows higher sensitivity or larger dynamic range than non-filtering probes.

Finally, we use the same lift-off distance for both the filtering probe and non-filtering probe and compare their PIM test performance, as shown in Fig. 10. The observed PIM level of the filtering probe is significantly higher than that of the non-filtering probe. Thus, it can be concluded that the filtering probe shows higher sensitivity or larger dynamic range than the non-filtering probe.

4 Conclusions

A filtering PIM probe is proposed for near-field PIM tests. Both simulations and measurements show that the filtering probe has potential advantages compared with conventional non-filtering probes. When the same coupling strength for PIM is obtained, the suppression of carrier power of filtering probes can be about 20 dB higher than that of non-filtering probes. Preliminary results also show that the dynamic range of filtering probes is larger than that of non-filtering probes, which indicates the filtering probe can measure lower PIM products than non-filtering probes. Another potential benefit of using a filtering probe is that it can relax the requirement for the duplexer and receiver of PIM test systems, which will help with system integration and cost reduction.



▲ Figure 10. Measured dependence of PIM on carrier power for both the filtering and non-filtering probes

References

- [1] BAYRAK M, BENSON F A. Intermodulation products from nonlinearities in transmission lines and connectors at microwave frequencies [J]. *Proceedings of the institution of electrical engineers*, 1975, 122(4): 361. DOI: 10.1049/iee:1975.0101
- [2] GOLIKOV V, HIENONEN S, VAINIKAINEN P. Passive intermodulation distortion measurements in mobile communication antennas [C]// *The 54th Vehicular Technology Conference*. IEEE, 2001: 2623 - 2625. doi: 10.1109/VTC.2001.957226
- [3] HOEBER C, POLLARD D, NICHOLAS R. Passive intermodulation product generation in high power communications satellites [C]// *The 11th Communications Satellite Systems Conference*. AIAA, 1986: 657. DOI: 10.2514/6.1986-657
- [4] SHITVOV A P, KOZLOV D S, SCHUCHINSKY A G. Nonlinear characterization for microstrip circuits with low passive intermodulation [J]. *IEEE transactions on microwave theory and techniques*, 2018, 66(2): 865 - 874. DOI: 10.1109/tmtt.2017.2758726
- [5] SHITVOV A, SCHUCHINSKY A G, STEER M B, et al. Characterisation of nonlinear distortion and intermodulation in passive devices and antennas [C]// *The 8th European Conference on Antennas and Propagation (EuCAP 2014)*. IEEE, 2014: 1454 - 1458. DOI: 10.1109/eu-cap.2014.6902055
- [6] KIMINO T, KUGA N. Basic consideration on non-contact localization for a PIM source in array antenna [C]// *International Symposium on Antennas and Propagation (ISAP)*. IEEE, 2021: 395 - 396. DOI: 10.23919/isap47053.2021.9391124
- [7] GOPALAN R, LENG L J, KOMINEK S, et al. Generalized virtual PIM measurement for enhanced accuracy: US11374661 [P]. 2022-06-28
- [8] SHITVOV A P, ZELENCHUK D E, SCHUCHINSKY A G, et al. Passive intermodulation generation on printed lines: Near-field probing and observations [J]. *IEEE transactions on microwave theory and techniques*, 2008, 56(12): 3121 - 3128. DOI: 10.1109/tmtt.2008.2007136
- [9] CAI Z H, LIU L, DE PAULIS F, et al. Passive intermodulation measurement: challenges and solutions [J]. *Engineering*, 2022, 14: 181 - 191. DOI: 10.1016/j.eng.2022.02.012
- [10] TARIQ R U, YE M, ZHANG K Y, et al. Wide-band high dynamic range variable passive intermodulation generator using fabric-over-foam gasket [J]. *International journal of electronics and communications*, 2020, 126: 153400. DOI: 10.1016/j.aeue.2020.153400
- [11] SHITVOV A P, ZELENCHUK D E, OLSSON T, et al. Transmission/reflection measurement and near-field mapping techniques for passive intermodulation characterisation of printed lines [C]// *The 6th International Workshop on Multipactor, Corona and Passive Intermodulation in Space RF Hardware, MULCOPIM*, 2008: 1 - 6
- [12] CHEN Z Y, ZHANG Y, DONG S Q, et al. Wideband architecture for passive intermodulation localization [C]// *MTT-S International Wireless Symposium (IWS)*. IEEE, 2018: 1 - 3. DOI: 10.1109/ieeee-iws.2018.8400921
- [13] YANG S, WU W, XU S, et al. A passive intermodulation source identification measurement system using a vibration modulation method [J]. *IEEE transactions on electromagnetic compatibility*, 2017, 59(6): 1677 - 1684. DOI: 10.1109/TEMC.2017.2705114
- [14] YONG S H, YANG S, ZHANG L, et al. Passive intermodulation source localization based on emission source microscopy [J]. *IEEE transactions on electromagnetic compatibility*, 2020, 62(1): 266 - 271. DOI: 10.1109/TEMC.2019.2938634
- [15] HIENONEN S, GOLIKOV V, MOTTONEN V S, et al. Near-field amplitude measurement of passive intermodulation in antennas [C]// *The 31st European Microwave Conference*. IEEE, 2001: 1 - 4. DOI: 10.1109/EUMA.2001.339019
- [16] CHEN X, AN L, YU M, et al. Waveguide cell with water filling for passive intermodulation localization on planar circuits [J]. *IEEE microwave and wireless components letters*, 2021, 31(11): 1247 - 1250. DOI: 10.1109/LMWC.2021.3090081

Biographies

BAI Yongjiang received his BS degree in computer science and technology science from Shangrao Normal University, China in 2021. He is currently with Xi'an University of Architecture and Technology, China. His research interests include passive intermodulation and microwave rotational speed measurement. He has published 7 papers in various journals and conferences.

YANG Jiye received his BS degree in electronic information from Xi'an University of Architecture and Technology, China in 2023. He is currently with Xi'an University of Architecture and Technology. His research interests include passive intermodulation detection and microwave measurement.

ZHU Shaohao obtained his PhD degree in underwater acoustic engineering from Northwestern Polytechnical University, China in 2021. He is currently serving as an RF algorithm engineer at ZTE Corporation. His research interests encompass a wide range of cutting-edge topics, including passive intermodulation (PIM) mechanisms, PIM cancellation techniques, source localization, array beamforming, and satellite navigation and positioning technologies. With a robust background in both theoretical and practical aspects of

RF engineering, he is dedicated to advancing the field through innovative research and development.

YANG Ye received his master's degree in electromagnetic field and microwave from Xidian University, China in 2013. He is currently working at ZTE Corporation as an antenna feeder development engineer. His research mainly focuses on base station antenna design and development, including base station antenna PIM elimination and suppression, antenna pattern optimization and forming, active and passive antenna integration, and green antennas.

YE Ming (yeming@xauat.edu.cn) received his BS degree in information and computation science from Chongqing University of Posts and Telecommunications, China in 2008, and his MS and PhD degrees in electronic science and technology from Xi'an Jiaotong University, China in 2010 and 2014, respectively. He is currently with Xi'an University of Architecture and Technology, China. His research interests include passive intermodulation, secondary electron emission, microwave breakdown, microwave measurement and sensors. He has published around 100 papers in various journals and conferences.



Unsupervised Motion Removal for Dynamic SLAM

CHEN Hao^{1,2}, ZHANG Kaijiong^{1,2}, CHEN Jun^{1,2},
ZHANG Ziwen^{1,2}, JIA Xia^{1,2}

(1. ZTE Corporation, Shenzhen 518057, China;
2. State Key Laboratory of Mobile Network and Mobile Multimedia
Technology, Shenzhen 518055, China)

DOI: 10.12142/ZTECOM.202404010

<https://kns.cnki.net/kcms/detail/34.1294.TN.20241031.1625.002.html>,
published online November 1, 2024

Manuscript received: 2024-02-29

Abstract: We propose a dynamic simultaneous localization and mapping technology for unsupervised motion removal (UMR-SLAM), which is a deep learning-based dynamic RGBD SLAM. It is the first time that a scheme combining scene flow and deep learning SLAM is proposed to improve the accuracy of SLAM in dynamic scenes, in response to the situation where dynamic objects cause pose changes. The entire process does not require explicit object segmentation as supervisory information. We also propose a loop detection scheme that combines optical flow and feature similarity in the backend optimization section of the SLAM system to improve the accuracy of loop detection. UMR-SLAM is rewritten based on the DROID-SLAM code architecture. Through experiments on different datasets, it has been proven that our scheme has higher pose accuracy in dynamic scenarios compared with the current advanced SLAM algorithm.

Keywords: dynamic RGBD SLAM; update module; motion estimation; scene flow

Citation (Format 1): CHEN H, ZHANG K J, CHEN J, et al. Unsupervised motion removal for dynamic SLAM [J]. *ZTE Communications*, 2024, 22(4): 67 - 77. DOI: 10.12142/ZTECOM.202404010

Citation (Format 2): H. Chen, K. J. Zhang, J. Chen, et al., "Unsupervised motion removal for dynamic SLAM," *ZTE Communications*, vol. 22, no. 4, pp. 67 - 77, Dec. 2024. doi: 10.12142/ZTECOM.202404010.

1 Introduction

Simultaneous localization and mapping (SLAM) is an important technology in computer vision and autonomous robot navigation research. Its main goal is to enable mobile devices (robots, autonomous vehicles, unmanned aerial vehicles or AR/VR devices) to achieve autonomous positioning and map building by interacting with sensors in unknown or changing environments. SLAM systems typically include the following key components: data collection and preprocessing, front-end data processing, state estimation, map construction, and backend optimization, such as the typical Oriented FAST and Rotated BRIEF (ORB)-SLAM system. At present, although SLAM technology faces many challenges, such as sensor accuracy errors, computational complexity, and real-time requirements, it is still the core technology of many autonomous systems, providing the possibility for machines and equipment to navigate and work efficiently in complex environments.

In recent years, many deep learning and traditional SLAM fusion schemes have been proposed to improve the performance and robustness of environmental perception and pose estimation. Deep neural networks can play a crucial role in image feature extraction, semantic map construction, and loop detection. Extracting feature points or descriptors

through deep learning models can improve the accuracy of image matching and feature tracking in visual SLAM. Deep learning can be used to establish a loopback detection model for visual and semantic contexts, which is used to detect whether the robot has returned to the previously visited position, and then perform global optimization to reduce cumulative errors. Deep learning can also be used for semantic map construction, enabling robots to understand the semantic information of different objects and regions in the environment, which contributes to autonomous decision-making and path planning in the field of autonomous driving. In addition, eliminating dynamic objects can also effectively improve the accuracy of pose estimation.

Semi-supervised or unsupervised SLAM is an emerging research field that explores how to train SLAM systems with unlabeled or limited labeled data. This method helps to address the dependency on large numbers of labeled data in traditional SLAM methods. Deep learning can also achieve end-to-end SLAM, directly generating maps and trajectories from sensor data without the need for intermediate steps. Recently, some research efforts have been devoted to designing more effective multimodal fusion strategies. The goal is to fuse data from different types of sensors, such as vision, light detection and ranging (LiDAR), GPS and inertial mea-

surement unit (IMU), together to improve the robustness and accuracy of SLAM systems. Real-time performance has always been a key challenge for SLAM systems. Researchers are striving to improve the computational efficiency of SLAM systems to meet the requirements of real-time applications such as autonomous driving, virtual reality, and robot navigation. Their main tasks include hardware acceleration, low-power algorithms, and distributed SLAM.

The current state-of-the-art algorithm DROID-SLAM^[30] combines traditional methods with deep learning and has the advantages of high accuracy, strong robustness, and good generalization. However, it does not perform well in dynamic scenarios like the KITTI dataset, and pose estimation is easily affected by passing vehicles and pedestrians. As shown in Fig. 1, when a truck moves from left to right across the camera frame, the algorithm may mistakenly perceive the camera as undergoing a left-turning motion, leading to erroneous pose estimation outputs. Therefore, based on DROID-SLAM, we propose a new SLAM scheme to address the issue of dynamic objects affecting algorithm accuracy. The main contributions of our work are summarized as follows:

- We propose for the first time a scheme that combines scene flow and deep learning SLAM to improve the accuracy of SLAM in dynamic scenes while outputting dynamic object masks. The entire process does not require explicit object segmentation as supervisory information.
- We propose a new update module that can iteratively update the camera pose.
- We propose a loop detection scheme that combines optical flow and feature similarity to improve the accuracy of loop detection without increasing additional computational complexity.

2 Related works

2.1 Dynamic SLAM

SLAM solutions typically assume that the scene is almost static or has a low level of dynamism. However, there are often a large number of dynamic objects in real-world scenarios, including pedestrians, animals, cars, bicycles, and other dynamic objects, which can cause erroneous changes in feature matching relationships, resulting in inaccurate results due to the lack of reliable features in SLAM solutions.

To solve the above problem, some methods adopt object detection or semantic segmentation schemes to eliminate potential dynamic targets^[1-4]. However, a large number of semantic segmentation objects in the camera's field of view may lead to insufficient features, which in turn can lead to problems with map matching and motion tracking, such as decreased system accuracy, tracking failures, and trajectory loss. In fact, dynamic objects may be static in the scene. Due to the limitations of semantic categories, on the one hand, they cannot cover all potential dynamic targets; on the



▲ Figure 1. Two images from the KITTI07 sequence

other hand, some static objects are dynamic in the scene, such as books in people's hands. Many studies have introduced additional constraints to confirm the true dynamic objects in the scene. Based on semantic segmentation, authors in Ref. [5] utilize deep inconsistency checking to remove potential dynamic objects. Some methods do not rely on prior semantic information but distinguish between dynamic and static through the association with feature points^[6-9]. Refs. [10] and [11] use dense optical flow methods and semantic segmentation to estimate the motion of objects in the scene, which helps to construct a globally consistent scene map and improve the robustness and accuracy of the system. Refs. [12] and [13] predict the camera's self-motion iteratively by correlating the camera's self-motion with the segmentation of dynamic objects, achieving their joint optimization in a single learning framework. Unlike the above research, the method proposed can output pixel-level pose changes unsupervised, segment true dynamic objects, and have higher robustness to different dynamic scenes.

2.2 Optical Flow and Scene Flow

In SLAM algorithms, optical flow is commonly used to represent motion information between adjacent frames in a video sequence. This motion information can help SLAM systems estimate camera motion more accurately when processing dynamic scenes.

Deep learning-based optical flow estimation methods have gradually become a mainstream research direction. The FlowNet series^[14-15] is the first to use an end-to-end deep learning architecture for optical flow estimation, emphasizing the importance of the training data sequence. Ref. [16] introduces many novel improvements of unsupervised optical flow models to enhance performance metrics. Refs. [17] and [18] consider the use of coarse-to-fine techniques to improve the performance metrics of optical flow networks. Refs. [19] and [20] construct multi-scale 4D correlation volumes for all pixels and iteratively update the optical flow

field through recurrent units that search the correlation volumes. Refs. [21] and [22] use multi-frame information for optical flow fusion to enhance optical flow computation performance. Additionally, some approaches^[23-24] have made significant efforts to improve the computational efficiency of lightweight optical flow estimation networks for mobile and low-power usage scenarios.

2.3 Loop Detection

Backend optimization is a key step in SLAM systems to improve the accuracy of positioning and mapping. Usually, graph optimization or nonlinear optimization techniques are used to minimize estimation errors. Closed loop detection is the key to optimizing the backend of SLAM systems. Closed loop detection or position recognition is also an important module for reducing trajectory errors in the SLAM backend. The traditional loop detection scheme is based on a bag of words (BoW)^[25] for storage and uses manually designed visual features. The BoW method first extracts features, including scale invariant feature transform (SIFT), speeded-up robust features (SURF), ORB, etc., from a large number of training images, and classifies these features (Word) with K-means clustering algorithms to obtain leaf nodes called dictionaries. Therefore, an image can be described as a vector under the dictionary based on whether the corresponding word (Word) appears. However, changes in lighting, weather, viewpoints, and moving objects in real-world scenes makes this problem more complex. Different from traditional word bag-based methods, deep networks can typically learn complex internal structures in image data without manual design of visual features.

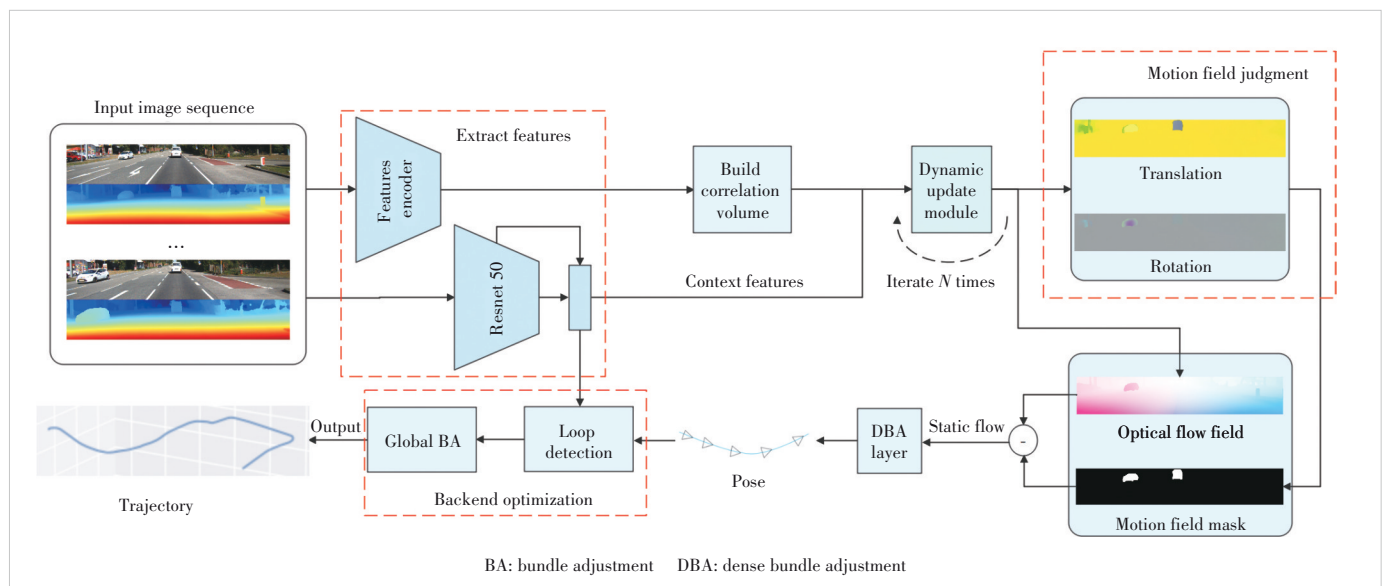
To address this issue, previous research works like Ref.

[26] use ConvNet features that are more robust to changes in viewpoints and conditions and derived from pretrained models on a universal large-scale image processing dataset. This scheme can predict the matching landmark candidate boxes between images and extract features. To improve the algorithm's efficiency, Gaussian random projection (GRP) is used to reduce the data dimension for feature similarity calculation. However, for high-dimensional data with partially non-uniform distribution, using GRP is not conducive to preserving the original variance.

Other representative works^[27-29] are based on deep automatic encoder structures to extract compact representations that compress scenes unsupervisedly.

3 Proposed Method

Our proposed simultaneous localization and mapping technology for unsupervised motion removal (UMR-SLAM) structure is shown in Fig. 2. We input a set of RGBD image sequences and use encoders to extract features and context features respectively. By calculating the correlation volume through the feature dot product, the update operator iteratively updates the pose changes of each pixel, and calculates the optical flow and dynamic region mask based on the pixel-by-pixel pose. After removing the optical flow from the dynamic region, the camera pose is obtained through bundle adjustment (BA) optimization. Finally, in the backend optimization, the global pose and trajectory are optimized based on the loop detection results to reduce cumulative errors. This method takes RGBD image sequences as input and outputs camera pose. UMR-SLAM has an end-to-end differentiable architecture, which combines the advantages of classical methods and deep learning networks. We use the scene



▲ Figure 2. System structure of UMR-SLAM

flow method to unobservedly remove dynamic objects, and integrate the results of the two detection schemes, optical flow and feature similarity in loop detection, making the SLAM system more robust in dealing with challenging dynamic scenes. Specifically, distinguished from DROID-SLAM, which iteratively updates camera pose and depth, we iteratively update the poses of all pixels. In DROID-SLAM, the optical flow is used to perform every update of camera poses, while we only use the optical flow caused by camera motion to calculate camera poses. Next, we elaborate on the details of our method.

3.1 Network Architecture

The core of the proposed dynamic SLAM network is to use a dynamic update module to estimate the 3D rigid body motion of all pixels in the scene, and then calculate the optical flow and dynamic region. The camera pose is optimized through BA. Compared with DROID-SLAM, which uses optical flow as the intermediate motion representation, we can determine the pixels of dynamic objects by unsupervised learning technology and only use the static optical flow caused by camera motion to calculate camera pose, which can greatly improve the positioning accuracy of the algorithm in dynamic scenes.

In contrast to DROID-SLAM, we directly input the RGBD images for feature extraction and optical flow calculation. For each pair of RGBD images, in the dynamic update module, we iteratively update the 3D motion of all pixels, rather than the camera pose and inverse depth map. Our update iteration not only runs on adjacent frames but can be applied to any number of frames to obtain higher accuracy scene flow information and achieve joint global refinement of all camera poses, which helps to minimize long trajectories and loop drift. In the backend optimization, we also use the Gaussian Newton method to execute BA to adjust the camera pose T to minimize the cost function.

We use a frame graph to represent the covisibility between frames. We determine whether two frames are co-viewed through optical flow and establish a coview frame map. Differing from DROID-SLAM, we use the completed depth map instead of the original one to calculate the frame graph. In the coview, nodes represent each input image, and edges, which are the connections between nodes, indicate that the two images are covisible. During the training and inference process of the model, the frame graph is dynamically constructed and updated. Each time a new optical flow is calculated to remove dynamic objects, the frame map with new visibility is updated.

3.1.1 Features Extraction

In the feature extraction module, we use conventional residual modules and downsampling convolution modules to obtain high-dimensional dense feature maps with a resolu-

tion of 1/8 of the original image. At the same time, we use pretrained ResNet50 with skip connections to extract context features at 1/8 resolution. ResNet50 can extract features with a greater degree of semantic information and a larger receptive field, which can be better used for loop detection and rigid motion object grouping.

3.1.2 Building Correlation Volume

1) Correlation pyramid: For two frames I_i and I_j with a common view, the correlation volume C is calculated using the dot product of two position feature vectors in the feature map f , as shown in the following equation.

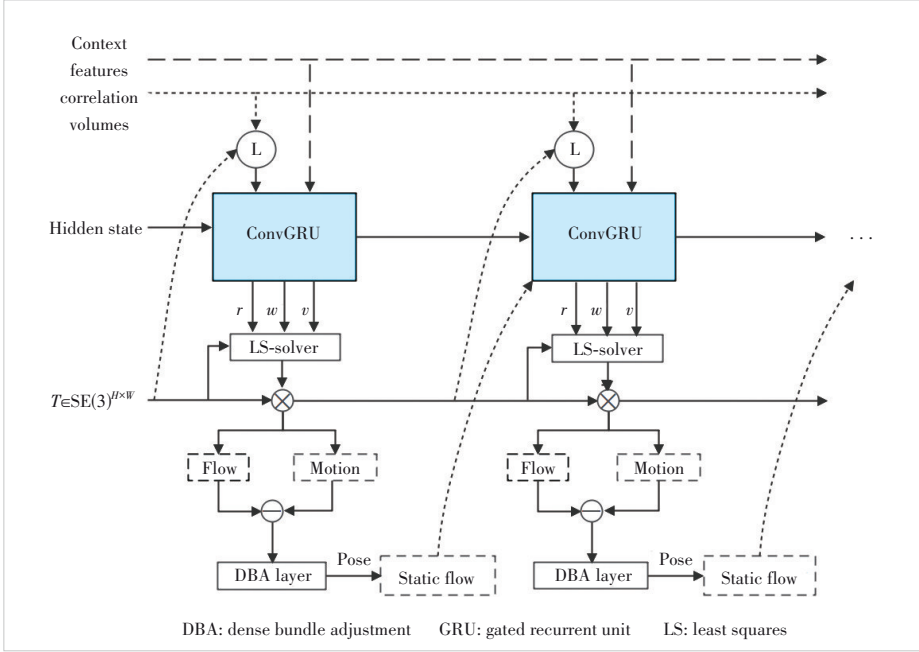
$$C_{u_1 v_1 u_2 v_2}^{ij} = f(I_i)_{u_1 v_1} \cdot f(I_j)_{u_2 v_2}, \quad (1)$$

where $C_{u_1 v_1 u_2 v_2}^{ij} \in R^{H \times W \times H \times W}$ represents the correlation between the features of image I_i at position (u_1, v_1) and image I_j at position (u_2, v_2) . Then we use average pooling concatenation to establish a four-layer correlation pyramid.

2) Correlation lookup: The lookup operator is $L_r: R^{H \times W \times H \times W} \times R^{H \times W \times 2} \rightarrow R^{H \times W \times (r+1)^2}$. This operator uses bilinear interpolation to index the relevant volume using an optical flow field coordinate grid with a radius of r . Splice the relevant features found at each layer of the relevant pyramid into a feature vector.

3.1.3 Dynamic Update Module

Fig. 3 shows the dynamic update module of UMR-SLAM. We find the relevant features of the optical flow calculated by the current pixel pose through the relevant volume. The obtained features are fed together with static optical flow and global feature dynamics into two convolutional layers, resulting in intermediate features. These features are then fed into convolutional gated recurrent unit (ConvGRU), and then optical flow residuals, their confidence levels, and rigid motion embedding vectors are obtained through convolutional layers. The dense pixel pose T can be updated using the least squares method. According to the dense pose calculation, the dynamic region of the optical flow is deducted and fed into the DBA layer, which combines the optical flow confidence to optimize the camera pose. Finally, the optimized camera pose is used to calculate optical flow and provided for the next iteration. Not similar to the iterative operation of the update module in DROID-SLAM, the update operator combines neural networks and optimization algorithms to update the dense pixel pose, and then performs subsequent optical flow and camera pose calculations based on the pixel pose. The update operator is based on the ConvGRU of recurrent neural networks (RNN) for iterative updates. The optical flow and the pixel density pose are fed into the next iteration as new optimization terms. During each iteration of the update process, the module generates dense pixel pose increments, optical flow generated by cam-



▲ Figure 3. Dynamic update module

era motion, dynamic object masks, and camera pose.

1) Update operator: The update operator is a GRU unit based on a recurrent neural network, mainly composed of 3×3 convolutional kernels with dilation rates of 1 and 3. It uses index operators to retrieve features from correlated volumes and output optical flow correction quantities. We use depth maps and the current estimated pose to estimate the 2D correspondence. Taking the edges in the frame graph $(i, j) \in \mathcal{E}$ as an example, p_i is the grid coordinate of frame i . p_{ij} is the corresponding projection coordinate of frame i in frame j , and the projection transformation process is as follows:

$$p_{i,j} = \left(T_{s_{i,j}} \cdot \prod_c^{-1}(p_i, d_i) \right), \quad (2)$$

where \prod_c is a pinhole camera model that maps a set of 3D points to the image, while \prod_c^{-1} is the inverse projection function that maps the inverse depth map d_i and p_i to the 3D point cloud. The pose transformation matrix between image i and image j is $T_{s_{i,j}}$. We can obtain p_{ij} through the transformation of 3D points in the world coordinate system and the pinhole camera model.

Based on the corresponding relationship, we can retrieve correlation features in the correlation volume and calculate the optical flow field $p_{ij} - p_j$. The input of GRU includes optical flow field, current dense pixel pose, depth residual $d' - d^*$, and correlation features. In the depth residual term, the inverse depth d' is the depth component of p_{ij} , and d^* is the inverse depth map of p_{ij} index image frame j . Each feature is extracted with high-dimensional information through two convolutional layers, and then fed into the GRU module.

Then, three two-layer convolutions are applied to the hidden states of the GRU output to calculate the rigid motion embedding map V , the revision map optical flow field correction map $r = (rx, ry, rz)$, and the corresponding confidence $w \in [0, 1]$. The correction amount r is the correction of the optical flow caused by the current SE3 field. Three outputs serve as inputs to the dense-SE3 layer to generate updates to the SE3 sports field. The confidence level of w as the optical flow correction is used to calculate the cost function.

The resolution of the SE3 motion field estimated by the network is 1/8 of the original image resolution. To obtain the original resolution map, we perform convex upsampling in Lie Algebra and then use exponential mapping back to the manifold.

2) Dense-SE3 layer: This layer is a differentiable optimization layer used to update the current pose of pixels. It maps the optical flow revision mapping r to the SE3 field update. The rigid motion embedding vector v is used to soft-group pixels into rigid objects. We use embedding vectors to build an attention matrix between all pairs of (i, j) . We calculate the similarity $a_{ij} \in [0, 1]$ between two embedding vectors v_i and v_j by taking the sigmoid activation function σ of the negative L2 distance.

$$a_{ij} = 2 * \sigma \left(-\|v_i - v_j\|^2 \right) \in [0, 1]. \quad (3)$$

We use similarity to define an objective function based on reprojection error to solve the updated pose δ_i for each pixel i :

$$E(\delta) = \sum_{i \in \Omega} \sum_{j \in \mathcal{N}_i} a_{ij} \left\| r_j + \prod_c(T_j X_j) - \prod_c(e^{\delta} T_i X_j) \right\|_{w_j}^2, \quad (4)$$

where $\|X\|_w^2 = X^T \text{diag}(w)X$. The above equation indicates that for each pixel i in the image area Ω , the transformation T_i is described as a transformation of pixel j in the neighborhood \mathcal{N}_i of pixel i . Only objects with similar embedding vectors that may belong to the same rigid motion as (i, j) have a significant contribution to the objective function. To reduce the memory footprint when solving Eq. (4), we implement Gaussian Newton updates in CUDA to estimate the next SE3 pose.

3) Motion field judgment: Moving objects in the image

greatly affects the calculation of camera pose. Therefore, it is very necessary to remove dynamic objects. We filter the rotation and translation of each pixel predicted by the scene flow algorithm as shown in Figs. 4b and 4c, and if the pose τ_i and ϕ_i of pixel i differ from the average motion pose τ_{mean} and ϕ_{mean} of the entire image by more than a certain threshold (μ set to 0.01), it is regarded as a motion point as shown in Fig. 4d. We set the optical flow mask M of the moving point directly to 0, without performing subsequent camera pose estimation.

$$M_i^{\text{motion}} = [\|\tau_i - \tau_{\text{mean}}\| \geq \mu_\tau] + [\|\phi_i - \phi_{\text{mean}}\| \geq \mu_\phi]. \quad (5)$$

4) DBA: After obtaining the corrected static flow field, we use the Gaussian Newton-based dense bundle adjustment (DBA) layer algorithm in DROID-SLAM to optimize the camera pose G . The DBA layer does not affect gradient back-propagation. The error function is defined as follows:

$$E(G') = \sum_{(ij) \in \mathcal{E}} \left\| p_{ij}^* - \prod_c (G'_{ij} \cdot \prod_c^{-1}(p_i, d'_i)) \right\|_{\Sigma_{ij}}^2, \quad (6)$$

$$\Sigma_{ij} = \text{diag} w_{ij}, \quad (7)$$

where $p_{ij}^* = r_{ij} + p_{ij}$ represents the updated and corrected p_{ij} . Eq. (7) calculates the Mahalanobis distance weight, and the error term is weighted based on the combined confidence w_{ij} . The $H\Delta x = g$ problem can be solved by Schur elimination using the sparsity property of matrix H to accelerate the solution process.

3.2 Supervision

We use pose loss and flow loss supervision to train our network. Both loss functions are applied to paired training sequences. We calculate the static optical flow f_{static} based on the camera pose predicted through each iteration. The optical flow calculated from the true depth and camera pose truth is used as the supervisory information f_{gt} .

$$f_{\text{static}}^k = \prod_c \left(G \cdot \prod_c^{-1}(p) \right) - p, \quad (8)$$

where G represents the camera pose, p represents the image coordinate grid, and k represents the number of iterations. We design the loss as the average L2 distance between two optical flow fields.

$$L_{\text{flow}} = \sum_{k=1}^N \gamma^{N-k} \left\| f_{\text{static}}^k - f_{gt} \right\|_2, \quad (9)$$

with $\gamma = 0.9$. We also apply an additional loss function to the GRU-predicted optical flow increment and set the weight to 0.2.

Pose loss uses the actual pose T and the predicted camera pose G after each update to calculate the loss.

$$L_{\text{pose}} = \sum_{k=1}^N \gamma^{N-k} \left\| \text{Log}_{\text{SE3}}(T^{-1} \cdot G_k) \right\|_2, \quad (10)$$

The overall loss function is the sum of pose loss and optical flow loss. To ensure that the two types of losses are on the same order of magnitude, we use coefficients w_1 and w_2 to adjust the weights of the two types of losses. We set w_1 to 0.1 and w_2 to 1.

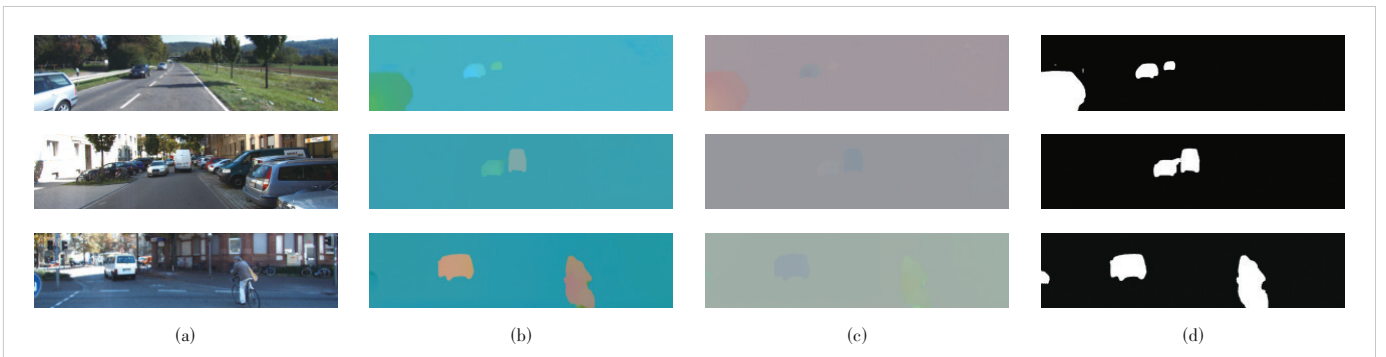
$$L = w_1 L_{\text{flow}} + w_2 L_{\text{pose}}. \quad (11)$$

3.3 SLAM System

In terms of input modes, our SLAM system only supports RGBD data input. In the inference stage, we embed the above network structure into the entire SLAM system.

During initialization, our algorithm accumulatively receives 12 keyframes based on optical flow differences, constructs frame maps for them, and uses our dynamic update module to calculate their initial pose. In addition, we process on the depth image.

1) Depth image estimation: The importance of depth information has been well demonstrated by a large amount of re-



▲ Figure 4. (a) Original image; (b) visualization image of translation amount; (c) visualization image of rotation amount; (d) dynamic region mask

search work in the past. Usually, we use depth sensors to obtain accurate and reliable distance measurements, while also possessing real scene scales. However, neither LiDAR nor other commonly used RGBD cameras can provide dense pixellevel depth maps. The holes and blank pixels in sparse depth maps indicate a serious lack of information at the application level, leading to algorithm reliability failure. Therefore, it is necessary to fill in these blank pixels in practical applications.

Specifically, for the KIITI dataset, we directly obtain laser data from the odometer dataset and convert it into depth images. Obviously, as shown in Fig. 5, the lack of depth information is very severe, with only 5% of the available pixel points in the entire image. Here, we use the CompletionFormer^[31] algorithm to complete the depth map. Before and after processing, as shown in Fig. 5, we also attempt to use the GA-net^[32] algorithm to estimate disparity maps using binocular data and obtain depth maps.

In front-end processing, when a new frame arrives, the system uses the three closest adjacent frames and the new frame to create a temporary graph, and optimize and calculate the pose of the new frame.

In backend optimization, the system creates a new frame graph containing each reserved keyframe. The edges between key frames are generated according to specific rules to eliminate excess edges. We use a dynamic update module to optimize the final pose of the entire shape. Then, through the proposed loop detection scheme, we directly add edges between the two frames with loops to the frame graph for sub-

sequent global BA optimization.

2) Loop detection: In backend optimization, closed-loop detection is used to detect and correct path drift. It identifies features that appear on previously visited locations and uses this information to adjust device location estimates and maps to reduce cumulative errors. We found that DROID-SLAM uses optical flow for loop detection, which often fails to detect loops well in real-world scenarios and has poor robustness. Using only optical flow to determine whether a loop exists may lead to missed detection.

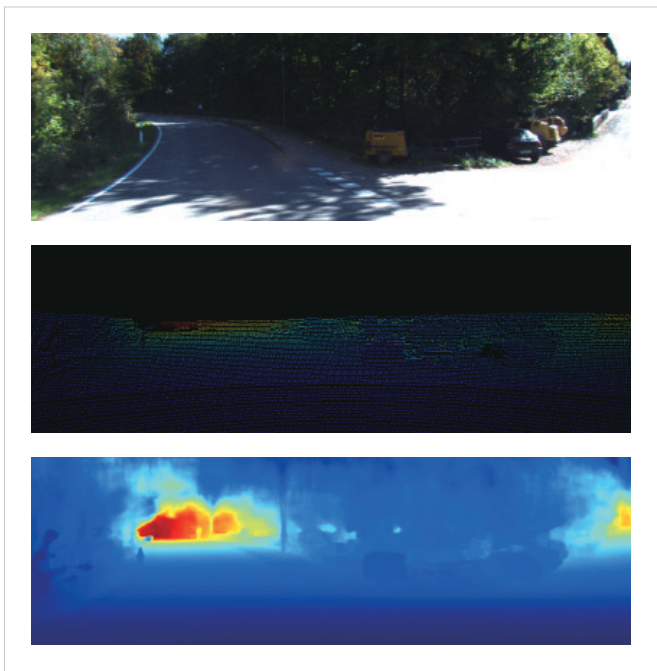
In UMR-SLAM, we propose a solution that combines high-dimensional image feature similarity with optical flow calculation to improve loop detection accuracy. Image feature similarity schemes typically handle image noise more robustly, especially in scenarios with lighting changes, occlusions, or other complex environments, where similarity is more reliable than solely relying on optical flow. Compared with optical flow, which focuses only on local motion information, image feature similarity schemes compare the content of entire images, capturing similarity between images from a global perspective. This can compensate for the limitation of local motion and improve matching accuracy. Combining image feature similarity schemes with optical flow calculation provides additional information to validate the existence of loops. For example, if optical flow calculation detects significant motion but the image feature similarity is high, it may indicate environmental similarity, allowing for more confident loop detection and reducing missed detection. Integrating these two types of information enhances loop detection accuracy and robustness, particularly in situations where optical flow calculation may be affected by noise or encounters significant motion. Therefore, we add a branch to the entire SLAM system for loopback detection. We directly utilize the global context Resnet50 features of existing keyframes for feature similarity comparison.

To improve the algorithm's efficiency, we use the principal component analysis (PCA) for feature dimensionality reduction before feature similarity comparison. PCA can identify the intrinsic patterns of data based on the relationship between features. By calculating the eigenvalues of the covariance matrix and corresponding eigenvectors, the direction of maximum variance is found in high-dimensional data, and the data are mapped to a new subspace with a dimensionality not greater than the original data. We use the feature maps of the first 128 channels for PCA dimensionality reduction to 128×30.

Next, cosine distance d is used to measure the distance between two features for loop detection.

$$d_{\cos} = \cos(\mathbf{v}_1, \mathbf{v}_2), \quad (12)$$

where \mathbf{v}_1 and \mathbf{v}_2 represent the feature vector expressions of the



▲ Figure 5. RGB, original laser depth map, and completed depth map: from top to bottom

image pair. If it is less than a certain threshold τ (set to 0.12), it is considered that a loopback has been detected.

4 Experiments

Initially, UMR-SLAM is trained on datasets Virtual KITTI2^[33] and KITTI^[34], followed by a comprehensive evaluation of the methodologies on various real and synthetic datasets, encompassing dynamic sequences from Virtual KITTI2, KITTI, and TUM-RGBD^[35]. During the experimentation phase, the absolute trajectory error (ATE) serves as the metric for assessing the accuracy of the estimated camera trajectory. Subsequently, a series of ablation experiments are devised to validate the efficacy of the proposed method in dynamic scenarios. Afterward, comparisons are drawn between our method and other advanced algorithms in dynamic scenarios, such as ORB-SLAM2^[36], DROID-SLAM, and DynaSLAM^[37], to showcase the effectiveness of our method and the robustness of pose estimation.

4.1 Datasets

We train and test using partial Virtual KITTI2 and KITTI datasets. KITTI is a dataset captured in real-world traffic conditions, ranging from highways in rural areas to city-center scenes with many static and dynamic objects. The KITTI dataset is typically used as a benchmark test set for stereo vision, optical flow, depth prediction, object detection, and visual mileage calculation methods. We mainly use 00 - 08 of the visual odometer data as the training set, and 09 and 10 as the test set.

Virtual KITTI2 is a synthetic dataset modeled after the KITTI dataset, consisting of 5 sequences. These sequences enhance data by overlaying different weather conditions (such as fog and rain) and modifying camera directions and angles. In the ablation study, we use the default camera orientation as the training set and configurations of 15 and 30 degrees as the validation set.

4.2 Training Implementation Details

We use 8 NVIDIA GPU V100 for training. Considering the possibility of inaccurate depth completion values in the sky and limited graphics memory, we randomly crop 208×960 sized images below the images for training, while modifying the internal parameter data.

We make minor adjustments to KITTI to perform an additional 50k iterations with an initial learning rate of 5×10^{-5} , and perform spatial and photometric enhancements. To estimate parallax, we provide input depth maps for our method using GA-Net.

For all experiments, we use the AdamW optimizer with weight attenuation set to 1×10^{-5} , and expand the update operator for 12 iterations. We use partial model weights from ImageNet and RAFT-3D as pretrain weights. Training RAFT-3D involves differentiating a computational graph

composed of Euclidean tensors (such as network weights and feature activation) and Lie group elements (such as the SE3 transformation domain). We use the LieTorch library to perform backpropagation in the tangent space of manifold elements in computational graphs.

Adjusting the weights of the two loss functions simultaneously to make their order of magnitude similar. Due to the fast camera movement in the KITTI dataset, we optimize the optical flow filtering threshold and expand the range of optical flow selection when establishing frame maps before training. For pixels with missing depth, we directly assign their depth value to 0.01, resulting in an inverse depth of 100. This point is not considered when calculating the overall optical flow, and the mask is set to 0.

4.3 Results

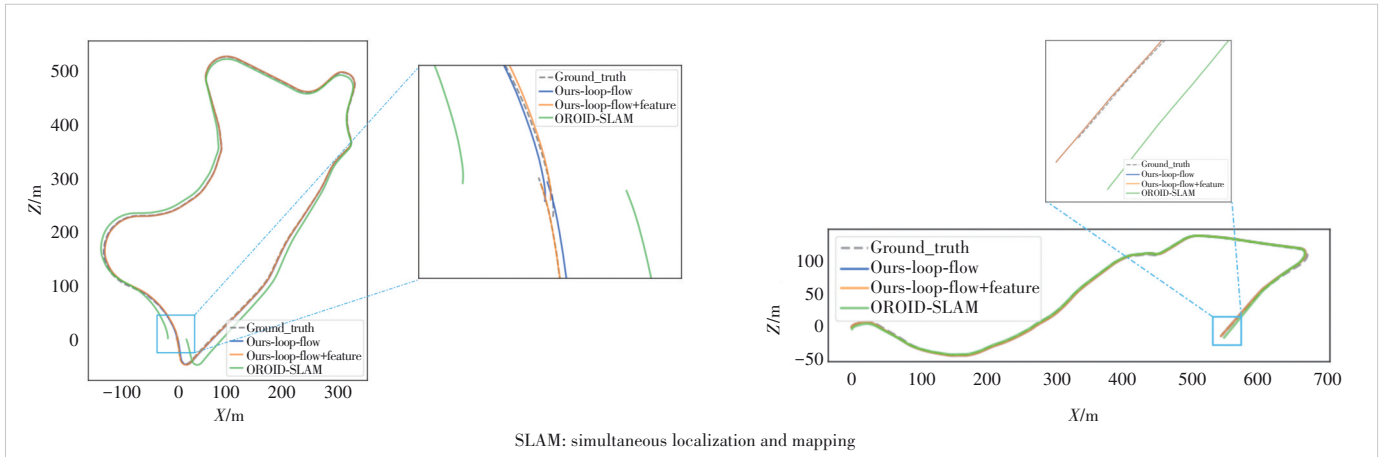
In this section, we compare our proposed approach with current state-of-the-art methods on the main-stream SLAM datasets.

1) Ablations experiment: We conduct ablation experiments on various components of the UMR-SLAM model on the Virtual KITTI2 and KITTI datasets, and report the results in Table 1. We compare the indicators using different depth completion methods and also provide indicators on whether to use loopback detection and whether to use dynamic object removal. The indicators in Table 1 are all tested using RGBD data, and the test indicator is automatic test equipment absolute trajectory error (ATE)[M] (RMSE).

We use different depth estimation algorithms to test the final algorithm metrics. The PENet and CompletionFormer methods both complete the depth map converted by laser, while GA-net calculates the disparity map using binoculars and then uses camera internal references to obtain the depth map. We found that the depth maps obtained by GA-net can provide better performance. We also test the impact of deducting dynamic objects on SLAM, and the experiment shows that the ATE index after deducting dynamic objects would decrease by about 2.5. We also attempt to use differ-

▼ Table 1. Ablations experiment of UMR-SLAM, where the best results are displayed in bold

Experiment	Configuration	K09	K10	
Depth estimate	-	11.527	4.775	
	PENet	4.413	3.366	
	CompletionFormer	3.569	2.748	
	GA-net	2.689	1.414	
Dynamic region removal	No	5.131	2.351	
	Yes	2.689	1.414	
Loop detection	-	4.058	1.412	
	Flow	3.835	1.414	
	Flow and feature	$\tau=0.5$	3.665	1.414
		$\tau=1.2$	2.689	1.420
		$\tau=2$	3.872	1.427



▲ **Figure 6. Trajectory comparison between our method and different loop detection algorithms and DROID-SLAM in KITTI sequences 09 (Left) and 10 (Right)**

ent detection schemes in loop detection, with the highest accuracy achieved when optical flow is used together with features and the feature similarity threshold is 1.2. Fig. 6 shows a trajectory comparison between our UMR-SLAM and the DROID SLAM algorithm, and the results indicate that our trajectories are closer to the ground truth.

We test the performance of the proposed UMR-SLAM on sequences 09 and 10 of the KITTI dataset and all sequences of the Virtual KITTI2 dataset, and provide camera motion trajectories. The ATE results are shown in Table 2 below. Compared with DROID-SLAM, our UMR-SLAM is more accurate and robust in dynamic scenarios. We also evaluate TUM RGBD dynamic sequences with different dynamic ratios, and the comparison results in Table 3 indicate that UMR-SLAM achieves competitive and even the best performance compared with other classical methods such as DVO-SLAM, ORB-SLAM2, PointCorr, DROID-SLAM. All methods in the table are tested using the RGBD dataset.

5 Conclusions

In this paper, we introduce UMR-SLAM, an end-to-end visual SLAM algorithm. We combine scene flow with deep learning SLAM to improve SLAM accuracy in dynamic scenes, without the need for explicit object segmentation as supervisory information throughout the entire process. In the backend optimization section, we propose a loop detection scheme that combines optical flow and feature similarity, which can improve the accuracy of loop detection. The results of experiments on different datasets prove that our

▼ **Table 2. ATE [M] metric for dynamic SLAM on the KITTI (K) and Virtual KITTI2 (VK) datasets, where we achieve the best results. All test results are based on RGBD**

Method	K09	K10	VK01	VK02	VK06	VK18	VK20
DROID-SLAM	5.453	2.514	0.197	0.192	0.007	1.030	3.041
Our URM-SLAM	2.689	1.414	0.128	0.030	0.007	0.812	1.189

SLAM: Simultaneous localization and mapping

▼ **Table 3. Dynamic SLAM results of TUM dynamic sequences, measured as ATE [M]. The best results are displayed in bold**

Method	Input Modes	DVO-SLAM ^[58]	ORB-SLAM2	PointCorr ^[39]	DROID-SLAM	Ours
Slightly dynamic	fr2/desk-person	0.104	0.006	0.008	0.019	0.014
	fr3/sitting-static	0.012	0.008	0.010	0.006	0.007
	fr3/sitting-xyz	0.242	0.010	0.009	0.011	0.009
	fr3/sitting-rpy	0.176	0.025	0.023	0.022	0.020
	fr3/sitting-halfsphere	0.220	0.025	0.024	0.023	0.022
Highly dynamic	fr3/walking-static	0.752	0.408	0.011	0.007	0.004
	fr3/walking-xyz	1.383	0.722	0.087	0.015	0.013
	fr3/walking-rpy	1.292	0.805	0.161	0.050	0.045
	fr3/walking-half-sphere	1.014	0.723	0.035	0.029	0.032

SLAM: simultaneous localization and mapping

scheme has higher accuracy compared with the current state-of-the-art deep learning scheme, DROID-SLAM, especially in dynamic scenarios. Overall, the flexibility of deep learning and powerful feature extraction capabilities provide new solutions to SLAM systems, which can cope with various complex environments and tasks. However, the integration of deep learning and SLAM still faces significant challenges in real-time performance and computational complexity, and further research and innovative methods need to be sought to address them.

References

- [1] ZHONG F W, WANG S, ZHANG Z Q, et al. Detect-SLAM: making object detection and SLAM mutually beneficial [C]//Proceedings of IEEE

- Winter Conference on Applications of Computer Vision (WACV). IEEE, 2018: 1001 – 1010. DOI: 10.1109/WACV.2018.00115
- [2] WU W X, GUO L, GAO H L, et al. YOLO-SLAM: a semantic SLAM system towards dynamic environment with geometric constraint [J]. *Neural computing and applications*, 2022, 34(8): 6011 – 6026. DOI: 10.1007/s00521-021-06764-3
- [3] YU C, LIU Z X, LIU X J, et al. DS-SLAM: a semantic visual SLAM towards dynamic environments [C]//International Conference on Intelligent Robots and Systems (IROS). IEEE, 2018: 1168 – 1174. DOI: 10.1109/IROS.2018.8593691
- [4] LIU Y B, MIURA J. RDS-SLAM: Real-time dynamic SLAM using semantic segmentation methods [J]. *IEEE access*, 2021, 9: 23772 – 23785. DOI: 10.1109/ACCESS.2021.3050617
- [5] BESCOS B, FÁCIL J M, CIVERA J, et al. DynaSLAM: tracking, mapping, and inpainting in dynamic scenes [J]. *IEEE robotics and automation letters*, 2018, 3(4): 4076 – 4083. DOI: 10.1109/LRA.2018.2860039
- [6] WANG C J, LUO B, ZHANG Y, et al. DymSLAM: 4D dynamic scene reconstruction based on geometrical motion segmentation [J]. *IEEE robotics and automation letters*, 2021, 6(2): 550 – 557. DOI: 10.1109/LRA.2020.3045647
- [7] SUN Y X, LIU M, MENG Q H. Motion removal for reliable RGB-D SLAM in dynamic environments [J]. *Robotics and autonomous systems*, 2018, 108: 115 – 128. DOI: 10.1016/j.robot.2018.07.002
- [8] DAI W C, ZHANG Y, LI P, et al. RGB-D SLAM in dynamic environments using point correlations [J]. *IEEE transactions on pattern analysis and machine intelligence*, 2022, 44(1): 373 – 389. DOI: 10.1109/TPAMI.2020.3010942
- [9] YUAN C F, XU Y L, ZHOU Q. PLDS-SLAM: point and line features SLAM in dynamic environment [J]. *Remote sensing*, 2023, 15(7): 1893. DOI: 10.3390/rs15071893
- [10] ZHANG J, HENEIN M, MAHONY R, et al. VDO-SLAM: a visual dynamic object-aware SLAM system [EB/OL]. (2020-05-22) [2021-12-14]. <http://arxiv.org/abs/2005.11052>
- [11] CHO H M, KIM E. Dynamic object-aware visual odometry (VO) estimation based on optical flow matching [J]. *IEEE access*, 1961, 11: 11642 – 11651. DOI: 10.1109/ACCESS.2023.3241961
- [12] YE W C, LAN X Y, CHEN S, et al. PVO: panoptic visual odometry [C]//Proceedings of IEEE/CVF Conference on Computer Vision and Pattern Recognition (CVPR). IEEE, 2023: 9579 – 9589. DOI: 10.1109/CVPR52729.2023.00924
- [13] SHEN S H, CAI Y L, WANG W S, et al. DytanVO: joint refinement of visual odometry and motion segmentation in dynamic environments [C]//International Conference on Robotics and Automation (ICRA). IEEE, 2023: 4048 – 4055. DOI: 10.1109/ICRA48891.2023.10161306
- [14] DOSOVITSKIY A, FISCHER P, ILG E, et al. FlowNet: learning optical flow with convolutional networks [C]//International Conference on Computer Vision (ICCV). IEEE, 2015: 2758 – 2766. DOI: 10.1109/ICCV.2015.316
- [15] ILG E, MAYER N, SAIKIA T, et al. FlowNet 2.0: evolution of optical flow estimation with deep networks [C]//Conference on Computer Vision and Pattern Recognition (CVPR). IEEE, 2017: 1647 – 1655. DOI: 10.1109/CVPR.2017.179
- [16] JONSCHKOWSKI R, STONE A, BARRON J T, et al. What matters in unsupervised optical flow [M]//Lecture notes in computer science. Cham: Springer International Publishing, 2020: 557 – 572. DOI: 10.1007/978-3-030-58536-5_33
- [17] RANJAN A, BLACK M J. Optical flow estimation using a spatial pyramid network [C]//Conference on Computer Vision and Pattern Recognition (CVPR). IEEE, 2017: 2720 – 2729. DOI: 10.1109/CVPR.2017.291
- [18] SUN D Q, YANG X D, LIU M Y, et al. PWC-net: CNNs for optical flow using pyramid, warping, and cost volume [C]//Conference on Computer Vision and Pattern Recognition. IEEE, 2018: 8934 – 8943. DOI: 10.1109/CVPR.2018.00931
- [19] TEED Z, DENG J. RAFT: recurrent all-pairs field transforms for optical flow [M]//Lecture notes in computer science. Cham: Springer International Publishing, 2020: 402 – 419. DOI: 10.1007/978-3-030-58536-5_24
- [20] TEED Z, DENG J. RAFT-3D: Scene Flow using Rigid-Motion Embeddings [C]//Conference on Computer Vision and Pattern Recognition (CVPR). IEEE, 2021: 8371 – 8380. DOI: 10.1109/CVPR46437.2021.00827
- [21] REN Z L, GALLO O, SUN D Q, et al. A fusion approach for multi-frame optical flow estimation [C]//IEEE Winter Conference on Applications of Computer Vision (WACV). IEEE, 2019: 2077 – 2086. DOI: 10.1109/WACV.2019.00225
- [22] SHI H, ZHOU Y F, YANG K L, et al. CSFlow: learning optical flow via cross strip correlation for autonomous driving [C]//Intelligent Vehicles Symposium (IV). IEEE, 2022: 1851 – 1858. DOI: 10.1109/IV51971.2022.9827341
- [23] GARREPALLI R, JEONG J, RAVINDRAN R C, et al. DIFT: dynamic iterative field transforms for memory efficient optical flow [C]//Conference on Computer Vision and Pattern Recognition Workshops (CVPRW). IEEE, 2023: 2220 – 2229. DOI: 10.1109/CVPRW59228.2023.00216
- [24] HUI T W, TANG X O, LOY C C. A lightweight optical flow CNN: revisiting data fidelity and regularization [J]. *IEEE transactions on pattern analysis and machine intelligence*, 2021, 43(8): 2555 – 2569. DOI: 10.1109/TPAMI.2020.2976928
- [25] GALVEZ-LÓPEZ D, TARDOS J D. Bags of binary words for fast place recognition in image sequences [J]. *IEEE transactions on robotics*, 2012, 28(5): 1188 – 1197. DOI: 10.1109/TRO.2012.2197158
- [26] SUENDERHAUF N, SHIRAZI S, JACOBSON A, et al. Place recognition with ConvNet landmarks: viewpoint-robust, condition-robust, training-free [C]//Proceedings of Robotics: Science and Systems XI. Robotics: Science and Systems Foundation, 2015: 1 – 10. DOI: 10.15607/rss.2015.xi.022
- [27] GAO X, ZHANG T. Unsupervised learning to detect loops using deep neural networks for visual SLAM system [J]. *Autonomous robots*, 2017, 41(1): 1 – 18. DOI: 10.1007/s10514-015-9516-2
- [28] MERRILL N, HUANG G Q. Lightweight unsupervised deep loop closure [EB/OL]. (2018-05-24) [2023-10-10]. <http://arxiv.org/abs/1805.07703>
- [29] MEMON A R, WANG H S, HUSSAIN A. Loop closure detection using supervised and unsupervised deep neural networks for monocular SLAM systems [J]. *Robotics and autonomous systems*, 2020, 126: 103470. DOI: 10.1016/j.robot.2020.103470
- [30] TEED Z, DENG J. DROID-SLAM: deep visual SLAM for monocular, stereo, and RGB-D cameras [J]. *Advances in neural information processing systems*, 2021, 34: 16558 – 16569
- [31] ZHANG Y M, GUO X D, POGGI M, et al. CompletionFormer: depth completion with convolutions and vision transformers [C]//Conference on Computer Vision and Pattern Recognition (CVPR). IEEE, 2023: 18527 – 18536. DOI: 10.1109/CVPR52729.2023.01777
- [32] ZHANG F H, PRISACARIU V, YANG R G, et al. GA-net: guided aggregation net for end-to-end stereo matching [C]//Proceedings of IEEE/CVF Conference on Computer Vision and Pattern Recognition (CVPR). IEEE, 2019: 185 – 194. DOI: 10.1109/CVPR.2019.00027
- [33] CABON Y, MURRAY N, HUMENBERGER M. Virtual KITTI 2 [EB/OL]. (2020-01-29) [2023-10-10]. <http://arxiv.org/abs/2001.10773>
- [34] GEIGER A, LENZ P, STILLER C, et al. Vision meets robotics: the KITTI dataset [J]. *The international journal of robotics research*, 2013, 32(11): 1231 – 1237. DOI: 10.1177/0278364913491297
- [35] SCHUBERT D, GOLL T, DEMMEL N, et al. The TUM VI benchmark for evaluating visual-inertial odometry [C]//International Conference on Intelligent Robots and Systems (IROS). IEEE, 2018: 1680 – 1687. DOI: 10.1109/IROS.2018.8593419
- [36] MUR-ARTAL R, TARDÓS J D. ORB-SLAM2: An open-source SLAM

- system for monocular, stereo, and RGB-D cameras [J]. *IEEE transactions on robotics*, 2017, 33(5): 1255 - 1262. DOI: 10.1109/TRO.2017.2705103
- [37] BESCOS B, FÁCIL J M, CIVERA J, et al. DynaSLAM: tracking, mapping, and inpainting in dynamic scenes [J]. *IEEE robotics and automation letters*, 2018, 3(4): 4076 - 4083. DOI: 10.1109/LRA.2018.2860039
- [38] KERL C, STURM J, CREMERS D. Robust odometry estimation for RGB-D cameras [C]//*IEEE International Conference on Robotics and Automation*. IEEE, 2013: 3748 - 3754. DOI: 10.1109/ICRA.2013.6631104
- [39] DAI W C, ZHANG Y, LI P, et al. RGB-D SLAM in dynamic environments using point correlations [J]. *IEEE transactions on pattern analysis and machine intelligence*, 2022, 44(1): 373 - 389. DOI: 10.1109/TPAMI.2020.3010942
- [40] YE W C, YU X Y, LAN X Y, et al. DeFlowSLAM: self-supervised scene motion decomposition for dynamic dense SLAM [EB/OL]. [2023-10-10]. <https://arxiv.org/pdf/2207.08794v2>

Biographies

CHEN Hao (chen.hao16@zte.com.cn) received his BS and MS degrees in control theory and control engineering from Harbin Engineering University, China in 2018 and 2020. He has been engaged in deep learning technologies in ZTE Corporation since his graduation. His research interests include digital humans, SLAM, and image recognition.

ZHANG Kaijiong received his MS degree from Shanghai Jiao Tong University, China in 2020. He is currently an algorithm engineer with ZTE Corporation. His research interests include computer vision, image/video processing and artificial intelligence.

CHEN Jun received his master's degree in aerospace science and technology from Nanjing University of Aeronautics and Astronautics, China. He has been engaged in the R&D of computer graphics, computer vision, and cloud computing for more than 10 years in ZTE Corporation, and has accumulated rich experience in solution and engineering.

ZHANG Ziwen received his bachelor's degree in instrument science and technology and master's degree in instrument engineering from Harbin Institute of Technology, China in 2018 and 2020 respectively. After graduation, he worked at ZTE Corporation as a computer vision algorithm engineer. He has been engaged in algorithm research, design, improvement and end-to-end deployment optimization in the fields of face detection and recognition, image matching, SLAM, digital human generation, and portrait stylization migration for a long time, and has accumulated rich experience in these fields.

JIA Xia received her BS and MS degrees in control theory and control engineering from Taiyuan University of Technology, China, and Dalian University of Technology, China in 1995 and 2001, respectively. She joined ZTE Corporation in 2001 and worked in the State Key Laboratory of Mobile Network and Mobile Multimedia Technology. Her main research interests include deep learning techniques, face detection and recognition, Re-ID, and activity detection and recognition.

Video Enhancement Network Based on CNN and Transformer



YUAN Lang¹, HUI Chen¹, WU Yanfeng¹,
LIAO Ronghua¹, JIANG Feng², GAO Ying³

(1. Harbin Institute of Technology, Harbin 150001, China;
2. Sichuan University of Science & Engineering, Zigong 643002, China;
3. ZTE Corporation, Shenzhen 518057, China)

DOI: 10.12142/ZTECOM.202404011

<https://kns.cnki.net/kcms/detail/34.1294.TN.20241120.1435.004.html>,
published online November 20, 2024

Manuscript received: 2023-07-29

Abstract: To enhance the video quality after encoding and decoding in video compression, a video quality enhancement framework is proposed based on local and non-local priors in this paper. Low-level features are first extracted through a single convolution layer and then processed by several conv-tran blocks (CTB) to extract high-level features, which are ultimately transformed into a residual image. The final reconstructed video frame is obtained by performing an element-wise addition of the residual image and the original lossy video frame. Experiments show that the proposed Conv-Tran Network (CTN) model effectively recovers the quality loss caused by Versatile Video Coding (VVC) and further improves VVC's performance.

Keywords: attention fusion mechanism; H.266/VVC; transformer; video coding; video quality enhancement

Citation (Format 1): YUAN L, HUI C, WU Y F, et al. Video enhancement network based on CNN and transformer [J]. *ZTE Communications*, 2024, 22(4): 78 - 88. DOI: 10.12142/ZTECOM.202404011

Citation (Format 2): L. Yuan, C. Hui, Y. F. Wu, et al., "Video enhancement network based on CNN and transformer," *ZTE Communications*, vol. 22, no. 4, pp. 78 - 88, Dec. 2024. doi: 10.12142/ZTECOM.202404011.

1 Introduction

According to the 2023 China Internet Annual Report released by QuestMobile^[1], online video platforms continue to catch users' attention through a series of show content. In September 2023, the number of active users of Tencent Video had reached 416 million. Meanwhile, the emergence of 4K and 8K ultra-high definition (HD) videos and the rapid development of concepts such as virtual reality and meta-universe, have led to a fast rise in the total amount of video data flowing across the Internet. These developments have placed higher requirements for video technologies, such as high definition, small data transmission resources, and little storage space.

The current video compression technology^[2-3] typically exploits data redundancy in the spatial and temporal domains for compression. Based on the final effect, the compression methods can be classified into two categories: lossless compression and lossy compression. The former optimizes the way data is stored without affecting the content, but its compression ratio is not high enough. In contrast, lossy compression takes the

advantage of the human eye's insensitivity to color and sensitivity to brightness, and intentionally removes trivial information. Though the final decoded video is not identical to the original, it maintains the visual effect and can achieve an ideal compression ratio. However, when the compression ratio is limited, lossy compression introduces serious artifacts.

In recent years, deep learning technology has achieved great progress in various task fields. We can effectively obtain local information using convolutional neural networks (CNN). However, limited by the receptive field of the small kernel, CNN can only scan local areas step by step, which means global features are thus ignored. To alleviate the problem, we can utilize Transformer that uses a self-attention mechanism to construct long-range correlations and directly capture global textures. In visual tasks, to reduce computational complexity, Transformer splits the whole image into non-overlapping patches and then calculates the similarity between them. However, this method breaks the continuity of the adjacent block's edge, leading to inferior local modeling results. To combine the strengths of both models, we design a feature extractor based on both CNN and Transformer to obtain restoring features from different perspectives, and thus enhance the quality of video frames. To further improve the effectiveness of the network, we introduce the channel attention fusion mechanism, which selects the features extracted by CNN

This work was supported by the Key R&D Program of China under Grant No. 2022YFC3301800, Sichuan Local Technological Development Program under Grant No. 24YRGZN0010, and ZTE Industry-University-Institute Cooperation Funds under Grant No. HC-CN-03-2019-12.

and Transformer with an adaptive fusion ratio.

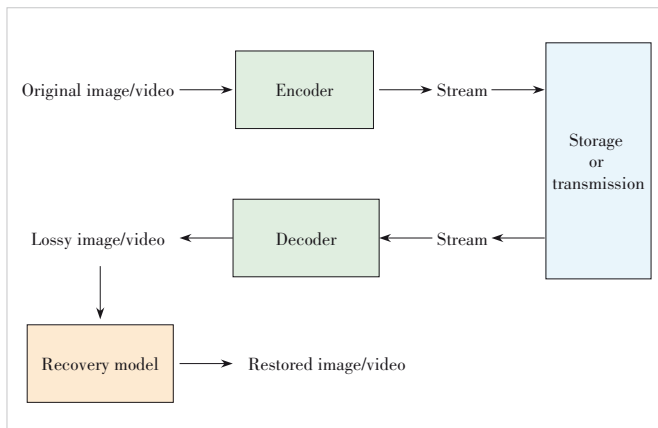
To effectively improve the quality of the decoded lossy video, we propose a video enhancement network based on convolution and Transformer, dubbed Conv-Tran Network (CTN). We use two feature extraction modules containing CNN and Transformer respectively as the backbone and introduce a multi-branch structure to ensure that the two modules do not interfere with each other while extracting recovery features. First, we employ a convolution layer to fuse the lossy video frame and its corresponding quantization-parameter (QP) value information, which raises the dimension and obtains low-level features. Second, these features are processed by several conv-tran blocks (CTB) and then transformed into a residual image after another convolution layer. The final reconstructed video frame is obtained by adding the residual image and the original lossy frame. Overall, the main contributions of CTN are as follows:

- 1) We propose a novel video enhancement network based on CNN and Transformer, which utilizes the local representations and global similarity to improve the reconstruction quality of videos.
- 2) A channel attention fusion mechanism is presented, which can effectively exploit the local and non-local priors to enhance the correlation between inter-components.
- 3) Compared to the existing methods, CTN can extensively recover quality loss after Versatile Video Coding (VVC) decoding and further enhance the coding performance of VVC.

2 Related Work

The vision restoring tasks can be divided into image compression restoring and video compression restoring. The specific process is shown in Fig. 1.

First, the encoder compresses the original lossless images or videos to generate a data stream for reducing the bandwidth utilization and storage space. Then, the decoder decodes the data stream to restore the images or videos when needed. However, the encoding and decoding processes usually introduce compression noise into the data, requiring additional recovery



▲ Figure 1. Process of restoring quality

algorithms to restore the lossy data. The final goal is to ensure that the images or videos recovered by the model are as similar as possible to the original ones.

2.1 Recovery Task

Image coding has been developed earlier than video coding and is easier to study, so many works are based on the Joint Photographic Experts Group (JPEG) or JPEG2000 to test the quality enhancement results of the recovery algorithms. The earliest work using neural networks to enhance the performance of codec is Artifacts Reduction CNN (ARCNN)^[4] proposed by DONG et al., which uses four layers of convolutional neural networks to recover JPEG compression artifacts through four steps: feature extraction, feature enhancement, map learning, and reconstruction, and finally improves the peak signal-to-noise ratio (PSNR) by more than 1 dB on five classic test pictures. WANG et al. used the prior knowledge of image splitting and discrete cosine transform in JPEG and proposed a dual-domain recovery method^[5] to enhance images from the frequent and spatial domain, which obtains better enhancement results with less time complexity than ARCNN. Moreover, some works concentrate on network structures, such as an iterative approach proposed by ORORBIA et al., to enhance JPEG images using recurrent neural networks^[6].

The first work for video coding recovery is Variable-filter-size Residue-Learning CNN (VRCNN)^[7] proposed by DAI et al., which draws from ARCNN. They designed a four-layer post-processing convolutional neural network to replace the deblocking filter and sample adaptive offset for enhancing video quality, saving an average bit rate of about 4.6% on High Efficiency Video Coding (HEVC) in the luminance component. Different video frames that are compressed differently produce different compression noise. YANG et al.^[8] designed and trained the Decoder-Side Scalable Convolutional Neural Network (DS-CNN). According to the types of encoded frames, they trained DS-CNN-I for I frames and DS-CNN-B for B frames. Experiments have shown that DS-CNN-I can improve the quality of 0.35 dB in HEVC codec for I frames, while DS-CNN-B achieves the same improvement of 0.35 dB for B frames.

During the 26th meeting of the JVET Video Joint Expert Group held in April 2022, QI et al.^[9] proposed that video quality enhancement should not just rely on the information extracted from the spatial domain but also utilize some essential information from the frequent domain to improve the decoded frame. They introduced a multi-scale frequent-domain recovery network, which starts from the network structure and saves the bit rate of 3.07% on the Y component.

2.2 Transformer

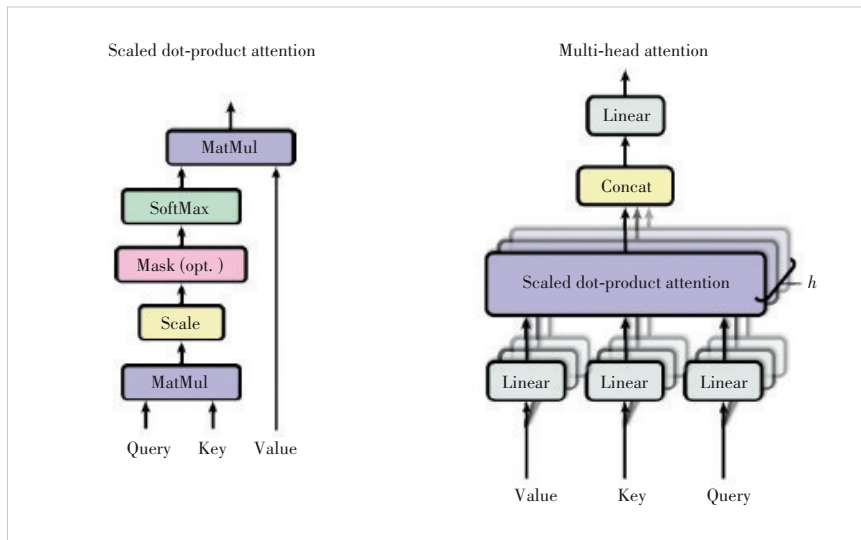
Classical neural network structures, such as multilayer perceptron (MLP), CNN, recurrent neural networks (RNN), and long short-term memory (LSTM), have been proven effective in

some specific tasks and domains. Transformer is first proposed in natural language processing^[10], which utilizes a self-attention structure (shown in Fig. 2) to mine the global correlation between word vectors. This non-recursive global attention calculation method reduces training time and decreases the performance degradation caused by long-term dependencies.

The first vision work that introduces the Transformer structure is the Vision Transformer (ViT),^[11] proposed by DOSOVITSKIY et al. To extract the global correlation of the entire image, the network divides the whole image into several blocks (i. e., patches) by analogy with the words in the field of natural language processing. Each block is projected and flattened to form a one-dimensional token, and these token sequences are exactly input into the network for encoding. Another task-oriented token is concatenated to extract the features for the recognition task, and positional encoding is used to preserve the absolute position information of the image blocks. Experiments show that the structure achieves better image recognition results than classical CNN structure models, proving the feasibility and superiority of the pure Transformer structure in the field of vision.

Swin Transformer^[12] proposed by LIU et al. is a recent work inspired by the Transformer architecture in 2021. Its goal is to reduce the computational complexity of the original Transformer while maintaining or even improving its performance. To achieve this, instead of computing the correlation between all pairs of patches, Swin Transformer only calculates the correlation between patches within a certain window. This reduces the computational complexity from $O(n^2)$ to $O(wn)$, where n is the number of patches and w is the size of the window. To achieve global modeling capabilities, Swin Transformer shifts the windows in the former layer, allowing information to flow between different parts of the image. Swin Transformer can use this window shifting mechanism to achieve high performance with much less computation than the original Transformer.

CHEN et al.^[13] proposed a Transformer-based pre-trained image processing model called Image Processing Transformer (IPT) for image restoration tasks. The model employs the classical Transformer structure as the backbone and is composed of a transformer encoder and decoder. To handle various recovery tasks, IPT uses multiple CNN-based task headers and task tails. The IPT model surpasses previous single-task image-processing models in multiple image-processing tasks. However, IPT also reveals some of the Transformer structure’s characteristics: to make a pure Transformer model to accomplish visual tasks, a surprisingly large training set is required,



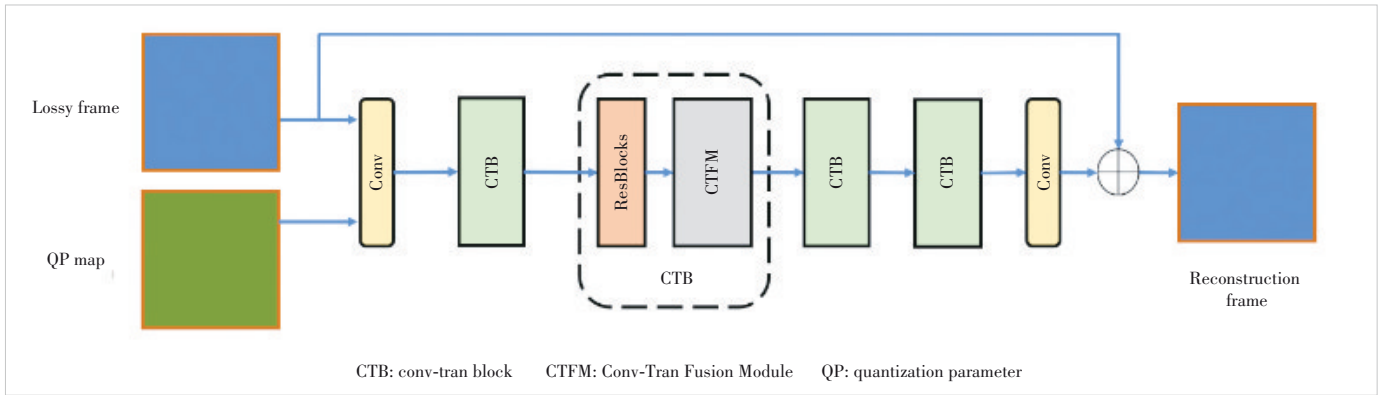
▲ Figure 2. Self-attention mechanism

and the model should be trained for a large number of epochs to learn the characteristics of visual image data.

LIANG et al.^[14] proposed a new super-resolution network, SwinIR, which combines the self-attention and CNN structures to design the Residual Swin Transformer Block (RSTB). Experiments demonstrate that SwinIR achieves better super-resolution image results than the IPT model with fewer parameters. To explore the potential of the network structure, ZHANG et al.^[15] also combined CNN and Transformer to build a recovery network. Unlike the serial structure, this work uses Swin Transformer and residual convolution modules in parallel to extract features and concatenate them and then uses a 1×1 convolutional layer to fuse the features adaptively. To further improve the performance, the work employs the classic U-Net framework, which fully utilizes the priority of different features extracted from the images by multi-scale methods. Finally, the structure achieves a competitive denoising result to SwinIR with lower computational complexity, which shows that the fusion network structure still has much potential to be further exploited. Inspired by this work, we propose a Conv-Tran Fusion Module (CTFM), combining the local and global modeling structures of CNN and Transformer to provide stronger feature extraction capabilities.

3 Proposed Method

The general structure of CTN is shown in Fig. 3. The input consists of two parts: the video frame with noise and the corresponding QP value. We focus on restoring the video frames that are generated by VVC in the random access coding mode. The compressed video sequences in this mode have different coding time series and orders, which means the video frames are assigned different QP values according to their time series layers. Meanwhile, different quantization parameters usually represent different degrees of distortion. Therefore, introduc-

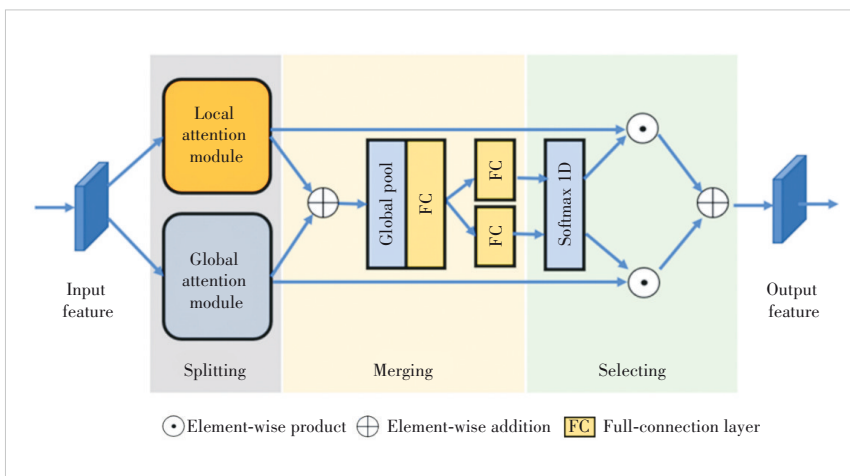


▲ Figure 3. Proposed video restoring network structure

ing this auxiliary information facilitates guiding the network to learn and eliminate different degrees of compression noise.

3.1 Overall Pipeline

We first apply a convolution layer to fuse the lossy video frame and the corresponding QP value information. The designed structure raises the channel dimension and extracts the low-level features of the image. Then the features above go through several CTBs (Fig. 3) and are transformed into a residual image by another convolution layer. The final reconstructed video frame is obtained by adding the residual image and the original lossy frame. Moreover, we normalize the QP value by scaling it to 1/63 of the original value. Through the whole process, CTB deeply extracts features from the input. CTB itself includes several residual blocks ahead to preprocess the input image and obtain a representation suitable for the CTFM (Fig. 4) to recover the features. The structure of Res-Block includes a 3×3 convolution layer at the beginning and the end. For the non-linear part, we use a Parametric Rectified Linear Unit (PReLU) activation function in the middle, and an addition connection is then created to obtain a stronger generalization ability of the residual block.



▲ Figure 4. Conv-tran fusion module

Specifically, the network input is a video frame consisting of three channels: Y, U, and V. After the local and global feature fusion of several CTB blocks, the correlation of luminance and chrominance components has been improved. Moreover, in the following formulas, our designed loss function in Eq. (8) weights the three components separately based on the human eye's sensitivity to different visual information. This will fully exploit the correlation between luminance and chrominance to achieve better performance.

3.2 Conv-Tran Fusion Module

The purpose of the proposed fusion sub-module CTFM is to integrate the characteristics of CNN and Transformer and thus provide stronger feature extraction capability for CTB blocks. The combination modes of CNN and Transformer can be divided into two types: serial combination, such as SwinIR, and parallel combination, such as Swin-Conv-Unet. We comprehensively design the fusion structure with reference to the latter's parallel combination and further improve their fusion mode by using the channel attention mechanism. Specifically, instead of dividing the input features during the combination process, we first make the whole input go through the CNN and Transformer respectively to ensure the integrity of the input features. Secondly, we introduce a channel attention fusion structure inspired by SKNet^[16]. The final output of the CTFM module is a weighted sum of the recovery information output by the two branches.

CTFM is structured into three parts: splitting, merging, and selecting. In the splitting step, the input feature F_{in} is sent to a Local Attention Module (LAM) that is based on the convolution layer, and a Global Attention Module (GAM) that consists of a Transformer. The two modules analyze the features from different perspectives to obtain a local representation F_{la} and a global representation F_g respectively. In order to deeply com-

pute the correlation between local and global features, we use element-wise multiplication to fuse the local and global features. The final output of the CTFM module is a weighted sum of the recovery information output by the two branches.

bine the modeling capabilities of LAM and GAM, in the merging step, we obtain the weights of the above two modules. The channel fusion mechanism of SKNet is actually adopted in this step, and we can get the two weights \tilde{W}_{la}^c and \tilde{W}_{ga}^c of the two channels. In the implementation, the merging module first performs an additional operation on the representations output by the two modules, as shown in Eq. (1). And then, F_{gla} is processed by a global average pooling layer to get the statistical information on the channel. The information passes through a full connection layer (FCS), which transfers the information from the recovery domain to the weight domain. Finally, the channel weights \tilde{W}_{la}^c and \tilde{W}_{ga}^c of the two modules are extracted through another linear layer, as shown in Eq. (2).

$$F_{gla} = F_{la} + F_{ga}, \quad (1)$$

$$\tilde{W}_{la}^c, \tilde{W}_{ga}^c = \text{FCS}\left(\text{GlobalPool}\left(F_{gla}\right)\right). \quad (2)$$

In the selection part, first, we use SoftMax (“SM” in the equation) to normalize the two above channel weights \tilde{W}_{la}^c and \tilde{W}_{ga}^c , to obtain the final fusion weights W_{la}^c and W_{ga}^c , as shown in Eq. (3). Then the restoration features output by the LAM and GAM modules are weighted and summed with these weights to obtain a deep fusion result F_{out} , as shown in Eq. (4).

$$W_{la}^c, W_{ga}^c = \text{SM}\left(\tilde{W}_{la}^c, \tilde{W}_{ga}^c\right), \quad (3)$$

$$F_{out} = W_{la}^c \times F_{la} + W_{ga}^c \times F_{ga}. \quad (4)$$

3.3 Module Details

The fusion method used by CTFM contains the local feature extraction module LAM and the global feature extraction module GAM, which are based on CNN and Transformer respectively. Their module details are shown in Fig. 5.

The local feature extraction module LAM is based on the CNN structure, using three cascaded 3×3 convolution layers, and after each convolution layer, the PReLU activation function is used for nonlinear mapping. LAM uses the limited receptive field of the convolution kernel to observe and process the local area features and obtains the feature representation from the local angle. The global feature extraction module GAM extracts features based on the structure of the Swin Transformer^[12]. The input image is three-dimensional, but Transformer can only process two-dimensional information. Therefore, the two problems that need to be solved are how to convert three-dimensional fea-

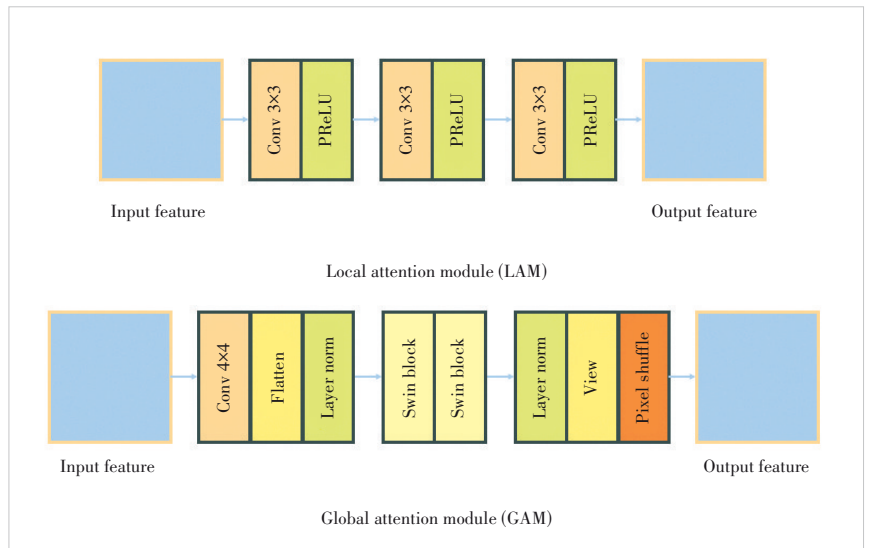
tures into two-dimensional features for Transformer to process (embedding), and how to convert the dimension back after Transformer outputs features. Our design scheme for the above two problems is as follows. For the GAM (W, H, C) shaped input, we first use the 4×4 convolution layer with the kernel size equal to the stride to complete the block-splitting operation. After this, the shape turns to $(W/4, H/4, 16 \times C)$, and then we use the transpose and flatten functions to obtain a two-dimensional shape of $(16 \times C, W/4 \times H/4)$.

For the output of Transformer, on the contrary, the output of the features by Swin Block needs to be embedded reversely. First, we use the view function to transform the features from 2D to 3D ($W/4, H/4, 16 \times C$). Then we employ pixel-shuffle to up-sample the feature (W, H, C). It should be noticed that the window size of the Swin Transformer block is set to 8, that is, each window calculates the global similarity of 8×8 on $16C$ -dimensional vectors; the shift distance is set to 4, which is half of the window size, to ensure that the information can be fully exchanged between the shifted windows. The number of multi-headed self-attention blocks is set to 4, which ensures that the global feature representation can be extracted from multiple angles.

4 Experiments

4.1 Datasets

We use BVI-DVC^[17] as the training set, and the standard test sequence defined in JVET Common Test Condition (CTC)^[18] as the test set. BVI-DVC includes 800 video sequences in the YUV420 format, with various resolutions: 3840×2176 , 1920×1088 , 960×544 , and 480×272 . Each resolution category contains 200 video sequences and we choose 191 video sequences from each resolution of BVI-DVC under CTC. The standard test sequences defined by CTC (Table 1) cover differ-



▲ Figure 5. Detailed structure of LAM and GAM

ent resolutions, frame rates, bit depths, and video sequences with features such as complex foreground, complex background, simple or strenuous movement, and complex textures.

Before the experiment, we obtain the video sequence with compressed noise for the training and test by encoding and decoding the original video using the VVC codec. We use the VTM11.0-NNVC coding framework^[19] to compress and encode all video sequences and decode the stream output to obtain a video sequence with compressed noise. These lossy video sequences and the original lossless video sequences contribute to the dataset together. We employ the random access encoding pattern, which has the maximum compression ratio and can effectively test the recovery effect of our recovery model. To train and test the recovery effect of the model under different bit-rate conditions, each video sequence is encoded and decoded on the following five QP values: 22, 27, 32, 37, and 42.

The dataset details are as follows. To simplify the training set, only the first 16 frames are compressed into the training set for videos with a resolution of 3 840×2 176. While for other lower resolution sequences, the first 64 frames are compressed and included in the training set. Each video is produced to get five corresponding lossy videos according to the mentioned QP value requirements. The final training set contains a total of 198 640 images. It should be noted that the bit depth of the test set video sequence is different. Therefore, to normalize the dataset, all 8-bit test videos are processed to 10 bits in advance.

4.2 Training Details

All experiments in this paper are performed on Ubuntu

▼ **Table 1. Standard testing sequences in CTC**

Class	Video Sequence	Frames	Resolution	FPS	Bit Depth
Class A1	Tango2	294	3 840×2 160	60	10
	FoodMarket4	300	3 840×2 160	60	10
	Campfire	300	3 840×2 160	30	10
Class A2	CatRobot	300	3 840×2 160	60	10
	DaylightRoad2	300	3 840×2 160	60	10
	ParkRunning3	300	3 840×2 160	50	10
Class B	MarketPlace	600	1 920×1 080	60	10
	RitualDance	600	1 920×1 080	60	10
	Cactus	500	1 920×1 080	50	8
	BasketballDrive	500	1 920×1 080	50	8
	BQTerrace	500	1 920×1 080	60	8
Class C	RaceHorses	300	832×480	30	8
	BQMall	600	832×480	60	8
	PartyScene	500	832×480	50	8
	BasketballDrill	500	832×480	50	8
Class D	RaceHorses	300	410×240	30	8
	BQSquare	600	410×240	60	8
	BlowingBubbles	500	410×240	50	8
	BasketballPass	500	410×240	50	8

CTC: Common Test Condition FPS: frames per second

18.04.1 using NVIDIA GeForce RTX 3060 with a total video memory size of 24G. Pytorch 1.10.0 is used as the deep learning framework with the CUDA version 11.4. We update the network model parameters using the Adam optimizer with the optimization coefficients set to 0.9 and 0.999. The initial learning rate is set to 2e-4, and for every 1e5 epoch, the learning rate decreases by 0.5, with the final learning rate decreasing to 5e-5. The video frames to be recovered are in the YUV420 format, where every four luminance components share a pair of chromaticity components. As neural networks cannot accept irregular input, we convert the YUV420 video frame into the YUV444 format using the nearest neighbor interpolation method before the input lossy video frame is restored. After we obtain the recovered video frame, the components of the restored frame are down-sampled back to the YUV420 format using 2×2 average pooling to compare with the lossy video frame.

As to the parameters, for all the resblocks in the model, we set the kernel size, padding and stride to 3, 1, and 1. In Swin Transformer, the window size is 8 while the extraction depth is 6. Considering the input frame 256×256, the average decoding time for four classes from D to A is 52.99 s, 193.26 s, 1 188.66 s, and 4 232.59 s. Furthermore, we measure the computational complexity of the proposed model. Under the metrics of floating point operations (FLOPs), our model achieves a complexity of 1.673 1×10¹¹ FLOPs.

During training, we randomly divide video frames into several blocks with the size of 256×256 from the dataset, randomly flip them, rotate them for data augmentation, and then put them into the network. The batch size is set to 6, and the model is trained for 2×10⁶ iterations. To be noticed, Class B, C and D video frames are fully input into the network for the recovery test. However, the resolution of Class A is too high because it occupies too many video memory resources during the calculation. Therefore, the video frames of Class A are divided into image blocks of 960×960 with 32 overlapping pixels for testing, and the output is the average value of the corresponding position of each image block.

4.3 Evaluation Criteria

In video coding enhancement tasks, two commonly used evaluation methods are the video quality after decoding and the stream size during video encoding. To assess video quality, PSNR is the most commonly used metric for measuring the similarity between the original and the recovered signals. The equation is as follows:

$$\text{PSNR} = 10 \times \lg \left(\frac{(255 \ll (\text{bitDepth} - 8))^2}{\text{MSE}} \right), \quad (5)$$

$$\text{MSE} = \frac{1}{M \times N} \sum_{i=1}^M \sum_{j=1}^N (x_{i,j} - \widetilde{x}_{i,j})^2, \quad (6)$$

where bitDepth represents the bit depth of the video frame, MSE is the mean square error, x is the original signal, \tilde{x} represents the signal to be evaluated, and M and N are the length and width of the video frame, respectively. The larger the PSNR is, the smaller the distortion of the signal. Other visual evaluation criteria, such as structural similarity (SSIM) and multi-scale structural similarity (MS-SSIM)^[20], are designed based on the human eye's view of the image to extract structured information and thus are more sensitive to local structure transformations. PSNR is commonly used due to its convenience and consistency with image quality, while MS-SSIM is also used as an auxiliary evaluation index to make up for the deficiency of the PSNR. To obtain quantitative results, we calculate the outputs of all video frames according to the quantitative indicators, and the mean value of all video frames is the final quantitative result of the video. The bit rate is also important for measuring coding performance, as a lower bit rate indicates higher compression. To test the recovery effect of the enhancement model on the decoded videos under different QP, we select Bjontegaard Delta-Rate (BD Rate) as the evaluation metrics of coding performance. When the BD Rate is negative, a higher bit rate is saved under the same objective quality, and the codec has a better effect after using this recovery method. We calculate the BD Rate based on PSNR and SSIM to measure the enhancement effect of the mode on VVC.

We employ Charbonnier Loss as the loss function for train-

ing CTN. It has two advantages: firstly, it alleviates the problem that small gradients occur when L1 Loss approaches 0. Secondly, for values far from zero, Charbonnier Loss does not cause gradient explosions. Assuming the original lossless data is represented as x and the data recovered by the model after restoration is represented as \tilde{x} , with N samples used for each iteration during training, the expression of Charbonnier Loss is shown in the following equation.

$$L_{chb}(x, \tilde{x}) = \frac{1}{N} \sum_{i=1}^N \sqrt{(x - \tilde{x}) + \epsilon^2} \quad (7)$$

Due to the human eye's different sensitivity to luminance and chrominance, we use different weights for YUV. Specifically, the weight ratio is Y:U:V = 10:1:1, and the final loss function used for model optimization is as follows.

$$L_{total} = 10 \times L_{chb}(x_Y, \tilde{x}_Y) + L_{chb}(x_U, \tilde{x}_U) + L_{chb}(x_V, \tilde{x}_V) \quad (8)$$

4.4 Results and Analysis

The CTN-Channel (CTN-C) model is tested on a GPU throughout the whole process. After training, the recovery effect is tested under QP = 32. The quantitative outcomes are presented in Table 2, which reveals that our proposed restoration model, CTN-C, can improve the average PSNR of the decoded lossy video on Y, U, and V components by 0.07 dB,

▼Table 2. PSNR under the random access mode

Class	Video Sequence	VTM11.0-NNVC				VTM11.0-NNVC with CTN-C			
		Y-PSNR /dB	U-PSNR /dB	V-PSNR /dB	Decoding Time/s	Y-PSNR /dB	U-PSNR /dB	V-PSNR /dB	Decoding Time/s
A1	Tango2	38.86	47.51	44.89	65.64	38.88	47.63	44.83	4 181.96
	FoodMarket4	41.21	46.00	46.16	70.30	41.23	46.02	46.19	4 234.27
	Campfire	36.52	35.97	39.81	80.85	36.54	36.03	39.86	4 267.28
A2	CatRobot	38.41	40.82	41.37	65.04	38.45	40.90	41.44	4 250.03
	DaylightRoad2	36.47	44.15	41.85	69.64	36.51	44.29	41.91	4 278.40
	ParkRunning3	36.50	32.89	34.59	106.77	36.53	33.00	34.63	4 285.42
B	MarketPlace	36.86	41.96	42.80	36.46	36.89	42.16	42.93	1 270.89
	RitualDance	38.73	44.30	44.25	35.87	38.80	44.44	44.45	1 269.88
	Cactus	35.60	38.87	41.22	27.34	35.61	38.92	41.30	1 059.97
	BasketballDrive	36.31	42.06	42.23	46.94	36.33	42.16	42.39	1 078.13
	BQTerrace	34.38	40.84	43.44	30.64	34.35	40.96	43.48	1 265.19
C	BasketbalDrill	35.79	39.87	40.10	6.83	35.85	40.05	40.32	204.68
	BQMall	35.82	41.07	42.03	10.80	35.91	41.34	42.26	247.90
	PartyScene	32.59	38.04	38.89	10.98	32.71	38.34	38.98	208.78
	RaceHorses	33.75	37.51	39.50	9.57	33.79	37.69	39.65	128.08
D	BasketballPass	34.18	39.82	38.13	3.20	34.33	40.12	38.42	58.09
	BQSquare	32.64	40.59	41.68	1.91	32.98	40.76	41.92	67.57
	BlowingBubbles	32.58	37.51	38.28	2.88	32.71	37.81	38.38	58.01
	RaceHorses	33.13	37.16	38.49	1.37	33.24	37.44	38.70	34.16
Overall	35.81	40.37	41.04	35.95	35.88	40.53	41.16	1 707.83	

CTN: Conv-Tran Network PSNR: peak signal-to-noise ratio

0.17 dB and 0.12 dB, respectively. For the video sequence that has the best effect, our obtained PSNR improvement is 0.34 dB, 0.30 dB and 0.29 dB. Additionally, the model enhances video quality in almost all video sequences, indicating its good generalization ability. Furthermore, the model takes both luminance and chrominance as inputs and effectively utilizes the correlation between different components in the image space to significantly enhance the visual effect of the chrominance components.

According to the JVET CTC, we also perform tests under five quantization factors $QP = 22, 27, 32, 37$ and 42 . Compared to the decoded lossy video after VTM11.0-NNVC, the BD-rate evaluation results based on PSNR and MS-SSIM (MSIM in the table) are presented respectively. The evaluation data are shown in Table 3.

The recovery effect of CTN-C on VTM11.0-NNVC shows the following characteristics:

1) It achieves quality recovery for all test classes, with the most significant effect on Class D, which achieves a bit rate saving effect of 4.09% in the luminance component. This indicates that the proposed model performs better in recovering sequences with a small resolution.

2) CTN-C demonstrates more effective performance on the chrominance component than the luminance component. The main reason is that, during video compression, chrominance information is always down-sampled and much sparser because of the human visual system's greater sensitivity in luminance than chrominance. In the YUV420 format dataset used in our study, the luminance component maintains the same shape as the resolution, but the chrominance component has only half the width and height of the resolution. Meanwhile, the human eye is more sensitive to luminance than to chrominance^[21-22]. Therefore, video coding and compression algorithms typically apply stronger compression to chrominance (U and V components). As a result, the chrominance becomes relatively sparser compared to the luminance in the video data and is easier to obtain better gain effects.

3) On average, the decoding time required by CTN-C increases by about 30 times, which is a weakness of the neural network compared to traditional image processing algorithms. Although GPU acceleration is used in the experiment, the decoding time still significantly increases.

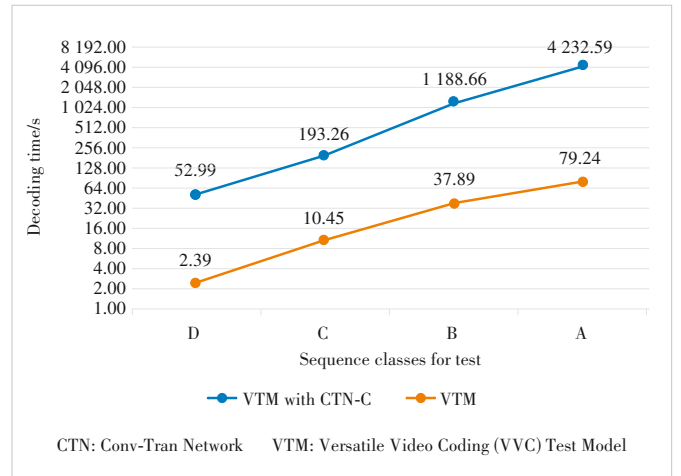
To further analyze the decoding time of the CTN-C at different resolutions, we summarize the average time for each test class in Fig. 6.

In Fig. 6, we can observe that the decoding time of CTN-C increases with video resolution since the neural network's calculation complexity on each pixel is fixed. As the resolution goes higher, the time consumption of CTN-C is proportional to it. In contrast, the time consumption of the VTM decoder is gradually lower than this proportional line, so the ratio of the two models' decoding time (CTN-C and VTM) increases with the test class resolution.

▼ **Table 3. Improvement of CTN-C compared with VTM11.0-NNVC under the random access mode**

Class	Y-PSNR	U-PSNR	V-PSNR	Y-MSIM	U-MSIM	V-MSIM	DecT
Class A1	-0.80%	-2.87%	-0.12%	-1.02%	-5.32%	-1.28%	5 415%
Class A2	-1.54%	-6.75%	-2.47%	-1.45%	-5.30%	-1.35%	5 268%
Class B	-0.27%	-6.22%	-4.84%	-1.21%	-5.91%	-4.31%	3 137%
Class C	-1.91%	-8.13%	-5.53%	-1.40%	-6.47%	-3.67%	1 849%
Class D	-4.09%	-8.58%	-6.39%	-1.99%	-6.53%	-3.91%	2 220%
Overall	-1.70%	-6.68%	-4.19%	-1.42%	-5.97%	-3.15%	3 087%

MSIM: multi-scale structural similarity PSNR: peak signal-to-noise ratio



▲ **Figure 6. Decoding time with respect to the test class**

However, in Table 3, it is paradoxical that the ratio of Class D with a smaller resolution is higher than that of Class C. This is because, to satisfy the minimum pixel partition condition of the Swin Transformer window, an additional mirror-filling operation on the borders of the video frame is required for Class D. As a result, CTN-C takes more time to recover the filled area. Consequently, the recovery time per pixel for the original video frame becomes longer, specifically $5.4e-4$ unit time for D and $4.8e-4$ for C, and the ratio of the two models' decoding time in Class D is longer than that in Class C.

Table 4 presents the details of the bit rate optimization of CTN-C for VTM11.0-NNVC on each video sequence. The average recovery effects on video frame quality at high QP (27 - 42) are -1.85%, -7.23%, and -4.50%, compared with the recovery effects of -1.62%, -6.14%, and -4.01% at low QP values (22 - 37). The increased QP value results in a higher compression ratio, leads to more information loss, and provides more space for the quality recovery model.

4.5 Ablation Study

We present ablation experiments to validate the effect of the recovery model's channel attention fusion mechanism proposed in the CTFM fusion module. Specifically, the channel attention fusion structure is removed from CTFM, and the outputs of LAM and GAM are directly added. Then we retrain

▼Table 4. BD rate (PSNR) of CTN-C on VTM11.0-NNVC under the random access mode

Class	Video Sequence	Low QP (22 - 37)			High QP (27 - 42)		
		Y	U	V	Y	U	V
A1	Tango2	-0.78%	-6.16%	2.14%	-1.04%	-7.10%	2.35%
	FoodMarket4	-0.62%	-0.21%	-0.73%	-0.87%	-0.56%	-0.82%
	Campfire	-0.48%	-1.16%	-1.46%	-1.07%	-2.00%	-2.27%
A2	CatRobot	-1.75%	-6.47%	-3.11%	-1.98%	-7.69%	-3.81%
	DaylightRoad2	-2.41%	-7.77%	-2.61%	-2.13%	-9.33%	-1.95%
	ParkRunning3	-0.35%	-3.96%	-1.70%	-0.70%	-4.78%	-1.68%
B	MarketPlace	-1.05%	-9.68%	-6.17%	-1.23%	-10.11%	-7.17%
	RitualDance	-1.53%	-4.21%	-5.29%	-1.50%	-5.12%	-6.41%
	Cactus	-0.19%	-3.63%	-3.08%	-0.59%	-5.55%	-3.28%
C	BasketballDrive	-0.54%	-4.98%	-5.63%	-0.90%	-4.91%	-5.62%
	BQTerrace	3.18%	-6.99%	-3.04%	1.66%	-5.73%	-2.75%
	BasketballDrill	-1.49%	-5.63%	-6.27%	-1.58%	-6.37%	-6.36%
D	BQMall	-2.26%	-8.41%	-6.42%	-2.37%	-10.39%	-7.65%
	PartyScene	-3.22%	-9.02%	-2.67%	-2.88%	-11.47%	-3.38%
	RaceHorses	-0.57%	-6.47%	-5.76%	-1.05%	-8.04%	6.85%
Overall	BasketballPass	-2.97%	-8.83%	-7.96%	-3.24%	-10.70%	-8.35%
	BQSquare	-8.20%	-6.02%	-7.88%	-8.13%	-6.53%	-8.39%
	BlowingBubbles	-3.14%	-8.62%	-2.49%	-3.11%	-10.78%	-3.70%
	RaceHorses	-2.39%	-8.40%	-6.13%	-2.42v	-10.26%	-7.32%
	Overall	-1.62%	-6.14%	-4.01%	-1.85%	-7.32%	-4.50%

BD rate: Bjontegaard Delta-Rate CTN: Conv-Tran Network PSNR: peak signal-to-noise ratio QP: quantization-parameter

the model based on the experimental environment configuration. The modified model is named CTN-E. Table 5 shows the recovery outcomes obtained by CTN-E on VTM11.0-NNVC and we compare them with the gain effect of CTN-C. The results demonstrate that the channel attention fusion mechanism enhances the image recovery model’s performance by saving 1.06%, 3.61% and 3.56% in the BD rate for the Y, U, and V components respectively. This indicates that the fusion mechanism effectively improves the model’s image recovery capabilities.

To better demonstrate the superiority of the feature extraction module proposed in our study, we conduct extra ablation experiments to prove that both LAM and GAM are necessary parts of our model. Concretely, we remove LAM and the fusion mechanism from CTFM, remain only GAM, and name the

modified model CTN-G. Then we also remove GAM and the fusion structure, leave LAM alone, and name it CTN-L. The two models are then trained under the same experimental environment and hyperparameters. Table 6 shows the output of three models on VTM.

It is observed that CTN-C performs the best in almost all classes, owing to its two-perspective feature extraction module and adaptive fusion mechanism. Moreover, due to Transformer employed by CTN-G, it can better explore global features and has superior modeling capabilities compared to traditional CNNs, leading to better performance on the test set compared with CTN-L.

4.6 Visualization

The video quality enhancement model is evaluated using the

▼Table 5. Gain effects of CTN-C compared with CTN-E

Class	VTM with CTN-C			VTM with CTN-E		
	Y-PSNR	U-PSNR	V-PSNR	Y-PSNR	U-PSNR	V-PSNR
Class A1	-0.80%	-2.87%	-0.12%	-0.20%	-1.91%	-0.41%
Class A2	-1.54%	-6.75%	-2.47%	-0.74%	-3.04%	-0.40%
Class B	-0.27%	-6.22%	-4.84%	-0.11%	-2.82%	-0.36%
Class C	-1.91%	-8.13%	-5.53%	-0.59%	-3.38%	-0.96%
Class D	-4.09%	-8.58%	-6.39%	-1.88%	-3.98%	-0.99%
Overall	-1.70%	-6.68%	-4.19%	-0.64%	-3.07%	-0.63%

CTN: Conv-Tran Network PSNR: peak signal-to-noise ratio VTM: Versatile Video Coding (VVC) Test Model

▼ **Table 6. Comparison of CTN-G and CTN-L with CTN-C on VTM**

Class	VTM with CTN-C			VTM with CTN-G			VTM with CTN-L		
	Y-PSNR	U-PSNR	V-PSNR	Y-PSNR	U-PSNR	V-PSNR	Y-PSNR	U-PSNR	V-PSNR
Class A1	-0.80%	-2.87%	-0.12%	-0.42%		-0.37%	-0.33%	-1.74%	-0.15%
Class A2	-1.54%	-6.75%	-2.47%	-1.13%	-3.77%	-1.75%	-0.69%	-3.58%	-0.95%
Class B	-0.27%	-6.22%	-4.84%	-0.33%	-2.79%	-2.06%	-0.18%	-2.23%	-1.36%
Class C	-1.91%	-8.13%	-5.53%	-0.92%	-3.19%	-2.24%	-0.74%	-2.93%	-1.58%
Class D	-4.09%	-8.58%	-6.39%	-1.64%	-3.53%	-3.35%	-1.13%	-2.46%	-1.87%
Overall	-1.70%	-6.68%	-4.19%	-0.88%	-2.83%	-2.25%	-0.49%	-1.17%	-1.07%

CTN: Conv-Tran Network PSNR: peak signal-to-noise ratio VTM: Versatile Video Coding (VVC) Test Model

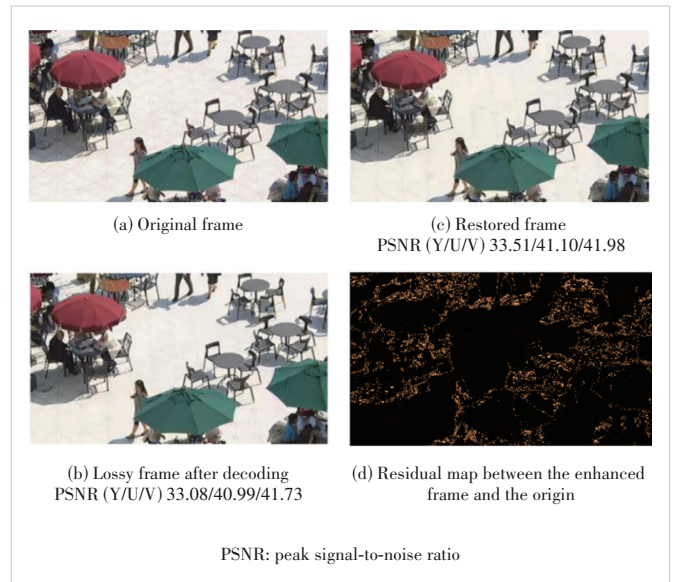
fourth frame of the BQSquare in the CTC test video sequence Class D at QP value 32. The output recovery frame of CTN-C is visualized and analyzed, and the findings are presented in Fig. 7. To get a straightforward understanding of the lossy position after encoding and the effect of video enhancement, we generate a residual map as shown in Fig. 7d on the luminance component. In Fig. 7d, the enhanced lossy frame in Fig. 7c is compared with the original video frame in Fig. 7a to observe the position of the video frame after being enhanced. The different positions with brighter colors indicate a higher difference in the residual map. As shown in Fig. 7d, the loss of the luminance component is gathered in the texture complex areas like tables, sunshade edge areas, chairs, and human bodies, indicating that the proposed video quality-enhancement model CTN-C can effectively identify the damaged areas and repair them, but still cannot be identical to the origin.

5 Conclusions

In this paper, we propose the adaptive fusion restoration model CTN based on CNN and Transformer, which effectively removes compression noise introduced by video codec in the random access coding mode. We focus on designing the fusion module CTFM of CTN, where a multi-branch structure is used to extract restoration features from two perspectives using CNN and Swin Transformer. Then a channel attention mechanism is used to deeply fuse the two features. We also show the detailed structure of the local and global modules LAM and GAM. Experiments show that the proposed model, CTN, takes both brightness and chroma components as inputs, effectively utilizes the inter-component correlation in the spatial domain, and significantly restores the visual effect on the chroma component. Compared with existing methods, CTN can extensively recover quality loss after VVC coding and further enhance the coding efficiency of VVC.

References

- [1] QuestMobile. QuestMobile's 2023 annual report on china internet core trends (condensed version) [R/OL]. (2023-12-19) [2024-03-20]. <https://www.questmobile.com.cn/research/report/1737028262113153026>
- [2] WIEGAND T, SULLIVAN G J, BJONTEGAARD G, et al. Overview of the



▲ **Figure 7. Visualization of the enhanced frame and the original**

- [3] H.264/AVC video coding standard [J]. IEEE transactions on circuits and systems for video technology, 2003, 13(7): 560 - 576. DOI: 10.1109/TCSVT.2003.815165
- [4] SULLIVAN G J, OHM J R, HAN W J, et al. Overview of the high efficiency video coding (HEVC) standard [J]. IEEE transactions on circuits and systems for video technology, 2012, 22(12): 1649 - 1668. DOI: 10.1109/TCSVT.2012.2221191
- [5] DONG C, DENG Y B, LOY C C, et al. Compression artifacts reduction by a deep convolutional network [C]//Proc. IEEE International Conference on Computer Vision (ICCV). IEEE, 2015: 576 - 584. DOI: 10.1109/ICCV.2015.73
- [6] WANG Z Y, LIU D, CHANG S Y, et al. D3: deep dual-domain based fast restoration of JPEG-compressed images [C]//Proc. IEEE Conference on Computer Vision and Pattern Recognition (CVPR). IEEE, 2016: 2764 - 2772. DOI: 10.1109/CVPR.2016.302
- [7] ORORBIA A G, MALI A, WU J, et al. Learned neural iterative decoding for lossy image compression systems [C]//Proc. Data Compression Conference (DCC). IEEE, 2019: 3 - 12. DOI: 10.1109/DCC.2019.00008
- [8] DAI Y Y, LIU D, WU F. A convolutional neural network approach for post-processing in HEVC intra coding [M]//Lecture notes in computer science. Cham: Springer International Publishing, 2016: 28 - 39. DOI: 10.1007/978-3-319-51811-4_3
- [9] YANG R, XU M, WANG Z L. Decoder-side HEVC quality enhancement

- with scalable convolutional neural network [C]/Proc. IEEE International Conference on Multimedia and Expo (ICME). IEEE, 2017: 817 – 822. DOI: 10.1109/ICME.2017.8019299
- [9] QI Z Y, JUNG C, LIU Y, et al. CNN-based post-processing filter for video compression with multi-scale feature representation [C]/Proc. IEEE International Conference on Visual Communications and Image Processing (VCIP). IEEE, 2022: 1 – 5. DOI: 10.1109/VCIP56404.2022.10008797
- [10] VASWANI A, SHAZEER N, PARMAR N, et al. Attention is all you need [C]/Proc. 31st International Conference on Neural Information Processing Systems. NIPS, 2017: 6000 – 6010. DOI: 10.48550/arXiv.1706.03762
- [11] DOSOVITSKIY A, BEYER L, KOLESNIKOV A, et al. An image is worth 16×16 words: transformers for image recognition at scale [EB/OL]. (2020-10-22)[2024-03-20]. <https://arxiv.org/abs/2010.11929>
- [12] LIU Z, LIN Y T, CAO Y, et al. Swin transformer: hierarchical vision transformer using shifted windows [C]/Proc. IEEE/CVF International Conference on Computer Vision (ICCV). IEEE, 2021: 9992 – 10002. DOI: 10.1109/ICCV48922.2021.00986
- [13] CHEN H T, WANG Y H, GUO T Y, et al. Pre-trained image processing transformer [C]/Proc. IEEE/CVF Conference on Computer Vision and Pattern Recognition (CVPR). IEEE, 2021: 12294 – 12305. DOI: 10.1109/CVPR46437.2021.01212
- [14] LIANG J Y, CAO J Z, SUN G L, et al. SwinIR: image restoration using swin transformer [C]/2021 IEEE/CVF International Conference on Computer Vision Workshops (ICCVW). IEEE, 2021. DOI: 10.1109/ICCVW54120.2021.00210
- [15] ZHANG K, LI Y W, LIANG J Y, et al. Practical blind image denoising via swin-conv-UNet and data synthesis [J]. Machine Intelligence Research, 2023, 20: 822 – 836. DOI: 10.1007/s11633-023-1466-0
- [16] LI X, WANG W H, HU X L, et al. Selective kernel networks [C]/Proc. IEEE/CVF Conference on Computer Vision and Pattern Recognition (CVPR). IEEE, 2019: 510 – 519. DOI: 10.1109/CVPR.2019.00060
- [17] MA D, ZHANG F, BULL D R. BVI-DVC: a training database for deep video compression [J]. IEEE transactions on multimedia, 2022, 24: 3847 – 3858. DOI: 10.1109/TMM.2021.3108943
- [18] LIU S, SEGALL A, ALSHINA E, et al. Common test conditions and evaluation procedures for neural network-based video coding technology [Z]. JVET-W2016, 2021
- [19] JVET. VTM-11.0-NNVC, VVC test model [EB/OL]. [2024-03-20]. https://vcgit.hhi.fraunhofer.de/jvet-ahg-nnvc/VVCSoftware_VTM/-/tree/VTM11.0_nnvc
- [20] WANG Z, BOVIK A C, SHEIKH H R, et al. Image quality assessment: from error visibility to structural similarity [J]. IEEE transactions on image processing, 2004, 13(4): 600 – 612. DOI: 10.1109/tip.2003.819861
- [21] CHEN L H, BAMPIS C G, LI Z, et al. Perceptual video quality prediction emphasizing chroma distortions [J]. IEEE transactions on image processing, 2021, 30: 1408 – 1422. DOI: 10.1109/TIP.2020.3043127
- [22] HEINDEL A, PRESTELE B, GEHLERT A, et al. Enhancement layer coding for chroma sub-sampled screen content video [J]. IEEE transactions on circuits and systems for video technology, 2022, 32(2): 788 – 801. DOI: 10.1109/TCSVT.2021.3061944

Biographies

YUAN Lang (1190201114@stu.hit.edu.cn) is now a senior student at Harbin Institute of Technology (HIT), China. He is working at the Research Center of Intelligent Interface and Human-Computer Interaction, HIT. His research interests include deep learning, image coding, and compressive sensing.

HUI Chen received his BS degree in software engineering from Yanshan University, China in 2017, MS degree in software engineering, and PhD in computer science and technology from Harbin Institute of Technology, China in 2020 and 2024, respectively. He has been a visiting scholar with the College of Computing and Data Science, Nanyang Technological University, Singapore since 2023. He is currently with the School of Future Technology, Nanjing University of Information Science and Technology, China. His research interests include image compression, quality assessment, and multimedia security.

WU Yanfeng is currently an undergraduate student at Harbin Institute of Technology (HIT), China. He has joined the Research Center of Intelligent Interface and Human-Computer Interaction, HIT. His research interests include machine learning and deep learning, with a current focus on video coding and compressive sensing.

LIAO Ronghua is pursuing a master's degree at the Department of Computing, Harbin Institute of Technology, China. His research interests include compressed sensing and video quality assessment.

JIANG Feng received his BS, MS and PhD degrees from the Harbin Institute of Technology (HIT), China in 2001, 2003, and 2008, respectively, all in computer science. He is currently a professor with the Department of Computer Science, Sichuan University of Science & Engineering, China and a visiting scholar with the School of Electrical Engineering, Princeton University, USA. His research interests include computer vision, image and video processing, and pattern recognition.

GAO Ying received her master's degree in mathematics from Hohai University, China in 2011. Since then, she has been engaged in the research on Internet of Things (IoT), video surveillance, video transmission, and video coding. She has applied for over 100 patents in these fields. She is currently a chief engineer of standard pre-research at ZTE Corporation and a member of the State Key Laboratory of Mobile Network and Multimedia Technology in China, where she mainly focuses on the research and standardization of video coding technology.



A Privacy-Preserving Scheme for Multi-Party Vertical Federated Learning

FAN Mochan¹, ZHANG Zhipeng¹, LI Difei¹,
ZHANG Qiming^{2,3}, YAO Haidong^{2,3}

(1. School of Information & Communication Engineering, University of Electronic Science and Technology of China, Chengdu 611731, China;

2. ZTE Corporation, Shenzhen 518057, China;

3. State Key Laboratory of Mobile Network and Mobile Multimedia Technology, Shenzhen 518055, China)

DOI: 10.12142/ZTECOM.202404012

<https://kns.cnki.net/kcms/detail/34.1294.TN.20241122.1626.002.html>,
published online November 22, 2024

Manuscript received: 2023-11-14

Abstract: As an important branch of federated learning, vertical federated learning (VFL) enables multiple institutions to train on the same user samples, bringing considerable industry benefits. However, VFL needs to exchange user features among multiple institutions, which raises concerns about privacy leakage. Moreover, existing multi-party VFL privacy-preserving schemes suffer from issues such as poor reliability and high communication overhead. To address these issues, we propose a privacy protection scheme for four institutional VFLs, named FVFL. A hierarchical framework is first introduced to support federated training among four institutions. We also design a verifiable replicated secret sharing (RSS) protocol $\binom{3}{2}$ -sharing and combine it with homomorphic encryption to ensure the reliability of FVFL while ensuring the privacy of features and intermediate results of the four institutions. Our theoretical analysis proves the reliability and security of the proposed FVFL. Extended experiments verify that the proposed scheme achieves excellent performance with a low communication overhead.

Keywords: vertical federated learning; privacy protection; replicated secret sharing

Citation (Format 1): FAN M C, ZHANG Z P, LI D F, et al. A privacy-preserving scheme for multi-party vertical federated learning [J]. *ZTE Communications*, 2024, 22(4): 89 - 96. DOI: 10.12142/ZTECOM.202404012

Citation (Format 2): M. C. Fan, Z. P. Zhang, D. F. Li, et al., "A privacy-preserving scheme for multi-party vertical federated learning," *ZTE Communications*, vol. 22, no. 4, pp. 89 - 96, Dec. 2024. doi: 10.12142/ZTECOM.202404012.

1 Introduction

The development of big data has promoted the rise of artificial intelligence, which plays a vital role in modern society. In various fields, such as economics, climate research, personalized services, and medical services, the collection and analysis of data provide important support for researchers. However, with the massive data collection and analysis, some data privacy issues have arisen. As an emerging technology of artificial intelligence, federated learning^[1] enables users to use private data for model training locally and share gradients under the coordination of the server, to obtain a higher-precision global model. Federated learning protects user data by eliminating the need for data disclosure.

Vertical federated learning (VFL)^[2] enables multiple institutions to train on the same user samples and has received extensive attention from both industry and academia. For example, it facilitates federated analysis of financial data, where infor-

mation about the same user may come from different banks. However, VFL needs to share user features or intermediate training results among multiple institutions, raising concerns about user data privacy leakage.

Some schemes propose to use secure multi-party computation^[3] to address the VFL privacy leakage issue^[4-6]. NI et al.^[7] proposed FedVGCN, a federated graph convolutional network (GCN) learning paradigm suitable for node classification tasks. Participants exchange intermediate results under homomorphic encryption, thus protecting the data privacy of participants. Similarly, YANG et al.^[8] proposed a distributed logistic regression privacy protection scheme using homomorphic encryption and eliminated the third-party coordinator. Although the above schemes guarantee the feature or label privacy of the participating parties, they only support two-party VFL and cannot be applied to multi-party joint training. Therefore, some multi-party VFL privacy protection schemes have been proposed^[9-10]. LI et al.^[9] proposed a tree-based multi-party VFL privacy-preserving system, using homomorphic encryption and differential privacy to protect histogram privacy. However, this scheme requires a large communication overhead, and the model performance suffers due to the addition of noise. XIE et

This work was supported in part by ZTE Industry-University-Institute Cooperation Funds under Grant No. 202211FKY00112, Open Research Projects of Zhejiang Lab under Grant No. 2022QA0AB02, and Natural Science Foundation of Sichuan Province under Grant No. 2022NSFSC0913.

al.^[10] proposed a multi-party VFL privacy protection scheme MP-FedXGB using secret sharing. Each participant directly performs model training on the secret shares, resulting in a large communication overhead. These multi-party VFL schemes not only require a high communication overhead but also have poor reliability. Participants are not allowed to exit. Once a participant exits, model training will be interrupted.

Taking into account the issues of poor reliability and high communication overheads in existing schemes, we propose a privacy-preserving VFL scheme that supports four-party federated training, named FVFL. This scheme supports four institutions for VFL training, consisting of three institutions with intersection feature sets (passive and unlabeled) and one institution with a different feature set (active and labeled) from these three institutions. First, the three passive parties utilize the proposed repeated secret-sharing algorithm to realize the private summation of intersection features under overlapping user sets. The proposed repeated secret-sharing algorithm satisfies the requirement that the feature sums of three passive parties can still be recovered when one passive party quits the secret reconstruction process. Then, any of the three passive parties can perform model training with the active party to realize the function of four-party federated training. This ensures a low communication overhead and high reliability during VFL training in multiple institutions.

The contributions of this paper include the following aspects:

1) We propose an effective four-party VFL federated training framework, which reduces the system communication overhead through a hierarchical structure, and any of the three passive parties cooperates with the active party to achieve VFL training on four-party data.

2) We design $\binom{3}{2}$ -sharing, a verifiable replicated secret sharing (RSS) protocol. Any two parties can cooperate to recover the sum of the three-party features, and the protocol only requires additional operations with a low computational overhead.

3) Our theoretical analysis proves the security of the scheme. Experimental results verify the advantages of FVFL in terms of model performance and communication overhead.

The remainder of this paper is organized as follows. Section 2 introduces the work related to VFL privacy protection. Section 3 provides an overview of the FVFL system model, threat model, and security requirements. Section 4 presents the FVFL construction details. Section 5 proves the safety of the proposed FVFL, and Section 6 demonstrates the effectiveness of FVFL through experiments. Finally, the paper is concluded in Section 7.

2 Related Work

VFL enables multiple institutions to conduct model training on the same user samples in a distributed manner. While this approach has received widespread attention in both academia

and industry, concerns about privacy leakage among participants have become increasingly prominent. Some schemes^[11-12] propose the use of cryptography technology to encrypt intermediate results to protect data privacy. However, they all require a third party to act as a coordinator for scheduling the training process. FANG et al.^[13] proposed a VFL privacy protection scheme that cancels the third party and uses secret sharing to avoid leakage of intermediate information in the training process, thereby enabling safe model prediction. However, the solutions mentioned above only support VFL training between two institutions. Obviously, multi-party VFL would better meet actual needs.

Therefore, several VFL privacy-preserving schemes supporting multi-party joint training have been proposed^[14-15]. WU et al.^[16] proposed a vertical decision tree scheme to preserve the privacy of intermediate information. In this approach, each participant first uses homomorphic encryption to generate statistical information and then employs secret sharing to determine the best split of tree nodes. Finally, the secret is reconstructed, and each participant updates the model with encrypted data. However, this scheme requires secret segmentation and transmission of the homomorphic encrypted ciphertext, resulting in a significant communication overhead. HUANG et al.^[17] proposed a multi-party VFL privacy protection scheme designed for generalized linear models. Participants first segment the gradients using secret sharing algorithms, and then homomorphically encrypt the segmented gradients and propagate them to each other. Ultimately, the receiver decrypts and reconstructs the gradient, thereby achieving gradient privacy protection. However, this scheme has a high communication overhead and is limited to simple linear models.

In addition, the schemes mentioned above face the issue of poor reliability. If any participant is accidentally disconnected, the training will be interrupted. Therefore, it is essential to design a multi-party VFL privacy protection scheme with high reliability and a limited communication overhead.

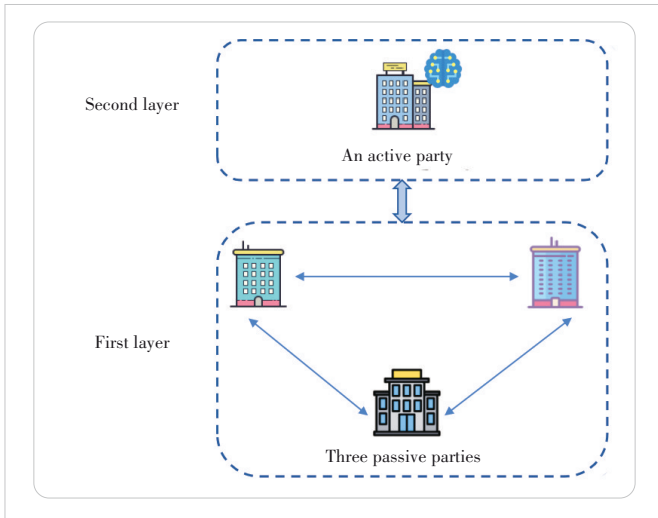
3 Problem Description

In this section, we outline the FVFL system model, analyze potential security threats, and then describe the security requirements.

3.1 System Model

The FVFL system model mainly includes two types of entities: one active party and three passive parties. The architecture of the FVFL system is shown in Fig. 1.

1) Active participant: The active party is the organization (such as an operator) that owns the label among the four organizations and has a different set of features compared to the three passive parties. The active party plays a leading role in the four-party VFL training, denoted as P_0 . After the three passive parties perform $\binom{3}{2}$ -sharing, P_0 and any of the parties use



▲ Figure 1. Architecture of the proposed FVFL framework

the data of the four institutions for model training. Furthermore, the intermediate results are encrypted using a homomorphic encryption algorithm to ensure data privacy.

2) Passive participants: Three institutions with intersection features (such as three banks) are passive parties of FVFL and do not have labels, denoted as $P_i, i \in \{1, 2, 3\}$. Before conducting model training with P_0 , the three passive parties utilize the proposed verifiable RSS protocol $\binom{3}{2}$ -sharing for feature sharing. Through this protocol, P_i can obtain the sum of the intersection features of users overlapping in three institutions. Then, according to the hierarchical structure, any party in P_i performs model training with the active party P_0 of another layer.

3.2 Threat Model

Participants may not be completely trustworthy and could exhibit malicious behavior. In addition, there may be external attackers on the network that want to steal private data from participants or hinder model training. Next, we analyze the potential threats faced by VFL participants and the network.

First, assuming that the passive parties P_i are malicious in the RSS process, they may transmit illegal information. For example, during the secret split phase, they may distribute the wrong secret shares to other parties, making it impossible to reconstruct the secret. During the secret reconstruction phase, P_i may transmit the wrong secret shares to the partner or maliciously exit the reconstruction process, causing the other party to fail to recover the correct secret.

Second, during the model training process with the active party P_0 , the passive party P_i will honestly conduct the training, but wants to steal the other party's private data from the intermediate results.

Finally, we assume that there is a malicious attacker in the network, which wants to steal secret shares or intermediate re-

sults by listening to the channel to infer the private data of the participants.

3.3 Security Requirements

Considering the possible security threats of FVFL, the following security requirements should be met.

1) Confidentiality: During the process of secret sharing, malicious P_i or attackers may infer the secrets of other participants from the received or stolen secret shares. In addition, P_0 and P_i may infer each other's privacy data through intermediate results of interaction during model training. Therefore, FVFL should be able to ensure the confidentiality of the participant data.

2) Reliability: When P_i is performing secret reconstruction or model training with P_0 , it may subjectively or passively exit the system, which makes it impossible to reconstruct the secret or directly interrupt the model training. Therefore, it is necessary to ensure that even if any participants exit, FVFL can still reconstruct the secret and perform model training normally.

3) Verifiability: Malicious P_i may distribute or transmit wrong secret shares to other parties during secret splitting or reconstruction, making it impossible to recover the secret. Therefore, FVFL needs to ensure that P_i transmits the correct share of the secret so that the secret can be reconstructed.

4 Construction Details

In this section, we introduce the construction details of the proposed FVFL, and the symbols involved in this paper are summarized in Table 1.

4.1 $\binom{3}{2}$ -Sharing Secret Split for FVFL

Three passive parties P_i generate random numbers a_1, a_2 and a_3 through pseudo-random functions^[18], satisfying $a_1 + a_2 + a_3 = 0$, where a_1, a_2 and a_3 are held and saved by P_1, P_2 and P_3 , respectively. Assume that P_1, P_2 and P_3 hold secrets x, y , and z , respectively (the values of each intersection feature at the three passive parties). They split the secret through a secret split algorithm and distribute the secret shares to the other two passive parties.

As shown in Algorithm 1, the secret split algorithm includes three steps. First, each passive party splits its respective secrets x, y , and z into multiple secret shares. Then, the

▼ Table 1. Description of the symbols involved in this paper

Symbol	Description
P_0	Active participant (holding labels)
$P_i, i \in \{1, 2, 3\}$	Passive participants
x, y, z	Secrets held by P_1, P_2 and P_3 respectively
x_i, y_i, z_i	Secret shares
$H(\cdot)$	One-way hash function

passive party hashes the secret shares. Finally, the three passive parties distribute secret shares and corresponding hash values to each other. This $\binom{3}{2}$ -sharing protocol ensures the privacy of the passive party's secret and the verifiability of the secret share by introducing random numbers and hash operations.

Algorithm 1. $\binom{3}{2}$ -Sharing Secret Split

Input: $a_1, a_2, a_3, x, y,$ and z

Output: Secret shares and corresponding hash values of three passive parties

- 1: P_1 splits secret $x: x = x_1 + x_2 + x_3$.
- 2: P_2 splits secret $y: y = y_1 + y_2 + y_3$.
- 3: P_3 splits secret $z: z = z_1 + z_2 + z_3$.
- 4: P_1 calculates $x^\wedge = H(x + a_1)_{p_1}, H(x_1)_{p_1}, H(x'_2)_{p_1},$ and $H(x_3)_{p_1}$, where $x'_2 = x_2 + a_1$.
- 5: P_2 calculates $y^\wedge = H(y + a_2)_{p_2}, H(y_1)_{p_2}, H(y'_2)_{p_2},$ and $H(y_3)_{p_2}$, where $y'_2 = y_2 + a_2$.
- 6: P_3 calculates $z^\wedge = H(z + a_3)_{p_3}, H(z_1)_{p_3}, H(z'_2)_{p_3},$ and $H(z_3)_{p_3}$, where $z'_2 = z_2 + a_3$.
- 7: P_1 sends $(x_1, x'_2), H(x_1)_{p_1}, H(x'_2)_{p_1}, H(x_3)_{p_1}$ and x^\wedge to P_2 , and sends $(x'_2, x_3), H(x_1)_{p_1}, H(x'_2)_{p_1}, H(x_3)_{p_1}$ and x^\wedge to P_3 .
- 8: P_2 sends $(y_1, y'_2), H(y_1)_{p_2}, H(y'_2)_{p_2}, H(y_3)_{p_2}$ and y^\wedge to P_1 , and sends $(y'_2, y_3), H(y_1)_{p_2}, H(y'_2)_{p_2}, H(y_3)_{p_2}$ and y^\wedge to P_3 .
- 9: P_3 sends $(z_1, z'_2), H(z_1)_{p_3}, H(z'_2)_{p_3}, H(z_3)_{p_3}$ and z^\wedge to P_1 , and sends $(z'_2, z_3), H(z_1)_{p_3}, H(z'_2)_{p_3}, H(z_3)_{p_3}$ and z^\wedge to P_2 .

Return: Secret shares and corresponding hash values of three passive parties.

4.2 $\binom{3}{2}$ -Sharing Secret Reconstruction for FVFL

Once each passive party receives the secret shares of the other two passive parties, it can recover the sum of the three-party secrets by executing the secret reconstruction algorithm. At this stage, even if a passive party actively or passively withdraws, the algorithm can still run normally. Assuming that P_3 is accidentally disconnected during the secret reconstruction process, the following describes how P_1 and P_2 reconstruct the sum of the three-party secrets.

As shown in Algorithm 2, the secret reconstruction algorithm includes three steps. First, P_1 and P_2 send the different secret shares to each other. Then, P_1 and P_2 respectively use the hash function to determine the consistency of the received secret shares. Finally, P_1 and P_2 carry out secret reconstruction, respectively, to obtain the sum of the secrets of the three parties.

Algorithm 2. $\binom{3}{2}$ -Sharing Secret Reconstruction

Input: $x + a_1, (z_1, z'_2), y + a_2$ and (z'_2, z_3) .

Output: $x + y + z$.

- 1: P_1 sends $x + a_1$ and (z_1, z'_2) to P_2 .
- 2: P_2 sends $y + a_2$ and (z'_2, z_3) to P_1 .
- 3: P_1 calculates $H(y + a_2), H(z_1), H(z'_2)$, and $H(z_3)$ and determines whether $H(y + a_2) = y^\wedge, H(z_1) = H(z_1)_{p_3},$
 $H(z'_2) = H(z'_2)_{p_3},$ and $H(z_3) = H(z_3)_{p_3}$ are valid.
- 4: P_2 calculates $H(x + a_1), H(z_1), H(z'_2)$, and $H(z_3)$ and determines whether $H(x + a_1) = x^\wedge, H(z_1) = H(z_1)_{p_3},$
 $H(z'_2) = H(z'_2)_{p_3},$ and $H(z_3) = H(z_3)_{p_3}$ are valid.
- 5: If all the equations hold, P_1 and P_2 calculate $x + a_1 + y + a_2 + z_1 + z'_2 + z_3 = x + y + z$ locally, respectively.

Return: $x + y + z$.

4.3 Homomorphic Encryption for FVFL

After the three passive parties perform the feature summation, any of them can cooperate with the active party P_0 to perform model training to achieve four-party VFL training. Here, the homomorphic encryption algorithm is used to ensure the privacy of the intermediate results of the interaction. The specific execution process is as follows.

- P_0 first uses the label to calculate the first-order derivative g_i and the second-order derivative h_i of the gradient, and then uses the homomorphic encryption algorithm to encrypt g_i and h_i , followed by sending the encrypted $\langle g_i \rangle$ and $\langle h_i \rangle$ to P_i .
- After receiving the ciphertexts $\langle g_i \rangle$ and $\langle h_i \rangle$, P_i uses them to calculate the local gradient histogram and sends the gradient histogram to P_0 .
- P_0 decrypts the gradient histogram sent by P_i , finds the optimal split point, and then sends it to P_i .
- P_0 and P_i determine which party has the best split point and then receive the sample division result of the party with the best split point.
- Both parties update the index between samples and tree nodes, as well as their respective tree models.

5 Security Analysis

In this section, we analyze the security and reliability of the proposed FVFL scheme.

Theorem 1. Although the passive party P_i is malicious, it must share a clear secret during RSS. In addition, if malicious P_i transmits incorrect secret shares, other passive parties will discover it.

Proof: According to the design of the secret sharing protocol, each P_i will transmit the secret shares and their corresponding hash values to other passive parties during the secret distribution phase. For example, in the secret distribution phase, P_1 must transmit $(x_1, x'_2), H(x_1)_{p_1}, H(x'_2)_{p_1}, H(x_3)_{p_1}$ and x^\wedge to P_2 , as well as $(x'_2, x_3), H(x_1)_{p_1}, H(x'_2)_{p_1}, H(x_3)_{p_1}$ and x^\wedge to P_3 . If P_1 is compromised, it may transmit illegal $x^\circ + a_1$ to P_2 or P_3 during the secret reconstruction phase. At this

time, P_2 or P_3 can judge that $H(x^\circ + a_1) = x^\circ$ is not established through the hash, and thus perceive the malicious behavior of P_1 . Therefore, even if P_1 is malicious, it must share a clear secret to make $H(x + a_1) = H(x + a_1)_{p_1}$ valid. Similarly, P_2 and P_3 can verify the legitimacy of the secret shares transmitted by P_1 by judging whether $H(x_1) = H(x_1)_{p_1}$, $H(x'_2) = H(x'_2)_{p_1}$, etc. are established.

Theorem 2. The proposed FVFL scheme will not leak the private data of any participant during the secret sharing and model training stages.

Proof: Firstly, assume that P_1 and P_2 cooperate to reconstruct the sum of the three-party secrets. In the secret reconstruction phase, P_1 and P_2 need to transmit $x + a_1$ and $y + a_2$ to each other. According to the protocol settings, P_1 holds $x + a_1$ and (z_1, z'_2) , and P_2 holds $y + a_2$ and (z'_2, z_3) . They can calculate the secret sum of the three parties $(x + a_1) + (y + a_2) + (z_1 + z'_2 + z_3) = x + y + z$, respectively. Because P_1 does not know the random numbers a_2 and a_3 of P_2 and P_3 , and P_2 does not know the random numbers a_1 and a_3 of P_1 and P_3 , they can only obtain $y + a_2$ and $z + a_3$, respectively, but fail to obtain y or z , thus ensuring the privacy of the passive party's secret values.

Secondly, when the active party P_0 conducts model training with any of the three passive parties P_i , P_0 performs homomorphic encryption on the intermediate results to ensure data privacy. Moreover, P_i uses the sum of three-party data to perform model training, and it will not leak the data privacy of a single passive party.

Theorem 3. If one or two passive parties exit during secret reconstruction or model training, the proposed FVFL can still run as usual.

Proof. Assuming P_1 exits the secret reconstruction phase maliciously or passively, the remaining P_2 and P_3 can still successfully reconstruct the sum of the three-party secrets. This is because P_2 and P_3 not only hold their respective secrets y and z , but also hold P_1 's secret shares (x_1, x'_2) and (x'_2, x_3) , respectively. Therefore, P_2 and P_3 can collaborate to calculate $(y + a_2) + (z + a_3) + (x_1 + x'_2 + x_3) = x + y + z$. Furthermore, during model training, since all three passive parties hold the sum of their secrets, P_0 only needs to collaborate with any of the three passive parties to achieve model training.

6 Performance Evaluation

In this section, we evaluate the advantages of the proposed FVFL in terms of communication overhead and performance through extended experiments.

6.1 Experimental Setup

Experiments ran on the Ubuntu 18.04.6 LTS operating system, equipped with 62 GB of memory and an Intel(R) Xeon(R) CPU E5-2650 v4 clocked at 2.20 GHz. We performed Secure-

Boost model training on the FATE v1.9.0 platform to verify the effectiveness of FVFL. SecureBoost is a decentralized vertical federated learning security tree model based on gradient-boosting decision trees. It supports multi-party cooperation, that is, federated training of multiple unlabeled data holders and one labeled data holder. MP-FedXGB is the benchmark, as it also supports four-party VFL federated training.

The experiments were carried out on two datasets: GiveMeSomeCredit and UCI Credit Card. The data in the GiveMeSomeCredit dataset was used to determine whether users would suffer financial difficulties in the future. It included 150 000 data samples and 10 features. The data in the UCI Credit Card dataset was used to judge whether a person would default, and it included 30 000 data samples and 24 features. We split both datasets into 25 000 training samples and 5 000 testing samples. Features were converted into multi-dimensional vectors using one-hot encoding, distributed to active and passive parties at a ratio of [0.5, 0.5], followed by the passives being distributed at a ratio of [0.2, 0.3, 0.5].

The experiments verified the training and prediction time of FVFL under different hyperparameter settings. The parameters and default settings involved in the experiment are shown in Table 2. Each experiment was performed five times, and the average results were reported.

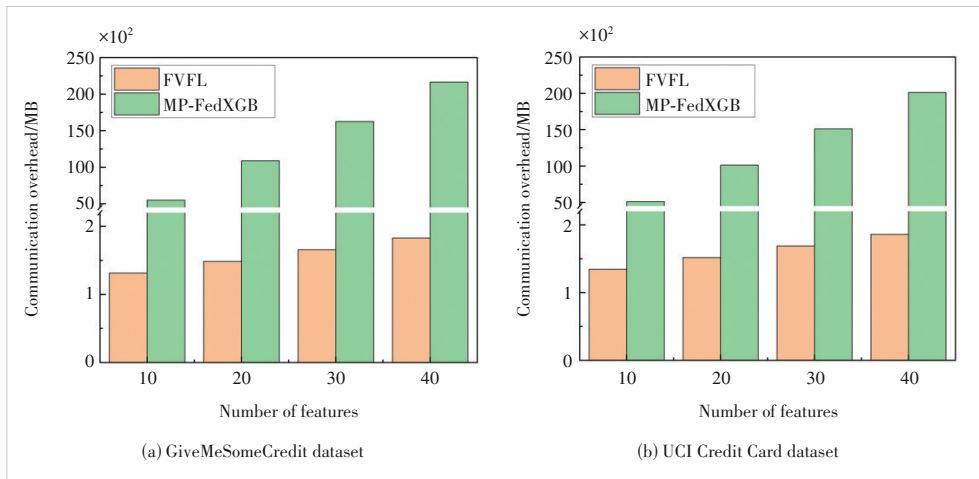
6.2 Communication Overhead Comparisons

In this section, we discuss the communication overhead required for FVFL to perform four-party federated training, including feature secret sharing among the three passive parties, as well as intermediate result interaction between the active party and any passive party. We compare the communication costs of FVFL and MP-FedXGB under the same settings.

1) Varying F . Fig. 2 shows the trends of communication costs for FVFL and MP-FedXGB on the two datasets as F increases. Regardless of which data set, as F increases, the communication overheads of the two schemes will gradually increase. However, compared to MP-FedXGB, the communication overhead of FVFL is significantly lower. For example, when $F=40$, the amount of communication MP-FedXGB needs to transmit on both datasets is 118.4 times and 108.0 times that of FVFL, respectively. This is because according to the design of the FVFL scheme, only the feature shares need to be transmitted between the three passive parties, and then any of the three passive parties and the active party can perform model training. However, MP-FedXGB must use feature

▼Table 2. Parameters and their default values

Parameter	Description	Value	Default
F	Number of features	{10, 20, 30, 40}	10
T	Number of trees	{3, 4, 5, 6, 7}	3
D	Number of depths	{3, 4, 5, 6, 7}	3
I	Number of data samples	{5k, 10k, 15k, 20k, 25k}	25k



▲ Figure 2. Communication overheads for different numbers of features (F)

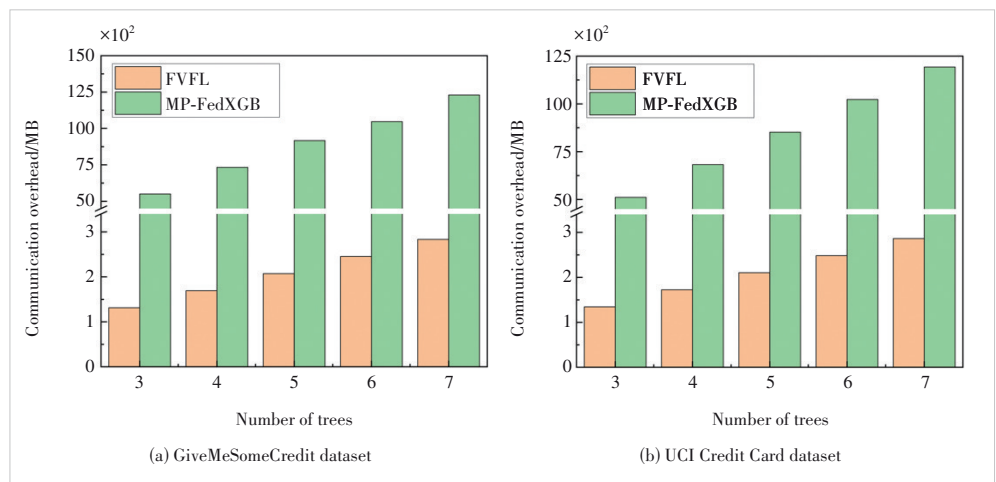
shares to perform model training among four parties, and its communication cost will be higher. The results show that our FVFL is more suitable for model training with more features.

2) Varying T . Fig. 3 shows the trends of communication costs of FVFL and MP-FedXGB on the two data sets as T increases. Although the communication overheads of FVFL and MP-FedXGB increase with the increase of T , the communication cost of FVFL is always smaller than that of MP-FedXGB. For example, when MP-FedXGB has three trees, its traffic on the two datasets is 41.9 times and 37.9 times that of FVFL, respectively. This is because MP-FedXGB requires multiple rounds of iterations using parameter shares among the four participants and the coordinator to build a tree model, while FVFL only needs to iterate among two participants. The results show that FVFL is more suitable for multiple decision tree models.

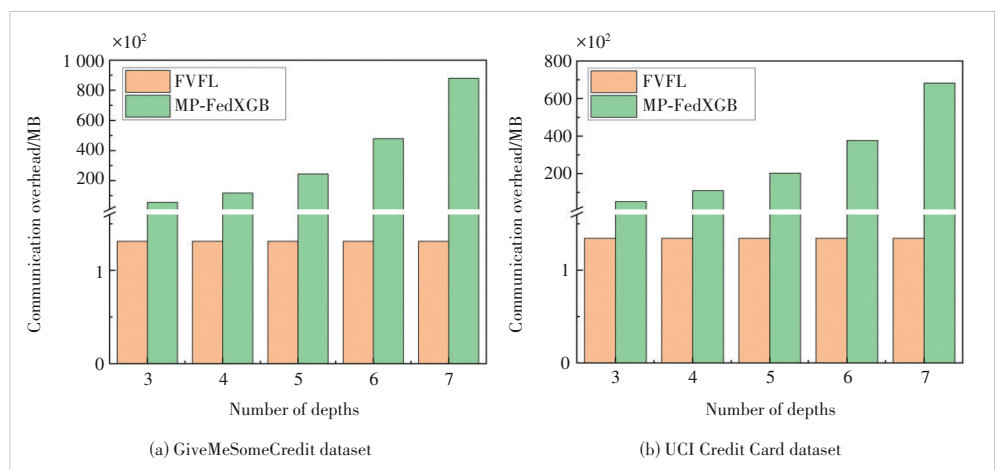
3) Varying D . Fig. 4 shows the trends of communication costs of FVFL and MP-FedXGB on the two data sets as D increases. It can be seen that the communication overhead of FVFL will not change as D increases, but the

communication cost of MP-FedXGB will increase rapidly as D changes. Regardless of the value of D , the traffic of MP-FedXGB is significantly higher than that of FVFL. As D increases, the communication advantages of FVFL will become more prominent. The communication cost of FVFL will not change with the increase in D , because D is not involved in secret sharing among the three passive parties. D is only involved in model training between the active party and any passive party, but D does not affect the interaction of gradient information after homomorphic encryption.

4) Varying I . Fig. 5 shows the trends of communication



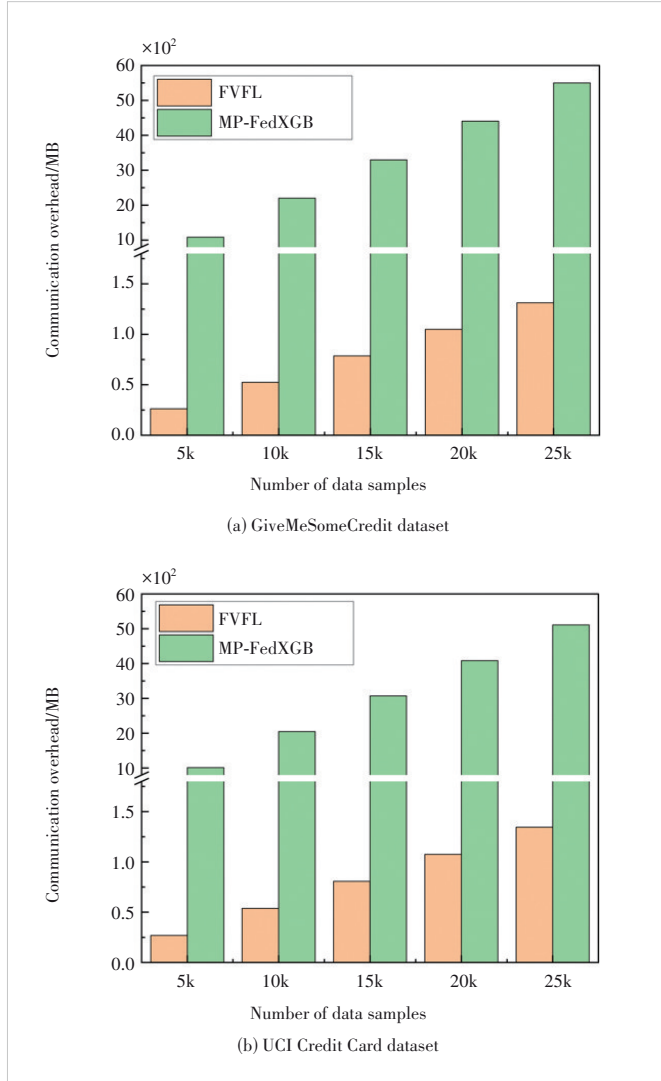
▲ Figure 3. Communication overheads for different numbers of trees (T)



▲ Figure 4. Communication overheads for different numbers of depths (D)

costs of FVFL and MP-FedXGB on the two data sets as I increases. Although the communication overheads of FVFL and MP-FedXGB increase with increasing I on both datasets, it is obvious that the communication overhead of FVFL is

lower and increases slowly. This is because, to build the tree model, MP-FedXGB has to complete multiple rounds of iterations among the four parties under the coordination of a third party. The results show FVFL is well suited for training on large datasets.



▲ Figure 5. Communication overheads for different numbers of data samples (I)

▼ Table 3. Model performance comparison under different parameters

		GiveMeSomeCredit						UCI Credit Card					
		FVFL			MP-FedXGB			FVFL			MP-FedXGB		
		ACC	F1	AUC	ACC	F1	AUC	ACC	F1	AUC	ACC	F1	AUC
T	3	0.933 3	0.245 7	0.827 0	0.930 6	0.213 1	0.719 4	0.823 2	0.466 7	0.752 5	0.822 5	0.458 8	0.768 6
	4	0.933 9	0.244 2	0.829 5	0.932 6	0.235 8	0.746 5	0.824 2	0.447 2	0.760 9	0.823 7	0.475 2	0.770 1
	5	0.934 2	0.247 4	0.829 9	0.933 4	0.292 9	0.749 7	0.825 8	0.462 0	0.763 4	0.824 9	0.473 8	0.773 5
D	3	0.933 3	0.245 7	0.827 0	0.930 6	0.213 1	0.719 4	0.823 2	0.466 7	0.752 5	0.822 5	0.458 8	0.768 6
	4	0.934 7	0.280 5	0.828 6	0.931 8	0.201 4	0.737 9	0.824 4	0.451 8	0.762 8	0.823 9	0.446 1	0.769 0
	5	0.935 4	0.278 2	0.847 9	0.932 2	0.264 6	0.738 3	0.824 8	0.453 4	0.764 7	0.824 3	0.454 6	0.770 7

ACC: accuracy AUC: area under curve

6.3 Model Performance Comparisons

We compare the performance of FVFL and MP-FedXGB in training SecureBoost models on the GiveMeSomeCredit and UCI Credit Card datasets, where the number of decision tree T and depth D increases from 3 to 5, respectively. The comparison is carried out mainly from three aspects: accuracy (ACC), F1 score, and area under curve (AUC), and the results are shown in Table 3. It can be seen that under the two variables T and D , the performance of FVFL is almost better than that of MP-FedXGB in various indicators. This can be attributed to the scheme design of FVFL, which uses the features of the four parties directly for model training by the active party and any of the three passive parties. However, the participants in MP-FedXGB have to reshape the model splitting criterion based on the secret share of each party's private data.

7 Conclusions

This paper proposes an FVFL privacy protection scheme that supports the federated training of four parties. FVFL introduces a layered framework with three passive parties as one layer and active parties as another layer. Furthermore, a verifiable RSS algorithm is designed so that three passive parties can achieve the private summation of feature intersection sets. Moreover, the algorithm ensures that when a passive party exits the secret reconstruction stage, the remaining two parties can still restore the sum of the three-party features. The active party cooperates with any of the three passive parties to achieve four-party VFL training. This ensures a low communication overhead and high reliability of the FVFL. Theoretical analysis and extended experiments have verified the security and effectiveness of our FVFL.

Acknowledgment

We acknowledge Prof. YU Hongfang, XIONG Xiankui, Dr.

LI Zonghang, and JI Kailai for their invaluable guidance and efforts in the research presented in this paper.

References

- [1] KAIROUZ P, MCMAHAN H B, AVENT B, et al. Advances and open problems in federated learning [J]. Foundations and trends® in machine learning, 2021, 14(1 - 2): 1 - 210. DOI: 10.1561/22000000083
- [2] YANG Q, LIU Y, CHEN T J, et al. Federated machine learning: concept and applications [J]. ACM transactions on intelligent systems and technology (TIST), 2019, 10(2): 1 - 19. DOI: 10.1145/3298981
- [3] CHOUDHURY A, PATRA A. Secure multi-party computation against passive adversaries [M]. Cham: Springer International Publishing, 2022. DOI: 10.1007/978-3-031-12164-7
- [4] OU W, ZENG J H, GUO Z J, et al. A homomorphic-encryption-based vertical federated learning scheme for risk management [J]. Computer science and information systems, 2020, 17(3): 819 - 834. DOI: 10.2298/isis190923022o
- [5] WANG C, LIANG J, HUANG M, et al. Hybrid differentially private federated learning on vertically partitioned data [J]. 2020. DOI: 10.48550/arXiv.2009.02763
- [6] HE D J, DU R M, ZHU S S, et al. Secure logistic regression for vertical federated learning [J]. IEEE Internet computing, 2022, 26(2): 61 - 68. DOI: 10.1109/MIC.2021.3138853
- [7] NI X, XU X L, LYU L J, et al. A vertical federated learning framework for graph convolutional network [EB/OL]. (2021-06-22)[2023-06-13]. <https://arxiv.org/abs/2106.11593>
- [8] YANG S W, REN B, ZHOU X H, et al. Parallel distributed logistic regression for vertical federated learning without third-party coordinator [EB/OL]. (2019-11-22)[2023-06-13]. <https://arxiv.org/abs/1911.09824v1>
- [9] LI Q B, WU Z M, CAI Y Z, et al. FedTree: a federated learning system for trees [C]//Proc. Machine Learning and Systems 5. MLSys, 2023
- [10] XIE L C, LIU J Q, LU S T, et al. An efficient learning framework for federated XGBoost using secret sharing and distributed optimization [J]. ACM transactions on intelligent systems and technology, 2022, 13(5): 1 - 28. DOI: 10.1145/3523061
- [11] XU R H, BARACALDO N, ZHOU Y, et al. FedV: privacy-preserving federated learning over vertically partitioned data [C]//Proc. 14th ACM Workshop on Artificial Intelligence and Security. ACM, 2021. DOI: 10.1145/3474369.3486872
- [12] YANG K, FAN T, CHEN T, et al. A quasi-newton method based vertical federated learning framework for logistic regression [EB/OL]. (2019-12-01)[2023-07-11]. <https://arxiv.org/abs/1912.00513>
- [13] FANG W J, ZHAO D R, TAN J, et al. Large-scale secure XGB for vertical federated learning [C]//Proc. 30th ACM International Conference on Information & Knowledge Management. ACM, 2021. DOI: 10.1145/3459637.3482361
- [14] CHEN W J, MA G Q, FAN T, et al. Secureboost+: a high performance gradient boosting tree framework for large scale vertical federated learning [EB/OL]. (2021-10-21) [2023-07-12]. <https://arxiv.org/abs/2110.10927v2>
- [15] SHI H R, XU Y H, JIANG Y L, et al. Efficient asynchronous multi-participant vertical federated learning [J]. IEEE transactions on big data, 2024, 10(6): 940 - 952. DOI: 10.1109/TBDATA.2022.3201729
- [16] WU Y C, CAI S F, XIAO X K, et al. Privacy-preserving vertical federated learning for tree-based models [J]. Proceedings of the VLDB endowment, 2020, 13(12): 2090 - 2103. DOI: 10.14778/3407790.34078112020.
- [17] HUANG Y M, FENG X Y, WANG W W, et al. EFMVFL: an efficient and flexible multi-party vertical federated learning without a third party [EB/OL]. (2022-01-17)[2023-07-15]. <https://arxiv.org/abs/2201.06244>
- [18] ABSPOEL M, DALSKOV A, ESCUDERO D, et al. An efficient passive-to-active compiler for honest-majority MPC over rings [C]//International Conference on Applied Cryptography and Network Security. ACNS, 2021: 122 - 152. DOI: /10.1007/978-3-030-78375-4_6

Biographies

FAN Mochan is a PhD candidate at University of Electronic Science and Technology of China (UESTC). She received her BS degree from Suzhou University of Science and Technology, China and MS degree from Jiangxi University of Science and Technology, China. Her research interests include network security, blockchain, and federated learning.

ZHANG Zhipeng (2474297092@qq.com) is pursuing a master's degree at University of Electronic Science and Technology of China (UESTC). He received his bachelor's degree from UESTC. His research interests include network security and distributed machine learning.

LI Difei is pursuing a master's degree in communication and information system at University of Electronic Science and Technology of China. His research focuses on machine learning.

ZHANG Qiming is a senior system architect at ZTE Corporation. He received his bachelor's degree from Zhejiang University, China in 1992. His research interests include MEC and heterogeneous computing.

YAO Haidong is a senior system architect at ZTE Corporation. He is engaged in the research and design of deep learning, large model network architecture, and compilation conversion technology.

ZTE Communications

Table of Contents, Volume 22, 2024

Volume-Number-Page

Special Topic

Near-Field Communication and Sensing Towards 6G

Editorial	WEI Guo, CHEN Li, ZHAO Yajun	22-01-01
Towards Near-Field Communications for 6G: Challenges and Opportunities	LIU Mengyu, ZHANG Yang, JIN Yasheng, ZHI Kangda, PAN Cunhua	22-01-03
Link Budget and Enhanced Communication Distance for Ambient Internet of Things	YANG Yibing, LIU Ming, XU Rongtao, WANG Gongpu, GONG Wei	22-01-16
Impacts of Model Mismatch and Array Scale on Channel Estimation for XL-HRIS-Aided Systems	LU Zhizheng, HAN Yu, JIN Shi	22-01-24
Degree of Freedom Analysis for Holographic MIMO Based on a Mutual-Coupling-Compliant Channel Model	SUN Yunqi, JIAN Mengnan, YANG Jun, ZHAO Yajun, CHEN Yijian	22-01-34
Near-Field Beam Training for Holographic MIMO Communications: Typical Methods, Challenges and Future Directions	SHEN Jiayu, YANG Jun, ZHU Chen, DENG Zhiji, HUANG Chongwen	22-01-41
Near-Field Wireless Power Transfer, Sensing and Communication with Bessel Beams	CAO Xinghan, YIN Huarui, YOU Changsheng	22-01-53

Advancements in Web3 Infrastructure for the Metaverse

Editorial	Victor C. M. LEUNG, CAI Wei	22-02-01
Building a Stronger Foundation for Web3: The Advantages of 5G Infrastructure	FENG Jianxin, PAN Yi, WU Xiao	22-02-03
MetaOracle: A High-Throughput Decentralized Oracle for Web3.0-Empowered Metaverse	CHEN Rui, LI Hui, LI Wuyang, BAI He, WANG Han, WU Naixing, FAN Ping, KANG Jian, Selwyn DENG, ZHU Xiang	22-02-11
Optimization of High-Concurrency Conflict Issues in Execute-Order-Validate Blockchain	MA Qianli, ZHANG Shengli, WANG Taotao, YANG Qing, WANG Jigang	22-02-19
Utilizing Certificateless Cryptography for IoT Device Identity Authentication Protocols in Web3	WU Zhihui, HONG Yuxuan, ZHOU Enyuan, LIU Lei, PEI Qingqi	22-02-30
Hierarchical Federated Learning Architectures for the Metaverse	GU Cheng, LI Baochun	22-02-39

Integrated Sensing and Communication (ISAC) Technologies for Future Wireless Communication

Editorial	YUAN Jinhong, FEI Zesong, WEI Zhiqiang	22-03-01
Kullback-Leibler Divergence Based ISAC Constellation and Beamforming Design in the Presence of Clutter	TANG Shuntian, WANG Xinyi, XIA Fanghao, FEI Zesong	22-03-04
Joint Beamforming Design for Dual-Functional Radar-Communication Systems Under Beampattern Gain Constraints	CHEN Guangyi, ZHANG Ruoyu, REN Hong, LIN Xu, WU Wen	22-03-13
On Normalized Least Mean Square Based Interference Cancellation Algorithm for Integrated Sensing and Communication Systems	YU Xiaohui, YU Shucheng, LIU Xiqing, PENG Mugen	22-03-21
Trajectory Tracking for MmWave Communication Systems via Cooperative Passive Sensing	YU Chao, LYU Bojie, QIU Haoyu, WANG Rui	22-03-29
Integrated Sensing and Communication: Who Benefits More?	DU Ruolin, WEI Zhiqiang, YANG Zai	22-03-37
Low-Complexity Integrated Super-Resolution Sensing and Communication with Signal Decimation and Ambiguity Removal	DAI Qianglong, OU Zhiwen, XIAO Zhiqiang, ZENG Yong, YANG Fei, CHEN Yan	22-03-48
Tensor Decomposition-Based Channel Estimation and Sensing for Millimeter Wave MIMO-OFDM V2I Systems	WANG Jilin, ZENG xianlong, YANG yonghui, PENG lin, LI Lingxiang	22-03-56
Sensing and Communication Integrated Fast Neighbor Discovery for UAV Networks	WEI Zhiqing, ZHANG Yongji, JI Dana, LI Chenfei	22-03-69

Optoelectronic Integrated Chips, Systems, and Key Technologies

Editorial	WANG Yongjin	22-04-01
-----------	--------------	----------

Monolithically Integrated Photonic Structures for Stable on-Chip Solar Blind Communications	HE Rui, HU Qiang, RAN Junxue, WANG Junxi, WEI Tongbo	22-04-03
Research on High-Precision Stochastic Computing VLSI Structures for Deep Neural Network Accelerators	WU Jingguo, ZHU Jingwei, XIONG Xiankui, YAO Haidong, WANG Chengchen, CHEN Yun	22-04-09
Design of LCoS-Based Twin 1×40 Wavelength Selective Switch	WANG Han, LIU Maoqi, FENG Zhenhua, LIU Minghuan, MAO Baiwei	22-04-18
Ultra-Low Linewidth Frequency Stabilized Integrated Lasers: A New Frontier in Integrated Photonics	GU Zhenqian, YANG Zhen, ZHA Lulu, HU Junhui, CHI Nan, SHEN Chao	22-04-29
Monolithically Integrating a 180° Bent Waveguide into a III-Nitride Optoelectronic On-Chip System	ZHANG Hao, YE Ziqi, YUAN Jialei, LIU Pengzhan, WANG Yongjin	22-04-40
Performance Characterization of Visible Light Communication Based on GaN High-Voltage LED/PD	LU Meixin, JIANG Zitong, FANG Li, YAN Yiqun, YAN Jiabin	22-04-46

Review

Recent Advances in Video Coding for Machines Standard and Technologies	ZHANG Qiang, MEI Junjun, GUAN Tao, SUN Zhewen, ZHANG Zixiang, YU Li	22-01-62
RIS-Assisted Cell Free MIMO: A Survey	ZHAO Yaqiong, KE Hongqin, XU Wei, YE Xinquan, CHEN Yijian	22-01-77
Research on Multi-Core Processor Analysis for WCET Estimation	LUO Haoran, HU Shuisong, WANG Wenyong, TANG Yuke, ZHOU Junwei	22-01-87
Learned Distributed Query Optimizer: Architecture and Challenges	GAO Jun, HAN Yinjun, LIN Yang, MIAO Hao, XU mo	22-02-49
Review on Service Curves of Typical Scheduling Algorithms	GAO Yuehong, NING Zhi, HE Jia, ZHOU Jinfei, GAO Chenqiang, TANG Qingkun	22-02-55
Deadlock Detection: Background, Techniques, and Future Improvements	LU Jiachen, NIU Zhi, CHEN Li, DONG Luming, SHEN Taoli	22-02-71
A Survey on Task Scheduling of CPU-GPU Heterogeneous Cluster	ZHOU Yiheng, ZENG Wei, ZHENG Qingfang, LIU Zhilong, CHEN Jianping	22-03-83
Multi-View Image-Based 3D Reconstruction in Indoor Scenes: A Survey	LU Ping, SHI Wenzhe, QIAO Xiuquan	22-03-91
Intelligence Driven Wireless Networks in 5G and 6G Era: A Survey	GAO Yin, CHEN Jiajun, LI Dapeng	22-03-99

Research Papers

Filter Design of Wireless Base Station Power Supply	LI Wei, GUO Wei, WANG Zhida	22-01-95
Real-Time 4-Mode MDM Transmission Using Commercial 400G OTN Transceivers and All-Fiber Mode Multiplexers	REN Fang, LI Yidan, YE Bing, LIU Jianguo, CHEN Weizhang	22-01-106
A Distributed Acoustic Sensing System for Vibration Detection and Classification in Railways	ZHU Songlin, WANG Zhongyi, XIE Yunpeng, SUN Zhi	22-02-80
Adaptive Hybrid Forward Error Correction Coding Scheme for Video Transmission	XIONG Yuhui, LIU Zhilong, XU Lingmin, HUA Xinhai, WANG Zhaoyang, BI Ting, JIANG Tao	22-02-85
Waveguide Bragg Grating for Fault Localization in PON	HU Jin, LIU Xu, ZHU Songlin, ZHUANG Yudi, WU Yuejun, XIA Xiang, HE Zuyuan	22-02-94
Cooperative Distributed Beamforming Design for Multi-RIS Aided Cell-Free Systems	ZHU Yuting, XU Zhiyu, ZHANG Hongtao	22-02-99
Secure SSL/TLS Communication System Based on Quantum Keys	WANG Jigang, LU Yuqian, WEI Liping, JIANG Xinzao, ZHANG Han	22-03-106
Differential Spatial Modulation Mapping Algorithms	WANG Chanfei, CHAI Jianxin, XU Yamei	22-03-116
Multi-View Structured Light 3D Measurement System	LU Ping, ZHANG Yingjie, DENG Fangwei, LIU Wei, HUANG Shijun	22-04-53
A Filtering Coaxial Probe for Passive Intermodulation Characterization	BAI Yongjiang, YANG Jiye, ZHU Shaohao, YANG Ye, YE Ming	22-04-59
Unsupervised Motion Removal for Dynamic SLAM	CHEN Hao, ZHANG Kaijiong, CHEN Jun, ZHANG Ziwen, JIA Xia	22-04-67
Video Enhancement Network Based on CNN and Transformer	YUAN Lang, HUI Chen, WU Yanfeng, LIAO Ronghua, JIANG Feng, GAO Ying	22-04-78
A Privacy-Preserving Scheme for Multi-Party Vertical Federated Learning	FAN Mochan, ZHANG Zhipeng, LI Difei, ZHANG Qiming, YAO Haidong	22-04-89

The 1st Youth Expert Committee

for Promoting Industry-University-Institute Cooperation

Director CHEN Wei, Beijing Jiaotong University
Deputy Director QIN Xiaoqi, Beijing University of Posts and Telecommunications
LU Dan, ZTE Corporation

Members (Surname in Alphabetical Order)

CAO Jin Xidian University
CHEN Li University of Science and Technology of China
CHEN Qimei Wuhan University
CHEN Shuyi Harbin Institute of Technology
CHEN Siheng Shanghai Jiao Tong University
CHEN Wei Beijing Jiaotong University
GUAN Ke Beijing Jiaotong University
HAN Kaifeng China Academy of Information and Communications Technology
HE Zi Nanjing University of Science and Technology
HOU Tianwei Beijing Jiaotong University
HU Jie University of Electronic Science and Technology of China
HUANG Chen Purple Mountain Laboratories
LI Ang Xi'an Jiaotong University
LIU Chunsen Fudan University
LIU Fan Southern University of Science and Technology
LIU Junyu Xidian University
LU Dan ZTE Corporation
LU Youyou Tsinghua University
NING Zhaolong Chongqing University of Posts and Telecommunications
QI Liang Shanghai Jiao Tong University
QIN Xiaoqi Beijing University of Posts and Telecommunications
QIN Zhijin Tsinghua University
SHI Yinghuan Nanjing University
TANG Wankai Southeast University
WANG Jingjing Beihang University
WANG Xinggang Huazhong University of Science and Technology
WANG Yongqiang Tianjin University
WEN Miaowen South China University of Technology
WU Qingqing Shanghai Jiao Tong University
WU Yongpeng Shanghai Jiao Tong University
XIA Wenchao Nanjing University of Posts and Telecommunications
XU Mengwei Beijing University of Posts and Telecommunications
XU Tianheng Shanghai Advanced Research Institute, Chinese Academy of Sciences
YANG Chuanchuan Peking University
YIN Haifan Huazhong University of Science and Technology
YU Jihong Beijing Institute of Technology
ZHANG Jiao Beijing University of Posts and Telecommunications
ZHANG Yuchao Beijing University of Posts and Telecommunications
ZHANG Jiayi Beijing Jiaotong University
ZHAO Yuda Zhejiang University
ZHAO Zhongyuan Beijing University of Posts and Telecommunications
ZHOU Yi Southwest Jiaotong University
ZHU Bingcheng Southeast University

ZTE COMMUNICATIONS

中兴通讯技术(英文版)

ZTE Communications has been indexed in the following databases:

- Abstract Journal
- Cambridge Scientific Abstracts (CSA)
- China Science and Technology Journal Database
- Chinese Journal Fulltext Databases
- Index Copernicus
- Scopus
- Ulrich's Periodicals Directory
- Wanfang Data
- WJCI 2021-2023

Industry Consultants:

DUAN Xiangyang, GAO Yin, HU Liujun, HUA Xinhai, LIU Xinyang, LU Ping, SHI Weiqiang, TU Yaofeng, WANG Huitao, XIONG Xiankui, ZHAO Yajun, ZHAO Zhiyong, ZHU Xiaoguang

ZTE COMMUNICATIONS

Vol. 22 No. 4 (Issue 89)

Quarterly

First Issue Published in 2003

Supervised by:

Anhui Publishing Group

Sponsored by:

Time Publishing and Media Co., Ltd.

Shenzhen Guangyu Aerospace Industry Co., Ltd.

Published by:

Anhui Science & Technology Publishing House

Edited and Circulated (Home and Abroad) by:

Magazine House of ZTE Communications

Staff Members:

General Editor: WANG Xiyu

Editor-in-Chief: WANG Li

Executive Editor-in-Chief: HUANG Xinming

Deputy Editor-in-Chief: LU Dan

Editorial Director: WANG Pingping

Editor-in-Charge: ZHU Li

Editors: REN Xixi, XU Ye, YANG Guangxi

Producer: XU Ying

Circulation Executive: WANG Pingping

Assistant: WANG Kun

Editorial Correspondence:

Add: 12F Kaixuan Building, 329 Jinzhai Road,

Hefei 230061, P. R. China

Tel: +86-551-65533356

Email: magazine@zte.com.cn

Website: <http://zte.magtechjournal.com>

Annual Subscription: RMB 120

Printed by:

Hefei Tiancai Color Printing Company

Publication Date: December 25, 2024

China Standard Serial Number: ISSN 1673-5188
CN 34-1294/TN